Tunable Bose-Fermi and Fermi-Fermi Mixtures of Potassium and Lithium:

Phase Separation, Polarons, and Molecules

Rianne S. Lous, MSc.

The work described in this thesis was performed in the research group of Ultracold Quantum Matter at the Institute for Quantum Optics and Quantum Information (IQOQI) of the Austrian Academy of Sciences and at the Institute for Experimental Physics at the University of Innsbruck, both located in Innsbruck, Austria.

Photo back cover: IQOQI / M. R. Knabl

universität
innsbruck

Tunable Bose-Fermi and Fermi-Fermi Mixtures of Potassium and Lithium:

Phase Separation, Polarons, and Molecules

DISSERTATION

by

Rianne Semaja Lous, MSc.

submitted to the Faculty of Mathematics, Computer Science, and Physics of the University of Innsbruck, in partial fulfillment of the requirements for the degree of Doctor of Philosophy (PhD)

Innsbruck, July 2018

Advisor:
Univ.-Prof. Dr. Rudolf Grimm,

Co-advisor:
Prof. Dr. Florian E. Schreck,

Wetenschap is een regel;
mensen de uitzondering.

Abstract

Ultracold quantum gases, once prepared and trapped, give a wealth of possibilities for exploring various kinds of many-body systems. Selecting just two alkali metals, as in this thesis, already opens up the possibility to study mixtures where the elements differ in mass and in quantum statistics. Additionally, the presence of heteronuclear Feshbach resonances provides tunability of the interspecies interactions and gives access to the strongly interacting regime. Moreover, by realizing a population imbalance between the two species, the physics of quasiparticles in a Fermi sea, i.e. polaron physics, can be studied.

This thesis describes experiments with tunable Bose-Fermi and Fermi-Fermi mixtures of lithium and potassium, with a special focus on phase separation, polarons, and molecules. As a first insight, it shows how a ^{41}K Bose-Einstein condensate can be used to measure the temperature of a ^{6}Li deeply degenerate Fermi gas. Then, the thesis demonstrates the spatial phase separation that occurs for strong repulsion in this double-degenerate Bose-Fermi mixture and quantifies the residual spatial overlap between the two components by measuring three-body recombination losses. In a second series of experiments, a ^{40}K impurity interacting with a Li Fermi sea is studied with frequency- and time-domain spectroscopy. The lifetime and formation dynamics of polarons are measured for both attractive and repulsive interactions, as well as for varying interaction strengths. Finally, the thesis describes experiments with an interacting atom-dimer mixture. It shows that the mass imbalance between K and Li influences the interactions between the K atoms and Li-K Feshbach molecules up to the point where repulsion is turned into attraction. Furthermore, the lifetime of the atom-dimer mixture close to the Feshbach resonance is characterized.

All experiments are compared to theoretical models and excellent agreement is found. This illustrates how experimental studies of interacting ultracold quantum gases provide benchmarks for theoretical models on quantum matter. Increasing our knowledge of these many-body systems and their peculiar properties is important as similar systems exist in a multitude of physics domains, and scientific insights lead to new discoveries and can contribute to future technologies.

Kurzfassung

Sobald Quantengase gekühlt und gefangen sind, bieten sie eine Vielzahl an Möglichkeiten zur Erforschung verschiedener Arten von Vielteilchensystemen. Allein die Wahl zweier verschiedener Sorten von Alkaliatomen, wie in dieser Arbeit beschrieben, ermöglicht die Untersuchung von Mischungen, bestehend aus Elementen mit verschiedener Masse oder unterschiedlicher Quantenstatistik. Darüber hinaus erlaubt die Existenz heteronuklearer Feshbach-Resonanzen die Variation der Interspezies-Wechselwirkung und den Zugang zum stark wechselwirkenden Regime. Außerdem ermöglicht die Realisierung eines Populationsungleichgewichts die Untersuchung von Quasiteilchen im Fermisee, d.h. Polaronphysik.

Diese Dissertation beschreibt Experimente an Fermi-Bose und Fermi-Fermi-Mischungen, bestehend aus Lithium und Kalium mit durchstimmbarer Wechselwirkung. Im Fokus der Arbeit stehen Phasenseparation, Polaronen und Moleküle. Der erste Teil dieser Arbeit beschreibt wie ein Bose-Einstein-Kondensat aus ^{41}K Atomen verwendet werden kann, um die Temperatur eines entarteten Fermigases bestehend aus ^{6}Li zu messen. Anschließend wird gezeigt, dass in Anwesenheit einer starken repulsiven Wechselwirkung zwischen dieser doppelt entarteten Fermi-Bose-Mischung eine räumliche Phasenseparation auftritt und wie der verbleibende räumliche Überlapp zwischen den beiden Komponenten durch Messung von Drei-Körper-Rekombinationsverlusten beschrieben werden kann. In einer zweiten Gruppe von Experimenten werden ^{40}K-Minoritätsteilchen, welche mit einem Li-Fermisee wechselwirken, mittels Spektroskopie im Frequenzraum und in der Zeitdomäne untersucht. Damit werden sowohl die Lebensdauer als auch die Dynamik der Bildung von Polaronen für starke und schwache, sowie anziehende und abstoßende Wechselwirkungen gemessen. Abschließend beschreibt diese Dissertation Experimente mit wechselwirkenden Atom-Dimer-Mischungen. Es wird gezeigt, dass die ungleichen Massen von K und Li die Wechselwirkung zwischen den K-Atomen und Li-K-Feshbachmolekülen stark beeinflussen. Die Folgen reichen so weit, dass aus einer ursprünglich abstoßenden Wechselwirkung eine anziehende wird. Außerdem wird die Lebensdauer der Atom-Dimer-Mischungen in der Nähe der Feshbach-Resonanz charakterisiert.

Der Vergleich aller unserer Experimente mit theoretischen Modellen liefert eine vortreffliche Übereinstimmung. Dies zeigt, wie experimentelle Studien mit wechselwirkenden ultrakalten Quantengasen nützliche Vergleiche mit theoretischen Modelle der Quantenmaterie ermöglichen. Unser Wissen über diese Vielteilchensysteme und ihre besonderen Eigenschaften zu erweitern, ist insofern wichtig, als dass ähnliche

Systeme in einer Vielzahl von physikalischen Bereichen existieren und die neugewonnenen Erkenntnisse nicht nur zum Forstschritt in der Wissenschaft, sondern auch zur Entwicklung zukünftiger Technologien beitragen können.

Contents

CHAPTER 1

Introduction

Understanding complex states of matter and their properties is of essential importance for the science of today and the technologies of tomorrow. It led us from the first computer, which barely fitted into a single room, to the powerful pocket-size versions we carry around each day. Facilitated by a better fundamental understanding of semiconductor materials and their functionality, this strong minimization of the electronics was accompanied by an increase in computational power and decrease in manufacturing costs. With the electrical circuits down to the scale of a few atoms (10^{-9} m), the laws of quantum mechanics come more and more into play. Shifting from the classical to the quantum world there is a lot to explore and learn about matter whose peculiar properties can only be explained by quantum physics, so-called quantum matter. Just as with the first computer, it is hard to envision where studying quantum matter will lead us, but the potential is remarkable. Not only in the field of electronics, but also in the fields of metrology, sensors, computers, cryptography, and networks, quantum technologies and corresponding applications are emerging, using to their benefit the effects of quantum physics and the insights gained from fundamental research. This thesis is about a particular type of quantum matter, namely mixtures of ultracold quantum gases of neutral atoms. It describes the experiments performed with two different mixtures and the insights on interacting quantum matter derived from these studies.

To understand quantum matter, it is important to look into the interactions between particles and the laws of quantum mechanics that govern them. One interesting concept is the description of matter as both particles and waves — the wave-particle duality. The wavelength in relation to the phenomenon observed indicates which interpretation is easier to grasp. For instance, a gas of atoms is described as a gas of particles when the distance between the atoms is relatively large. However, when this distance is comparable to the length of the waves that describe the atoms, the physics is better understood by representing the atoms as waves. In that case the gas of atoms can be seen as a gas of overlapping waves and quantum statistics comes into play. The gas is said to be degenerate and the atoms will form either a degenerate Fermi gas (DFG) or a Bose-Einstein condensate (BEC). A BEC is formed when the atoms are bosons and a DFG when they are fermions. Bosons and fermions are the two classes of particles

that Nature knows. Fermions are the building blocks of matter, e.g. electrons, protons and neutrons, while bosons are mostly associated with the force-carrying particles, e.g. photons, gluons and Higgs bosons. Combining an even (uneven) number of fermions results in a bosonic (fermionic) composite particle and atoms can therefore be either one of the two classes. A degenerate atomic gas is a prime example of a many-body system that shows quantum behavior. It is interesting to study, since quantum phenomena closely related to a BEC lie at the basis of the operation of a laser and the explanation of frictionless flow, i.e. superfluidity.

The most commonly known fermionic many-body systems are electrons in a metal or semiconductor. The interactions between the electrons, especially the pair formation, are important for understanding superconductivity, one of the intriguing quantum phenomena visible in materials. Magnetic resonance imaging (MRI) in hospitals and superconducting power lines are examples of applications already available today because of the discovery of this feature. In a superconductor, below a certain temperature, the electrons flow without resistance and, in contrast to normal conductors, no energy is lost when a current is applied. Explaining why superconductivity is possible in only a few materials and why it is limited to temperatures typically below -200°C, is one of the major theoretical challenges for condensed matter physicists nowadays. Ideally, a better understanding of this phenomenon would create materials that show superconductivity at room temperature, which enables a wealth of applications. For instance, it would speed-up the development of high-speed "levitating" trains and a superconducting power grid, which could save us a lot of energy. By studying mixtures of fermionic quantum gases, more insight into the superconducting phenomenon and into quantum matter in general can be obtained [Cal18].

A variety of other systems would benefit from increasing our knowledge of interacting quantum matter. Quantum many-body systems exist everywhere in Nature and can be found in a multitude of physics domains, ranging from high-energy to condensed-matter and nuclear physics. Besides electrons in semiconductors, other examples are neutron stars, white dwarfs, atomic nuclei, and quark-gluon plasmas. The latter is a state of matter in quantum chromodynamics. Studying these quantum many-body systems by themselves is experimentally and theoretically challenging. Neutron stars and white dwarfs are at astronomical distances, while the quantum phenomena of electrons in semiconductors happen on femto second time scales (10^{-15} s), which is at the limit of what one can observe with current methods. Moreover, an exact numerical simulation of these many-particle systems is difficult. The computational power needed to give a microscopic theoretical description including quantum mechanics increases exponentially with the number of particles involved. This large amount of degrees of freedom, which is exploited in quantum computation, limits the possibilities of theorists as quantum computers are not yet available for them. Furthermore, it is hard to

test the validity of theoretical models that describe strongly interacting matter. This is because in the limit of strong interactions, most theories are no longer exact and rely on numerical approximations that need to be benchmarked by experiments.

Fortunately, as long as the underlying equations are the same, the quantum physics of these complex systems can be experimentally simulated by studying another well-controlled system that is accessible in a laboratory [Fey82]. This so-called quantum simulation is one of the major drives behind the research with ultracold quantum gases [Blo12]. For example, although the overall behavior and the forces involved are different, a core element in the above mentioned systems is the interacting many-body ensemble of fermions. A cloud of electrons in a metal can be described as a gas of charged fermionic particles (electrons) that interact via Coulomb interaction in the presence of a periodic lattice. The interior of a neutron star has a relatively low density region of neutron matter (fermions) which is expected to be similar to a strongly interacting two-component Fermi gas [Gez08, Sed18]. In white dwarfs, the star is prevented from collapsing under its own gravity by the Fermi pressure, a property associated with a many-body system of fermions. Furthermore, a nucleus can be described as a system of fermions held together by nuclear forces [Cal18], while the theoretical description of a quark-gluon plasma is based on interacting fermions with the interactions given by the color force [Ada12]. The universality of the physics involved is remarkable as the common factor in all of these systems is an interacting fermionic many-body system [Gio08]. Therefore, creating, probing, and studying a quantum gas of interacting fermionic neutral atoms provides a test bed to simulate the universal physics present in these systems [Blo08]. Some of the insights obtained can also be extended to cosmology [Hun13] or when considering pair formation to the chemistry of cold molecules [Boh17].

Quantum matter and its properties can be simulated and studied with ultracold quantum gases [Blo08, Tör14, Zwe12]. These well-controlled many-body ensembles of neutral atoms are created in an ultra-high vacuum setup. The gas has a temperature of a few hundreds of nanokelvin, which is one billionth of a degree above absolute zero (-273,15 °C). At these ultracold temperatures, the effects of quantum mechanics can be probed and the gas forms a BEC or DFG. The atoms are trapped using laser light and magnetic fields which also control the external and internal degrees of freedom of the gas. Moreover the interactions between the atoms can be tuned by changing the magnetic field thanks to the occurrence of Feshbach resonances [Chi10]. By exploiting this phenomenon, strongly interacting gases can be created and pair formation can be studied both for repulsive and attractive interactions. Both fermionic and bosonic ensembles as well as mixtures thereof can be studied. Mixtures are especially important when trying to study interactions in a fermionic many-body system. At ultracold temperatures, single component Fermi gases can not interact because of Pauli's exclu-

sion principle, which states that identical fermions can not occupy the same quantum state. Therefore, only a mixture of different fermions will show tunable interactions. The high degree of experimental control and the possibility to tune the interactions between the atoms are the core reasons why ultracold quantum gases can be used as quantum simulators. Experiments on ultracold quantum gases are a test bed for finding new states of quantum matter and for improving our understanding and theoretical description of complex many-body systems.

This thesis describes the experimental research with mixtures of ultracold quantum gases performed in the **Fe**rmionic **Li**thium (**Bo**sonic) **K**alium[1] lab, in short FeLi(Bo)Kx, at the Institute of Quantum Optics and Quantum Information in Innsbruck. The mixtures consist of fermionic lithium (^{6}Li) and either bosonic potassium (^{41}K) or fermionic potassium (^{40}K), which results in either a Bose-Fermi or a Fermi-Fermi mixture. The interaction between the two species can be tuned and this gives access to the strongly interacting regime. The research resulted in six publications, which can be found in Chap. 4-9. Among the research highlights are the observation of a spatial phase separation between a BEC and the DFG, when tuning the repulsive interaction between them. This observation is similar to what one observes when trying to mix water and oil; they won't mix. However, in our case the separation is a quantum effect. Another highlight are the measurements with a DFG of lithium that is interacting with a small amount of K, an impurity. It is known that the impurity dresses itself with the environment and forms a so-called polaron, a quasiparticle which can be described as an entity of its own and we studied the lifetime and formation of this polaron. The third highlight is the observation that the mass-imbalance between K and Li influences the interactions between atoms and Li-K molecules up to the point where repulsion is turned into attraction. Phase separation, polarons, and molecules are the main themes of this thesis. A more in depth overview of the research topics can found in the next chapter (Sec. 2.5), together with an overview of the field of ultracold quantum mixtures. This is followed by a brief account of to the FeLi(Bo)Kx experimental details, before presenting the publications.

The research presented in this thesis shows the large versatility of two-species ultracold quantum gas experiments and how these type of experiments contribute to our understanding of various kinds of strongly interacting quantum matter. Many-body systems are ubiquitous in Nature, yet the universality in their building blocks enables us to simulate and study them with ultracold quantum gases. It is a beauty of Nature that such universality exists and an ingenuity of human kind that the technologies are available to create, control and manipulate quantum simulators such as ultracold quantum gases.

[1] Kalium is the German name for potassium

CHAPTER 2

Ultracold Mixtures and Research Topics

The field of ultracold quantum gases is an important and active subfield of Atomic, Molecular and Optical (AMO) physics. It researches quantum many-body physics and the many-body systems of interest are dilute gases of neutral atoms, in contrast to the dense liquids or solids in solid-state and condensed matter physics. However, analogies between both fields allow for quantum simulation of condensed matter with ultracold quantum gases [Blo12] and this is one of the major drives behind the research field.

In this thesis experiments with tunable Bose-Fermi and Fermi-Fermi mixtures are presented and the aim of this Chapter is to give an overview of the research field and discuss the research topics addressed in this thesis. After introducing degenerate Bose and Fermi gases (Sec. 2.1), I will give a brief account of the history of the field, focusing on experimental achievements (Sec. 2.2). In Sec. 2.3, I will highlight the research performed with ultracold mixtures followed by a discussion of impurity physics in the context of ultracold atoms (Sec. 2.4). The Chapter is concluded by describing the research topics of this thesis (Sec. 2.5).

2.1 Degenerate Bose and Fermi gases

Interacting atomic gases show interesting quantum behavior, which is explored in the field of ultracold quantum gases. In this Section I will discuss the distinction between Fermi and Bose gases and what the requirements for such gases are to reach the quantum-degenerate regime. For an introduction into the making of an ultracold gas, Ref. [Jer14] is a good starting point. For more details on the properties of ultracold quantum gases, especially in harmonic traps, the excellent reviews on Fermi gases [Ing08, Gio08, Zwe12, Tur12] and Bose gases [Ket99] can be consulted.

Ultracold quantum gases can be divided into two types based on the Fermi or Bose quantum statistics that describes their constituents. This division is unambiguous in nature and every elementary or composite particle is either a fermion or a boson. Examples of bosons are photons and phonons, where as commonly known fermions are

electrons, protons and neutrons. The distinction between the two classes is made by a property called spin. When this quantized intrinsic angular momentum is an integer value, the particle is a boson and follows Bose-Einstein statistics. For half-integer values the particle is a fermion and follows Fermi-Dirac statistics. Combining two fermions into a pair creates a composite bosonic particle and therefore, atoms are either fermions or bosons. Due to the neutral charge of an atom the number of protons and the number of electrons is equal, leaving the number of neutrons to dictate whether the atom is bosonic (even number) or fermionic (odd number). Different isotopes of the same element can thus have different quantum statistics.

The distinction of whether a quantum gas consists of bosons or fermions is important when the quantum-degenerate regime is probed. In classical gases, each particle is distinct and interchanging two particles leads to a different system. In the quantum-degenerate regime, the particles are identical and indistinguishable; the individuality of the particles is lost. The gas has reached quantum degeneracy and the macroscopic behavior of this many-body system is governed by its particle statistics. The wavefunction of a many-body system of bosons is symmetric under the exchange of particles, while that of fermions is antisymmetric. For fermions, this results in Pauli's exclusion principle, where no two identical fermions can occupy the same quantum state. Thus a system of N identical fermions will occupy N different quantum states. For temperatures close to zero, these fermions fill the energy levels up from the lowest level to the Fermi energy and form a degenerate Fermi gas (DFG). The energy of the highest filled quantum state, the Fermi energy, depends on the number of fermions in the system. Associated with the Fermi energy is the Fermi pressure and this pressure prevents the Fermi gas inside of neutron stars and white dwarfs from collapsing under its own gravity. On the contrary, all atoms in a system of N identical bosons can occupy the same quantum state. Moreover, the occupation of the same state is actually favored. When N bosons occupy the same state, the probability to get an additional boson in that state is enhanced by a factor of (N+1). Thus, for temperatures close to zero, a macroscopic occupation of a single quantum state takes place, the so-called Bose-Einstein condensate (BEC) is formed. This macroscopic behavior relies on the microscopic properties of the particles and lies at the foundation of phenomena such as lasers, superfluidity and superconductivity.

To reach quantum degeneracy with atomic gases and observe a DFG or a BEC, it is important to compare the length scales involved. Two length scales should be considered when discussing a non-interacting gas and a third one if interactions come into play. First, there is the mean distance between particles $d = n^{-1/3}$, which depends on the spatial density n. An ultracold gas typically has densities of about $10^{19}\,\mathrm{m}^{-3}$, which corresponds to a spacing of a few hundreds of nanometers between the particles. Second, there is the temperature of the gas, or better said the de Broglie wavelength

of the particles. This wavelength characterizes the wave nature of particles in context of the wave-particle duality. This length scale changes with temperature T according to its definition $\lambda_T = \sqrt{2\pi\hbar^2/mk_B T}$, where $\hbar$ is the reduced Planck constant, m the mass of the particle and k_B the Boltzmann constant. A non-interacting quantum gas becomes degenerate when the interparticle spacing between atoms is smaller then the thermal de Broglie wavelength ($d \leq \lambda_T$), which is equivalent to a phase-space density $d^{-3}\lambda_T^3 > 1$. At these temperatures the waves that describe each particle overlap, interfere, and the distinction between individual waves is lost. At the typical densities of an ultracold gas, the temperatures required to obtain degeneracy are around a few hundred of nanokelvins. Of course increasing the density of the gas would give less constrains on the temperature, but this shortens the lifetime of the gas and thus the measurement time of an experiment.

The quantum gas discussed so far is a metastable state of matter. It can be created by confining a gas in a wall-free trap such that nucleation on surfaces, which triggers the phase transition into a solid, is prevented. In these traps the lifetime of the gas is determined by two- and three-body loss processes. Through collisions the particles can gain enough kinetic energy to leave the trap and this gives an upper bound on the densities that quantum gases can have. The rate of three-body recombination, where three atoms collide and form a bound molecule and a free atom that carries away the binding energy, scales as the density cubed. It is this inelastic loss process that drives the transition towards chemical equilibrium. A second constraint on the density comes from the elastic scattering between the particles, which enables them to rethermalize and reach a kinetic equilibrium. If the density is too low, collisions between particles take a long time to occur and thermalization might not happen within the lifetime of the gas. These density constrains leads us back to the typical densities of about $10^{19}\,\mathrm{m}^{-3}$ most commonly seen in experiments with ultracold gases.

For an interacting gas a third length scale comes into play, the range of the atom-atom interaction r_0. The particles are in the gas phase ($d \gg r_0$) and only interact pairwise during collisions. The interactions between particles stems from an induced electric dipole moment and this second order electric dipole-dipole interaction, more often called van der Waals interaction, is short-ranged and isotropic. Additionally, many ground-state atoms have a permanent magnetic dipolar moment, which leads to a long-range anisotropic dipole-dipole interaction. However, for alkali atoms this type of interaction is roughly two orders of magnitude weaker than the induced van der Waals interaction. Elements like erbium, dysprosium and chromium, for instance, do have a strong magnetic dipolar moment and these systems, along with polar molecules or Rydberg atoms, are used to study long-range dipolar physics. Here, we focus on alkali atoms where, for low temperatures, r_0 is given by the s-wave scattering length

parameter a.

In an interacting ultracold quantum gas, the effects of quantum mechanics can be seen once the temperature is cold enough that the thermal fluctuations no longer mask the quantum effects. Quantum mechanics comes into play when r_0 or d is smaller than λ_T. For high temperatures, in the regime of $\lambda_T \ll r_0 \ll d$, the system is described as a classical gas. For colder temperatures, when the s-wave scattering picture applies, the collisions between particles are affected by quantum mechanics once $a \ll \lambda_T \ll d$ and collisions require explicit quantum mechanical treatment. Quantum degeneracy is obtained for $a \ll d < \lambda_T$ and the system can be described as a weakly interacting BEC or DFG within the mean-field approximation. By tuning the interaction in an ultracold quantum gas, one can also reach the strongly interacting regime where $d < a < \lambda_T$. Here, the description of the degenerate many-body system as a single macroscopic wavefunction fails and rich physics and complex quantum phases are expected.

2.2 Historical Review

The history of the field of ultracold quantum gases is marked by the year 1995. At that time, almost 70 years after their initial prediction, the first degenerate gases, namely Bose-Einstein condensates, were observed [And95, Dav95]. The concept of a BEC dates back to the 1920's, when Bose postulated his Bose statistics for photons [Bos24] and Einstein extended this to non-interacting atoms [Ein24, Ein25]. This Bose-Einstein statistics predicts that for low temperatures a large fraction of atoms would occupy the lowest energy state. London and Tisza [Lon38, Tis38] pointed out that the concept of condensation is actually quantum behavior on a macroscopic size-scale and could be an underlying mechanism of superfluidity in liquid helium. Shared between laser light[1], superconductivity[2], and superfluidity[3], the remarkable behavior of a macroscopic occupation of one single quantum state motivated the pursuit of realizing a BEC in a gas [Cor02]. Although spin-polarized hydrogen, which remains a gas down to zero temperature [Stw76], seemed the prime candidate, it were gases of rubidium and sodium that showed this new state of matter. Both the characteristic signatures of a bimodal density distribution and an anisotropic expansion were observed. In 2001, E. A. Cornell, W. Ketterle and C. E. Wieman received the Nobel Prize for their observations of a BEC [Cor02, Ket02].

It is not straightforward to create a gas of atoms cold enough to see BEC formation and many studies preceded the discovery of the BEC. Creating a trap without walls is

[1] The Nobel Prize in Physics 1964
[2] The Nobel Prize in Physics 1913, 1962, 1972, 1973, 1987, 2003
[3] The Nobel Prize in Physics 1996, 2003

essential for creating a degenerate gas, as nucleation on material surfaces causes the gases to condense into a liquid and/or freeze into a solid when cooled down. The development of the laser in the late 1960s and the studies of atom-light interaction that followed, led to the idea that laser light could be used for cooling down as well as trapping atoms in ultra-high vacuum environments. Techniques such as Magneto-Optical Traps (MOTs) and Zeeman slowers were invented, most of which are still at the basis of any ultracold quantum gas experiment today[4]. In 1997, S. Chu, C. Cohen-Tannoudji and W. D. Phillips received the Nobel Prize for the development of these powerful methods [Chu98, CT98, Phi98]. Realizing that these techniques made it possible to keep a gas of atoms long enough in the gas phase to allow for condensation, was an important step for BEC creation. To make the first quantum gas, the technologies of laser cooling and trapping were used as a first cooling step to reach the mircokelvin temperature range. This was followed by evaporative cooling [Ket96] and degeneracy was reached.

With a cold BEC at hand, the properties of this macroscopic matter wave could be studied [Ing99]. Some key experiments were, e.g. collective excitations [Jin96, Mew96], the interference between two BECs [And97], the demonstration of an atom laser [Blo99], and the creation of vortices as a direct evidence for superfluidity [Mat99, Mad00, AS01]. Over the years, the cooling techniques developed further and BECs have now been demonstrated in thirteen chemical elements, i.e. H [Fri98], metastable He [Rob01, PDS01], Na [Dav95], Li [Bra95, Bra97], K [Mod01], Rb [And95], Cs [Web03a], Ca [Kra09], Sr [Ste09, Mar09, Ste10], Cr [Gri05], Dy [Lu11], Er [Aik12], and Yb [Tak03, Fuk07a, Fuk09]. This led to an incredible amount of experiments on single-component BECs as well as on multicomponent BECs. A special case of the latter are the so-called called spinor condensates, where multiple spin states coexist and in which both superfluidity and magnetic order can be investigated [SK13].

With the field of ultracold bosonic quantum gases growing, the eyes turned towards fermions, the other type of particles. The Fermi-Dirac statistics, as derived by Fermi and Dirac separately [Fer26, Dir26], describes how fermions at low temperatures form a degenerate Fermi gas. Because of the Pauli exclusion principle[5] [Pau46], fermions can not occupy the same quantum state, in contrast to bosons. As a consequence identical fermions must collide in odd partial waves and thus at low temperatures, where collisions are described by s-waves only, no collisions happen between identical fermions[6]. Therefore either a mixture of different internal spin states or of

[4] An introduction into laser cooling and trapping is given in Ref. [Met99]

[5] The Nobel Prize in Physics 1945

[6] This is the case for alkali atoms. However, for dipolar gases like Cr, Dy, and Er, where the dipole-dipole interaction plays an important, single-component Fermi gases can be evaporatively cooled as the collisions are not restricted to the s-wave regime for ultracold temperatures [Aik14].

different atoms was needed to cool a Fermi gas to quantum degeneracy.

A couple of years after the first BEC, Fermi degeneracy was achieved by cooling a spin mixture of fermionic potassium in 1999 [DeM99] and in 2001 through sympathetic cooling fermionic lithium in a mixture with its bosonic isotope [Sch01a, Tru01]. The latter experiments also showed the first simultaneous quantum degeneracy of bosonic and fermionic gases. Most of the early work on Fermi gases was done with ^{6}Li and ^{40}K, but gradually more fermions were cooled. To date, Fermi degeneracy has been demonstrated for isotopes of eight chemical elements, i.e. He [McN06], Li [Tru01, Sch01a], K [DeM99], Cr [Nay15], Sr [DeS10, Tey10], Dy [Lu12], Er [Aik14], and Yb [Fuk07b]. Certain phenomena are still obscured by temperature and considerable effort is made to decrease the degeneracy of Fermi gases. For example, for lithium and potassium, gray-molasses cooling on the D1 line is now realized [Fer12, Gri13, Bur14a, Sie15], improving the starting conditions before evaporative cooling of the gas.

Especially once Feshbach resonances were discovered [Cou98, Ino98], the possibilities of studies with bosonic and fermionic quantum gases and mixtures thereof became numerous. A Feshbach resonance (FR) occurs when a molecular bound state of almost no energy couples resonantly to the free state of two colliding atoms. The difference in the magnetic moment between those two states, can be used to tune the states in and out of resonance by changing the magnetic field. On the repulsive side of a FR, a weakly bound state exists and this allows the creation of weakly bound pairs [Köh06]. Feshbach resonances can occur between atoms in the same spin state, in different spin states and between spin states of different elements. Due to a FR, the interaction between atoms can be tuned from weak to strong and from attractive to repulsive. The lifetime of a gas with strong interactions is limited by three-body recombination, and often atom loss measurements are used to characterize FRs. These FRs were first observed in a BEC of sodium [Ino98] through atom loss measurements and in a rubidium gas [Cou98] by photoassociation spectroscopy. For fermionic gases the first FRs were seen in ^{40}K [Lof02] and ^{6}Li [O'H02], while the first heteronuclear FR, was observed in ^{7}Li-^{23}Na [Sta04], followed by the Fermi-Bose mixture of ^{40}K-^{87}Rb [Ino04].

Feshbach resonances are an incredibly useful phenomenon and soon became a workhorse in the field [Chi10]. They allow experimentalists to control the two-body interactions between particles by tuning a magnetic field. Feshbach resonances were used to enhance evaporative cooling and many elements reached degeneracy through their use. With FRs, strongly interacting many-body systems can be studied and universal physics can be explored. A prime example is the observation of the Efimov effect [Kra06] and the subsequent study of this universal few-body physics phenomenon in many gases trough measurements of three-body recombination [Gre10, Fer11].

Another example of key experiments with FRs in bose gases, is the demonstration of beyond mean-field effects in a BEC. When the scattering length is smaller than the interparticle spacing, a BEC can be described by the Gross-Pitaevskii equation, which takes interactions into account via a mean-field potential [Dal99]. To go beyond this description, a FR can be used to increase the interactions between the bosons. However, the limitations due to the fast inelastic decay of a Bose gas close to a FR [Cor00] have to be overcome and in 2008 beyond-mean-field behavior in an interacting atomic Bose gas was finally seen [Pap08a][7]. Furthermore, FRs in Bose gases enable the study of non-interacting condensates by tuning the scattering length to zero, the study of phase separation for strong attractive interactions [Chi10] and the study of strongly correlated Bose gases [Che16].

Fermi gases are remarkably stable near *s*-wave FRs due to a Pauli suppression effect [Cub03, Joc03b, Reg04a, Pet04b, Pet05b, Pet05a]. For low temperatures, only *s*-wave collisions take place and these only happen between different spin states. *p*-wave FRs in the same fermionic spin state have also been observed and they show significantly more loss than their *s*-wave counterparts [Reg03, Zha04, Sch05]. The exploration of ultracold Fermi gases [Ing08, Tur12] is mostly done with mixtures and a more detailed discussion of the research directions can be found in Sec. 2.3.2. Research highlights were, e.g. the observation of molecular condensates [Joc03a, Gre03, Zwi03, Bou04] and the study of the BEC-BCS crossover [Zwe12, Cal18].

Optical potentials offer another remarkable possibility for controlling ultracold quantum gases. They can be used to change the dimensionality of the system, create homogeneous potentials [Gau13, Sch14, Nav15, Cho15, Muk17] and make periodic potential arrays, i.e. optical lattices [Blo08]. With optical lattices, the gas of atoms can be confined to a periodic structure, which mimics the crystal lattice of a solid. Moreover, strong correlations between particles can be created by strong confinement. Examples are the superfluid to Mott-insulator transition [Gre02], which can be crossed by tuning the depth of the lattice [Jak98], and the realization of the Fermi-Hubbard model [Ess10]. Furthermore, new phases such as, e.g. the Tonks-Girardeau Bose gas in 1D [Pet00, Kin04b, Par04], and the Kosterlitz-Thouless crossover in 2D [Had06], can emerge when controlling confinement and dimensionality. Additionally, with the development of the quantum gas microscope [Bak09, She10, Che15, Hal15, Par15b, Omr15, Edg15], the observation and control of individual atoms became available. The research performed with atoms in optical lattices focuses on the engineering of lattice-based many-body systems for quantum simulation and quantum information [Lew12, Gro17] and complements the research in the bulk.

In recent years, systems with strong dipole-dipole interactions have also become

[7] Previously, beyond-mean-field effects were observed in a molecular BEC [Alt07].

available. In contrast to the contact interaction mostly studied with alkali atoms, the dipole-dipole interaction is long-range and anisotropic. Gases of atoms with a large permanent magnetic moment like Cr, Dy and Er, show this type of interaction and these dipolar gase have now been cooled to degeneracy [Gri05, Lu11, Aik12]. An example of the competition between contact and dipolar interactions that can be studied with those systems, are the quantum droplets recently seen [Kad16, FB16b, Cho16, Sch16, FB16a, Wen17]. Similar features have also been observed in a mixture of potassium BECs [Cab18]. Here, although only contact interaction is present, the droplets stabilize due to quantum fluctuations. Other systems that show long-range interactions are heteronuclear polar ground-state molecules [Car09, Mos17], Rydberg atoms [Saf10], and cold molecules [Boh17]. Molecules have an electric dipole, which leads to a strong interaction with other molecules due to dipole forces. Efforts are under way to cool molecules, such as CaF, SrF, YO directly from the gas phase and magneto-optical traps have been created. However, the manifold of electronic, vibrational, and rotational degrees of freedom on top of the hyperfine and Zeeman splittings, makes it much less straightforward to apply the standard laser and cooling techniques developed for atoms. All these systems offer the possibility to study dipolar many-body physics, which is of special interests due to its analogies with condensed-matter systems [Bar12].

Now, a few decades after the realization of the first quantum gas, the research field of ultracold quantum gases has spread out into many exciting research directions. Topics range from few- to many-body physics and from getting even colder to precisely mimicking condensed matter systems and beyond. Quantum gases are explored all over the world and provide valuable fundamental insights into complex many-body phenomena. Throughout the years, new directions have opened up, e.g. dipolar gases, nevertheless intriguing questions remain with regards to bulk mixtures of fermions and bosons, especially on topics such as strong interactions and mixture with mass or population imbalance.

This year will mark the beginning of the study of ultracold quantum gases in the microgravity environment of space. In may 2018 the cold atom laboratory (CAL) arrived at the International Space Station. On board are rubidium and potassium isotopes as well as lasers and magnetic field coils to cool, trap and manipulate the species by themselves or mixtures thereof. This is but one example of the future of the field of ultracold quantum gases. Other prospects are the quantum simulation of systems beyond what can be theoretically modeled [Gro17] and the extension of our knowledge on topics such as quantum magnetism, itinerant ferromagnetism [Val17, Mas14], dipolar physics [Bar12], and controlled cold chemistry [Boh17].

2.3 Ultracold Mixtures

Once single-component quantum gases can be well controlled, mixtures are the next logical step. One can mix different spin states, different isotopes of the same element or different elements. Mixtures give the opportunity to study the interplay between two different gases as well as the effect of unequal populations. Additionally, heteronuclear mixtures allow the study of mass imbalanced many-body systems and combinations of mixed quantum statistics. Moreover the response to external fields for each component can be different and mixed-dimensional systems can be created, e.g. by using a species-selective optical lattice [LeB07]. Another advantage is the possibility to use one of the components as a sensitive probe of the properties of the other component in the gas. For example, a second species can be used to measure the temperature of an ultracold gas with which it is in thermal equilibrium (Chap. 4, [Lou17b]) and an atomic gas with known polarizibility can be used as a probe for the polarizibility of another element [Rav18].

A first choice for combining different atoms is the creation of bialkali mixtures due to the extensive knowledge available to cool and trap alkali atoms. Here, in Innsbruck, two alkali atoms, lithium and potassium, were chosen to create one of the first heteronuclear Fermi-Fermi mixtures. Every new element which reaches degeneracy gives another possibility for mixing and mixtures beyond alkali atoms are becoming available, e.g. Dy-Er [Ilz18], Sr-Rb [Bar18], and Dy-K [Rav18]. Additionally mixtures with metastable noble gases [Vas12] and with extreme mass ratios [Pir14, Tun14, Roy17, Kon16] are being created. Reaching degeneracy with two species is not an easy task and quite often the scattering properties of a mixture are not previously known. Nevertheless it is worth the effort, because of the fascinating research opportunities they provide. In this Subsection, I give a brief overview of the different types of ultracold mixtures and the research directions that are being pursued with them.

2.3.1 Bose-Bose Mixtures

The first mixture created was a Bose-Bose mixture between two hyperfine states of ^{87}Rb [Mya97]. Soon a mixture of sodium spin states followed [Ste98] and with it the discovery of two major topics that can be studied with Bose-Bose mixtures: spinor condensates [SK13] and miscibility. A spinor condensate is a condensate in which the spin state of the atoms is left as a degree of freedom. In contrast to scalar BECs, where often the trap dictates which hyperfine state is stable, in spinor BECs spin changing collisions can occur. Studying the dynamics and equilibrium properties of these mixtures leads to a wealth of phases and the study of topological defects as well as spin textures [SK13].

In these spinor condensate, for the first time, miscible and immiscible condensates were observed [Ste98]. Following Ref. [Lee16], the miscibility of Bose-Bose mixtures, for a homogeneous system, is characterized by the miscibility parameter Δ and depends on the ratio of the intra- and interspecies scattering lengths as,

$$\Delta = \left(g_{11}g_{22}/g_{21}^2\right) - 1, \tag{2.1}$$

where $g_{ij} = 2\pi\hbar a_{ij}/\mu_{ij}$ is the effective interaction strength, $\mu_{ij} = \left(m_i^{-1} + m_j^{-1}\right)^{-1}$ is the reduced mass and a_{ij} is the scattering length between components i and j. If the miscibility parameter is positive, the two components can spatially overlap, while for negative values they phase separate. With the aid of FRs, the miscible-immiscible transition has been studied in several mixtures of, e.g. ^{87}Rb [Toj10], ^{87}Rb- ^{85}Rb [Pap08b], ^{87}Rb-^{133}Cs [McC11], ^{87}Rb-^{23}Na [Wan16], and ^{87}Rb-^{39}K [Wac15].

Another research direction for Bose-Bose mixtures is the production of ultracold polar molecules. These systems are used to study dipolar physics and controlled quantum chemistry [Car09, Mos17]. Heteronuclear ground state molecules have an electric dipole moment, which makes it an interesting system to study long-range interactions. The molecules can be created by transferring Feshbach dimers to the ground-state via two-photon stimulated Raman adiabatic passage [Ber98]. Feshbach dimers are formed by ramping over a Feshbach resonance and associating the atoms into weakly bound dimers. However, if the mixture is immiscible, the creation of Feshbach dimers becomes difficult. Therefore, most often the atoms are loaded into optical lattices before Feshbach association takes place, e.g. [Rei17]. Furthermore, by creating these molecules in a lattice, one can simulate how this many-body system of dipoles reacts to the periodic structure formed by the atom cores inside a semiconductor. The physics described here is the Bose-Hubbard model when the molecules are bosonic or the Fermi-Hubbard model when the molecules are fermionic. The latter is the case for molecules created from a Bose-Fermi mixture and comes closer to the analogy of electrons in a semiconductor. To date, ground state molecules from Bose-Bose mixtures have been demonstrated in the singlet state in Cs_2 [Dan10], RbCs [Tak14, Mol14] and NaRb [Guo16] and in the triplet state in Rb_2 [Lan08b]. By creating the dimers in the triplet groundstate, the dimers additionally have a magnetic moment, which leads to another interesting system to study.

2.3.2 Fermi-Fermi Mixtures

From the beginning of the research on ultracold Fermi gases Fermi-Fermi mixtures have been explored. The Pauli effect makes Fermi gases stable near FRs, but also

prevents collisions between particles in the same quantum states. Thus, exploring interacting Fermi gases and their phase diagrams with ultracold alkali gases required ultracold mixtures. This suppression of atom loss, called the Pauli suppression effect [Pet04b, Pet05b, Pet05a], was observed in strongly interacting spin mixtures of ^{6}Li [Cub03, Joc03b] and ^{40}K [Reg04a]. The special interest in fermionic pairing and Fermi superfluidity comes from the important role fermionic many-body systems play in matter, e.g. high T_c superconductors or neutron stars [Cal18]. Studying fermionic ultracold gases can give a quantitative comparison between theoretical models and experiments [Blo08]. Here, I will highlight three of the research directions of interacting Fermi gases: the BEC-BCS crossover, the unitary Fermi gas and strongly interacting heteronuclear mixtures.

The BEC-BCS crossover [Zwe12] is an important universal phenomenon in interacting Fermi gases and shows how pairing changes due to many-body effects. It describes the transition of a many-body system from a BEC of composite bosons to a superfluid of Cooper pairs, when the two-body interaction is tuned from repulsion to attraction across a FR. In the limit of weak interactions the system can be described with either BCS theory (attractive interactions) or BEC theory (repulsive interactions). On the repulsive side of the FR, the atoms are associated into weakly bound Feshbach dimers and the size of the dimer is smaller than the interparticle distance. The system of weakly bound pairs of fermions can be seen as a gas of composite bosons and below a critical temperature T_c shows Bose-Einstein condensation [Gre03, Joc03a, Zwi03, Bou04]. Above the critical temperature the bosons act as normal Bose gas of molecules and only for a temperature higher than their binding energy these pairs will break up.

On the attractive side the story is vastly different. Above T_c, the system is described by Landau's Fermi liquid theory. This interacting Fermi gas can be understood in terms of a non-interacting gas of quasiparticles, where the quasiparticles are atoms dressed by excitations of the Fermi sea. When the system is cooled, pair formation happens almost simultaneously with the condensation of these pairs. The temperatures for pair formation and for condensation are close. The pairing is described by the BCS theory and happens between particles with opposite momentum such that a bound pair of zero center-of-mass momentum is created, a Cooper pair. The size of the Cooper pairs is much larger than the interparticle distance and the bound pair can not be described as a composite bosonic particle. The fermionic nature of its constituents matters. Nevertheless, below T_c these pairs condense [Reg04b, Zwi04] and the system shows superfluidity [Zwi05].

The described phase diagram is universal for all Fermi gases, when expressed in the dimensionless parameters of interaction $(k_\mathrm{F}a)^{-1}$ and temperature T/T_F. Here, k_F is the Fermi wave vector, a the scattering length and T_F is the Fermi temperature. In

a homogenous gas, the critical temperature for condensation evolves from $T_c \ll T_F$ for very weak attraction, to $T_c \simeq 0.167(13)\,T_F$ [Ku12] for $|a| \to \infty$ and then settles at $T_c \simeq 0.218\,T_F$ on the BEC side [Hau07]. A wealth of studies have been made on the crossover between the BCS and BEC limit [Gri08, Zwe12], showing the powerful techniques which can be used to probe this many-body system, e.g. including collective excitations [Kin04a, Bar04], radio-frequency spectroscopy [Chi04, Sch08, Ste08b] and photoassociation [Par05]. The superfluidity along the crossover was confirmed by the observation of vortices [Zwi05] and its two-component nature by the observation of second sound [Sid13].

A region of special interest for the Fermi mixture is unitarity, where $|a| \to \infty$. Here, the thermodynamics of the Fermi gas follows universal behavior [Ho04]. For zero temperature the only relevant energy scale is the Fermi energy and the interparticle distance the only relevant length scale. The scattering length drops out of the description of the gas. Any Fermi gas at unitarity and at zero temperature can be described as a non-interacting Fermi gas with a simple scaling factor, called the Bertsch parameter ξ. This universality has led to a great interest in these unitary Fermi gases [Zwe12]. Several experiments have measured the equation of state and the Bertsch parameter, e.g. [Nas10, Nav10], with the latest result indicating $\xi = 0.376(4)$ [Ku12]. For an overview of the theoretical predictions and numerical models, see Ref. [Zwe12].

Away from unitary but at strong interactions (for $(k_F|a|)^{-1} < 1$) the behavior of Fermi-Fermi mixtures is not yet fully understood and experiments accessing this regime can provide useful insights and tests for theoretical models. Tuning the interaction with FRs enables the study of these strongly interacting Fermi gases, which were first observed in 2002 [O'H02, Bou03]. Especially in the case of population imbalanced mixtures [Mas14] (see Sec. 2.4) or in the case of mass imbalance, strongly interacting Fermi gases are interesting to study. Population imbalance can easily be obtain by selectively varying the atom number of the two spin states involved, while mass imbalance comes from having a heteronuclear mixture of fermions.

The first double-degenerate heteronuclear Fermi-Fermi mixture created was with Li and K and this mixture has been studied both by our group [Wil08] as well as in Munich/Singapore [Tag08], Amsterdam [Tie10], Paris [Rid11] and Cambridge [Wu11]. To study strong interactions in heteronuclear mixtures, it is beneficial to find an s-wave Feshbach resonance whose character is entrance-channel dominated [Chi10, Köh06]. For these type of FRs, the mixture is more stable against elastic and inelastic atom losses even for strong interactions. Several resonances in the Li-K mixture were investigated [Wil09, Tie09b, Tie10, Cos10, Nai11] and the Feshbach resonances turned out to be relatively narrow, i.e. closed-channel dominated. Nevertheless, the properties of the FR at 155 G were favorable enough to study the strongly interacting regime. We studied the expansion dynamics of the mixture for tunable interactions and found

pronounced effects of hydrodynamic behavior, associated with this strong interaction between the two species [Tre11]. On the repulsive side of this FR, we additionally studied the effects of mass-imbalance in an atom-dimer mixture as is discussed in Chap. 8 [Jag14]. The stability of the mixture close to the FR and the suppression of losses due to the Pauli effect is studied in Chap. 9.

With the achievement of Fermi degeneracy in many more elements beyond Li and K, there is a wealth of possible Fermi-Fermi mixtures that can be realized, e.g. Dy-K [Rav18] and Li-Cr. These new systems can extend the research on heteronuclear Fermi-Fermi mixtures, e.g. [Liu03, Bar08, Nis09a, Ors10, Key11, Sot12, Dai12, Cui13, Bra15, Wan17] as well as explore the wide variety of many-body physics that can be probed in fermionic mixtures, e.g. [Pet07, Isk08, Bau09c, Gez09, Gub09].

2.3.3 Bose-Fermi Mixtures

The two components in a mixture do not have to follow the same quantum statistics. By selecting different isotopes or elements, Bose-Fermi mixtures can be created. These mixtures can have a small difference in mass when isotopes of the same element are combined or additionally feature mass imbalance when two different elements are used. A prominent example is the mixture of bosonic ^{4}He and fermionic ^{3}He [Ebn71], which is now commonly used in dilution refrigerators [Das65, Pob07] and shows the intriguing phenomenon of phase separation. Bose-Fermi mixtures become especially interesting when degeneracy is reached and both a degenerate Fermi gas (DFG) and Bose-Einstein condensate (BEC) are present at the same time. Here, I will discuss the three most common research directions with Bose-Fermi mixtures: the BEC-DFG phase diagram, ground-state polar molecules and double superfluidity.

The phase diagram of a BEC-DFG mixture is very interesting because phenomena like collapse and phase separation occur [Mar08b]. A lot of theory effort is devoted to the study of this phase diagram and in this brief review I will focus on the experimental observations and the instability criteria as introduced by Ref. [Mø98, Viv00, Rot02]. Within the mean-field approximation, a degenerate Bose-Fermi system is unstable for densities of [Viv00]

$$n_{\mathrm{f}}^{1/3} \leq \frac{\left(6\pi^2\right)^{2/3}}{3\pi} \frac{m_{\mathrm{f}} m_{\mathrm{b}}}{\left(m_{\mathrm{f}} + m_{\mathrm{b}}\right)^2} \frac{a_{\mathrm{bb}}}{a_{\mathrm{bf}}^2}, \tag{2.2}$$

where n_{f} is the fermionic density, $m_{\mathrm{f(b)}}$ the fermionic (bosonic) mass, a_{bb} the boson-boson scattering length and a_{bf} the interspecies scattering length. In the case of positive interspecies scattering length, the system finds a new equilibrium by phase separating the BEC and DFG. However, for strong negative scattering lengths no such equilibrium exists and the system collapses. In the case of trapped quantum gases,

both components are strongly attracted to each other and pull themselves toward the center of the harmonic trap, where their density is increased. This can be interpreted as if the components feel an additional mean-field confinement. Below a critical negative scattering length, the Bose-Fermi mixture becomes unstable and the increase in density leads to enhanced three-body recombination processes which lead to a sudden loss of atoms. Afters this collapse, a new equilibrium is created with less particles. The collapse can be seen by either varying a_{bf} or preparing a too high fermionic density and watch the system collapse. A similar kind of collapse was observed in mixtures of two BECs either by tuning the interactions [Don01] or preparing mixtures with large particle numbers [Sac99].

The first double-degenerate Bose-Fermi mixtures were created when trying to cool fermionic lithium either with its bosonic isotope ^{7} Li [Tru01, Sch01a] or with another element like ^{23}Na [Had02]. The primary focus of these experiments was the physics of degenerate Fermi gases. The ^{87}Rb-^{40}K mixture followed [Roa02, Gol04] and strong losses were seen when preparing mixtures of large particle numbers [Mod02, Osp06a], which were associated with the predicted mean-field collapse. Another way to study this phenomenon became available with the discovery of Feshbach resonances between Rb and K [Ino04]. While tuning the interspecies interaction, the mean-field collapse was observed as well as strong indications of a phase separation occurring on the repulsive side of the FR [Osp06c, Zac06]. A closer look into the phase separated regime with the Rb-K mixture is difficult because of the large background scattering length and the strong losses on the repulsive side of the FR. Chap. 5 demonstrates phase separation in our ^{41}K-^{6}Li mixture by probing the three-body loss at the interface of the phase-separated state [Lou18].

Besides studying the phase diagram, ground-state polar molecules are another research direction of Bose-Fermi mixtures. Bose-Fermi mixtures are a favorable starting point for creating Feshbach dimers that can be seen as composite fermions. Due to the Pauli exclusion principle, the fermionic dimers have an increased stability against three-body recombination [Zir08]. The Feshbach dimers can be transferred to their ground-state via two-photon stimulated Raman adiabatic passage and thus offer the possibility to create ground-state polar molecules and study long range interaction and, when loaded into a lattice, the Fermi-Hubbard model [Car09, Mos17]. After the creation of a double-degenerate mixture of ^{87}Rb-^{40}K, further studies in optical lattices followed [Lew04, Osp06b] and led to the creation of the first high phase-space density of ground-state polar molecules [Ni08]. Fermionic ground-state molecules have been demonstrated in the singlet state for RbK [Ni08, Mos15] and NaK [Par15a] and in the triplet state for ^{23}Na-^{6}Li [Rva17].

A third research direction of Bose-Fermi mixtures is the study of double superfluidity and the interaction between two superfluids. When apart from a bosonic spin state,

two spin states of the fermionic component are present in the mixture, the fermions can pair with each other. If the temperatures are low enough with respect to the critical temperature for forming a BEC and a Fermi condensate a double superfluid mixture can be created. Double superfluidity was shown for the isotope mixture of lithium, ^{7}Li-^{6}Li, [FB14] and the mass imbalanced cases of ^{41}K-^{6}Li [Yao16] and ^{174}Yb-^{6}Li [Roy17]. In Ref. [FB14] and [Roy17] they demonstrated the double superfluidity by observing a coupling between the center-of-mass oscillations of the Fermi and Bose superfluids, while in Ref. [Yao16] they rotated the superfluid mixture and observed vortices. Fermionic lithium offers a very interesting FR at 832 G, with which the fermionic intraspecies interactions can be easily tuned. Thus the Bose-Fermi superfluid mixture can be studied over the whole BEC-BCS crossover, as was shown in the ^{7}Li-^{6}Li mixture [Del15]. These systems offer the possibility to study the phase diagram of Bose-Fermi superfluids and observe new and exotic states, e.g. dark-bright solitons [Tyl16] and the Fulde-Ferrell-Larkin-Ovchinnikov (FFLO) phase [Oza14]. Also other phenomena, e.g. phase separation [Ram11] and second sound in a double superfluid mixture [Vol75], could be observed.

Many more Bose-Fermi mixtures than those mentioned are created or being created, consisting of either the default fermionic alkali atoms of K and Li or more exotic ones such as Sr, Yb, Er, or Dy. Examples of the wealth of Bose-Fermi mixtures available are ^{41}K-^{40}K [Wu11], ^{133}Cs-^{40}K [Grö16], ^{23}Na-^{6}Li [Rva17], ^{87}Rb-^{6}Li [Mar09], ^{85}Rb-^{6}Li [Deh10], ^{133}Cs-^{6}Li [DeS17], ^{84}Sr-^{87}Sr [Tey10], ^{87}Rb-^{87}Sr [Bar18], ^{87}Rb-^{171}Yb [Vai15], ^{133}Cs-^{171}Yb [Kem16], Er-Dy [Ilz18], and K-Dy [Rav18]. Studies of these systems will enrich the research on Bose-Fermi mixtures and could give insight into, e.g. boson-mediated Cooper pairing [Bij00, Efr02] or new phases of matter [Pow05, Suz08, Mar08b, Lud11, Ber13, Kin15].

2.4 Impurity Physics with Ultracold Atoms

In all the above mentioned mixtures, the ratio between the number of atoms of each species can be readily controlled. This creates a population imbalanced mixture, which is typically characterized by the polarization $P = (N_1 - N_2)/(N_1 + N_2)$, with $N_1(N_2)$ the number of atoms of species 1 (2). In the limit of $P \to \pm 1$, we enter the realm of impurity physics. Here, a few particles are immersed in and interact with a many-body environment. These population imbalanced systems can be used to study impurity many-body related phenomena, e.g. polaron physics, the Anderson's orthogonality catastrophe (OC) [And67, Kna12] or the Kondo effect [Kon64, Nis13]. Although impurity physics is also studied in 1D chains, e.g. [Cat12], I will here focus on the experiments in 3D.

For weak to moderate interactions with the environment, the impurities can be described as polarons [Mas14]. A polaron is a quasiparticle, representing an impurity that dresses itself with excitations of the surrounding environment. A polaron acts as an entity of its own with an effective mass and energy different from the impurity particle itself. If the many-body environment is a single-component Fermi gas, the term Fermi polaron is used, while an impurity immersed in a BEC is called a Bose polaron. Quasiparticles are most commonly known from solid-state physics, where they describe the conduction of electrons in a dielectric medium. The gas of interacting electrons can be as best described by Landau's Fermi liquid theory [Bay91], which shows how an interacting Fermi gas can be understood in terms of a non-interacting gas of quasiparticles. In the dielectric medium the electrons dress themselves with the excitations in the electron cloud, i.e. they are coupled to a bath of phonons. Polarons are widely used to describe interacting Fermi systems, yet not easy to explore in the limit of strong interactions. This sparked the interest of studying them in population imbalanced ultracold mixtures.

The first studies on population-imbalanced Fermi gases [Zwi06b, Par06] focused on how pairing and superfluidity are affected if not all atoms can find a partner. The system was shown to separate into a phase with a superfluid core surrounded by a shell of normal unpaired fermions, confirming the Clogston-Chandrasekhar theory [Clo62, Cha62]. For strong interactions, another phase was observed [Zwi06b], which could be explained as an ideal gas of Fermi polarons immersed in a Fermi sea [Lob06]. The close relation between the Fermi polaron and the phase diagram of imbalanced Fermi mixtures, triggered the measurements of the properties of this quasiparticle.

In 2009, the attractive Fermi polaron [Sch09, Nas09] was observed in a fermionic spin mixture of lithium with negative scattering lengths. The energy of the quasiparticle as well as the quasiparticle residue was measured with radio-frequency (rf) spectroscopy [Sch09] and the effective mass by studying the collective excitations [Nas09]. Later, the existence of a repulsive polaron was predicted [Mas11]. However, its detection is hindered by the presence of a weakly bound state on the repulsive side of a FR into which the atoms rapidly decay. In 2012, the repulsive polaron was observed with our Li-K mixture and its properties were characterized by rf spectroscopy [Koh12]. The energy, lifetime, effective mass, and quasiparticle residue of both attractive and repulsive polarons were measured and good agreement with theory predictions based on Landau's theory of Fermi liquids was found. The lifetime of the polaron was long enough for our measurements and this was attributed to the relative narrowness of the FR involved. Simultaneously, the repulsive Fermi polaron was also observed in a two-dimensional gas of ^{40}K by the Bonn group [Kos12], where the reduced dimensionality stabilized the repulsive polaron, but their lifetime was a tenfold shorter. Only recently, the repulsive polaron in a Li spin mixture at a broad Feshbach resonance

was observed [Sca17]. In Chap. 6 a further study of the lifetime of the K polarons in the Li Fermi sea is presented and the strongly interacting regime is addressed [Cet15, Chr15, Sch18]. Here, the quasiparticle scattering rate is measured using time-domain spectroscopy [Goo11, Kna12]. In Chap. 7 this method is used to reveal the real-time formation dynamics of the polaron and to probe the quantum many-body dynamics of the strongly interacting regime [Cet16, Par16, Sch18, Liu18]

A topic closely related to the repulsive Fermi polaron is itinerant ferromagnetism, a form of magnetism found in transition metals. In transition metals, some of the electrons are delocalized and their mobile magnetic moment can be arrange to have either a zero or non zero total magnetic moment. There is a competition between the Fermi pressure, which favors pairing, and the repulsive interactions between electrons with opposite spin. The latter, favors domain formation with one single spin component per domain. In ultracold atoms, this phase transition from pairing to domain formation could be studied since the atom-atom interaction can be varied [Mas14]. The ground state of a two component Fermi gas is characterized by pair formation between the two components, which minimizes the Fermi energy of the system. However, for strong repulsive interactions, pairing might be too costly and the competition between the atom-atom interaction energy and the Fermi pressure could favor a metastable state where the two components are phase-separated into stable domains. Recently, evidence for the existence of such a ferromagnetic instability was shown [Val17].

Switching the environment from a Fermi sea to a BEC, gives access to the Bose polaron. Here the role of the environment is more complicated as one-component Bose gases allow for interactions within the environment and not just with the impurity. Thus three-body recombination becomes a limitation on the lifetime of polarons. The existence of the Bose polaron was shown in 2016 with rf spectroscopy [Hu16, Jør16]. For weak to moderate interactions the observations closely follow the model developed by Frölich in the 1950s [Frö50], but for strong interactions the three-body correlations become important and further studies in this regime would be highly interesting.

The interactions of an impurity with its environment can also be used to probe and learn about the environment itself. For example, an impurity can be used to probe the BEC-BCS crossover in a resonant Fermi gas [Lau17]. In Chap. 4, we show how a BEC impurity can be used for measuring the temperature of an interacting Fermi gas [Lou17b].

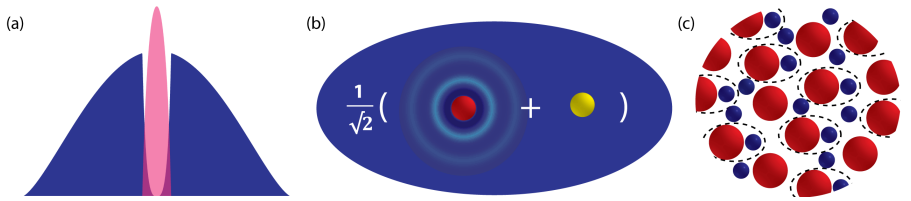

Figure 2.1: Illustration of the three tunable mixtures and topics presented in this thesis. (a) A small BEC of ^{41}K (magenta) that is immersed in a ^{6}Li Fermi sea (blue), enables the study of an interacting Bose-Fermi mixture. (b) Studying a ^{40}K impurity which is in a superposition of a spin state that interacts (red) with the Fermi sea and one that does not (yellow), gives insight into impurity physics. (c) An atom-dimer mixture of ^{40}K (red) -^{6}Li (blue) reveals the effect of mass imbalance on atom-dimer scattering.

2.5 Thesis Research Topics

This dissertation demonstrates the versatile physics that can be explored with ultracold two-species mixtures and the various measurement techniques which are available to probe their properties. It describes the experiments performed with three types of ultracold heteronuclear quantum mixtures: a Bose-Fermi mixture of ^{41}K and ^{6}Li, a fermionic impurity of ^{40}K in a ^{6}Li Fermi sea, and an atom-dimer mixture of ^{40}K and ^{6}Li. In essence, all these experiments address a cold cloud of two atomic species trapped and cooled by laser light, observed by absorption imaging and controlled in inter- and intra-species interaction strength by magnetically-tunable Feshbach resonances. A short introduction to the experimental details can be found in the next chapter. The tunability of the atom-atom interaction is essential for studying the behavior of Bose-Fermi mixtures, the decoherence of impurities coupled to a Fermi sea, and the effects of mass imbalance in an atom-dimer mixture.

Figure 2.1 illustrates the tunable mixtures and the three research topics explored with them. The research was done in the FeLi(Bo)Kx lab in Innsbruck from 2012-2018. The following chapters, Chap. 4-9, contain the articles to which the author actively contributed during her thesis work. At the beginning of each chapter a statement about the author's contribution can be found. These articles are clustered according to the mixture addressed and a short summary of each chapter is given below. All chapters are published in peer-review journals [Lou17b, Lou18, Cet16, Cet15, Jag16, Jag14]. For editorial and style reasons, the reprints might slightly differ from the referenced published versions.

Bose-Fermi mixtures

- **Chapter 4** presents a thermometry approach which provides a conceptually simple, accurate, and general way to measure the temperature of deeply degenerate Fermi gases. It also discusses our evaporation route to obtain a double-degenerate, mass imbalanced Bose-Fermi mixture of ^{41}K and ^{6}Li and shows the formation of a ^{41}K Bose-Einstein Condensate (BEC) through sympathetic cooling with lithium. The condensate, or more specifically the BEC-fraction obtained from bimodal fitting, acts as probe of the Fermi degeneracy of the Fermi sea. For a small number of potassium atoms and after thermalization, this mesoscopic impurity accurately measures the temperature of the mixture. Insight into the lowest achievable temperatures and Fermi degeneracies benchmarks the phenomena that can be observed experimentally.

- **Chapter 5** explores the repulsive side of the heteronuclear Feshbach resonance between the lowest Zeeman spin states of ^{41}K BEC and ^{6}Li Fermi sea at 335 G. Here, the two components phase separate for strong repulsive interaction and when K is a degenerate gas. This work shows that the region where the two components mix can be selectively probed by measuring a mechanism that only occurs in the overlap region at the interface between the two species. Therefore, we measure the three-body recombination rate of both a condensate and a thermal cloud of K in a Fermi sea. The measurements give information about the overlap between the two degenerate species and the results are compared with a numerical mean-field model. This comparison shows that the kinetic energy term of the bosons plays an essential role in maintaining the overlap well into the phase-separated regime. Selectively probing the overlap region offers intriguing possibility to further explore interface physics with ultracold atoms.

Impurity in a Fermi sea

- **Chapter 6** studies the decoherence of a fermionic ^{40}K impurity that arises from collisions with a ^{6}Li Fermi sea, extending the earlier studies on the repulsive polaron [Koh12]. For weak to moderate interactions, the measurements, performed using a spin-echo interferometry method, show a good agreement with theory calculations in the Fermi liquid picture [Chr15]. In this regime the decoherence of the impurity is dominated by quasiparticle scattering. For strong interactions we show that the decoherence can not be solely explained within the quasiparticle picture. To access the strongly interacting regime, this work introduces a fast-switching technique based on the AC stark shift given by the

optical dipole trap, which influences the position of the Feshbach resonance center. This method opens the way to study the dynamics of a strongly interacting population imbalanced Fermi mixture.

- **Chapter 7** addresses the dynamics of the impurity in the Fermi sea for moderate to strong interactions. The quantum evolution of a fermionic many-body system after the sudden switch on of the interactions with the impurity is shown in real time. The Anderson's orthogonality catastrophe remains elusive because of temperature effects and the mobility of the impurity. However, the formation dynamics of polarons and the quantum interference between the attractive and repulsive polaron branch is revealed. Both radio-frequency spectroscopy and time-domain spectroscopy measurements are presented and compared to two complementary theoretical methods: the truncated basis method [Par16] and the functional determinant approach [Sch18]. The methods and results of this work show that many-body interferometry is a powerful tool to study ultrafast processes in strongly interacting Fermi gases.

Atom-dimer mixture

- **Chapter 8** discusses the interaction between atoms and dimers, where the ^{6}Li-^{40}K Feshbach dimers are created by ramping across the interspecies Feshbach resonance. Radio-frequency spectroscopy shows that for strong repulsive atom-atom interactions, the repulsive atom-dimer interaction is turned into a strong attraction. Anologous to the H_2^+ cation, the light Li atom mediates an attraction between the fermionic K atoms. This three-body effect is a prime example of how mass imbalance in fermionic systems changes the character of interactions and how these systems address a much more complicated many-body problem than the mass-balanced case.

- **Chapter 9** presents lifetime measurements of the atom-dimer mixture close to two narrow interspecies Feshbach resonances. Both the dimer-dimer processes and atom-dimer processes that lead to collisional losses are investigated and compared to theoretical predictions [Lev11]. Similar as for mass imbalanced Fermi-Fermi mixtures near broad Feshbach resonances, the Pauli suppression of collisional losses is observed. The losses described set the timescale on which experiments can be performed. This joint experimental and theoretical work gives an estimate for the minimum required suppression of the losses in other strongly-interacting Fermi-Fermi systems, which enables the selection of suitable Feshbach resonances for future experiments.

Appendices
Since the FeLi(Bo)Kx experimental apparatus was designed for a ^{6}Li -^{40}K Fermi-Fermi mixture, an essential ingredient of this thesis is the changes I made to cool and trap the bosonic isotope of potassium ^{41}K. The experiment can now easily switch between the two potassium isotopes and between a Fermi-Fermi and a double-degenerate Bose-Fermi mixture. This new mixture enables the studies presented in Chap. 4 and Chap. 5 and further studies on the phase diagram of Bose-Fermi mixtures, bosonic impurities in a Fermi sea and mixtures of fermionic atoms and fermionic Feshbach dimers.

- **Appendix A** covers the changes made to the experimental setup to obtain the Bose-Fermi mixture and the details of the cooling and trapping of ^{41}K.
- **Appendix B** summarizes the atom loss measurements, which study the inter- and intraspecies Feshbach resonances between the two lowest Zeeman spin states of lithium and the three lowest Zeeman spin states of potassium. Avoiding these Feshbach resonances along the evaporation route is essential for preparing the double-degenerate, mass imbalanced Fermi-Bose mixture of ^{6}Li and ^{41}K close to their interspecies Feshbach resonance at 335 G, the starting point of the measurements in Chap. 5.

2.5.1 Outlook

The field of ultracold atoms and the FeLi(Bo)Kx experiment have some exciting times still to come. With the multitude of (exotic) species, lattice configurations and other tools to control and manipulate quantum gases at hand, a wealth of possibilities is available for further studies on these quantum simulators of condensed matter and many-body systems in general.

More specific to the research in this thesis, it would be interesting to continue the studies of impurities in a Fermi sea, either with a fermionic or bosonic impurity. For example, the BEC of ^{41}K could be seen as a mesoscopic impurity and one could study spin transport [Som11] in a spin mixture of lithium in the presence of this impurity. Spin transport is especially interesting in analogy to solid state physics [Chi15], where the transport of electrons is influenced by defects in the metal structure. Furthermore if the impurity could be pinned down by, for instance, a species-specific lattice [LeB07], phenomena like Anderson's orthogonality catastrophe [And67, Kna12] or the Kondo effect [Kon64, Nis13] might become observable. With the potassium atoms pinned into a lattice, it would be also possible to study fermion-mediated boson-boson interactions between lattice sites and a system of mixed dimensions. Furthermore, impurity-impurity interactions can be probed by allowing or disabling tunneling between lattice

sites. Since the quantum statistics can be changed by loading a different isotope of potassium, this can be studied for both fermionic and bosonic impurities. Additionally, focusing more on the few-body aspect, confinement of potassium in an optical lattice is predicted to lead to the formation of stable trimer states [Pet07, Nis09b, Lev09].

The Bose-Fermi mixture with tunable interactions also offers interesting physics. A natural extension of our measurements with the Bose-Fermi mixture would be to study the dynamics of the phase-separated system and to explore the Bose-Fermi phase diagram further. More technically, improving the resolution of our imaging system would enable in-situ imaging and a 3D reconstruction of the interface, with which the extend of the interface can be verified. Adding one spin component for lithium, which is already present for the evaporation, we could study a mixture of two mass imbalanced superfluids [Yao16, Roy17]. Moreover, the Bose-Fermi mixture can be used as the starting point to create a Fermi-Fermi atom-dimer mixture. Here, the dimer-dimer decay is expected to be less strong and this might give favorable timescales to study the equilibrium properties of a mass-imbalanced atom-dimer mixture, in particular for studying itinerant ferromagnetism, as pointed out in Ref. [Mas14]. It will be interesting to see were the exploration of these topics will lead the FeLi(Bo)Kx experiment in the near future.

CHAPTER 3

Introduction to the Experiments

The **Fe**rmionic **Li**thium (**Bo**sonic) **K**alium[1] lab, in short FeLi(Bo)Kx, created one of the first heteronuclear Fermi-Fermi mixtures. At the time of its design, homonuclear spin mixtures of potassium and lithium were widely used for exploring strongly interacting Fermi gases [Ing08] and Feshbach resonances were already found in heteronuclear Bose-Fermi mixtures [Sta04, Ino04]. This motivated the pursuit of an apparatus that combined the two alkali [Wil09] and would make it possible to study strongly interacting mass-imbalanced heteronuclear Fermi-Fermi systems.

In this Chapter, I will briefly discuss the experimental setup, Feshbach resonances, and the previous research done with the FeLi(Bo)Kx experiment [Wil08, Spi09, Spi10, Nai11, Tre11, Koh12]. This Chapter is not meant as an eleborate review of the experimental setup, which can be found elsewhere [Wil09]. However, it is the chapter's aim to provide the reader with the main concepts necessary to understand the experimental apparatus used and the measurements carried out in this thesis. The supplemental materials of the published articles are included in the following chapters and provide the chapter-specific experimental details. For more in-depth reviews of the experimental techniques involved I would like to refer to the well-documented literature about e.g., introduction into experimental methods [SK12, Tör14], preparation of quantum gases [Jer14], cooling and trapping [Met99], optical dipole traps [Gri00], Feshbach resonances [Chi10], collective modes [Gri08], and the properties of Fermi gases [Ing08, Zwe12, Tur12] and Bose gases [Ket99] in harmonic traps.

3.1 Experimental Setup

A simplified version of the core of the ultra-high vacuum setup of our experiment is shown in Fig. 3.1. It emphasizes the four main elements of a typical ultracold quantum gas setup; optical beams for cooling and trapping [Met99, Gri00]; magnetic field coils for cooling, trapping, and interaction tuning [Met99, Chi10]; radio-frequency (rf) antennae for spectroscopy [Tör16] and cameras for absorption imaging. Each

[1] Kalium is the German name for potassium

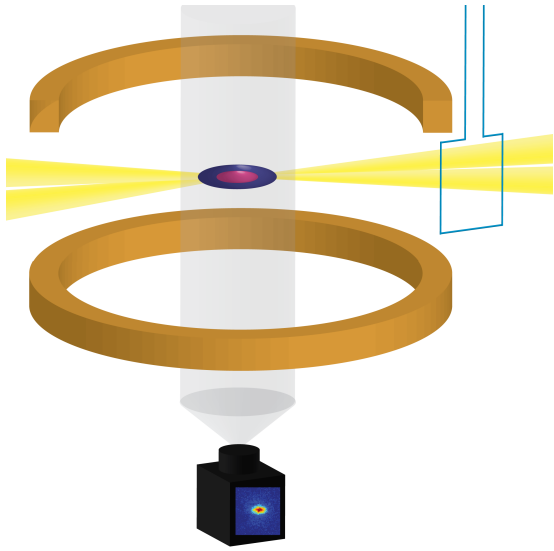

Figure 3.1: Schematics of a typical ultracold mixture experiment. The four main components are shown; magnetic field coils for trapping and tuning the interactions, laser light for optical trapping, a radio frequency (RF) antenna to switch between spin states and a CCD camera to take absorption images of the (trapped) clouds.

measurement begins with the creation of the gas by cooling and trapping the atoms from an atomic beam and ends with the destructive imaging of the cloud of atoms. The techniques behind this make-probe-discard cycle are well-established as are the requirements for the experimental setup [SK12, Tör14, Jer14]. The atomic isotopes selected determine the details of the optical and magnetic fields needed as well as the cooling and trapping cycle required to prepare the mixture at a specific temperature and density.

In our case, the source of the Li and K atomic beams is a multi-species oven in which solid potassium and lithium is heated up. The atomic beams are cooled using a Zeeman slower, before being collected in a dual-species magneto-optical trap (MOT) in the center part of the experimental setup [Wil09]. The two species are consecutively loaded into a single-beam optical dipole trap (ODT). Next, we evaporate a Li spin mixture close to an intraspecies Feshbach resonance and thereby sympathetically cool the K atoms without collisional loss. In most measurements we evaporate at 1180 G with a Li spin mixture of Li$|1\rangle$-Li$|2\rangle$, the lowest and second to lowest spin states. How-

ever, for our latest measurements (Chap. 5) we used an alternative evaporative cooling approach in which we evaporate at 483 G with a Li$|1\rangle$-Li$|3\rangle$ mixture, the lowest and third to lowest spin states. During the evaporation procedure, the atoms are transferred into a crossed cigar-shaped optical dipole trap and we employ a spin relaxation stage and pulses of resonant laser light to create pure spin mixtures of Li and K. The details of the procedure for the ^{6}Li and ^{40}K mixture can be found in Ref. [Spi10], while the preparation procedure for the Fermi-Bose mixture using the Li$|1\rangle$-Li$|3\rangle$ mixture is described in Sec. 5.6.1.

The starting point of most of our measurements is a mixture in a crossed optical dipole trap of about 10^5 Li atoms in one spin state and several 10^4 K atoms, also in a single spin state. The lithium atoms are degenerate and have a relative temperature of about 10-20% of the lithium Fermi temperature. The mixture is in thermal equilibrium and the temperature of the sample is extracted by either looking at the expansion of a thermal K cloud or by measuring the BEC-fraction of ^{41}K, as discussed in Chap. 4. The trap frequencies, which characterizes the trapping potential, are measured by addressing the collective excitations of the cloud of atoms. By briefly displacing the trap center of the ODT, sloshing modes can be excited which correspond to oscillations of the center-of-mass of the atoms. Measuring the size of the cloud for different wait times after this excitation is a convenient way to determine the species-specific trap frequency. Another mode, called the radial compression mode, can be excited by briefly compressing the cloud by increasing the trap depth of the ODT, followed by a release into the original trap. The oscillation that follows has a two times higher frequency than the trap frequency if the interactions within the mixture are negligible. The study of these and other collective modes provides, information about the interactions in the mixture and is a powerful tool to probe the properties of quantum gases [Gri08].

To transfer the Li and K atoms between different spin states, we have different rf antennae and we use rf pulses with a typical frequency of a few tenths of megahertz to change the population in the different spin states. With the rf antennae we can perform radio-frequency spectroscopy [Tör16], which measures the energy needed to transfer the atoms between two states. We use this technique to measure the binding energy of Feshbach dimers (Sec. 5.6.2), to measure the shift in interaction energy in an atom-dimer mixture (Chap. 8) and to obtain the rf spectrum of an impurity interacting with a Fermi sea (Chap. 7). By transferring the K atoms from a spin state which is interacting with Li to one that is non-interacting, the interactions between Li and K can be switched. Applying a $\pi/2$ pulse creates a superposition state of two spin states which are coupled by the rf and this facilitates time-domain spectroscopy, e.g. spin echo or ramsey sequences. This technique is discussed in more detail in Chap. 6 and 7, where we look at the time evolution of K impurity that is in a superposition of a spin state that interacts with lithium and one that is non-interacting. Besides spectroscopic

methods, measuring the atom loss as discussed in Chap. 5 and 9 is another way to gain insight into the properties of the system.

The final information on our mixture is obtained through species-selective absorption imaging after time of flight. We can simultaneously image one spin state of Li and one of K, by using two overlapping laser beams. The magnetic fields at which we operate allow us to selectively address the different spin states. The optical density of the atoms is too high to image them in situ and we create more dilute samples by switching off the optical dipole trap and letting the cloud expand for a certain time of flight. If the interactions between the atoms are negligible, the expansion after switching of the trapping potential is ballistic and the density profile imaged reflects the momentum distribution of the gas.

An absorption image is taken by shining light resonant to an optical transition on the atoms for a fixed duration. The atoms absorb the light and this leads to a depletion of the intensity of the probe beam depending on the optical density *OD* of the cloud at each specific spatial position. Subtracting images of the recorded light intensities with and without the atoms present gives the absorption image and information on the optical density of the cloud. For low intensities, resonant light, and a closed optical transition the optical density is related to the column density $n(x, y)$ by the resonance cross section σ, i.e. $OD = n(x, y)\,\sigma$. The absorption images are then directly related to the column density of the atomic cloud and by integrating along one direction a 1D density distribution is obtained. This density profile can then be fitted with the appropriate distribution function [Ing08, Ket99]. The 1D density profile of a pure K BEC follows a parabola, while a thermal cloud is fitted with a Gaussian distribution function. For a partial BEC a bimodal distribution function is used and the 1D density profile of a degenerate Lithium gas follows a polylogarithmic function, which can be approximated with a Gaussian fit. By fitting the 1D density profile, the atom number, size of the cloud, and the BEC-fraction in the case of a partial BEC, are extracted. These are the main observables of the experiment.

In reality the relation between column density and optical density is more complex, as most optical transitions are not a closed two-level system and the imaging beam might not be low enough in intensity or exactly resonant with the optical transition. This leads to a miscounting of the atom number. Especially in the case of lithium the effect of the radiation pressure exerted by the photons during the imaging pulse is important and Sec. 6.6.4.1 describes in detail how the lithium atom number is calibrated.

With the making of an absorption image, the experimental cycle ends. The atoms are heated up by the resonant laser pulse and are discarded. The experimental sequence starts again from the beginning by loading the Li and K atoms into the MOT. For the next data point, a new sample is prepared, manipulated, and imaged.

3.2 Feshbach Resonances

The inter-and intra- species interactions in the mixture can be tuned with the aid of Feshbach resonances [Chi10]. At a FR, in a two channel picture, a closed channel that supports a bound state and an entrance channel that corresponds to two free atoms in the long distance limit, couple resonantly. The difference in the magnetic moment between those channels can be used to tune the states in and out of resonance by changing the magnetic field B. The scattering length a diverges and is given by

$$a(B) = a_{\mathrm{bg}}\left(1 - \frac{\Delta}{B - B_0}\right). \tag{3.1}$$

Here, a_{bg} is the background scattering length, Δ is the width of the FR, and B_0 is the FR position at which a diverges. The scattering length equals zero whenever $B = B_0 + \Delta$ and resonance width therefore indicates the range between the FR pole and the zero-crossing. On the repulsive side of the FR, a bound state exists and Feshbach dimers can be associated. A common way to create those dimers is to ramp from the attractive side of the FR to the repulsive side, as described in Chap 8 and 9. By measuring the binding energy of these Feshbach dimer for various magnetic fields, the FR position can be experimentally determined, while a_{bg} and Δ are usually obtained from theory.

In this thesis we exploit three interspecies Feshbach resonances between lithium and potassium, to tune the interspecies interaction. The Li-K FRs have two peculiarities. They are relatively narrow and their position depends slightly on the trap depth. Both aspects influence our determination of B_0 from binding energy measurements. For broad resonances, i.e. entrance-channel dominated FRs, the universal formula for the binding energy $E_b \approx \hbar^2/\left(2m_r a^2\right)$ applies. However, for narrow resonances, i.e. closed-channel dominated, the momentum dependence of the interaction should be taken into account. Thus, to fully characterize our FRs, a fourth parameter is needed. We use the range parameter R^* as defined in Ref. [Pet04a], $R^* = \hbar^2/\left(2m_r\,\delta\mu\,a_{\mathrm{bg}}\Delta\right)$, where m_r is the reduced mass and $\delta\mu$ the differential magnetic moment between the closed and open channel. For $a \to \pm\infty$, R^* is related to the effective range $r_{\mathrm{eff}} = -2R^*$. The universal formula for the binding energy only holds when $a \gg R^*$, which usually corresponds to a small magnetic field range. Outside of this range, the binding energy E_{b} not only depends on B_0, a_{bg} and Δ but also on R^* and can be accurately described as [Pet04a]

$$E_{\mathrm{b}}(B) = \frac{\hbar^2}{8\,(R^*)^2\,m_{\mathrm{r}}}\left(\sqrt{1 - \frac{4\,R^*\,(B - B_0)}{a_{\mathrm{bg}}\,\Delta}} - 1\right)^2. \tag{3.2}$$

We measure the binding energy by either magnetic modulation spectroscopy or radio-frequency spectroscopy and fit the results with the above formula to determine B_0 and R^*, as described in Sec. 5.6.2.

The second special feature of our FRs is the dependence of B_0 on the trap depth of the optical dipole trap, as was pointed out in Ref. [Koh12]. The trap light of 1064 nm causes a differential light shift between the atom pair state and the molecular state that resonantly couple at the FR. Thus, for every trap we use, we need to measure the trap-specific B_0. In Chap. 6 and 7, this light-induced shift is used to quickly change the interaction of the sample by turning on an additional trap. This changes the position of the FR and therefore the scattering properties of the mixture. For more details on the the light-induced shift of B_0, see Sec. 5.6.2 and 6.6.

3.3 Previous Research

The previous research with FeLi(Bo)Kx focused on realizing a strongly interacting Fermi-Fermi mixture and observing the repulsive polaron in a population imbalanced gas. In 2008, the first measurements on the ^{6}Li-^{40}K mixture were carried out and together with the Amsterdam group we observed both *s*-wave and *p*-wave Feshbach resonances for different spin mixtures of the two elements [Wil08]. Around the same time, the Munich group created a double-degenerate mixture of Li and K in a magnetic trap by sympathetic cooling the fermionic gases with bosonic Rubidium [Tag08]. In contrast, we rely an all-optical production of this degenerate mixture and use the magnetic field for interaction tuning. Since we evaporate a lithium spin mixture close to an intraspecies FR, we first investigated the collisional stability of K across this FR [Spi09] before demonstrating the all-optical production scheme, where K is sympathetically cooled [Spi10].

Once the cooling scheme was characterized, we looked into the interaction properties and investigated several Feshbach resonances within the mixture [Wil09, Spi10, Nai11], before focusing on the FR at 155 G FR. The FR at 155 G occurs between Li in the lowest Zeeman spin state and K in the third to lowest spin state. At this FR, we observed the expansion dynamics of the mixture across the whole FR [Tre11] and saw hydrodynamic behavior at particular magnetic fields. This showed that the strongly interacting regime was accessible with this mixture and that the lifetime of the mixture close to the FR was long enough for performing measurements. The next step, was the observation of the repulsive polaron by measuring the excitation spectrum of a ^{40}K impurity in a Li Fermi sea with rf spectroscopy [Koh12]. The energy and lifetime of the polaron was measured, as well as its coherence properties and the measurements were compared to theory which took into account the narrowness of the FR used. This

was the start of our impurity studies, which are continued in Chap. 6 and 7.

3

CHAPTER 4

Thermometry of a Deeply Degenerate Fermi Gas with a Bose-Einstein Condensate

Published as:
R. S. Lous, I. Fritsche, M. Jag, B. Huang (黄博) and R. Grimm
Phys. Rev. A **95**, 053627 (2017)

Author contribution
The author took a leading role in the experiments described in this paper. She adjusted the experimental setup and control software to load, cool, and trap the new isotope ^{41}K and wrote the Matlab analysis program which performs the bimodal fitting of the BEC data. In collaboration with the other authors, she performed the measurements, analyzed the data and wrote the paper.

We measure the temperature of a deeply degenerate Fermi gas, by using a weakly interacting sample of heavier bosonic atoms as a probe. This thermometry method relies on the thermalization between the two species and on the determination of the condensate fraction of the bosons. In our experimental implementation, a small sample of ^{41}K atoms serves as the thermometer for a ^{6}Li Fermi sea. We investigate the evaporative cooling of a ^{6}Li spin mixture in a single-beam optical dipole trap and observe how the condensate fraction of the thermometry atoms depends on the final trap depth. From the condensate fraction, the temperature can be readily extracted. We show that the lowest temperature of 5.9(5)% of the Fermi temperature is obtained, when the decreasing trap depth closely approaches the Fermi energy. To understand the systematic effects that may influence the results, we carefully investigate the role of the number of bosons and the thermalization dynamics between the two species. Our thermometry approach provides a conceptually simple, accurate, and general way to measure the temperature of deeply degenerate Fermi gases. Since the method is independent of the specific interaction conditions within the Fermi gas, it applies to both weakly and strongly interacting Fermi gases.

4

4.1 Introduction

Since the first demonstration of Fermi degeneracy in an ultracold gas [DeM99], experimental progress has provided unprecedented access to a great wealth of exciting phenomena, as highlighted by the prominent example of a crossover superfluid [Zwe12]. The great interest in fermionic quantum gases results from the fact that fermions constitute the elementary building blocks of matter and provide the possibility to investigate various phenomena of strong interactions. The experimental availability of degenerate Fermi gases has led to new insights into intriguing few- and many-body behavior, the many facets of which are studied in a great variety of current experiments.

The lowest achievable temperature is crucial for the experimental observation of many phenomena. While fermionic superfluidity [Pit16] is now routinely achieved in many experiments worldwide, other phenomena like antiferromagnetic ordering [Har15] require much lower temperatures, which are still very hard to obtain experimentally. In the range of very low temperatures, well below one tenth of the Fermi temperature T_{F}, thermometry becomes increasingly difficult. In deeply degenerate Fermi systems, one faces the general problem that only a small fraction of atoms near the Fermi surface carry the temperature information, which reduces the detection sensitivity for

common imaging methods. For strongly interacting systems, the interpretation of density profiles is not straightforward and requires detailed knowledge of the equation of state [Luo07, Nas10, Ku12] to extract temperature information from thermodynamic observables. For the specific case of a unitary Fermi gas with resonant interactions, where thermodynamics follows universal behavior [Ho04], thermometry is now well established, but not for the general situation of Fermi gases in strongly interacting regimes.

The conceptually most simple way of thermometry is to use a probe in thermal equilibrium with the object under investigation and to rely on a phenomenon with an easily detectable and well-understood temperature dependence. This is the working principle of thermometers in our daily life, where the underlying phenomenon is thermal expansion or temperature-dependent resistivity. We apply the same basic idea to a deeply degenerate Fermi sea, using a small sample of weakly interacting bosonic atoms as a probe, and we rely on the sensitive detection of the condensate fraction.

Our Fermi gas is a spin mixture of deeply degenerate ^{6}Li atoms with resonantly tuned interactions, as it is used in many current experiments worldwide. For such a system, temperatures around 10% of the Fermi temperature T_F or even below have been reported by various groups (see [Yef13, Lin14, Bur14b, Del15, Rev16] for a few recent examples). Our thermometer is a small sample of bosonic ^{41}K atoms immersed in the Fermi sea. In addition to the condensate formation serving as the main observable, our system takes advantage of the large mass ratio and the much smaller number of bosons as compared to the fermions. Related thermometry approaches that rely on coupling to a weakly interacting probe component, have been implemented in other Bose-Fermi systems [Roa02, FB14, Del15, Ono16], in population-imbalanced spin mixtures [Zwi06a], and in a Fermi-Fermi mixture [Spi09], but without combining all these three advantages. For our system, the critical temperature for Bose-Einstein condensation (BEC) corresponds to about $0.1\,T_F$, which makes the condensate fraction a sensitive and accurate probe right in the temperature range of main interest for deep cooling.

In this paper, we present a thorough experimental investigation of Fermi gas thermometry using a bosonic species. In Sec. 4.2, we discuss the basic principle of thermometry for a Fermi-Bose system in general and for the particular case of our mixture of ^{6}Li and ^{41}K. We then, in Sec. 4.3, describe the experimental procedures of preparation, cooling, trapping, and detection. In Sec. 4.4, we present the main experimental results on deep cooling of the ^{6}Li spin mixture, as probed by the ^{41}K BEC.

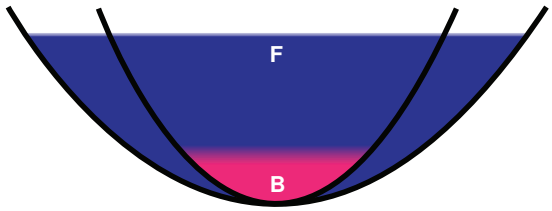

Figure 4.1: Basic idea of the thermometry. A small sample of bosonic atoms (B) is immersed in a large, deeply degenerate sea of fermions (F) under thermal equilibrium conditions. The harmonic trapping potentials (solid lines) are different for both species, depending on the particular trapping configurations used. The temperature is derived from the condensate fraction.

4.2 Bosons as a Fermi Gas Thermometer

Here, we first discuss the basic idea of our thermometry approach in general terms, before we turn our attention to the specific case of ^{41}K bosons in a ^{6}Li Fermi sea.

4.2.1 Basic Idea

The basic idea of our thermometry approach is illustrated in Fig. 4.1. We assume that both harmonically trapped species are in sufficient thermal contact with each other to establish a thermal equilibrium with a common temperature T. The main observable is the condensate fraction β of the bosonic cloud, from which T can be derived.

To obtain the temperature T of the two-component system in relation to the Fermi temperature T_F, we start with the identity $T/T_\mathrm{F} = (T/T_\mathrm{c}) \times (T_\mathrm{c}/T_\mathrm{F})$, where T_c is the critical temperature for BEC. The first factor, T/T_c, can readily be obtained from the condensate fraction of the bosonic component through the well-known relation

$$\frac{T}{T_\mathrm{c}} = (1-\beta)^{1/3}\,. \tag{4.1}$$

For calculating $T_\mathrm{c}/T_\mathrm{F}$ we use the textbook formulas

$$k_\mathrm{B}T_\mathrm{c} = 0.940\,\hbar\omega_\mathrm{B}\,N_\mathrm{B}^{1/3}\,, \tag{4.2}$$

$$k_\mathrm{B}T_\mathrm{F} = 1.817\,\hbar\omega_\mathrm{F}\,N_\mathrm{F}^{1/3}\,, \tag{4.3}$$

where N_B and N_F represent the number of trapped bosons and fermions, and ω_B and ω_F are the respective geometrically averaged trap frequencies. Note that Eqs. (4.1) and

(4.2) are strictly valid only for non-interacting systems in the thermodynamic limit. In practice, the finite sample size and interaction effects may lead to corrections [Gio96].

By combining Eqs. (4.1)-(4.3) we arrive at the central equation that underlies our thermometry approach,

$$\frac{T}{T_F} = 0.518\,(1-\beta)^{1/3}\,\frac{\omega_B}{\omega_F}\left(\frac{N_B}{N_F}\right)^{1/3}. \tag{4.4}$$

In an experiment, the ratio of the trap frequencies, ω_B/ω_F, will be determined by the specific properties of the two different components and the particular trap configuration used for the experimental realization.

Equation (4.4) highlights the conditions for optimized thermometry in the deeply degenerate regime. A small ratio of the trap frequencies, ω_B/ω_F, is highly desirable. This favors heavy bosons in combination with light fermions. The number ratio N_B/N_F enters with its third root, which shows that a very large number imbalance ($N_B \ll N_F$) is required to take real advantage of this factor. In this case, the bosons can be considered as impurities in the large Fermi sea.

4.2.2 Case of the ^{6}Li-^{41}K Mixture

We now turn our attention to the specific situation of bosonic ^{41}K atoms in a Fermi sea of ^{6}Li atoms. The mixture [Wu11, Yao16] exhibits favorable properties for our purpose. The interspecies interaction is moderate, with a background scattering length of about $+60\,a_0$ [Han10], where a_0 is Bohr's radius. This is large enough to provide a sufficient cross section for thermalization on a realistic experimental time scale, but weak enough to avoid effects of strong interactions, such as a mutual repulsion or attraction or fast three-body decay.

We consider a hybrid trapping scheme, as realized in our experiment, where the atoms are confined radially by an infrared laser beam and axially by a curved magnetic field (see Sec. 4.3.2), under conditions ensuring that the trap frequency ratio for the two species is not changed by the gravitational sag (see Appendix 4.6). For such a trap, in a harmonic approximation, the frequency ratio in Eq. (4.4) can be expressed as

$$\frac{\omega_B}{\omega_F} = \left(\frac{m_K}{m_{Li}}\right)^{-1/2}\left(\frac{\alpha_K}{\alpha_{Li}}\right)^{1/3}\left(\frac{\mu_K}{\mu_{Li}}\right)^{1/6}, \tag{4.5}$$

For our experimental situation (Sec. 4.3.2), the mass ratio is $m_K/m_{Li} = 6.810$, the ratio of optical polarizabilities is $\alpha_K/\alpha_{Li} = 2.209$ [Tan10, Saf13], and the ratio of magnetic moments is $\mu_K/\mu_{Li} = 0.999$. With these accurately known numbers, Eqs. (4.4) and

(4.5) yield

$$\frac{T}{T_F} = 0.258\,(1-\beta)^{1/3}\left(\frac{N_B}{N_F}\right)^{1/3}, \tag{4.6}$$

which we will use for extracting T/T_F from our experimental data, as described in the following Sections.

The dynamical range of our thermometry approach as applied to the ^{41}K-^{6}Li mixture can now be illustrated by a numerical example, based on typical experimental conditions. We assume $N_B/N_F = 1/30$ and possible measurements of the condensate fraction in the range $0 \leq \beta \lesssim 0.95$. According to Eq. (4.6), this corresponds to a temperature range of $0.03 \lesssim T/T_F \lesssim 0.08$, right in the interesting regime for state-of-the art experiments in the deeply degenerate Fermi gases.

4

4.3 Experimental Procedures

In this Section, we present our general experimental procedures applied to a Fermi-Bose mixture of ^{6}Li and ^{41}K. In Sec. 4.3.1, we give an overview of the main preparation steps. In Sec. 4.3.2, we present in detail the optical dipole trap used in the final stage of deep evaporative cooling. In Sec. 4.3.3, we discuss the main detection schemes.

4.3.1 Preparation of the ^{6}Li-^{41}K Mixture

The mixture is prepared in an all-optical cooling and hybrid trapping approach, very similar to the one described in detail in Ref. [Spi10] and applied in various previous experiments on the mixture of ^{6}Li and ^{40}K atoms (see, e.g., Refs. [Spi09, Tre11, Koh12, Jag14, Cet16]). A spin mixture of ^{6}Li atoms in the lowest two sublevels of the electronic ground state is evaporatively cooled close to a Feshbach resonance [O'H02, Bou03, Joc03a] and serves as the agent to sympathetically cool a K minority component. For the whole cooling process, we found that it makes no difference whether the fermionic ^{40}K or the bosonic ^{41}K isotope is present, if we avoid any interspecies scattering resonances and rely on the background interaction with the ^{6}Li cooling agent, being about the same for both K isotopes.

The preparation process involves a spin relaxation stage, which we employ to prepare a single K spin state. Here, the parameters differ from our previous work on ^{40}K [Spi10]. For ^{41}K, the initial laser cooling stage provides an unpolarized sample in the three magnetic sublevels ($m_F = -1, 0, 1$) of the lowest hyperfine level ($F = 1$). We found that spin-exchange collisions with ^{6}Li atoms in the second-lowest sublevel can efficiently produce a polarized ^{41}K sample in the $m_F = -1$ state, which is the third-lowest Zeeman sublevel (see Appendix A). The spin relaxation is performed near a

magnetic field of 200 G, where the process appears to be resonantly enhanced. This stage has a duration of about 500 ms and is implemented right after loading the optical dipole trap, when the temperature is still rather high (few 100 μK). To remove a residual population of K in the $m_F = 0$ state (typically 15%), we apply a resonant laser pulse right before the final evaporation stage to push those atoms out of the trap. It is interesting to note that, without applying the spin cleaning, the evaporation process leads to a spinor condensate [SK13] with clear signatures of immiscibility [Liu16]. The s-wave background interaction between the bosons is relatively weak (intraspecies scattering length of $+60\,a_0$ [D'E07, Pat14]), which makes the condensate very stable against three-body decay.

4.3.2 Trap for Deep Evaporative Cooling

The whole evaporation process takes place in several stages [Spi10] within a total time of 12 s. Here, we focus on the final stage, where the power of a single laser beam is ramped down exponentially within 5 s, from an initial value of 440 mW to a final value in the range between 110 and 45 mW. Then, a hold time of 10 s is introduced to ensure full thermalization, before the two species are finally detected; see Sec. 4.3.3. As in our previous work [Spi09, Tre11, Koh12, Jag14, Cet16], the magnetic bias field of 1180 G is applied for standard Feshbach tuning of the interaction between the two ^{6}Li spin components. This leads to a large negative s-wave scattering length of $a = -2900\,a_0$ [Zür13], and thus facilitates highly efficient evaporative cooling with very low inelastic losses. We note that, because of the absence of any significant losses, the number of K atoms stays essentially the same during the whole evaporative cooling process.

We hold the spin mixture of ^{6}Li together with the single spin state of ^{41}K in a hybrid trap [Joc03a] as illustrated in Fig. 4.2(a). Here, the radial confinement (y, z directions) is provided by a single 1064-nm laser beam and the axial confinement (x direction) results from the curvature of the applied magnetic field. In the vertical direction, gravity also comes into play and decreases the trap depth, which influences both species differently. We apply an additional magnetic levitation field to compensate for the latter effect. The levitation potential is given by

$$U_{\mathrm{lev}}(z) = -\mu_{\mathrm{B}} B' z\,, \tag{4.7}$$

where μ_{B} is Bohr's magneton and B' represents the vertical gradient of the magnetic field. Note that for our high bias magnetic field of 1180 G the levitation potential is essentially the same for both species, since the magnetic moments of both species are within 0.1% close to μ_{B}. We use a gradient of 2.5(2) G/cm, for which we obtain

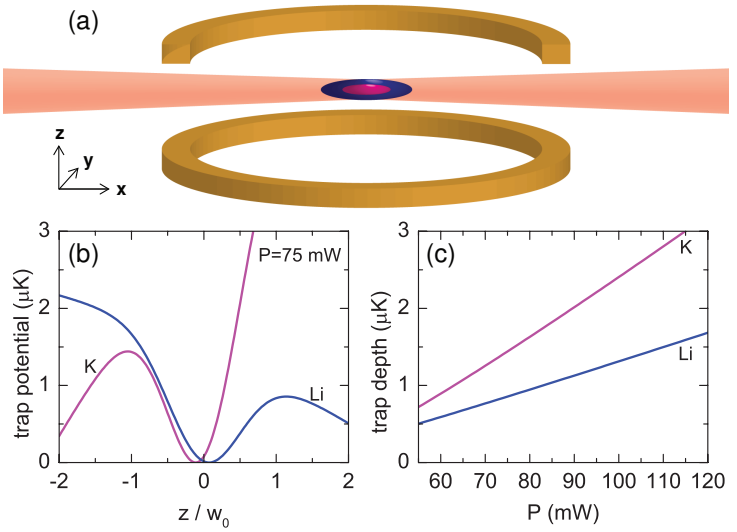

Figure 4.2: Trapping scheme in the final stage of evaporative cooling. (a) A single infrared laser beam for radial trapping (y, z directions) is used in combination with a magnetic field (coil setup schematically shown). The magnetic field serves multiple purposes, providing the bias field for Feshbach tuning, a curvature for axial trapping (x direction), and a vertical levitation gradient. (b) The vertical potentials $U^i_{\rm tot}(z)$ resulting from Eq. (4.8) for both Li (blue) and K (magenta) are shown for a typical laser power of $P = 75\,$mW. For illustrative purposes, we have introduced species-dependent offsets to shift the potential minima to zero. (c) The trap depths $U^i_{\rm trap}$ depend on the laser power P, with the K trap being always deeper than the Li trap.

$\mu_{\rm B} B'/m_{\rm K} g = 0.34(3)$, i.e., we realize a partial levitation of the K atoms by compensating one-third of the effect of gravity (gravitational acceleration g). For Li, we obtain $\mu_{\rm B} B'/m_{\rm Li} g = 2.36(20)$, which means a strong overlevitation. These conditions are close to a "magic" levitation condition, where the combined tilt effect of gravity and levitation on the trap depth is the same for both species; see Appendix 4.6 for a detailed description.

For both species (i =Li, K), the total potential along the vertical direction in the trap center can be written as

$$\begin{aligned} U^i_{\rm tot}(z) &= -U^i_{\rm opt}\,\exp(-2z^2/w^2) \\ &\quad +(m_i g - \mu_{\rm B} B')z - \frac{1}{2}\mu_{\rm B} B'' z^2\,, \end{aligned} \tag{4.8}$$

where U^i_{opt} is the optical potential depth and w is the waist of the single optical beam. The combined effect of gravity and magnetic levitation is represented by the term linear in z. The quadratic term describes a weak magnetic antitrapping effect, resulting from the negative curvature of the magnetic field. In the saddle-potential of our configuration [Fig. 4.2(a)], the curvature along the z axis is two times larger and of opposite sign as compared to the curvature along the x axis, the latter determining the axial magnetic confinement. Therefore, the curvature B'' is related to the axial trapping frequency ω^i_x by the formula $\mu_{\mathrm{B}} B'' = 2m_i(\omega^i_x)^2$.

The vertical trap potentials are shown in Fig. 4.2(b) for both Li and K atoms under typical conditions of our experiment ($P = 75\,\mathrm{mW}$). This clearly illustrates the different optical potentials and the effect of the opposite tilt on both Li and K. The tilt and the curvature substantially reduces the total trap depths U^i_{trap} to values below the respective depths of the optical potentials ($U^i_{\mathrm{trap}} < U^i_{\mathrm{opt}}$).

Figure 4.2(c) illustrates the dependence of the trap depths U^i_{trap} on the laser power in the range relevant for our final evaporative cooling stage. It is important to note that $U^{\mathrm{K}}_{\mathrm{trap}} > U^{\mathrm{Li}}_{\mathrm{trap}}$ is always fulfilled. The effect of the magnetic levitation ensures that evaporative cooling removes Li atoms, but leaves all K atoms in the trap. This is essential for our interpretation of the cooling process, where Li acts as the cooling agent and K is cooled sympathetically via collisions with Li and not directly.

We characterize the trap by measuring the frequencies of radial and axial sloshing oscillations of both the confined species. For the radial trap frequencies of Li and K, we find

$$\omega^{\mathrm{Li}}_r = 2\pi \times 37.6(5)\mathrm{Hz} \times \sqrt{P/\mathrm{mW}}\,, \tag{4.9a}$$

$$\omega^{\mathrm{K}}_r = 2\pi \times 21.0(6)\mathrm{Hz} \times \sqrt{P/\mathrm{mW}}\,, \tag{4.9b}$$

where P is the power of the trapping beam. The measured frequency ratio $\omega^{\mathrm{Li}}_r/\omega^{\mathrm{K}}_r = 1.79(6)$ is consistent with the more accurate value of 1.756 as calculated from the dynamic polarizabilities [Tan10, Saf13] and the mass ratio. For the single-beam optical dipole trap, assuming a Gaussian laser beam profile, we then obtain [Gri00] the waist $w = 44.3\,\mu\mathrm{m}$ and the optical potential depths

$$U^{\mathrm{Li}}_{\mathrm{opt}}/(k_{\mathrm{B}} \times \mathrm{nK}) = 19.8(3)\, P/\mathrm{mW}\,, \tag{4.10a}$$

$$U^{\mathrm{K}}_{\mathrm{opt}}/(k_{\mathrm{B}} \times \mathrm{nK}) = 43.7(6)\, P/\mathrm{mW}\,. \tag{4.10b}$$

For the axial frequencies, characterizing the magnetic confinement, we obtain

$$\omega^{\mathrm{Li}}_x = 2.61\, \omega^{\mathrm{K}}_x = 2\pi \times 25.6(1)\,\mathrm{Hz}\,. \tag{4.11}$$

We note that, for the trap frequencies, the optical contribution to the axial trapping and magnetic effects on the radial confinement remain negligibly small. Furthermore, the levitation field that counteracts gravity leaves the oscillation frequencies at the bottom of the trap essentially the same [Hun08], in spite of its substantial effect on the trap depths. This ensures that the frequencies according to Eqs. (4.9a) and (4.9b) remain a very good approximation for all our experimental conditions.

4.3.3 Detection

For detection of the two species we apply standard time-of-flight absorption imaging, realized with probe beams propagating along the z axis. From images of the ^{6}Li cloud, we selectively determine the number N_F of fermionic atoms in each of the two lowest spin states with relative uncertainties of about 15% [Cet15]. For ^{41}K, we detect the number N_B of bosonic atoms in the third-to-lowest spin state with an estimated relative uncertainty of 15%. From the images of the bosons, we also extract the condensate fraction β, which is the quantity of main interest for our thermometry approach.

Time-of-flight absorption imaging of the expanding ^{41}K component can, in principle, be implemented by turning off the trapping laser beam and letting the cloud expand in the same magnetic field configuration as it is used for evaporative cooling. However, in such a simple scheme, the magnetic field curvature causes a focusing effect [Don01] in the x, y plane (oscillation frequency $\sim$10 Hz), which occurs right in the time interval of main interest for the imaging. For analyzing the ballistic expansion of the thermal cloud, it is rather straightforward to take the focusing effect into account [Ket07], so that the temperature can be readily extracted. For the condensed part, however, the focusing effect leads to an increase of the density and the optical depth of the cloud, which makes a determination of the condensate fraction problematic.

We employ a modified scheme for time-of-flight absorption imaging, where we adiabatically transform our hybrid trap into a purely optical one, before the cloud is released into free space. To prevent any effect of interspecies interaction in the transfer stage, we remove the Li atoms before the transfer into the crossed-beam trap by smoothly applying a short stage with a magnetic gradient of about 8 G/cm, which levitates the K cloud and spills all Li atoms out of trap. Then we slowly ramp up a second trapping beam, which has a fixed final power of $P' = 70$ mW, and a waist of $\sim 50\,\mu$m and crosses the first beam under an angle of 16° [Cet15]. The magnetic field is simultaneously changed to a homogenous configuration without curvature, but with the same bias field. The potential of the resulting crossed-beam dipole trap is similar to the hybrid trap of the evaporation stage and the transfer is realized over a rather long time of 4 s, which ensures adiabaticity of the process. The transfer into the detection trap, being somewhat tighter than the cooling trap, implies a moderate adiabatic com-

pression. This increases the temperature by a factor of roughly 1.5, as easily obtained from the ratio of the trap frequencies[1]. This factor is taken into account when we determine the temperature of the thermal component from the temperature of the expanding cloud. To image the expanding cloud after time of flight, we apply a levitation field that counteracts gravity and facilitates long observation times up to 45 ms.

We have performed several tests on the performance of our detection scheme. We have carefully checked that the adiabatic transfer stage does not lead to any detectable loss of K atoms and that its influence on the condensate fraction remains negligibly small.

4.4 Cooling and Thermometry Results

In this Section, we present our experimental results. We focus on the final stage of the deep evaporative cooling process, where the lowest temperatures are achieved. In Sec. 4.4.1, we consider the fermionic ^{6}Li component only and identify the conditions where cooling crosses over into spilling of the Fermi sea. In Sec. 4.4.2, we turn our attention to the bosonic ^{41}K component and present measurements of the condensate fraction and the temperature, which allows us to determine T/T_F for the Fermi gas. In Sec. 4.4.3, we investigate the interspecies thermalization process, justifying the assumption of interspecies thermalization. In Sec. 4.4.4, we finally discuss the performance of our thermometry scheme in terms of measurement uncertainties and systematical effects.

4.4.1 Crossover from Evaporation to Spilling

In the final stage of evaporative cooling, when the laser power is reduced to very low values, a crossover between two regimes takes place [Joc03a]. Above a certain threshold, the continuous reduction of the trap power removes thermal atoms with some excess energy above the Fermi energy level, which efficiently cools down the sample. Then a threshold is reached where the Fermi energy level in the shallow trap reaches the trap depth. Below that threshold, the atoms are spilled out of the trap. We identify this crossover by measuring the number of ^{6}Li atoms remaining in the trap as a function of the final trap power at the end of the evaporation ramp.

Figure 4.3 shows our observations for a final trap power P between 45 and 110 mW. The crossover between the two different regimes can be clearly seen in the behavior

[1] At an intermediate power of $P = 75$ mW, the geometrically averaged trap frequency increases from 69 to 109 Hz. The frequency ratio depends on the value of P, but quite weakly. We have carried out measurements on the trap frequencies in the crossed-beam detection trap, from which we determine the change in trap frequencies with an accuracy of about a few percent.

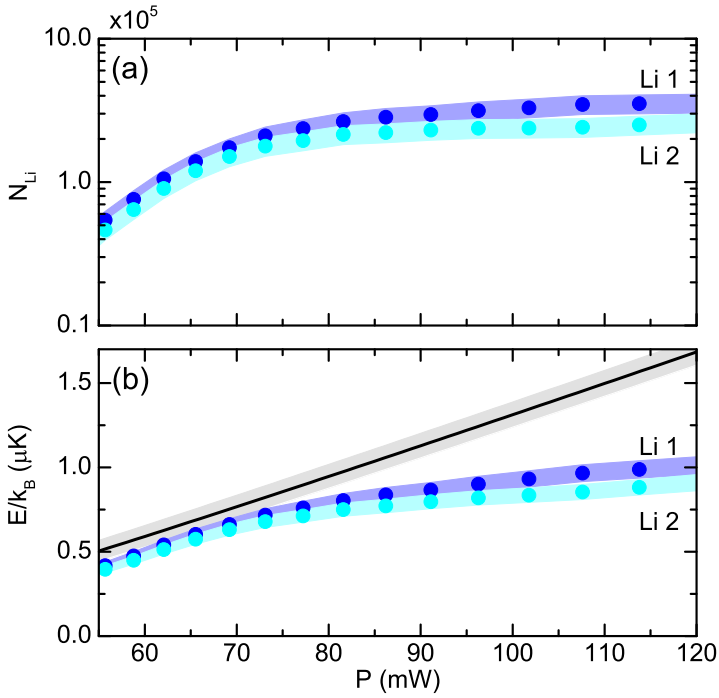

Figure 4.3: Crossover from the cooling to the spilling regime in deep evaporative cooling of ^{6}Li. In (a), we show the measured dependence of the atom number in both spin states as a function of the laser power P, which decreases during the evaporation ramp. Here the labels Li 1 and Li 2 refer to the lowest and second-to-lowest spin state of Li, respectively. The systematic calibration uncertainty in the number determination ($\pm 15\%$) is indicated by the shaded error band. In (b), we plot the corresponding behavior of the Fermi energy E_F and compare it with the decreasing trap depth $U_{\mathrm{trap}}^{\mathrm{Li}}$ (solid line). The shaded region indicates a systematic uncertainty in the trap depth resulting from the determination of the levitation gradient, which we consider as the dominant error source for E_F.

of both the atom numbers (a) and the resulting Fermi energies (b). The results reveal a change between 70 and 80 mW, which marks the crossover into the spilling regime. This interpretation is further confirmed by the behavior of the trap depth, as calculated from Eq. (4.8). Below a power of about 70 mW, the corresponding solid line in (b) gets very close to the data points and shows essentially the same slope[2]. It is also interesting to note that the spilling effect removes a small initial imbalance in the population of both spin states.

As we will see in Sec. 4.4.2, the deepest cooling takes place in the discussed crossover regime. We therefore summarize the relevant experimental parameters at $P = 75\,\mathrm{mW}$, where we have $N_\mathrm{F} = 2.0 \times 10^5$ atoms per spin state in a trap with an average frequency $\omega_\mathrm{F} = 2\pi\times140\,\mathrm{Hz}$. This results in a Fermi energy of $E_\mathrm{F} = k_\mathrm{B}\times710\,\mathrm{nK}$, corresponding to a peak number density of $n_\mathrm{F} = 1.3 \times 10^{12}\,\mathrm{cm}^{-3}$ per spin state and a Fermi wave number of $k_\mathrm{F} = 1/(4500\,a_0)$.

The interaction in the spin mixture [Zwe12] is characterized by the parameter $1/(k_\mathrm{F}a) \approx -1.6$, which shows that our gas is not in the strongly interacting regime as defined by $|1/(k_\mathrm{F}a)| < 1$, but also not far away from it. The attraction in the gas can be estimated [Nav10] to have ∼10% effect on the chemical potential and the number density as compared to the interaction-free values. We point out that this does not play any role for our thermometry approach, because we probe the temperature with another species. This is in contrast to temperature measurements that are based on the size and shape of the trapped cloud. The latter require knowledge of the temperature-dependent equation of state [Ku12] for the particular interaction conditions.

4.4.2 Condensate Fraction and Equilibrium Temperatures

Here, we first present our measurements of the condensate fraction, from which we derive the relative temperature T/T_F. Then we compare these results with direct temperature measurements of the thermal fraction of the bosons, and we finally investigate how the number of bosonic atoms affects our results.

Figure 4.4(a) shows the BEC fraction β, measured as a function of the final power P of the evaporation ramp. Each data point is the mean derived from images taken at seven different times of flight (12 to 24 ms), with the corresponding standard error of the mean. The total number of bosonic ^{41}K atoms is $N_\mathrm{B} \approx 1.3\times10^4$, independent of P. We locate the condensation threshold somewhere near 125 mW and, with decreasing power, we observe a steady increase of the condensate fraction until a maximum of

[2]The Fermi energy is calculated in the harmonic approximation. We estimate that the anharmonicity of the trap leads to an error on the order of 5%.

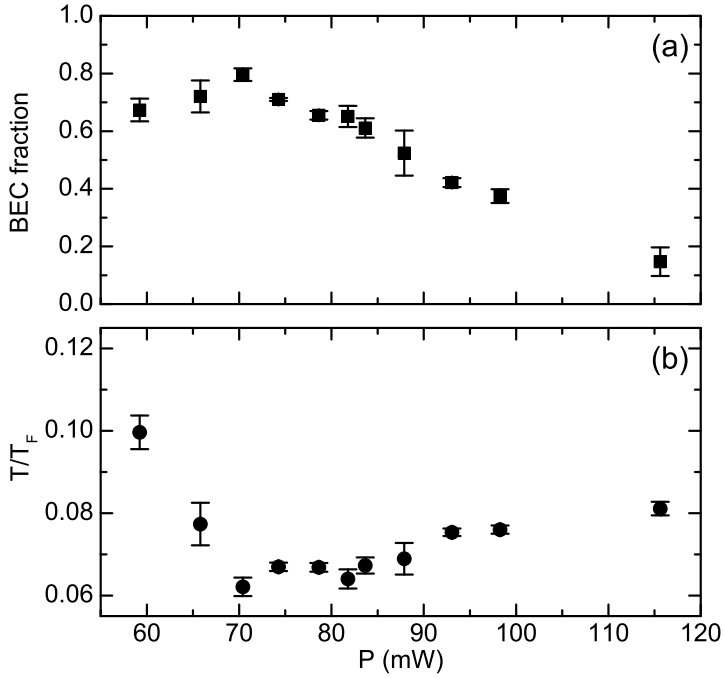

Figure 4.4: Fermi gas thermometry based on partially condensed bosons. (a) The measured condensate fraction β is shown as a function of the final power P of the evaporation ramp. Here the small error bars (most of them smaller than the symbol size) reflect the uncertainties of bimodal fits to time-of-flight images. In (b), we show the corresponding results for the relative temperature T/T_{F}. Here the error bars reflect the total statistical uncertainties from fitting the condensate fraction and the atom numbers, but not the calibration uncertainties in the atom numbers. The latter result in an additional systematic scaling uncertainty of $\pm 7\%$.

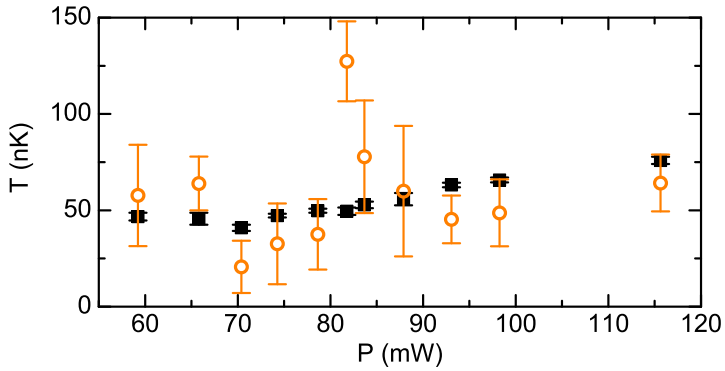

Figure 4.5: Comparison of two methods to obtain the temperature from time-of-flight images. The filled symbols represent the temperatures determined from the condensate fraction (see data in Fig. 4.4(a)) together with the total number of bosons and the separately measured trap frequency. The open symbols represent the temperatures that result from the expansion of the thermal component of the bosonic cloud. For the closed symbols, most of the errors derived are smaller than the symbol size. These errors represent the statistical uncertainties as derived from measurements at seven different expansion times. For the open symbols, the error bars are the uncertainties from fits to the expansion dynamics.

$\beta \approx 0.8$ is reached near 75 mW. The conditions of the Fermi sea of ^{6}Li atoms are exactly the ones already described in the preceding Section.

Using Eq. (4.6) and applying small finite-size and interaction corrections to the critical temperature [Gio96], we derive the relative temperature T/T_F for the degenerate Fermi gas[3]. The results are shown in Fig. 4.4(b). We observe lowest values of $T/T_F \approx 0.07$ for P between 70 and 85 mW. This power range corresponds to what we have identified before as the crossover regime between evaporative cooling and spilling. In the spilling regime, we see an increase in the relative temperature, due to a fast spilling of the Li atoms. We conclude that the deepest degeneracy of the Fermi gas is achieved when the evaporation is stopped just before the onset of spilling.

Figure 4.5 displays the absolute temperature T derived according to Eqs. (4.1) and (4.2) from the BEC fraction data already presented in Fig. 4.4(a). We compare these results with the temperature of the thermal component, which we ex-

[3] Finite-size effects and interaction effects lead to small downshifts of T_c. To derive the temperature from the condensate fraction, for the sake of simplicity, we use Eq. (4.1) with corrections to T_c from [Gio96]. Even at our smallest atom numbers, the temperature corrections stay well below 10%. Interaction corrections in our largest clouds stay below 2%.

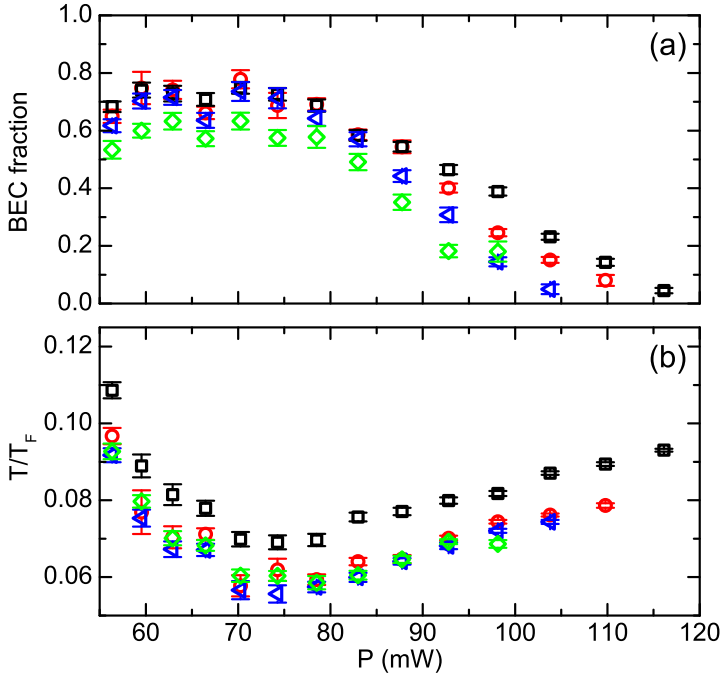

Figure 4.6: Influence of the number of bosons on (a) the condensate fraction β and (b) the resulting relative temperature T/T_F. Four different data sets are shown, with different numbers of bosonic K atoms: black squares, $N_B = 1.5(1) \times 10^4$; red circles, $1.2(1) \times 10^4$; blue triangles, $0.9(1) \times 10^4$; green diamonds, $0.76(6) \times 10^4$. The error bars represent the statistical uncertainties as derived from the fit errors of the condensate fraction.

tract from the same time-of-flight images by fitting the expansion dynamics. The comparison shows that both methods provide consistent results, but it also reveals much smaller statistical uncertainties (see error bars) for the first method. This observation highlights an important advantage for accurate thermometry of our method that is based on the determination of the condensate fraction.

In an additional set of experiments, we have addressed the question of whether the presence of the ^{41}K bosons has an influence on the cooling of the Fermi gas. We therefore reduced the number of K atoms from about 15,000 (similar to Fig. 4.4) down to about 7500. Here, for the sake of shorter data acquisition time, we applied a simpler,

but somewhat less accurate detection scheme than before[4]. In Fig. 4.6, we show the results for four different values of the K atom number. The BEC fraction in (a) decreases for a reduced number of bosons, but this can be fully attributed to the reduced critical temperature. The relative temperature in (b) shows a significant decrease for the lowest number of bosons.

Our results show that a reduction of the number of K atoms slightly improves the cooling performance of the Li Fermi gas. We interpret this observation as a consequence of the weak additional heat load associated with the bosons, which has to be removed by the evaporative cooling process. However, we do not observe any significant effect on the temperature of the Fermi sea if the number of K atoms stays below 12 000, which corresponds to about 3.0% of the total number of ^{6}Li atoms. The lowest temperature that we have observed in these measurements corresponds to $T/T_\mathrm{F} \approx 0.06$.

4.4.3 Thermalization and Heating Dynamics

A central assumption underlying our paper is thermal equilibrium between the boson "thermometer" and the Fermi sea. In order to test the validity of this assumption we have investigated the thermalization dynamics and residual heating effects that may affect our results. In all experiments discussed before, a hold time of 10 s was introduced between the end of the evaporation ramp and the temperature measurement. We now present measurements on the temperature evolution during this hold time at a constant trap power of $P = 75$ mW, again based on the detection of the condensate fraction. Figure 4.7(a) shows how the temperature drops from about 78 nK right after the evaporation ramp to its equilibrium value of 53 nK. An exponential fit yields a thermalization time scale of 2.5(5) s, which is short compared with the total hold time of 10 s. This ensures that the K cloud reaches its equilibrium temperature with negligible deviations well below 1 nK.

The thermalization time can be estimated from our experimental parameters, using the approximation

$$\frac{1}{\tau} = 2 \times \frac{3T}{2T_\mathrm{F}} \times \frac{\xi}{3} \times n_\mathrm{F} \sigma v_\mathrm{F}\,, \tag{4.12}$$

which is a product of four factors. The prefactor of 2 accounts for the two different spin states in the Fermi sea. The factor $3T/(2T_\mathrm{F}) \approx 0.1$ results from the Pauli blocking of

[4] In Fig. 4.6, we have used a single time of flight of 22 ms to reduce the total measurement time. This method may be somewhat less accurate, but produces results fully consistent with the method used in Fig. 4.4.

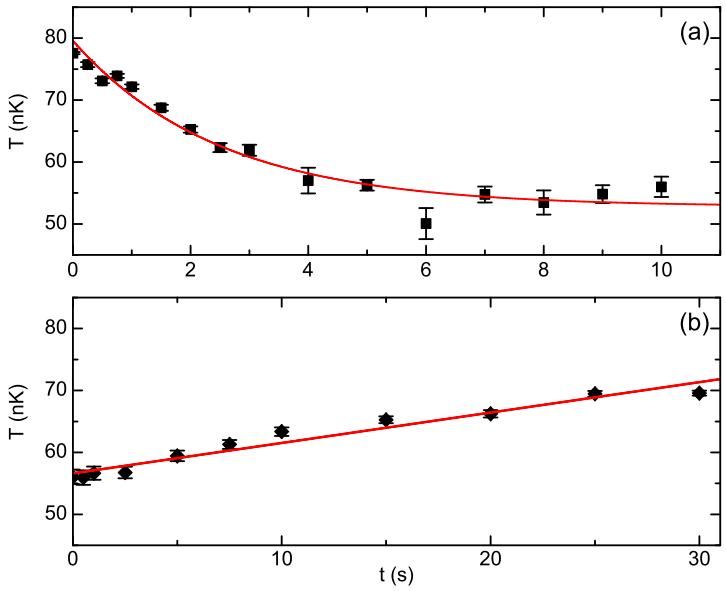

Figure 4.7: Thermalization and heating dynamics with and without the Fermi sea. (a) The data points show the measured temperature evolution of the bosonic ^{41}K cloud ($N_B = 1.6(2) \times 10^4$) after evaporative cooling of the ^{6}Li Fermi sea. The solid curve is an exponential fit, yielding a relaxation-time constant of 2.5(5) s. (b) The data points display the measured temperature increase of the ^{41}K cloud after full removal of the ^{6}Li coolant. The linear fit (solid line) yields a heating rate of 0.49(4) nK/s. The error bars represent the temperature uncertainties as derived from the fit errors of the condensate fraction.

collisions[5]. The third factor $3/\xi$ estimates the number of elastic collisions needed for thermalization, with $\xi = 4m_K m_{Li}/(m_K + m_{Li})^2 \approx 0.45$ for the specific mass ratio of our mixture [Mud02]. The last factor represents the elastic collision rate in the limit of relative velocities dominated by the light atoms at the top of the Fermi sea, with the corresponding Fermi velocity $v_F = \sqrt{2E_F/m} \approx 44$ mm/s. The cross section for elastic collisions between ^{6}Li and ^{41}K atoms is $\sigma \approx 1.3 \times 10^{-16}$ m^2 [Han10]. This results in a relaxation time of $\tau \approx 4.5$ s, which is larger than the observed value, but still within

[5] We approximate this effect by assuming that only the fraction of Li atoms with energies in an interval between $k_B(T_F - T/2)$ and $k_B(T_F + T/2)$ is thermally active. The factor 3/2 results from the number of states, which increases $\propto E^{3/2}$ for the approximately homogeneous environment sampled by the bosons in the trap center.

the errors of the simple estimation used.

We have also checked the influence of a possible effect of residual heating of the K cloud, which may be induced by trap light fluctuations. This heat would have to be removed by thermal contact with the coolant, i.e. the Fermi sea of ^{6}Li atoms, and the corresponding heat flow would require a temperature difference between the two components. We have experimentally investigated the heating of the K cloud after removing the Li atoms from the trap, by application of a magnetic gradient, and observed the temperature evolution over 30 s. Figure 4.7(b) reveals a very weak temperature increase, with a slope corresponding to a heating rate of $\gamma_{\mathrm{heat}} \approx 0.5\,\mathrm{nK/s}$. Here, for simplicity, we assume a linear heating model. With the relaxation time $\tau \approx 2.5\,\mathrm{s}$ discussed before, we obtain a temperature difference of $\gamma_{\mathrm{heat}}\tau \approx 1.2\,\mathrm{nK}$, which is negligibly small. In additional experiments, we have investigated heating in our detection trap, see Sec. 4.3.3, and found an effect of less than 2 nK/s within the 4 s when the atoms are kept in this trap.

4.4.4 Uncertainties

Our thermometry approach is based on Eq. (4.6) to determine the relative temperature T/T_{F}. The underlying model relies on the harmonic approximation of the trap potential, and we estimate that anharmonicity effects on T_{F} do not exceed a few percent.

The model also assumes the bosonic probe to be a weakly interacting gas, which is well fulfilled. We have checked that we are not near any intraspecies or interspecies Feshbach resonances. Furthermore, the intraspecies background scattering length of ^{41}K is about $+60\,a_0$ [D'E07, Pat14] and the background scattering length between ^{6}Li and ^{41}K is also about $+60\,a_0$ [Han10]. This means that for the reference power ($P = 75\,\mathrm{mW}$) and $N_{\mathrm{B}} \approx 1.2 \times 10^4$, the chemical potential of the bosons corresponds to $\sim 16\,\mathrm{nK}$. The peak number density of the fermions is about 26 times smaller than the one of the bosons. The mean field of the fermions as seen by the bosons is very small, only $\sim 2.3\,\mathrm{nK}$. The correction to the boson trap frequencies caused by the fermion mean field, is on the order of 10^{-3} , which is negligibly small. The mean field of the bosons on the fermions corresponds to $\sim 64\,\mathrm{nK}$, which is much smaller than the Fermi energy of about 710 nK.

In addition to these model assumptions, the experimental determination of the temperature is subject to four main error sources. First of all, there are the statistical measurement uncertainties. These come from the analysis of the time-of-flight images and give uncertainties of a few percent in both the atom number and the determination of the condensate fraction.

A second source that influences the measured values of T/T_{F} are calibration errors. For the atom number determination, we estimate calibration uncertainties of 15% for

both species. This results in a systematic scaling uncertainty in T/T_F of $\pm 7\%$. Another systematic error source is the trap frequency ratio, which slightly changes if the trap does not exactly fulfill the magic levitation condition. However, the effect on T/T_F for the range of powers used in our experiments is negligibly small.

Thirdly, the thermalization between the two species may be imperfect, owing to heating in combination with weak thermal coupling. We estimate that the corresponding temperature difference stays below 2 nK, which results in an effect below 3% on the relative temperature.

Furthermore, as a fourth error source, we observed a slight heating effect during the transfer into the detection trap, which may also affect the temperature by a few percent at most. We are confident that other heating sources are very weak and can be safely neglected. All these residual heating effects may somewhat increase the temperature of the bosonic probe atoms, and may thus lead to an overestimation of the temperature, but not by more than 10%.

Taking all statistical and systematic uncertainties into account, we can report a lowest observed temperature of $T/T_F = 0.059(5)$[6]. The true temperature of the Fermi gas may even be slightly below this value (about 5%) because of residual heating directly affecting the thermometry atoms.

4.5 Conclusion

We have thoroughly investigated a conceptually simple and accurate method for determining the temperature of a deeply degenerate Fermi gas. Our method essentially relies on detecting the condensate fraction of a second, weakly interacting bosonic species that is thermalized with the Fermi sea. High accuracy of the temperature measurements can be achieved, since the relevant trap frequency ratio can be very well determined and uncertainties in the atom number only weakly influence the results.

We have employed the method in experiments on a spin mixture of ^{6}Li, where we have used a small sample of ^{41}K bosons as the probe. The large mass ratio and a large number ratio have enabled us to measure the temperature in the range of 0.03 to 0.1 T_F, which is right in the regime of state-of-the art cooling experiments. We have investigated the final stage of deep evaporative cooling and we have observed that the deepest degeneracy of the Fermi gas, with $T/T_F = 0.059(5)$, is achieved when the evaporation is stopped just before the onset of spilling. We found the temperature not to be affected by the presence of the probe atoms if the number of K atoms stays below

[6]The reported temperature is the mean value of the red circles, blue triangles, and green diamonds in Fig. 4.6, in the range of $68 - 80$ mW.

3.0% of the number of Li atoms. The K atoms then represent impurities in a Fermi sea.

Our thermometry method provides us with a powerful tool to further optimize the cooling. For optimization, we can improve the starting conditions for evaporation by implementing a sub-Doppler cooling stage [Bur14b, Sie15] and we can optimize the evaporation sequence by variation of the magnetic field, the trap configuration and the details of the ramp. With sensitive and accurate thermometry, it will be very interesting to investigate the practical and fundamental limitations of the cooling process. Under our present conditions, we may be limited by residual trap light fluctuations [Sav97] or other sources of noise in the experiment or by inelastic losses in combination with the hole heating effect [Tim01].

For the interaction parameter of $1/(k_F a) \approx -1.6$, as chosen in our experiments, the predicted critical temperature for superfluidity is $\sim 0.03\, T_F$ [Blo08, Hau07]. Thus, even for our lowest temperatures, the Li spin mixture is not superfluid. However, the system is stable enough at resonant interaction conditions [Spi09], so that the realization of a mass-imbalanced Bose-Fermi double superfluid, as already demonstrated in Ref. [Yao16], would be straightforward. Thermometry on the bosons could be performed in a wide range of the BEC-BCS crossover, as long as the thermalization time stays much shorter than the timescale of inelastic losses[7]. While the BEC side may be problematic [Spi09], the method would work well in the unitary case and on the BCS side.

The implementation of the presented thermometry method should be straightforward for other Bose-Fermi mixtures. Extreme mass ratios [Pir14, Tun14, Roy17, Kon16] are of particular interest for pushing the accessible regime further down to temperatures on the order of $0.01\, T_F$. However, at such ultralow temperatures, the larger number of collisions required for thermalization and the increasing Pauli blocking effect will increase the thermalization time, which will make it more difficult to reach thermal equilibrium on a realistic experimental time scale. This may be compensated for by larger interspecies collision cross sections or higher number densities. Our paper shows how the conditions can be optimized for specific mixtures, including the role of optical polarizabilities, magnetic moments, magnetic levitiation for trapping, and the effect of interspecies collisions.

In our future work, we are particularly interested in the deep cooling of the Fermi sea. This reduces thermal decoherence effects as observed in studies of impurities coupled to the Fermi sea [Cet15] and opens up the possibility of observing new phenomena [Cet16], such as multiple particle-hole excitations and the onset of the or-

[7] Inelastic decay of ^{41}K is observed predominantly on the BEC side of the ^{6}Li Feshbach resonance, similar to what was observed on a strongly interacting ^{40}K-^{6}Li mixture [Spi09]

thogonality catastrophe [Kna12]. Moreover, we are interested in the collective zero-temperature dynamics of bosonic impurities in the Fermi sea close to an interspecies Feshbach resonance [Lou17a].

Acknowledgments

We thank J. Walraven for stimulating discussions, Y. Colombe for fiber fusing, L. Reichsöllner for support regarding the atomic-beam characterization, the Dy-K team for general discussions, and M. Cetina for contributions in the early stage of the ^{41}K implementation. We also thank F. Lehmann, E. Kirilov, and R. Onofrio for comments on the paper. We acknowledge support by the Austrian Science Fund FWF within the Spezialforschungsbereich FoQuS (Grant No. F4004-N23) and within the Doktoratskolleg ALM (Grant No. W1259-N27).

4.6 Appendix: 'Magic' Levitation Trap

We refer to a 'magic' levitation trap as an optical dipole trap for two different species, in which the corresponding potential depths and trap frequencies maintain a constant ratio at any optical power applied. In optical dipole trapping experiments, one often has to deal with the effect of gravity. Two species in the same trap are in general affected differently, in particular in the case of largely different masses or different optical polarizabilities. The tilted potentials usually give a different reduction of the effective trap depth as compared to the depth of the optical potentials. During evaporative cooling this often leads to a much faster reduction of the potential depth for the heavier species than for the lighter one, which may pose a severe limitation to the whole cooling process. Magnetic levitation [And95, Han01, Web03a] offers a solution to this problem and allows one to realize conditions, where the combined effect of gravity and levitation results in the same effect on the total shape of the potential.

The magic gradient can be derived from the condition that the combined magnetic and gravitational force is the same for both traps, if considered relative to the optical potential, the depth of which in turn is proportional to the optical polarizabilities. The condition reads

$$\frac{\mu_1 B'_{\pm} - m_1 g}{\alpha_1} = \pm \frac{\mu_2 B'_{\pm} - m_2 g}{\alpha_2}, \tag{4.13}$$

where m_i, μ_i, and α_i represent the different masses, magnetic moments, and optical polarizabilities of the two species, respectively. The lower sign refers to the situation illustrated in Fig. 4.8(a), where the trapping potentials are tilted in the opposite direction. The upper sign corresponds to the situation, where both potentials are tilted in the

same direction. Solving Eq. (4.13) yields the two corresponding magnetic gradients

$$B'_{\pm} = \frac{\alpha_2 m_1 \mp \alpha_1 m_2}{\alpha_2 \mu_1 \mp \alpha_1 \mu_2}\, g\,. \tag{4.14}$$

The solution B'_{-} means partial levitation for one species and overlevitation for the other one, so that the tilts have opposite signs. The other solution (B'_{+}) corresponds to the same direction of the tilt for both species. The application of B'_{-} causes a separation of the trap centers, similar to the gravitational sag effect. In contrast, B'_{+} does not cause such a spatial shift, but it may imply much stronger tilts. The optimum solution for an experiment depends on the specific situation.

For our situation of optically trapped ^{6}Li and ^{41}K at high magnetic bias fields ($\mu_1 = \mu_2 \approx \mu_B$), we obtain a magic levitation gradient of $B'_{-} = 2.97\,\mathrm{G/cm}$, corresponding to a partial levitation of 41.3% for K and an overlevitation of 281% for Li. The small spatial separation of the trap centers is irrelevant for our application. For the experimental power range we use, the separation between the trapcenters of the two species lies between 12 and 28 % of the optical beam waist. Note that the other solution ($B'_{+} = -4.02\,\mathrm{G/cm}$) does not correspond to levitation, but to an effective increase of the gravitational effect for both species. As described in Sec. 4.3.2, we realize a situation close to the magic levitation gradient B'_{-}.

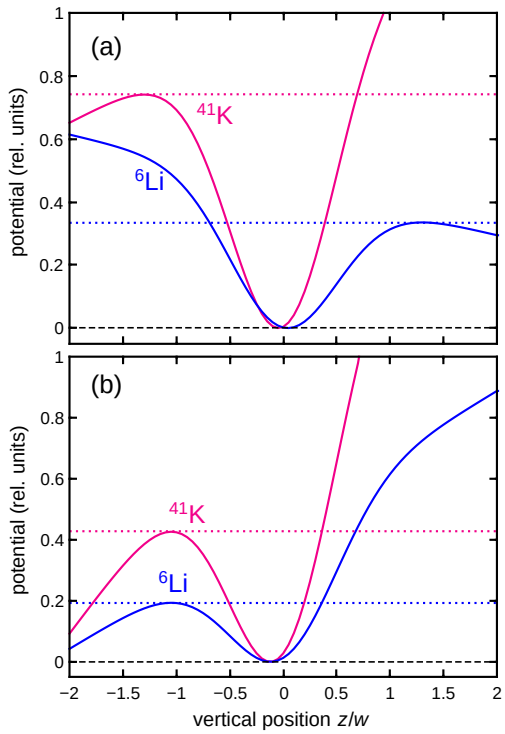

Figure 4.8: Illustration of magic levitation for ^{6}Li and ^{41}K. All potentials are normalized to the optical potential depth of K, and zero potential refers to the trapping potential minima. The combined magnetic and gravitational forces cause a trap depth reduction, as indicated by the horizontal dotted lines. For two distinct values of the magnetic gradient, see Eq. (4.14), the ratio of the resulting trap depths for K and Li remains constant and corresponds to the ratio of optical polarizabilities ($\alpha_K/\alpha_{Li} \approx 2.2$). (a) With the magnetic gradient set to B'_-, K is partially levitated, while Li is overlevitated. The relative tilt has the same magnitude, but opposite sign. (b) With the gradient set to B'_+, the magnetic force effectively increases the effect of gravity for both species, resulting in a tilt in the same direction.

CHAPTER 5

Probing the Interface of a Phase-Separated State in a Repulsive Bose-Fermi Mixture

Published as:
R. S. Lous, I. Fritsche, M. Jag, F. Lehmann, E. Kirilov,
B. Huang (黄博), and R. Grimm
Phys. Rev. Lett. **120**, 243403 (2018)

Author contribution

The author took one of the leading roles in the experimental part of this paper. In collaboration with the other authors, she designed the experiment, performed many of the measurements, analyzed the data, and wrote the experimental part of the manuscript.

We probe the interface between a phase-separated Bose-Fermi mixture consisting of a small Bose-Einstein condensate of ^{41}K residing in a large Fermi sea of ^{6}Li. We quantify the residual spatial overlap between the two components by measuring three-body recombination losses for variable strength of the interspecies repulsion. A comparison with a numerical mean-field model highlights the importance of the kinetic energy term for the condensed bosons in maintaining the thin interface far into the phase-separated regime. Our results demonstrate a corresponding smoothing of the phase transition in a system of finite size.

5.1 Introduction

Multicomponent systems and materials are ubiquitous in nature and technology. The interactions between the different constituents and the ways in which they coexist are essential for understanding the general properties of such systems. Repulsive interactions between different components can induce phase transitions to spatially separated states. The effects of phase separation appear in a wide range of different systems such as alloys, combinations of different liquids, colloids, polymers, glasses and biological systems. In a phase-separated state, the interaction between the components no longer takes place in the bulk but is restricted to the thin interface where the constituents still maintain some residual overlap. The physics of this interface has therefore attracted a great deal of attention in many different fields, e.g. in liquid-liquid systems [Dav96, Han13]. However, since the interaction takes place in a very small volume, it is generally much more difficult to obtain experimental information from these systems as compared to systems in which the components are mixed.

Quantum fluids exhibit a great wealth of phenomena related to phase separation. Early experiments with cryogenically cooled liquid helium have shown phase separation in
mixtures of the bosonic isotope ^{4}He and the fermionic ^{3}He [Ebn71]. This effect has found an important technological application in the working principle of dilution refrigerators [Das65, Pob07]. Ultracold gases, in particular, mixed-species systems have opened up many intriguing experimental possibilities to study phases of multicomponent quantum matter [Blo08]. The large experimental toolbox includes a variety of available bosonic and fermionic constituents, a superb level of control of confinement, and a wide tunability of interactions [Chi10]. Phase separation has been studied extensively in degenerate Bose-Bose mixtures [Pap08b, Toj10, McC11, SK13, Wac15, Wan16, Lee16], where interactions are dominated by mean-field potential energies. The situation becomes more complicated when fermionic constituents are involved, as

strong repulsion on the scale of the Fermi energy is required to observe phase separation. Superfluid fermionic mixtures [Shi08] and repulsive atomic Fermi gases [Val17] are examples of intriguing phase-separation effects. In a broad sense, mixtures involving fermionic constituents are promising candidates for realizing new phases, e.g., in Fermi-Fermi systems [Liu03, Isk06, Par07, Bar08, Baa10, Wan17] and in Bose-Fermi systems [Pow05, Suz08, Mar08b, Lud11, Ber13, Kin15].

In this Letter, we consider a Bose-Fermi model system that undergoes phase separation and study the interface between the constituents. We produce a Bose-Einstein condensate (BEC) of ^{41}K atoms in a large Fermi sea of ^{6}Li, and we use an interspecies Feshbach resonance for controlling the repulsive interaction. We characterize the overlap between the species by measuring three-body recombination losses and thus probe the thin interface between both components. By comparing the experimental results with theoretical model calculations, we demonstrate the importance of the kinetic energy of the condensed bosons at the thin interface.

5.2 General Idea

Figure 5.1(a) illustrates the onset of phase separation with an increasing interspecies repulsion, showing the density profiles of a small-sized BEC coexisting with a large Fermi sea in a harmonic trap. The main conditions and criteria for phase separation in such Bose-Fermi mixtures have been theoretically introduced in Refs. [Mø98, Viv00, Rot02]. For a vanishing interspecies interaction, the independent spatial profiles of the clouds show maximum overlap [I in Fig. 5.1(a)]. With an increasing repulsion, the density of the lithium atoms in the center of the trap decreases, the BEC is compressed, and the spatial overlap between the clouds is reduced (II). For strong repulsive interactions, the two clouds undergo phase separation (III), and the bosons reside at the center of the trap, forming a hole in the Fermi sea.

We can observe the depletion in the center of the Fermi sea by imaging the ^{6}Li cloud. As Fig. 5.1(b) shows, we observe a small dip in the radial column density profile taken from a thin slice of the fermion cloud. These data were taken under similar conditions as our main data presented later [1]. The hole in the fermion density becomes more visible when reconstructing the fermionic radial density profile using the inverse Abel transformation [Fig. 5.1(b)]. We see an essentially complete depletion of the fermionic density in the center, which indicates a significant reduction of the overlap with the BEC. A quantitative analysis of the physics at the interface is obstructed by the limited signal-to-noise ratio of the image, the small size of the overlap region

[1] The thin slice is taken from a typical absorption image of the Li cloud with a time of flight of 2 ms and at $a_{\mathrm{bf}} \approx 1480 a_0$

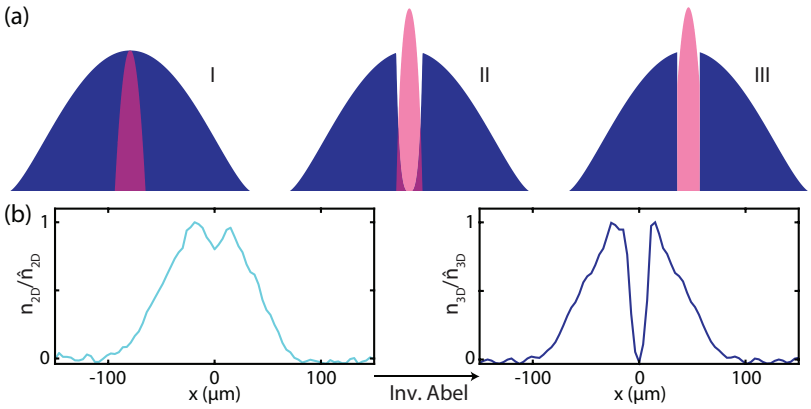

Figure 5.1: Emergence of phase separation. (a) Schematic density profiles for bosons (magenta) and fermions (blue) for an increasing repulsive interaction. The densities are normalized to the corresponding peak value without an interaction. Note that in reality the boson peak density is a factor of 40 larger than the fermion peak density. (b) Experimentally observed normalized column density of a cut through the fermionic cloud and normalized reconstruction of the corresponding radial density profile using the inverse Abel transformation.

5

compared to our imaging resolution, and the high optical density of the trapped cloud. Note that strong indications of phase separation in a Bose-Fermi mixture have been observed in earlier experiments on mixtures of ^{87}Rb and ^{40}K [Osp06c, Zac06], but these experiments did not provide quantitative information on the overlap reduction.

Here, we introduce an alternative approach to study the spatial overlap between the two species. Our observable is the boson-boson-fermion three-body recombination loss from the trap. We assume that all losses can be attributed to three-body processes, since two-body losses are energetically suppressed when both atomic species are in their lowest internal substates. In our system, decay processes of three ^{41}K atoms (three identical bosons) occur at a very low rate, since the intraspecies scattering length $a_{\mathrm{bb}} = 60.9a_0$ [Tie17], with a_0 being the Bohr radius, is small compared with the interspecies scattering length a_{bf} in the range of interest. On the other hand, recombination processes involving one ^{41}K atom and two ^{6}Li atoms (one boson and two identical fermions) are Pauli suppressed [Esr01]. At a large interspecies scattering length, this leaves the recombination events of two ^{41}K atoms with one ^{6}Li atom as the dominant three-body decay mechanism.

A favorable property of our system is the fact that the BEC is much smaller than

the fermion cloud and occupies a very small volume within the Fermi sea. Thus, the BEC can cause only a local perturbation of the Fermi sea with a negligible effect on the global scale. This scenario enables a description in terms of a *fermionic reservoir approximation* (FRA), which assumes a homogeneous environment characterized by a constant Fermi energy E_F and considerably simplifies our study of the overlap.

In the zero-temperature limit, where a pure BEC is formed, the bosonic atom loss can be related to the overlap integral as

$$\dot{N} = -\frac{1}{2} L_3 \int n_f \, n_b^2 \, dV, \tag{5.1}$$

where N is the total number of bosons and n_b and n_f represent the position-dependent number densities of the bosons and fermions, respectively. The parameter L_3 is the three-body loss coefficient, and the symmetry factor $1/2$ results from the suppression of thermal bunching in a BEC [Kag85, Bur97, Söd99, Hal11] for a process involving two identical bosons. The L_3 coefficient can be determined as a function of a_{bf} in a standard way [Web03b, Ulm16] using a noncondensed cloud instead of a BEC. In this case, the interspecies repulsion can be neglected, and the density profiles of the bosons and the fermions are well known.

In order to characterize the effect of the boson-fermion interaction on the spatial overlap between the BEC and the Fermi sea, we define the overlap factor

$$\Omega \equiv \frac{\int n_f \, n_b^2 \, dV}{\int \tilde{n}_f \, \tilde{n}_b^2 \, dV} \tag{5.2}$$

as the three-body density integral normalized to the case of vanishing interspecies interaction ($a_{bf} = 0$), where $\tilde{n}_f$ ($\tilde{n}_b$) is the fermionic (bosonic) noninteracting density.

The overlap integral for the case of a vanishing interspecies interaction, $\int \tilde{n}_f \, \tilde{n}_b^2 \, dV$, can be calculated analytically based on two approximations. First, we apply the FRA and replace $\tilde{n}_f$ by its peak value $\hat{n}_f$, which as a constant factor can be taken out of the integral. Second, for a not too small BEC, we can apply the Thomas-Fermi approximation and solve $\int \tilde{n}_b^2 \, dV$ as $\frac{4}{7} N_b \, \hat{n}_b$, with $\hat{n}_b$ the peak density of the BEC. Finally, with the overlap integral for the interacting case given by Eq. (5.1), the overlap factor can be experimentally obtained as

$$\Omega = \frac{7}{2 \, \hat{n}_f \, \hat{n}_b} \frac{\gamma}{L_3}, \tag{5.3}$$

where we introduce the normalized loss rate $\gamma = -\dot{N}/N$ as the experimental observable extracted from measuring the atom loss in a BEC.

5.3 Experimental Preparation and Results

For our experiments, we prepare an ultracold Bose-Fermi mixture of typically 10^4 K and 10^5 Li atoms in a cigar-shaped, crossed-beam optical dipole trap with a wavelength of 1064 nm and an aspect ratio of 1:7. The preparation procedures are similar to those described in Ref. [Lou17b] and earlier work on ^{6}Li-^{40}K mixtures [Spi09, Tre11, Koh12, Jag14, Cet16]. In addition, we employ a laser cooling scheme for lithium using the D1 line [Gri13, Bur14a, Fri15], which provides improved starting conditions, and we take advantage of an alternative evaporative cooling approach [Bur14a] (see Sec. 5.6.1).

A key ingredient of our experiment is the Feshbach resonance (FR) near 335 G [Han17, Tie17, Wu11] (see Sec. 5.6.2 and Appendix B), between the lowest spin states of the two species. The scattering length can be varied by magnetic field tuning according to $a_{\mathrm{bf}} = a_{\mathrm{bg}}\left[1 - \Delta/(B - B_0)\right]$ [Chi10], where $\Delta = 0.949\,\mathrm{G}$, $a_{\mathrm{bg}} = 60.9a_0$ and $B_0 = 335.057(1)\,\mathrm{G}$. The FR center B_0 somewhat depends on the optical trap intensity because of a light shift effect (see Sec. 5.6.2.3) and can be experimentally determined by radio-frequency spectroscopy. The other parameters are obtained from scattering models [Han17, Tie17] (see Sec. 5.6.2.1).

To obtain the critical interspecies scattering length for the onset of phase separation, we employ the FRA together with the results of Ref. [Viv00]. This yields the condition

$$a_{\mathrm{bf}} > 1.15\sqrt{a_{\mathrm{bb}}/k_{\mathrm{F}}}, \tag{5.4}$$

where $k_{\mathrm{F}} = (6\pi^2\hat{n}_{\mathrm{f}})^{1/3}$ is the Fermi wave number, corresponding to $E_{\mathrm{F}} = \hbar^2 k_{\mathrm{F}}^2/(2m_{\mathrm{f}})$ with m_{f} the mass of the fermions. For our typical experimental conditions ($\hat{n}_{\mathrm{f}} \approx 1.2 \times 10^{12}\,\mathrm{cm}^{-3}$), it gives a moderate value for the critical scattering length of about $600a_0$. This is well within our tuning range and allows us to explore the entire scenario from weak to strong repulsion, reaching far into the phase-separated regime.

We first present our measurements of L_3, which were obtained with noncondensed samples of ^{41}K in a degenerate Fermi sea of ^{6}Li at about $0.2\,T_{\mathrm{F}}$, with T_{F} the Fermi temperature. From the measured decay curves we obtain the L_3 values that are shown in Fig. 5.2(a). The K samples are prepared close to degeneracy at two different temperatures with a typical fermion peak density of $\hat{n}_{\mathrm{f}} \approx 4.5 \times 10^{12}\,\mathrm{cm}^{-3}$. In one set of measurements (set A1, see Sec. 5.6.3.1), we have $T = 440\,\mathrm{nK}$, corresponding to $T/T_{\mathrm{c}} = 1.7$ with T_{c} the critical temperature for condensation. In the other set (A2), we have $T = 240\,\mathrm{nK}$, corresponding to $T/T_{\mathrm{c}} \approx 1$. By applying a smoothing method (see Sec. 5.6.3.2), we interpolate between the data points and obtain L_3 for any a_{bf} between 80 and $2100a_0$. Our results on L_3 show the expected strong increase with a_{bf}, while the broad dent around $600a_0$ may point to an Efimov-related feature [Kra06, Joh17].

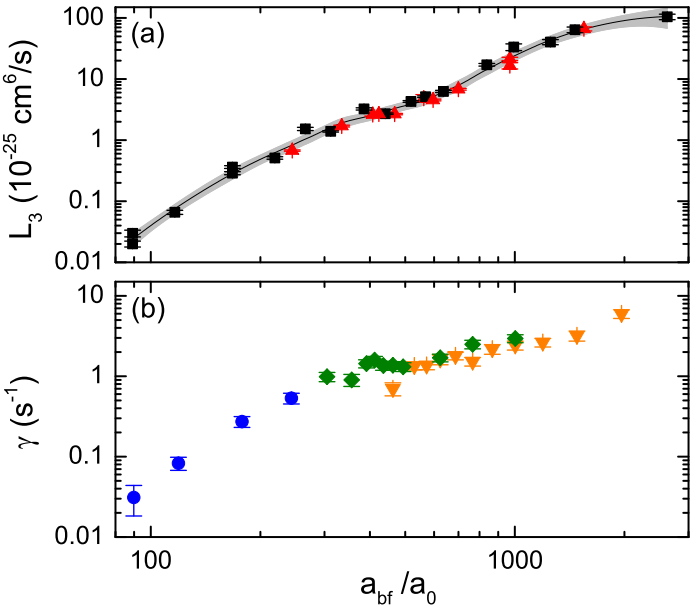

Figure 5.2: Loss measurements on noncondensed and condensed bosonic ^{41}K clouds in a ^{6}Li Fermi sea. The error bars represent 1σ fit uncertainties. (a) Three-body loss coefficient L_3 for $T = 440$ (set A1: squares) and 240 nK (set A2: triangles). The solid curve is an interpolation from applying a smoothing method (see Sec. 5.6.3.2), with the gray-shaded area representing the corresponding 95% confidence band. (b) Normalized loss rate γ of the total atom number of a partially condensed bosonic cloud for data sets B1-B3 (inverse triangles, diamonds, and circles, respectively).

Second, we present the boson loss rate γ in a degenerate Bose-Fermi mixture at various interaction strengths. Typically, we have $2.9{\times}10^4$ K atoms with a 50% condensate fraction in a Fermi sea of $1.4{\times}10^5$ Li atoms with a peak density of $\hat{n}_\mathrm{f} = 1.2{\times}10^{12}\,\mathrm{cm}^{-3}$ and a temperature of $\sim 0.13 T_\mathrm{F}$. The sample is first prepared at 200 mG below B_0, and then the magnetic field is changed in a near-adiabatic ramp of 2 ms to the specific field on the repulsive side of the FR, where we observe the loss of the K atoms for various hold times. We fit the initial decay of the total atom number with a linear curve and determine the normalized loss rate γ (see Sec. 5.6.3.3). Figure 5.2(b) shows the corresponding data points, which were recorded in three sets (B1-B3, see Sec. 5.6.3.1) with slightly varying parameters.

With the normalized loss rate γ and the three-body recombination coefficient L_3, we can now quantify the spatial overlap. In a real experiment, two complications arise that require an extension of our model beyond Eq. (5.3). First, at a finite temperature, we have only a partial BEC and the presence of the thermal component plays a significant role in the observed loss. Second, there is the possibility of observing secondary loss, where a short-lived LiK dimer, produced in a first recombination, recollides with another K atom, and therefore this leads to additional loss (see Sec. 5.6.3.5). This process is likely to happen for the dense BEC but negligible for the thermal K cloud. To take both effects into account, we extend Eq. (5.1) and include all loss contributions;

$$\dot{N} = -L_3 \int n_\mathrm{f} \left(\frac{1}{2} \alpha\, n_\mathrm{b}^2 + \alpha\, n_\mathrm{b}\, n_\mathrm{t} + n_\mathrm{t}^2 \right) \mathrm{d}V, \tag{5.5}$$

where n_t represents the thermal bosonic density and α is a factor that takes into account secondary loss. In our case, we assume $\alpha = 3/2$ (see Sec. 5.6.3.5). The density integral consists of three terms, which describe the loss caused by one fermion and two bosons. The bosons can either be two atoms from the BEC, one from the BEC and one from the non-condensed component, or two from the noncondensed bosonic cloud. Within the FRA and the Thomas-Fermi approximation, these integrals can be calculated, and an effective overlap factor results from an extension of Eq. (5.3) as

$$\Omega_\mathrm{eff} = \frac{1}{\hat{n}_\mathrm{f} \left[\frac{2}{7}\, \alpha\, \hat{n}_\mathrm{b}\, \beta + \alpha\, \hat{n}_\mathrm{t} \beta + \frac{1}{\sqrt{8}}\, \hat{n}_\mathrm{t} (1-\beta) \right]} \frac{\gamma}{L_3}, \tag{5.6}$$

where β is the BEC fraction and $\hat{n}_\mathrm{t}$ the peak density of a thermal Bose gas, as given by $\hat{n}_\mathrm{t} = \left[m_\mathrm{b}\, \bar{\omega}_\mathrm{b}^2 / (2\pi k_\mathrm{B} T) \right]^{3/2} (1-\beta)\, N$, with $\bar{\omega}_\mathrm{b}$ being the geometrically averaged trap frequency of the bosons, m_b their mass, and $T = T_\mathrm{c} (1-\beta)^{1/3}$ [Lou17b] (see Sec. 5.6.3.1).

Figure 5.3 shows the values of Ω_eff that result from the data in Fig. 5.2. We qualitatively distinguish three regions. Below $a_\mathrm{bf} \approx 250 a_0$, the values are close to one, and

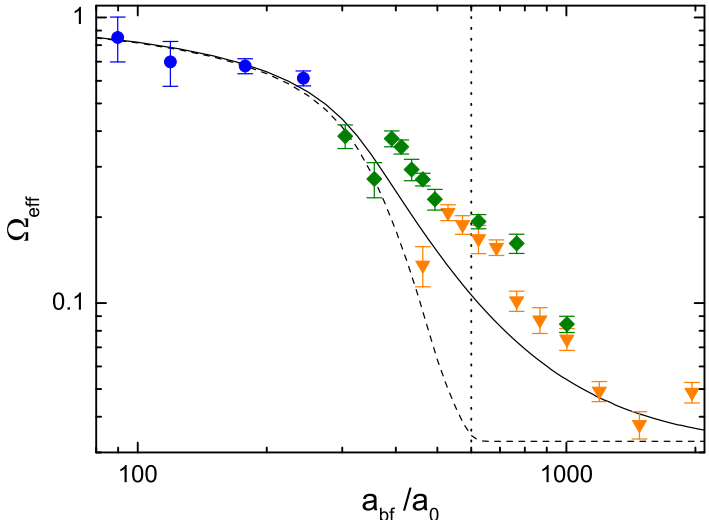

Figure 5.3: Effective overlap factor versus Bose-Fermi scattering length for data sets B1-B3 (inverse triangles, diamonds, and circles, respectively). The error bars reflect the statistical uncertainties of γ. The vertical dotted line shows the phase-separation point as predicted by Eq. (5.4). The solid line shows the results of our full numerical calculation (see the text) and the dashed line our results obtained within the Thomas-Fermi approximation.

there seems to be a downward trend for Ω_{eff} with increasing a_{bf}. Then, as a_{bf} further increases to about $1000a_0$, the spatial overlap drastically decreases to a small value of about 0.04. For larger scattering lengths, Ω_{eff} tends to remain at this small value. According to Eq. (5.4), phase separation is expected to happen at $\sim 600a_0$ (vertical dotted line). In contrast, we observe that beyond this point a considerable spatial overlap remains, which then smoothly decreases with a further increasing scattering length. The observed behavior does not reveal any discontinuity related to a phase transition.

5.4 Numerical Calculation

To interpret the observed behavior of Ω_{eff}, we construct a numerical mean-field model[2] (see Sec. 5.6.4) which allows us to calculate the density distributions for an interacting

[2] B. Huang *et al.*, *in preparation* (2018)

Bose-Fermi mixture at a zero temperature for our typical experimental parameters[3]. Our model starts from the energy functional of the mixture as given by Refs. [Ima06, Tra16], and we use imaginary time evolution to vary the BEC and the fermionic densities and to minimize the energy functional. At the end, the evolution gives the static solution of n_f and n_b at a zero temperature. Since we have a partial BEC, we additionally take into account the thermal bosonic density n_t including bosonic enhancement effects (see Sec. 5.6.4). With these density distributions, we numerically calculate the overlap integrals and the effective overlap factor Ω_{eff}.

The results of our numerical model are represented in Fig. 5.3 by the dashed and solid curves. For the dashed curve, the densities are obtained within the Thomas-Fermi approximation. The results indeed show a rapid decrease of Ω_{eff} until the onset of phase separation at about $600a_0$, as given by Eq. (5.4). Then, in a fully phase-separated regime, a plateau is reached where only the thermal bosonic component can lead to loss. Evidently, this theoretical behavior is not consistent with the experimental data points. A notably smoother decrease of Ω_{eff} results from our numerical model (solid line in Fig. 5.3), when we consider the full energy functional which includes the kinetic energy of the BEC as well as the much weaker density gradient correction from the Fermi gas [Ima06]. Within the residual uncertainties of our method (see Sec. 5.6.5), this model reproduces the observed behavior very well.

5.5 Conclusion and Outlook

Our results show that the kinetic energy term prevents the BEC density from changing abruptly. This plays an essential role in smoothing the density profiles of the separated components near the interface and, thus, in maintaining the residual spatial overlap. Accordingly, the relevant length scale that determines the thickness of the interface layer corresponds to the BEC healing length [Dal99], which for our present conditions can be estimated to $\xi = \left(8\pi\,\hat{n}_b\,a_{bb}\right)^{-1/2} \approx 0.50\,\mu$m. This length scale can be compared with the shortest macroscopic length scale of the system, which in our case is the radial size of the BEC of a few micrometers. The measured overlap factor can be understood as the volume ratio of the interface layer and the whole BEC, and the smoothing of the phase transition can thus be interpreted as a consequence of the finite size of the system [Bin84, Bré85].

The basic idea of our method to probe the interface between spatially separated components may be generalized to many other situations of interest. The working principle just relies on a mechanism that selectively addresses the region where the

[3] In our model, we consider an atom-atom mixture, neglecting any molecular component as the LiK Feshbach molecules are short-lived and decay rapidly.

different components mix. While in our case three-body recombination served this purpose, one may also apply photoassociative or radio-frequency-induced processes to stimulate loss or state-transfer processes.

The interface between two quantum fluids is a topic of broad interest yet largely unexplored in quantum gases. We speculate that future studies could focus on the role of quantum fluctuations, the two-dimensional character of the thin interface layer, and testing the validity of the mean-field approach. Unwinding the microscopic nature underlying the interface may give access to new phenomena such as Andreev bound states [Löf01, Sat17], familiar in superconductor physics. Concerning the phase-separated Bose-Fermi mixture, it would be natural to go beyond the static properties and to investigate the dynamics of the mixture. We expect a strong impact of phase separation on collective oscillation modes [VS09, Mar13] and on the behavior of the system after a quench [Wil15].

Acknowledgements

We acknowledge valuable discussions with M. Baranov and D. Yang on the theoretical model, with E. Tiemann and P. S. Julienne on the scattering properties, and with A. Turlapov on general topics. We thank J. T. M. Walraven for fruitful insights and our new team members C. Baroni, A. Bergschneider, T. W. Grogan and T. Öttl for comments on the manuscript. We acknowledge support by the Austrian Science Fund FWF within the Spezialforschungsbereich FoQuS (F4004-N23) and within the Doktoratskolleg ALM (W1259-N27).

5.6 Supplemental Material

5.6.1 Preparation of the ^{6}Li-^{41}K Mixture

In this Section, we describe the procedure applied for preparing an optically trapped mixture of K and Li atoms in their lowest Zeeman states near 335 G, where an interspecies Feshbach resonance (FR) is located [Han17, Tie17, Wu11] (See Appendix B).

Initially, the ^{6}Li and ^{41}K atoms are collected in a dual-species magneto-optical trap (MOT) and loaded consecutively into a single-beam optical dipole trap (ODT) with a wavelength of 1070 nm, power of 150 W and waist of 38 μm. The loading scheme of the ODT is optimized for a large number of Li atoms, since we evaporate with a Li spin mixture and cool K sympathetically. First, the K atoms are loaded by ramping up the magnetic field gradient and thus compressing the K MOT, while decompressing the Li MOT by increasing its detuning. With the K atoms transferred to the ODT, the K light

is turned off and the Li MOT is recompressed to facilitate loading into the ODT. Up to this point, the details of the procedure are similar to those described in our earlier work on the ^{6}Li and ^{40}K mixture [Spi10].

Next, we apply a gray-molasses cooling on the D1 line of lithium [Fri15, Gri13, Bur14a], to further improve the starting conditions for the evaporative cooling with Li. This gives an increase of the phase-space density of the lithium cloud by a factor of fifteen and a factor of five decrease in the initial temperature, while capturing the same amount of lithium as before in the ODT [Fri15]. With these improved starting conditions, after evaporative cooling, we reach a significant lower T/T_F and higher lithium atom number.

After the D1 cooling stage, we remove the hottest atoms, by linearly ramping down the ODT to 50% of its initial power and we create a Li spin mixture for evaporative cooling. Nearly all the lithium atoms captured in the ODT are found in the lowest Zeeman state Li$|1\rangle$ ($F = 1/2, m_F = 1/2$). To obtain a 50/50 Li spin mixture in the lowest $|1\rangle$ and second-lowest $|2\rangle$ spin state ($F = 1/2, m_F = -1/2$), we ramp the magnetic field, turned off during the D1 cooling stage, to 90 G and apply a radio-frequency (rf) $\pi/2$-pulse. This creates a superposition state which has enough time to decohere during the following stages and forms a incoherent Li spin mixture.

Then we exploit a spin relaxation stage to create a polarized sample of K. The K atoms in the ODT are a mixture of the three lowest Zeeman states. Thus, we ramp to a magnetic field of 200 G, where we previously observed the occurrence of spin relaxation [Lou17b], and wait for 500 ms. We end up with an almost fully polarized ^{41}K sample in the third-lowest Zeeman state K$|3\rangle$ ($F = 1, m_F = -1$) and a very small amount of K$|2\rangle$, the second-lowest spin state ($F = 1, m_F = 0$). After ramping to 335 G we observe complete polarization of the K sample and we speculate that the small amount of K$|2\rangle$ is lost by recombination with lithium during the magnetic field ramps we apply to reach 335 G. We note that the presence of the K$|2\rangle$ during evaporation does not lead to any observable immiscibility phenomena [Liu16], in contrast to what we observed with another evaporation scheme in Ref. [Lou17b]. After the spin relaxation stage, we further decrease the power of the ODT linearly to 15 W in 3 s. Besides the single beam ODT, the atoms also experience a trapping force from the magnetic curvature.

Subsequently we prepare a Li$|1\rangle$-Li$|3\rangle$ spin mixture to evaporatively cool at low magnetic fields [Bur14a], where Li$|3\rangle$ is the third-lowest Zeeman state ($F = 3/2, m_F = 3/2$). After the spin relaxation stage, we ramp to 580 G, where we use a rf π-pulse to transfer all Li$|2\rangle$ atoms to Li$|3\rangle$. At this magnetic field the interaction with Li$|1\rangle$ has the same strength for both Li$|2\rangle$ and $|3\rangle$ [Zür13]. Additionally the scattering length between Li$|2\rangle$ and $|3\rangle$ is negligible. The Li$|1\rangle$-Li$|3\rangle$ spin mixture is then used for evaporative cooling at about 483 G, where the scattering length is about $-635a_0$. This

magnetic field is chosen to avoid the region between 350-450 G where multiple Feshbach resonances occur and ramping over this with the Li$|2\rangle$, Li$|3\rangle$ and K$|3\rangle$ mixture leads to significant loss.

The evaporation sequence at 483 G contains several stages. First, we evaporate in the single beam ODT by exponentially ramping down its power and simultaneously load the atoms into another single beam ODT (1064 nm, 2.4 W, 44 μm). Then, we continue evaporation in this new trap and ramp up the power of a second beam (1064 nm, 0.22 W, 60 μm) to form a cigar-shaped (1:7) crossed-beam optical dipole trap (CDT). The two beams intersect at an angle of 17 °. In a third cooling step, we further exponentially ramp down the power of the CDT to the desired final trap depth. Depending on the final trap depth, we end up with a condensed or noncondensed bosonic cloud in a Fermi sea of lithium. Note that K$|3\rangle$ is sympathetically cooled along the evaporation route and we do not observe any evaporative loss of K. The fact that the trap depth for potassium is about twice as deep as that of lithium and the thermalization rate is high enough, enables the sympathetic cooling.

In the final stage of the sequence, we ramp to a magnetic field slightly below 335 G avoiding inter- and intraspecies resonances. However, we first switch to a different set of magnetic field coils, which removes the magnetic curvature and allows a high-precision control of the magnetic field. Then we ramp to 565 G, where we remove the Li$|3\rangle$ component by a resonant light pulse. At this magnetic field the zero crossing between Li$|1\rangle$ and Li$|3\rangle$ can be found and removing the Li$|3\rangle$ does not significantly heat up the remaining Li$|1\rangle$ atoms. Then we transfer K$|3\rangle$ to K$|2\rangle$ with a rf π-pulse. This is followed by a series of magnetic field ramps, where the final field of 335 G is reached with a pure mixture of Li$|1\rangle$ and K$|2\rangle$. Using a rf π-pulse we transfer K$|2\rangle$ to K$|1\rangle$ ($F = 1, m_F = 1$) and we can start with our measurements.

For the loss measurements we use the following sequence. At a magnetic field detuning ($\delta_B = B - B_0$) of -200 mG, we transfer K$|2\rangle$ to K$|1\rangle$ with a rf π-pulse of 0.056 ms and directly afterwards ramp adiabatically in 2 ms to a given δ_B. Since we stay on the repulsive side of the FR, no Feshbach molecules are associated and they can only be formed in three-body recombination processes. For various hold times at the given δ_B, we take spin-specific absorption images of Li and K after respectively, 2 and 8 ms time of flight.

5.6.2 Feshbach Resonance Parameters

The scattering length between the lowest Zeeman spin states of ^{6}Li and ^{41}K is tuned by a FR near 335 G [Han17, Tie17, Wu11] (see Appendix B). We first discuss the available theoretical predictions (Sec. 5.6.2.1) for the background scattering length a_{bg} and the resonance width Δ. Then, in Sec. 5.6.2.2, we show how we experimentally determine

the differential magnetic moment $\delta\mu$ and the resonance position B_0. In Sec. 5.6.2.3, we discuss how B_0 changes for different trap settings as a result of a light shift, and in Sec. 5.6.2.4 we discuss the measurements which verify the theoretical value for Δ.

5.6.2.1 Theory Predictions

Coupled-channel calculations by T. Hanna, E. Tiesinga and P. Julienne [Han17] and independently by E. Tiemann [Tie17] predict the magnetic-field dependent scattering length between Li$|1\rangle$ and K$|1\rangle$ around 335 G. These calculations are based on the potentials from Ref. [Tie09b]. Two FRs show up, a broader one around 335 G and a narrower one at 341 G. Experimentally, the 335 G FR was observed in Ref [Wu11] by detecting the loss of K atoms. The loss maximum, corresponding to B_0, was found at B=335.8 G and the width determined by a Gaussian curve fit gave a value of $\Delta B_{\mathrm{exp}} =$ 1.1 G. For the FR center B_0, the experimental value (335.8 G [Wu11]) and the two theoretical values (335.1 G [Han17] and 335.9 G [Tie17]) are only consistent within a Gauss. For a more accurate determination of B_0, we measure the binding energy of the dimers on the repulsive side of the FR (see Sec. 5.6.2.2).

We find that both coupled-channel calculations agree very well on the value of the scattering length if compared as a function of the magnetic detuning $\delta_{\mathrm{B}} = B - B_0$, and we use these calculations to extract theoretical values for a_{bg} and Δ. The predicted scattering length can be fitted with the simple formula

$$a_{\mathrm{bf}}(\delta_{\mathrm{B}}) = a_{\mathrm{bg}}\left(1 - \frac{\Delta}{\delta_{\mathrm{B}}} - \frac{\Delta_1}{\delta_{\mathrm{B}} - \delta_1}\right), \tag{5.7}$$

where $a_{\mathrm{bg}} = 60.865 a_0$, with a_0 being the Bohr radius, and $\Delta = 0.9487$ G is the width of the FR at 335 G. The width of the narrow FR is $\Delta_1 = 0.0566$ G and the detuning of this resonance with respect to the 335 G FR center is δ_1=6.1577 G. The free parameters are obtained by fitting the scattering length calculations for a detuning of -5 to $+7$ G and the expression is plotted in Fig. 5.4. The agreement between the calculations and the fit is excellent, with deviations of about 1 permille. Note that because of the narrow FR at 341 G the position of the zero crossing no longer corresponds to the width of the 335 G FR but instead is shifted down by 10 mG.

In our analysis of the data, we neglect the influence of the FR at 341 G and apply the common formula $a_{\mathrm{bf}} = a_{\mathrm{bg}}\left(1 - \Delta/\delta_{\mathrm{B}}\right)$ to describe the scattering length. Here, we use the values of $a_{\mathrm{bg}} = 60.865 a_0$ and $\Delta = 0.9487$ G from the fit to the theoretical predictions. The Feshbach resonance center B_0 is determined experimentally. On the repulsive side of the FR, the difference between this approach and Eq. 5.7 is very small.

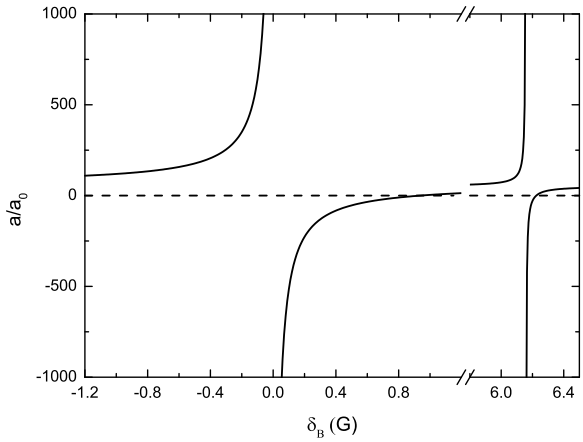

Figure 5.4: Scattering length between Li$|1\rangle$ and K$|1\rangle$ around 335 G versus magnetic field detuning as described by Eq. (5.7).

5.6.2.2 Obtaining the Feshbach Resonance Center B_0 by Binding Energy Measurements

To experimentally determine B_0, we measure the binding energy of the Li-K dimer by magnetic modulation ("wiggle") spectroscopy and/or radio-frequency spectroscopy [Chi10]. Fig. 5.5 shows the result of measuring the binding energy by applying both methods for a CDT with a power of 92 mW and 127 mW in the two beams. Magnetic modulation spectroscopy enables us to measure binding energies in the range of 0-2 MHz, while rf spectroscopy is typically performed up to a 100 kHz. This provides us with a wide range of binding energies which we can measure and fit with a known binding energy formula.

The magnetic modulation spectroscopy data is obtained by modulating the magnetic field and measuring which frequency is required to drive the transition between the free atom state and the molecular state at a various magnetic fields. At each magnetic field the duration and amplitude of the modulation are adjusted such that the transfer is measurable, without driving the transition too strongly. We observe the loss of K$|1\rangle$ atoms as a function of the modulation frequency. The center between the low-frequency onset of the loss of K atoms and the maximum loss is used as the modulation frequency that corresponds to the binding energy. We estimate the error as half of this range. The measurements are shown by the filled symbols in Fig. 5.5.

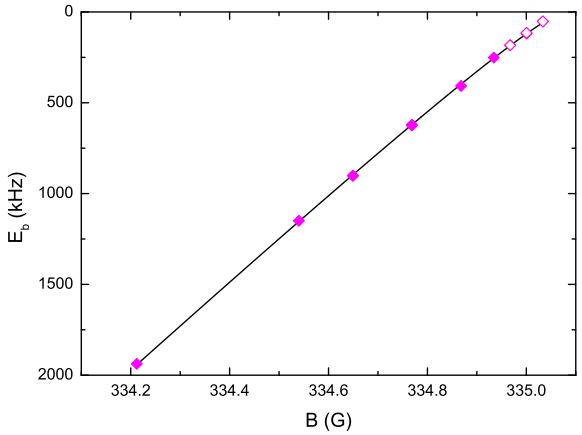

Figure 5.5: Binding energy versus magnetic field. The binding energy is determined either by magnetic modulation (filled diamonds) or rf (open diamonds) spectroscopy. The solid line represents the fit of Eq. (5.12) to the data, with $B_0 = 335.0795(9)$ G and $R^* = 2241(7)a_0$.

To measure the binding energy with rf spectroscopy we prepare a non-interacting mixture of Li$|1\rangle$ and K$|2\rangle$ at several tens of mG below the expected B_0 and measure the frequency needed for a strong 800-μs rf-pulse to associate Li$|1\rangle$-K$|1\rangle$ dimers [Jag14]. After the rf pulse, we ramp in 50 μs to roughly 100 mG above the resonance position. This dissociates the created dimers into Li$|1\rangle$ and K$|1\rangle$ atoms. By plotting the atom number in the K$|1\rangle$ state as a function of the rf frequency, we get the molecule association spectrum. From the spectrum we determine the lowest frequency ν, where the atom number is at roughly 20% of its peak height. We found that for a typical maximum transfer of 4000 K atoms, this gives a good estimate of the onset frequency for association. We estimate the error in ν as half of the range between ν and the peak frequency, which is 2 to 5 kHz. We obtain the rf detuning $\nu - \nu_0$ by subtracting the unperturbed K$|2\rangle \rightarrow$K$|1\rangle$ transition frequency ν_0, which corresponds to the Zeeman splitting of the two states as calculated from the Breit-Rabi formula. The rf detuning gives a direct measurement of the binding energy and the results are shown by the open symbols in Fig. 5.5.

To fit the data we use the binding energy formula derived in Refs. [Pet04a, Lev11] for a weakly bound molecule near a narrow resonance. Near the dissociation treshold,

E_b can be written as

$$E_b = \frac{\hbar^2 \kappa^2}{2\, m_r}, \tag{5.8}$$

where m_r is the reduced mass

$$m_r = \frac{m_f\, m_b}{m_f + m_b}, \tag{5.9}$$

with $m_{f(b)}$ the mass of Li (K). The wavenumber κ can be expressed in a second-order Taylor expansion as

$$-\kappa = -\frac{1}{a} + R^* \kappa^2, \tag{5.10}$$

where $a = -a_{bg}\Delta/\delta_B$ and the usual background scattering term is neglected. The length parameter R^* is related to the narrowness of the resonance [Pet04a]

$$R^* = \frac{\hbar^2}{2\, m_r\, \delta\mu\, a_{bg} \Delta}, \tag{5.11}$$

with $\delta\mu$ the differential magnetic moment of the closed and open channel. All together this gives the formula

$$E_b = \frac{\hbar^2}{8\,(R^*)^2\, m_r} \left(\sqrt{1 - \frac{4\, R^*\, \delta_B}{a_{bg}\, \Delta}} - 1 \right)^2. \tag{5.12}$$

We fit the measured binding energies with Eq. (5.12), leaving both B_0 and R^* as free parameters, as depicted in Fig. 5.5. For a_{bg} and Δ the values from the fit to the coupled-channel calculations of Sec. 5.6.2.1 are used and assumed to be free of any relevant uncertainties. The fit results give $B_0 = 335.0795(9)\,\mathrm{G}$, $R^* = 2241(7) a_0$ and thus $\delta\mu = h \times 2.660(8)\,\mathrm{MHz/G}$.

5.6.2.3 Light Shift of the Feshbach Resonance Center B_0

As already pointed out in Refs. [Koh12, Jag14, Cet16], for a similar FR in the ^{6}Li-^{40}K mixture, the trap light of 1064 nm causes a differential light shift between the atom pair state and the molecular state. This leads to a light-induced shift of the Feshbach resonance position B_0. Thus, for every trap we use, we need to measure the trap-specific B_0. We do this by performing rf spectroscopy of the Feshbach molecules. For the trap of Sec. 5.6.2.2 we have checked that the fit to rf spectroscopy data only, with fixed $\delta\mu$, agrees with the B_0 obtain from the two-parameter fit to both modulation and rf spectroscopy data. For each trap and at various magnetic fields we thus determine the

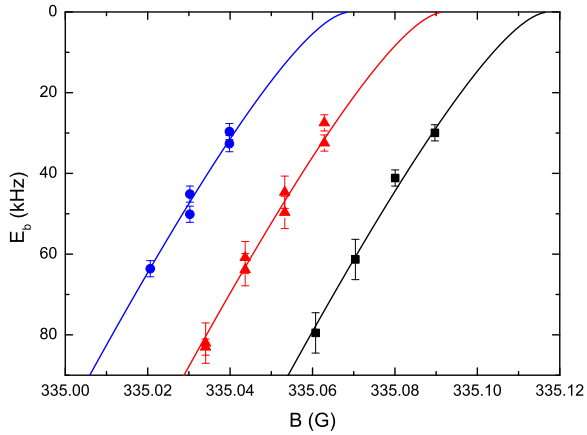

Figure 5.6: Binding energy versus magnetic field for the three trap settings of the main text. The solid lines are the fits of Eq. (5.12), with B_0 as the only free parameter. The blue circles show the rf spectroscopy measurements with the trap settings of data set B1-B3, red triangles those of data set A2 and the black squares those of data set A1. The error bars represent the estimated error (see text) in determining the onset frequency.

rf detuning $\nu - \nu_0$ via rf spectroscopy. This is a direct measurement of the binding energy E_b and Fig. 5.6 shows the measurements for the three trap settings discussed in the main text. The resulting values for B_0 are given in Table 5.1 and plotted depending on the optical trap depth U_{opt} for potassium in Fig. 5.7. The trap depth of the crossed dipole trap is calculated from the power and widths of the two intersecting laser beams, under the assumption that the beams are Gaussian. Here, we do not consider the reduction of the trap depth by gravity. Extrapolating a linear fit to the B_0 data as a function of trap depth, shows that the Feshbach resonance center in the absence of a trap is 335.057(1) G, where the error represents the fit uncertainty.

5.6.2.4 Verification of the Feshbach Resonance Width Δ

The width of the FR is given by the theoretical predictions to be 0.949 G. We verified this value by measuring the damping of the axial center-of-mass (COM) oscillations at different magnetic field detunings δ_{B} for the trap settings of data set A2 (see Table 5.1). We excite both the COM oscillations of K and Li, which oscillate at a different frequency, but measure only the oscillations in K. The interaction between Li and

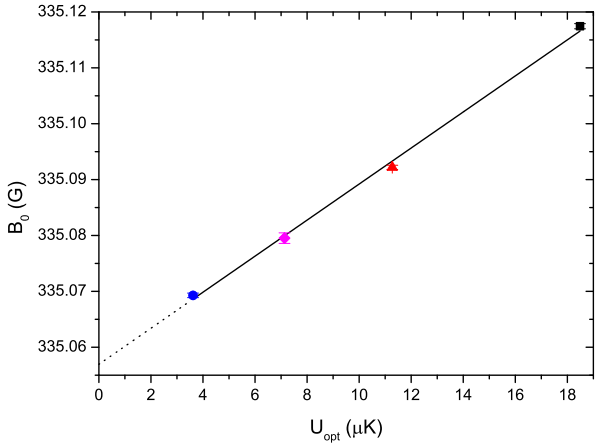

Figure 5.7: Feshbach resonance position as a function of the trap depth for potassium. The symbols correspond to the same trap settings as in Fig. 5.6 and the additional diamond corresponds to those of Fig. 5.5. Error bars represent fit errors in the determination of B_0. The solid line represents a weighted linear fit of $B_0 = A + D\,U_{\mathrm{opt}}$, with A=335.057(1) G and $D = 3.2(1) \times 10^{-3}\,G/\mu$K. The dashed line shows the extrapolation of the linear fit to zero trap depth.

K leads to friction and this damps the COM oscillations. At the point where the interspecies scattering length is zero, the least amount of damping is expected. Note that other types of damping will still be present. This method, as presented in Ref. [Nai11], enables us to determine the zero crossing of the Feshbach Resonance.

To excite the COM oscillations of the clouds (both Li and K) we use the following scheme. At a fixed magnetic field detuning we excite a non-interacting Li$|1\rangle$-K$|2\rangle$ sample by ramping up a strong additional trapping beam in 100 ms. This beam is slightly misaligned with one of the beams of the CDT and thus displaces the COM of the clouds. We hold the sample in this trap configuration for 100 ms and then release it in 1 ms into the original trap configuration by switching off the additional beam. With a rf π-pulse we transfer K$|2\rangle$ to K$|1\rangle$ in 56 μs and obtain a mixture of Li$|1\rangle$-K$|1\rangle$. Then we quickly ramp in 2 ms to the final δ_{B}. The final detuning determines the strength of the interaction between Li$|1\rangle$ and K$|1\rangle$. For different hold times, we observe the center position of the K cloud and obtain the K COM oscillations. We fit these oscillations with a damped sinusoidal curve to extract the damping rate Γ. This

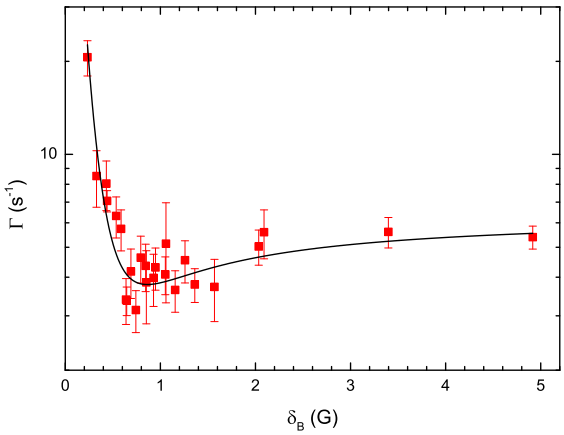

Figure 5.8: Damping rate of the axial COM mode versus magnetic field detuning. The solid line represents a fit by Eq. (5.13) with $B = 3.8(2)\,\mathrm{s}^{-1}$, $A = 2.6(5)\,\mathrm{s}^{-1}$ and $C = 0.86(5)\,\mathrm{G}$.

is repeated for several positive values of δ_B around the expected zero crossing of the scattering length, as is shown in Fig. 5.8.

The damping rate around the zero crossing can be fitted with

$$\Gamma = B + A\left(1 - \frac{C}{\delta_B}\right)^2 \tag{5.13}$$

where A, B and C are free parameters. Here, B represents the background damping, which is not caused by the interspecies scattering length, and A is a constant which is proportional to $(a_{bg})^2$. The fit gives C =0.86(5) G for the zero crossing and this is equivalent to the width of the Feshbach resonance if no other Feshbach resonances were close by. In our case the zero crossing is influenced by the close presence of the other rather narrower FR at 341 G and Eq. (5.7) shows that this shifts the zero crossing by about 10 mG. The width of the FR should therefore be 0.87(5) G.

From our measurements we obtain a value of 0.87(5) G for Δ, which deviates from the theoretical value by less than $2\,\sigma$. This deviation may be of statistical nature or may be explained by an oversimplification of the model [Eq.(5.13)] we use to fit to our data. The result can be considered to be consistent with the theoretical value for Δ, the latter being used in our calculations and analysis. Note that using the experimental

value for Δ would not significantly affect the B_0 determination, however it would give an about 10% lower scattering length a_{bf} near resonance, where a_{bg} can be neglected.

5.6.3 Measurement Procedures and Data Analysis

In this Section, we discuss the measurements and analysis behind the data points displayed in the figures of the main text. We summarize the experimental parameters for the data sets A1, A2 and B1-B3 in Sec. 5.6.3.1. The measurements and analysis of the three-body loss coefficient L_3 and the normalized loss rate γ are then described in Sec. 5.6.3.2 and Sec. 5.6.3.3. In Sec. 5.6.3.4 we show the experimental determination of the effective overlap factor Ω_{eff}, and in Sec. 5.6.3.5 we explain how we take into account secondary loss.

5.6.3.1 Experimental Parameters

Table 5.1 shows the experimental parameters for the data sets A1, A2 and B1-B3. We first show the parameters that are independent of the atom number for lithium N_{f} and potassium N in the given data set and the quantities derived thereof. The errors in the atom number represent the statistical errors due to fluctuations in the data points of the data sets. Additionally there is a systematic calibration error of about 10% for both Li and K. As described in Sec. 5.6.2.3, we measure B_0 for each trap by rf spectroscopy.

For each trap setting we measured the radial and axial trap frequencies for the bosons (ω_{b}^{r}, ω_{b}^{z}) by exciting the COM modes in axial and radial direction. The trap frequencies for the fermions can be calculated accurately by $\omega_{\mathrm{f}}^{i} = 1.756\,\omega_{\mathrm{b}}^{i}$, where the factor is derived from the ratio of the masses and the dynamical polarizabilities of the two species [Lou17b]. The estimated effective trap depth $U_{\mathrm{b}}(U_{\mathrm{f}})$ for the bosons (fermions) in the z-direction is also shown. This trap depth is calculated from the power and waist of the CDT beams under the assumption that the beams are Gaussian and we took into account the effect of gravity, which lowers the trap depth. For a non-condensed K cloud (data set A1, A2), the temperature is determined from the time of flight expansion of the K atoms. For the BEC cloud (B1-B3 data sets), the temperature is derived from the measured BEC fraction β [Lou17b]. When comparing the temperature with the trap depth of the bosons, we can see that the potassium atoms are trapped in a deep trap and loss can only happen due to recombination with lithium.

The peak density of lithium $\hat{n}_{\mathrm{f}}$ and the Fermi temperature T_{F} are derived from the atom number by the textbook equation (for $T = 0$)

$$\hat{n}_{\mathrm{f}} = \left(2\,\frac{k_{\mathrm{B}}\,T_{\mathrm{F}}\,m_{\mathrm{f}}}{\hbar^2}\right)^{3/2}\frac{1}{6\pi^2} = \frac{2\sqrt{N_{\mathrm{f}}}}{\sqrt{3}\,\pi^2}\left(\frac{\bar{\omega}_{\mathrm{f}}\,m_{\mathrm{f}}}{\hbar}\right)^{3/2}, \tag{5.14}$$

Table 5.1: Summary of the data sets and their experimental parameters.

data set symbol	A1 black squares	A2 red triangles	B1 orange inv. triangles	B2 green diamonds	B3 blue circles
B_0 (G)	335.1175(5)	335.0922(4)	335.0693(4)		
$\omega_b^r/2\pi$ (Hz)	376(1)	300(1)	171.1(6)		
$\omega_b^z/2\pi$ (Hz)	54.8(4)	42.2(1)	23.58(6)		
$\omega_f^r/2\pi$ (Hz)	660(2)	527(2)	300(1)		
$\omega_f^z/2\pi$ (Hz)	96.2(7)	74.1(2)	41.4(1)		
U_b (μK)	14.5	7.60	0.856		
U_f (μK)	7.68	4.46	1.10		
T (nK)	438(18)	238(7)	88(2)	93(2)	97(5)
N_f	$1.8(2)\times10^5$	$3.3(4)\times10^5$	$1.33(8)\times10^5$	$1.5(1)\times10^5$	$1.1(1)\times10^5$
$\hat{n}_f$ (cm^{-3})	$4.7(2)\times10^{12}$	$4.4(3)\times10^{12}$	$1.20(4)\times10^{12}$	$1.27(4)\times10^{12}$	$1.11(6)\times10^{12}$
T_F (nK)	$1.72(6)\times10^3$	$1.64(7)\times10^3$	690(13)	718(16)	656 (24)
T/T_F	0.25(1)	0.145(7)	0.128(4)	0.130(4)	0.148(9)
N	$2.6(6)\times10^4$	$4.3(2)\times10^4$	$2.60(7)\times10^4$	$2.96(5)\times10^4$	$3.0(3)\times10^4$
β	-	-	0.54(3)	0.50(2)	0.46(5)
$\hat{n}_b$ (cm^{-3})	-	-	$4.8(2)\times10^{13}$	$5.0(1)\times10^{13}$	$4.9(3)\times10^{13}$
$\hat{n}_t$ (cm^{-3})	$0.38(8)\times10^{13}$	$0.77(5)\times10^{13}$	$0.18(2)\times10^{13}$	$0.20(1)\times10^{13}$	$0.21(3)\times10^{13}$
T/T_c	1.7(1)	1.01(3)	0.78(2)	0.79(1)	0.82(5)

where k_B is the Boltzmann constant and $\hbar$ is the Planck constant. The geometrical average of the trap frequency as seen by lithium, $\bar{\omega}_f$, can be calculated as $\bar{\omega}_f = (\omega_f^r \omega_f^r \omega_f^z)^{1/3}$. When we compare T_F to the effective trap depth U_f, we see that the final trap settings are deep enough for lithium. We also give the relative temperature T/T_F, which shows that we are indeed very cold and justifies the use of Eq. (5.14), which is valid for T=0.

The BEC fraction is obtained from a bimodal fit to the absorption images after time of flight and we quote the average BEC fraction and its standard error for the given data sets. The peak density of the BEC $\hat{n}_b$ and the thermal peak density $\hat{n}_t$ are given by

$$\begin{aligned} \hat{n}_b &= \frac{15^{2/5}}{8\pi} \left(\frac{\bar{\omega}_b \, m_b}{\hbar \sqrt{a_{bb}}} \right)^{6/5} (\beta \, N)^{2/5}, \\ \hat{n}_t &= \left(\frac{\bar{\omega}_b^2 \, m_b}{2\pi \, k_B \, T} \right)^{3/2} (1 - \beta) \, N, \end{aligned} \tag{5.15}$$

where $a_{bb} = 60.9 a_0$ [Tie17], and we assume the thermal density to follow the Boltzmann distribution. When calculating the critical temperature T_c we correct for finite-size and interaction effects [Gio96], which leads to a down shift of the critical temperature of less then 10%, when compared to the common expression $k_B \, T_c = 0.940 \, \hbar \, \bar{\omega}_b \, N^{1/3}$.

5

5.6.3.2 Measurements of the Three-body Loss Coefficient L_3

For the two data sets (A1, A2) with noncondensed K atoms, we measure the loss of K atoms for various hold times t at different repulsive Bose-Fermi scattering lengths a_{bf} in order to determine L_3. The atom loss can be quantified as

$$\dot{N} = -L_3 \int n_f \, n_t^2 \, \mathrm{d}V = -L_3 \, \hat{n}_f \, \frac{\hat{n}_t}{\sqrt{8}} \, N. \tag{5.16}$$

Within the *fermionic reservoir approximation (FRA)*, we can assume that the fermion density as seen by the potassium atoms is constant and replace $\tilde{n}_f$ by the peak density $\hat{n}_f$ at zero temperature and take it out of the integral. The remaining integral is solved, assuming that the thermal density of the bosons follows the Boltzmann distribution.

The measured evolution of the atom number follows an effective two-body loss equation with $\dot{N} \propto -N^2$ and we fit the data with

$$N(t) = N_0 \, \left(1 + N_0 \, C \, t\right)^{-1}, \tag{5.17}$$

where the free parameters N_0 and C represent the initial atom number and the constant we extract. An example curve is displayed in Fig. 5.9(a) for $a_{\mathrm{bf}} \approx 850 a_0$. The L_3 coefficient is then calculated as

$$L_3 = C \frac{\sqrt{8}}{\hat{n}_{\mathrm{f}} \bar{\omega}_{\mathrm{b}}^3} \left(\frac{2\pi\, k_{\mathrm{B}}\, T}{m_{\mathrm{b}}} \right)^{3/2}. \tag{5.18}$$

The error in L_3 is propagated from the fit error in C. Additionally, there is about a 12% systematic error in the conversion from C to L_3, coming from the Li and K atom number calibration, the temperature, and the trap frequency determination.

There are two additional corrections to Eq. (5.18), both taken into account for the data points displayed in Fig. 5.2(a) of the main text. First of all, for temperatures close to the critical temperature for condensation, the bosonic system deviates from the classical Boltzmann distribution and Eq. (5.18) overestimates the value of L_3. The Bose enhancement of the density gives a correction factor to Eq. (5.18) of 0.97 for set A1 and 0.78 for set A2.

Second, for a_{bf} below $150 a_0$, the three-boson loss becomes significant. This adds a second term to the equation for the atom loss

$$\dot{N} = -L_3 \hat{n}_{\mathrm{f}} \int n_{\mathrm{t}}^2 \, \mathrm{d}V - K_3 \int n_{\mathrm{t}}^3 \, \mathrm{d}V. \tag{5.19}$$

We use this equation instead of Eq. (5.16) to correct for the influence of the additional loss term. Measurement of K_3 in the trap of A1, with a pure bosonic sample and $T = 536(20)\,\mathrm{nK}$, gives a rate constant of $K_3 = 0.012(3) \times 10^{-25}\ \mathrm{cm}^6/\mathrm{s}$. Here, we fitted the atom loss data with the solution to the differential equation $\dot{N}/N^3 = -A$, with A the free parameter. Solving the integral for the three-boson loss, K_3 can then be extracted as

$$K_3 = \frac{A\sqrt{27}}{\left(\frac{m_{\mathrm{b}}}{2\pi\, k_{\mathrm{B}}\, T} \right)^3 \bar{\omega}_{\mathrm{b}}^6} \tag{5.20}$$

This leads to a 4-12% correction of L_3 for the three points with the lowest a_{bf}. For the other L_3 data the effect of the three-boson loss compared to the boson-boson-fermion three-body recombination loss is two orders of magnitude smaller.

The value of L_3 for any a_{bf} between 80 and $2100\, a_0$ is approximated by applying the LOESS smoothing method [NIS12] to the data. LOESS is a locally weighted polynomial least squares regression method, based on the idea that any function can be well approximated in a small local region by a low-order polynomial. More weight is given to the data points close to the local region than to those farther away. The great

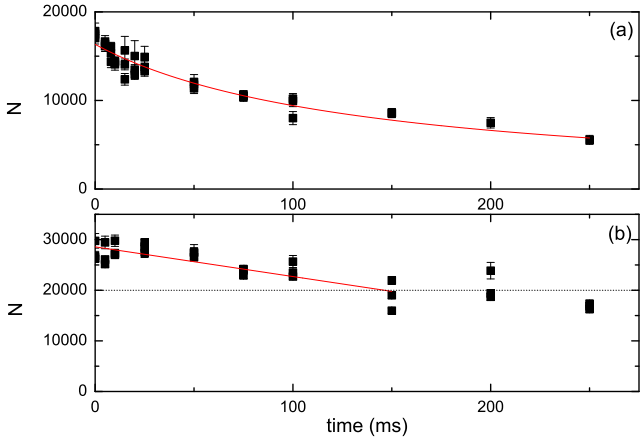

Figure 5.9: Decay curves of a thermal (a) and partial BEC (b) cloud of ^{41}K for a_{bf} of about $850a_0$. The red curves are the fitting curves used in the analysis and the vertical dashed line in (b) shows the cut-off criterion for the linear fit. The error bars represent the statistical uncertainties corresponding to the fit errors of the atom number obtained from the absorption images.

advantage of this method is the fact that it does not require a specific model to fit the data. We use a LOESS smoothing with a degree of 2 and $q = 0.5$ to fit the data of L_3, using the fitting program R [Ven17] and calculate the 2σ confidence interval of the smoothing as displayed in Fig. 5.2(a) of the main text. The degree of 2 means that we locally fit with a simple parabola. The smoothness parameter q determines how much of the data is being used for each local fit. The typical 1σ uncertainity in the smoothed data is about 10%.

5.6.3.3 Measurements of the Normalized Loss Rate γ

We observe the loss of the atom number of a partial BEC for various hold times and for different values of the scattering length. A typical loss measurement is shown in Fig. 5.9(b) for $a_{\mathrm{bf}} \approx 850a_0$. To fit the data, we approximate the initial loss as a linear decay given by $\dot{N}/N = -C$. In practice this means that we fit the data with $N(t) = N_0 - C\,t$, where N_0 and C are free parameters. We limit the fit to 30% of the initial atom number. Fig. 5.9(b) shows a typical fit and the cut-off criterion. We obtain the normalized loss rate as $\gamma = C/(0.85\,N_0)$. The thus obtained values of γ are displayed in Fig. 5.2(b) of the main text, where the error represents the fit error in C.

Three data sets (B1-B3) are taken in this way and Table 5.1 shows their parameters, where $N = 0.85\,N_0$. During the time in which the K atom number decreases by 30%, we observe that the BEC fraction only changes within 10% and heating due to the loss of K atoms does not lead to a substantial change in β. We assume this is because of sympathetic evaporation of lithium [Mos01].

Additional three-boson loss mostly affects the two data points taken below $150a_0$. For the other points the measured loss rate is an order of magnitude higher then the measured decay of a K partial BEC without lithium. We measured the decay of a pure K sample with a 39(4)% BEC fraction and $N_K = 2.7(2) \times 10^4$ and we found a normalized loss rate of the total atom number of $\gamma_{3b} = 0.01(1)/\mathrm{s}$. We correct for this additional form of loss by subtracting γ_{3b} from the measured γ. This significantly affects only the two points below $150a_0$ in Fig. 2(b) of the main text and the uncertainity in the measured three-boson decay is reflected in the error bar for γ. Moreover, these two data points show a very slow decay and therefore we fit their loss curves only up to 3 s instead of 30% of the initial atom number.

5

5.6.3.4 Experimental Determination of the Effective Overlap Factor Ω_{eff}

As an extension of Eq. (2) in the main text, we define the effective overlap factor Ω_{eff} for a partial BEC as

$$\Omega_{\mathrm{eff}} \equiv \frac{\int \left(\frac{1}{2}\alpha\, n_\mathrm{f}\, n_\mathrm{b}^2 + \alpha\, n_\mathrm{f}\, n_\mathrm{b}\, n_\mathrm{t} + n_\mathrm{f}\, n_\mathrm{t}^2\right) \mathrm{d}V}{\int \left(\frac{1}{2}\alpha\, \tilde{n}_\mathrm{f}\, \tilde{n}_\mathrm{b}^2 + \alpha\, \tilde{n}_\mathrm{f}\, \tilde{n}_\mathrm{b}\, \tilde{n}_\mathrm{t} + \tilde{n}_\mathrm{f}\, \tilde{n}_\mathrm{t}^2\right) \mathrm{d}V}, \tag{5.21}$$

which is the total three-body density integral including all loss contributions normalized to the corresponding non-interacting ($a_{\mathrm{bf}} = 0$) integral. It takes into account the additional loss because of the thermal bosonic density and the effect of secondary loss through the factor α (see Sec. 5.6.3.5).

With this definition, the atom loss equation [Eq. (5) in the main text] can be rewritten

$$\dot{N} = -L_3\, \Omega_{\mathrm{eff}} \int \tilde{n}_\mathrm{f} \left(\frac{1}{2}\,\alpha\, \tilde{n}_\mathrm{b}^2 + \alpha\, \tilde{n}_\mathrm{b}\, \tilde{n}_\mathrm{t} + \tilde{n}_\mathrm{t}^2\right) \mathrm{d}V = -L_3\, \Omega_{\mathrm{eff}}\, I_0, \tag{5.22}$$

where we have introduced I_0 as the overlap integral for the non-interacting mixture. This integral can be simplified by replacing $\tilde{n}_\mathrm{f}$ with the peak density $\hat{n}_\mathrm{f}$ at zero temperature and taking $\hat{n}_\mathrm{f}$ out of the integral, as justified by the FRA. The three integrals

left to solve are then

$$\int \tilde{n}_\mathrm{b}^2 \mathrm{d}V = \frac{4}{7}\hat{n}_\mathrm{b}\beta N, \tag{5.23}$$

$$\int \tilde{n}_\mathrm{b}\tilde{n}_\mathrm{t} \mathrm{d}V = \hat{n}_\mathrm{t}\beta N, \tag{5.24}$$

$$\int \tilde{n}_\mathrm{t}^2 \mathrm{d}V = \frac{1}{\sqrt{8}}\,\hat{n}_\mathrm{t}(1-\beta)\,N. \tag{5.25}$$

Here we treat the BEC within the Thomas-Fermi approximation and we use the Boltzmann distribution to describe the thermal bosonic density. For solving the second integral we assume that the BEC samples the peak density of the thermal cloud. With these three solutions, I_0 becomes

$$I_0 = \hat{n}_\mathrm{f}\left(\frac{2}{7}\alpha\,\hat{n}_\mathrm{b}\,\beta\,N + \alpha\,\hat{n}_\mathrm{t}\,\beta\,N + \frac{1}{\sqrt{8}}\,\hat{n}_\mathrm{t}\,(1-\beta)\,N\right). \tag{5.26}$$

We finally arrive at the central equation for our data analysis [Eq. (6) in the main text], which allows us to calculate Ω_eff from the measured values of γ and L_3 and the experimental parameters,

$$\boxed{\Omega_\mathrm{eff} = \frac{1}{\hat{n}_\mathrm{f}\left(\frac{2}{7}\alpha\,\hat{n}_\mathrm{b}\,\beta + \alpha\,\hat{n}_\mathrm{t}\,\beta + \frac{1}{\sqrt{8}}\,\hat{n}_\mathrm{t}\,(1-\beta)\right)}\frac{\gamma}{L_3}}. \tag{5.27}$$

For the atom number of lithium and potassium, and the BEC fraction we take the average value in the time frame set by the cut-off criterion of 30% K atom loss. The average values of the peak densities, atom numbers and the BEC fraction for each data set are listed in Table 5.1.

5.6.3.5 Secondary Loss

In our definition of Ω_eff in Eq. (5.21) we implemented a factor α, which gives an estimate on the importance of secondary loss. When $\alpha = 1$, there is no secondary loss and a three-body loss event leads to the loss of two K atoms and one Li atom. However, in a dense sample it may happen that further atoms are lost by collisions with the products of a previous recombination [Sch01b, Zac09].

A possible scenario for secondary loss is the following. In a first collision event of two bosons (b) and one fermion (f), a weakly bound dimer (bf*) is formed according

to $b + b + f \rightarrow bf^* + b + E_b$. In this recombination event the binding energy (E_b) of the dimer is released and distributed almost evenly into the motion of the K atom and Li-K dimer, where the K atom takes 47/88 and the dimer 41/88. The K atom and the Li-K dimer may quickly escape from the trap if their obtained kinetic energy is higher than the trap depth. The Li-K dimer can recollide with another K atom as $bf^* + b \rightarrow bf + b + E_{kin}$, whereby the dimer relaxes to a energetically lower internal state (bf) and releases the energy E_{kin}. Since E_{kin} is very large as compared to the trap depth, all products will be lost immediately. This inelastic atom-dimer decay is more likely to take place when the K sample is dense enough such that the Li-K dimer can find a collision partner in a reasonable amount of time.

Important in the discussion of secondary loss is also the comparison between the binding energy of the formed dimer and the trap depth. If there is not enough energy released for the dimer to leave the trap, there will be enough time for it to recollide with the other K atoms in the trap. The effective trap depth for K for the data sets B1-B3 is 0.856 μK, where the effect of gravity is taken into account. Thus, for scattering lengths below about 1500 a_0 (almost our entire measurement range), the recombination products will obtain enough energy to escape the trap. For higher scattering lengths, we expect the collisional products to remain trapped and the released energy will be redistributed among the other atoms in the trap, leading to additional heating and loss.

A typical rate constant for inelastic atom-dimer decay is $\beta_{AD} \approx 1.4 \times 10^{-10}\,\mathrm{cm}^3/\mathrm{s}$ [Jag16]. Together with the peak density of our BEC of $5 \times 10^{13}\,\mathrm{cm}^{-3}$, this gives a time scale for inelastic collisions of $\tau \approx (\beta_{AD}\,\hat{n})^{-1} \approx 140\,\mu$s, which is about one order of magnitude shorter than the oscillation period of the particles in the trap. After the three-body recombination event the dimer has an estimated kinetic energy of $\sim 5\,\mu$K, which gives a typical velocity for the dimer of $v_{AD} = 42\,$mm/s and thus it can travel a distance of $\sim 6\,\mu$m before undergoing an inelastic collision event. Given the size of the BEC (see Fig. 5.11) there is a high probability that the dimer encounters a K atom from the BEC before leaving the trap, and undergoes a transition to a deeply bound molecular level with a large release of kinetic energy. For the thermal potassium density, the time scale for the inelastic collision is more than an order of magnitude higher and it is therefore less likely that the Li-K dimer will recollide with a thermal K atom. Thus, the secondary collisions mostly happens with K atoms from the BEC and we add the factor alpha only to the overlap integrals in Eq. (5.21) which contains the BEC density.

Since the inelastic rate coefficient is not exactly known, the influence of secondary loss on Ω_{eff} cannot be *a* priori calculated, but we rather rely on estimates. We know that the factor α should be at least 1 (two K atoms lost per recombination event) and it is reasonable to assume that α does not exceed 3/2 (one additional K atom lost). In Fig. 5.10 we show a plot of Ω_{eff} versus a_{bf} for $\alpha = 3/2$ (same as in Fig. 5.3 of the

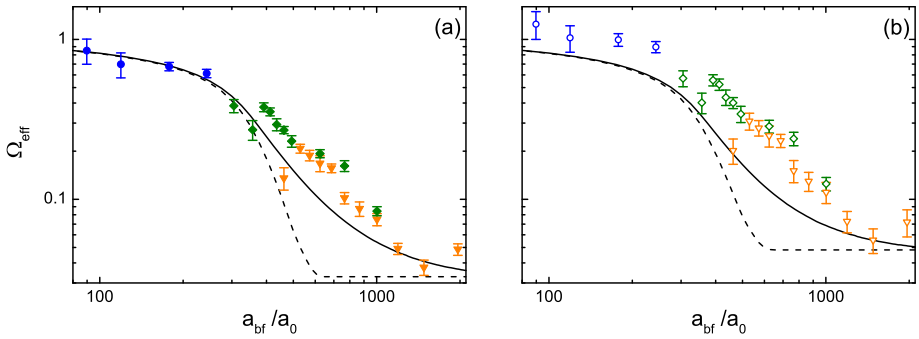

Figure 5.10: Effective overlap factor as a function of the Bose-Fermi scattering length for (a) $\alpha = 3/2$ (Fig. 5.3 in the main text) and (b) $\alpha = 1$.

main text) in comparison with the corresponding result for $\alpha = 1$. Note that α has also been adjusted for the theory curves. As is clearly visible, the plot with $\alpha = 3/2$ gives a better agreement between the data and the calculations. This indicates that the presence of secondary loss processes is very likely.

Additionally K atoms can be lost because of a boson-boson secondary collision. The typical mean free path for the identical bosons is $\ell \approx (8\,\pi\,a_{bb}^2\,n)^{-1}$ and this gives for our typical peak densities a mean free path of about 78 μm (BEC) and 1.4 mm (thermal). Thus, it is reasonable to assume that the K atom does not recollide and we can rule out that elastic collisions between the condensate atoms lead to an avalanche effect [Sch01b].

5.6.4 Theoretical Model and Numerical Solution

In this Section, we start with a zero temperature mean-field model for the boson-fermion mixture, and then extend it by introducing a thermal cloud to include finite temperature effects of the bosons. Finally, we calculate the effective overlap factor Ω_{eff} from the density of the different components.

5.6.4.1 Zero-temperature Approach

In order to study quantitatively our observations on the overlap factor Ω_{eff}, we construct a numerical mean-field model to calculate the density distributions of the BEC (n_b) and the fermions (n_f) for an interacting Bose-Fermi mixture at zero temperature. Our

model starts from the energy functional of the mixture as [Ima06, Tra16]

$$E = \int d^3r \Bigg[\frac{\hbar^2}{2m_\mathrm{b}} (\nabla \sqrt{n_\mathrm{b}})^2 + U_\mathrm{b} n_\mathrm{b} + \frac{1}{2} g_\mathrm{bb} n_\mathrm{b}^2 + \frac{1}{9} \frac{\hbar^2}{2m_\mathrm{f}} (\nabla \sqrt{n_\mathrm{f}})^2 + U_\mathrm{f} n_\mathrm{f} + \frac{\hbar^2}{2m_\mathrm{f}} \frac{3}{5} (6\pi^2)^{2/3} n_\mathrm{f}^{5/3} + g_\mathrm{bf} n_\mathrm{b} n_\mathrm{f} \Bigg], \tag{5.28}$$

where $U_\mathrm{b}(\vec{r})$ and $U_\mathrm{f}(\vec{r})$ are the bosonic and fermionic harmonic trapping potentials, and $g_\mathrm{bb} = 4\pi\hbar^2 a_\mathrm{bb}/m_\mathrm{b}$ and $g_\mathrm{bf} = 2\pi\hbar^2 a_\mathrm{bf}/m_\mathrm{r}$ are the boson-boson and boson-fermion coupling constants.

To obtain the densities within the Thomas-Fermi approximation, the term $(\nabla\sqrt{n_\mathrm{b}})^2$, which arises from the kinetic energy of the BEC, is ignored. Additionally the $(\nabla\sqrt{n_\mathrm{f}})^2$ term of the fermions is ignored as well. This term is the leading term for the density-gradient correction [Kir57], which is much smaller than the other terms under our typical experimental conditions.

To solve Eq. (5.28) numerically, we set up a numerical grid of 1024×1024 points in real space for n_b and n_f as our system has cylindrical symmetry. Then for each value of a_bf we minimize this energy functional by varying the densities with imaginary time evolution (also known as the steepest descent method [Ima06]), which is constrained by a fixed total atom number for each species (N_b and N_f) and finally gives the static solution for n_b and n_f.

Our typical experimental system has a total boson number of $N = 2.9\times10^4$, a BEC fraction of $\beta = 50\%$ and consequently $N_\mathrm{b} = 1.45\times10^4$, and a total fermion number of $N_\mathrm{f} = 1.4\times10^5$ (see sets B1-B2 in Table 5.1). Our elongated optical dipole trap has an aspect ratio of 7.3 and the radial trap frequency is 171.1 Hz for the bosons and 300.3 Hz for the fermions. The scattering length for the bosons is $a_\mathrm{bb} = 60.9a_0$ [Tie17]. With these parameters, we obtain the zero-T densities and the results of the full calculation, including both ∇ terms, are plotted in the upper four panels of Fig. 5.11. Panel (a) and (b) show n_b in the radial and the axial direction, and panel (c) and (d) show n_f. Different colors correspond to different values of a_bf (black for $0a_0$, red for $300a_0$ and green for $600a_0$). Note that the effect of the kinetic energy terms, which tends to smooth out the density distributions especially when n_b is near zero, is more visible in the radial plots (panels (a) and (c)) because of the different scales (aspect ratio) between the radial and axial direction.

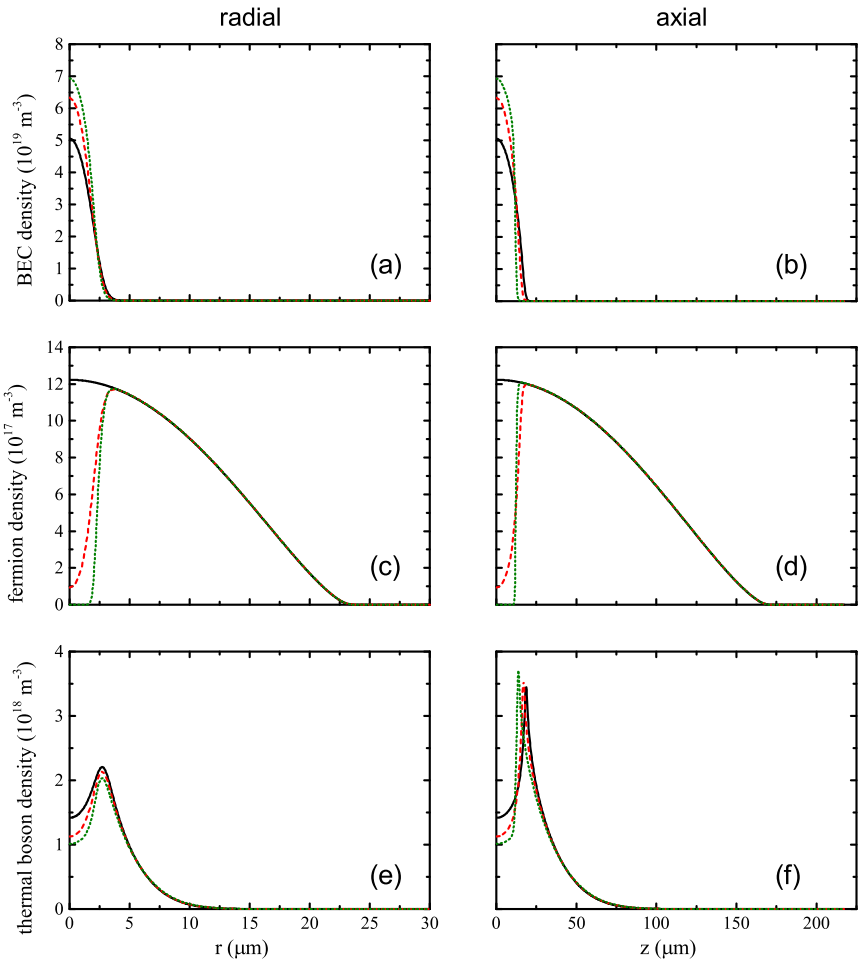

Figure 5.11: Number density profiles of the different components of the Bose-Fermi mixture at various values of the boson-fermion scattering length, i.e. $a_{\rm bf}$ is $0a_0$ for the curves in solid black, $300a_0$ for dashed red, and $600a_0$ for dotted green. Panel (a) and (b) show the radial and the axial density of the BEC. Panel (c) and (d) show the fermion densities and (e) and (f) the thermal boson densities. Note that different density scales are used for the three components. The densities are calculated by considering all terms in Eq. (5.28).

.

5.6.4.2 BEC at a Finite Temperature: Thermal Boson Cloud

Because of the finite temperature of the experiment, we only obtain a partial BEC and we have to take the non-degenerate component ($\sim$ 50% of N) into account. Thus we calculate the thermal boson density n_t, which is about two orders of magnitude smaller than n_b. It gives a small extra overlap between the bosons and fermions. In the main text and as outlined in Sec. 5.6.3.4, we approximate the thermal boson density n_t with a Boltzmann distribution and we obtain an analytical formula for the overlap integrals. For the theoretical model, we include boson statistics, which enhances the boson density in the trap center, as well as the mean-field interaction between the BEC and the thermal cloud, and we calculate n_t and the corresponding overlap integrals numerically.

We assume n_t to be the density of a trapped saturated thermal Bose gas influenced by the mean-field potential formed by the BEC. Other mean-field effects, e.g. the interaction between fermions and thermal bosons and the influence of the thermal gas on the BEC, are considered to be weaker and ignored. Finally, different from the Boltzmann distribution, the thermal boson density for the numerical model is given by the polylogarithm function g as

$$n_\mathrm{t} = \lambda^{-3} g_{3/2}\left(e^{-\frac{\mu - U_\mathrm{t}}{k_\mathrm{B}T}}\right), \tag{5.29}$$

where the thermal de Broglie wavelength is $\lambda = \sqrt{2\pi\hbar^2/(mk_\mathrm{B}T)}$, the total potential for thermal bosons is $U_\mathrm{t} = U_\mathrm{opt} + 2g_\mathrm{bb}n_\mathrm{b}$, the chemical potential μ for bosons is taken to be the minimum of $U_\mathrm{t}(r, z)$ so that the thermal gas is saturated in phase space, and T is the temperature which is obtained as a normalization factor for the total thermal boson number, i.e. $N_\mathrm{t} = \int n_\mathrm{t}(T)\,\mathrm{d}^3r$. Using the zero-$T$ densities of the BEC and the fermions, obtained in the previous Section, we calculate the thermal bosonic density with Eq. (5.29) and we get the radial and axial density profiles displayed in panel (e) and (f) of Fig. 5.11.

It is interesting to note that the bosonic enhancement effect in the thermal cloud substantially increases the peak density by a factory of ~ 2.4. However, the repulsion by the BEC has the opposite effect, and for the overlap with the Fermi gas, both effects approximately cancel each other. Therefore, we find that the approximation used for the thermal gas in our analysis and the derivation of Eq. (5.27) turns out to be a good one.

5.6.4.3 Effective Overlap Factor Ω_{eff}

With the numerically calculated densities the effective overlap factor Ω_{eff} at finite temperature can be calculated by numerically solving the overlap integrals in the interacting and non-interacting cases and using Eq. (5.21), where $\alpha = 3/2$ (see Sec. 5.6.3.5). The results are plotted in Fig. 5.3 of the main text (here Fig. 5.10a). In Fig 5.10b, the results for $\alpha = 1$ are shown.

We emphasize that this numerical model does not use the Boltzmann distribution for thermal bosons, and it does not rely on the peak density approximations used in Sec. 5.6.3.5, and it includes effects beyond the Thomas-Fermi limit. The value of the denominator in Eq. (5.21) from the analytical model is only about 9% higher than the numerical result in the non-interacting case and the remaining difference mostly comes from the TF approximation in the analytical model [Eq. (5.27)]. This agreement indicates the validity of the analytical model for the thermal bosons and Ω_{eff}.

5.6.5 Systematic Errors in Theory and Experiment

As Fig. 5.3 of the main text shows, the measured overlap is slightly higher than the calculated values and there can be several reasons for this discrepancy. In this Section, we discuss the possible systematic effects we have in the theoretical calculations as well as in the experimental procedures and data analysis .

5.6.5.1 The Fermion Density: Finite Temperature Effects and the FRA

In our analysis of the experimental data we use the FRA and the peak density at zero temperature. Both assumptions lead to a systematic error. When using the FRA, we assume the bosons to sample a fixed local fermion density. This assumption leads to an underestimation of the overlap between the fermions and the thermal bosons by about two percent. However, for the overlap with the BEC atoms the deviation from the FRA is negligible because of their small spatial extend.

Furthermore, we assume that the fixed fermion density as sampled by the bosons is given by the fermion peak density at zero temperature (See Eq. (5.18) and Eq. (5.18)). However, finite temperature effects and the gravitational sag on the bosonic cloud challenge this assumption. For the L_3 measurements, ignoring the finite temperature leads to an underestimation of L_3 of about 20% for the highest temperatures (data set A1). For the peak density used in Eq. (5.27), the finite-T effect is about 7% percent.

The gravitational sag on the bosonic cloud leads to a shift of the center of the cloud by about 8 μm, which, as can be seen in Fig. 5.11, leads to the bosons sampling a 20% lower fermion density than the peak density. Thus, using the lithium peak density in

Eq. (5.27) leads to an underestimation of Ω_{eff} by 20%. The effect for the L_3 measurements is less drastic because of the spatial extend of the thermal cloud.

For the final values of Ω_{eff} the effects of finite-temperature on the L_3 measurements and the gravitational sag on the lithium peak density in Eq. (5.27) cancel each other out. We estimate that when taking all the above mentioned corrections into account, we have an underestimation of Ω_{eff} by about 5%.

5.6.5.2 Systematic Errors in the Effective Overlap Factor Ω_{eff}

In Fig. 5.3 of the main text (see Fig. 5.10a), the uncertainty in the Ω_{eff} data points reflects the statistical uncertainties of γ. Additionally, there are systematic errors in determining Ω_{eff} via Eq. (5.27), which come from the determination of the atom number, BEC fraction, temperature and trap frequencies. The systematic calibration error in the determination of the Li and K atom number is about 8%, and we estimate the BEC fraction determination from the bimodal fit to have a 10% error. The systematic error in γ is therefore 11% and for the fermion and BEC peak density it is about 10%. The thermal peak density is estimated to have an error of 17%. The systematic error in L_3 is about 15% and has two main sources. First, the typical 1σ uncertainty in the smoothing of L_3 is about 10% and second there is a systematic error in all L_3 data points of about 12% which comes from the uncertainty in the atom numbers, temperature and trap frequencies. All together this leads to a systematic uncertainty in Ω_{eff} of about 26%.

5.6.5.3 Other Processes

When we prepare the samples, we assume that we ramp adiabatically to the final field, since we did not observe any noticeable excitation. However an unnoticeable yet weak excitation of the mixture can lead to additional overlap and losses. This would both affect the γ and L_3 measurements, and thus only have a weak influence on Ω_{eff}.

Moreover, we speculate that recombination in a degenerate sample may not be exclusively attributed to three-body recombination. Higher-order processes such as four-body rebombination may contribute. If at all important, such processes may be present at the high phase-space densitities of a BEC, but they will be suppressed for thermal clouds. Such processes would lead to increased values for Ω_{eff}.

The high density of the boson cloud may lead to another effect causing a spatial separation between the two species, as observed in Ref. [Bau11]. If the mean free path of a Li atom in the dense cloud of K is much smaller than the spatial extend of the boson cloud, then the motion is diffusive and it takes a long time for a Li atom to reach the center of the K cloud. If three-body processes happen at a shorter time scale than

this diffusive motion, the result will be an effective reduction of the spatial overlap of both species. The mean free path for a Li atom moving in a thermal cloud of K is about 20 μm ($a_{\mathrm{bf}} \approx 600 a_0$), so for our L_3 measurements, the motion of the Li atom stays essentially ballistic and the effect described in Ref. [Bau11] can be safely neglected. In the case of the K-BEC, the mean free path of the Li atom is an order of magnitude lower and the collision time is on the order of 20 μs. Comparing this to the typical time for three-body loss $\tau = 2(L_3\, n^2)^{-1} \approx 1.5$ ms, shows that also for our γ measurements the effect observed in Ref. [Bau11] cannot play a significant role.

5

CHAPTER 6

Decoherence of Impurities in a Fermi Sea of Ultracold Atoms

Published as:
M. Cetina, M. Jag, R. S. Lous, J. T. M. Walraven, R. Grimm,
R. S. Christensen, G. Bruun
Phys. Rev. Lett. **115**, 135302 (2015)

Author contribution

The author took parts of the measurements and contributed to the general lab work, the development and implementation of the experimental techniques, the interpretation and analysis of the data, the discussion with our theory collaborators, and the writing of the manuscript.

Note

The theory presented in this work, is described in more detail by Christensen and Bruun in Ref. [Chr15]. The experimental results of this paper were also discussed in a later theoretical publication by Schmidt *et al.* [Sch18], using a functional determinant approach.

We investigate the decoherence of ^{40}K impurities interacting with a three-dimensional Fermi sea of ^{6}Li across an interspecies Feshbach resonance. The decoherence is measured as a function of the interaction strength and temperature using a spin-echo atom interferometry method. For weak to moderate interaction strengths, we interpret our measurements in terms of scattering of K quasiparticles by the Fermi sea and find very good agreement with a Fermi liquid calculation. For strong interactions, we observe significant enhancement of the decoherence rate, which is largely independent of temperature, pointing to behavior that is beyond the scattering of quasiparticles in the Fermi liquid picture.

6.1 Introduction

Many-body fermionic systems with strong interactions play a central role in condensed-matter, nuclear, and high-energy physics. The intricate quantum correlations between fermions challenge our understanding of these systems. Mixtures of ultracold fermionic gases offer outstanding opportunities to study strongly interacting fermions experimentally. Since the turn of the century, the excellent control over the strength of the interaction and the composition of these mixtures has allowed investigations addressing the broad spectrum from few-body to many-body phenomena [Blo08, Gio08]. Tuning of the interaction is achieved using Feshbach resonances [Chi10]. The composition is varied by selecting internal states or by mixing different atomic species. This development has led to many exciting results concerning the quantum phases of fermionic mixtures, their excitations, superfluid behavior, and the equation of state [Zwi15].

In two-component fermionic systems with a large population imbalance, the minority atoms have been shown to form quasiparticles termed Fermi polarons, even for surprisingly large coupling strengths [Sch09, Koh12, Kos12, Mas14]. These are long-lived states described by Fermi liquid theory [Bay91]. Their lifetime is limited by scattering against the majority atoms, which is suppressed by Pauli blocking as the temperature approaches zero [Lan57, Lan56]. Although the quasiparticle scattering rate has been determined in two-dimensional electron gases [Ber95, Mur95, Slu96], measurements in well-defined three-dimensional (3D) fermionic systems have remained an experimental challenge.

Intriguing questions are related to the behavior of impurities and, more generally, Fermi mixtures in the strongly interacting regime [Mas14, Nas11, Sag15]. For investigating an impurity in a Fermi sea, Refs. [Goo11, Kna12] suggested a time-domain method that is applicable for a wide range of interaction strengths. This approach can be regarded as a measurement of the coherence of a superposition of internal states of

the impurity atoms using interferometry [Cro09]. Atom coherence has previously been used to probe many-body demagnetization in fermionic systems [Bar14] and impurity scattering in bosonic systems [Sce13].

In this Letter, we report on measurements of decoherence of K atoms immersed in a Fermi sea of Li using the method proposed in Ref. [Kna12], in the regime of strong population imbalance. We tune the interaction between the Li and K atoms using an interspecies Feshbach resonance (FR). For weak to moderately strong interactions, we interpret the measured decoherence in terms of the scattering of K quasiparticles by the Li Fermi sea. We find very good agreement with a Fermi liquid calculation. This provides a determination of the quasiparticle scattering rate in a clean 3D fermionic system. We extend our measurements to strong Li-K interactions and find decoherence rates that are comparable to the fastest dynamics available in our system. These rates do not increase with temperature, which is an indication of zero-temperature quantum dynamics in a fermionic many-body system.

6.2 Experimental Method and Results

The starting point of our experiments is an evaporatively cooled, thermally equilibrated mixture of typically, $3{\times}10^5$ ^{6}Li atoms and $1.5{\times}10^4$ ^{40}K atoms, trapped in a crossed-beam 1064-nm optical dipole trap under conditions similar to those in Ref. [Koh12]. The Li cloud is degenerate, with $k_{\mathrm{B}}T/\epsilon_{\mathrm{F}}$ as low as 0.15, where T is the temperature and $\epsilon_{\mathrm{F}} \approx h{\times}35$ kHz is the average Li Fermi energy sampled by the K atoms. Because of the Li Fermi pressure and the more than two times stronger optical potential for K, the K cloud is much smaller than the Li cloud [Tre11], and, therefore, samples a nearly homogenous Li environment, with a standard deviation in the local Li Fermi energy of less than $0.1\,\epsilon_{\mathrm{F}}$. In spite of the smaller size of the K cloud, the concentration of K in the Li sea remains low, with $\bar{n}_{\mathrm{K}}/\bar{n}_{\mathrm{Li}}{\approx}0.3$, where $\bar{n}_{\mathrm{K}}$ ($\bar{n}_{\mathrm{Li}}$) is the average K (Li) number density sampled by the K atoms. The K ensemble is correspondingly nondegenerate, with $k_{\mathrm{B}}T/E_{\mathrm{F}}^{\mathrm{K}} > 0.9$, where $E_{\mathrm{F}}^{\mathrm{K}}$ is the peak K Fermi energy.

We tune the interaction between the K and Li atoms using an interspecies FR between the Li atoms in the lowest Zeeman sublevel Li$|1\rangle$ and K atoms in the third-lowest sublevel K$|3\rangle$ [Nai11]. We quantify the interactions between Li and K by the dimensionless interaction parameter $-1/\kappa_{\mathrm{F}}a$, where $\kappa_{\mathrm{F}}{=}\hbar^{-1}\sqrt{2m_{\mathrm{Li}}\epsilon_{\mathrm{F}}}$ is the Li Fermi wave number with m_{Li} the Li mass, and a is the s-wave interspecies scattering length. The latter can be tuned as $a{=}a_{\mathrm{bg}}[1{-}\Delta/(B{-}B_0)]$ by applying a magnetic field B, where $B_0{\approx}154.7$ G is the resonance center, $a_{\mathrm{bg}}{=}63.0\ a_0$ (a_0 is Bohr's radius) and $\Delta{=}880$ mG [Nai11]. The relatively narrow nature of our FR causes significant momentum dependence of the interspecies interaction. We characterize this effect by the length

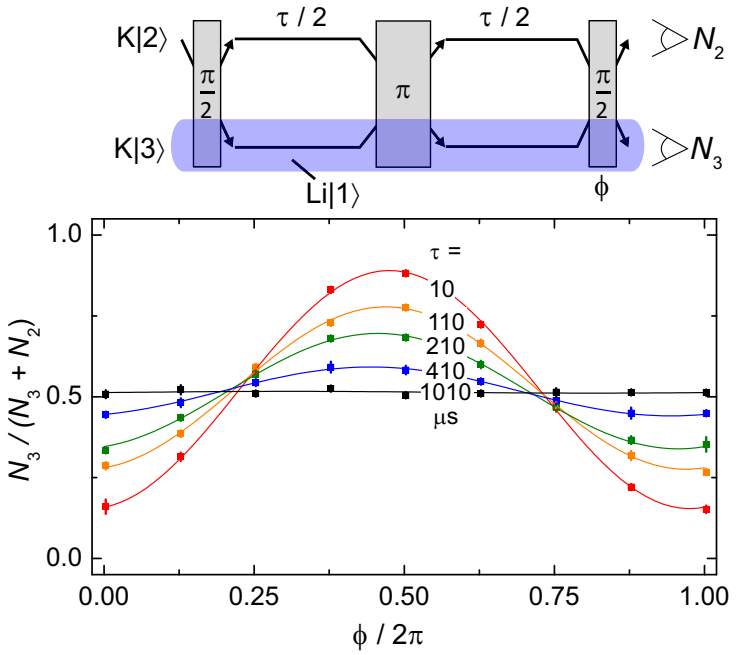

Figure 6.1: Interferometric method for measuring the decoherence of K in a Li Fermi sea. The upper illustration shows a schematic of the rf pulse sequence. The atoms in the K|3⟩ state interact with a Fermi sea of Li|1⟩ atoms, as indicated by the shaded region. The graph shows the fraction of the K atoms transferred to the K|3⟩ state as a function of the relative phase of the final $\pi/2$ rf pulse for various interaction times τ and for $-1/\kappa_F a$=2.1, T=0.16 ϵ_F/k_B.

parameter R^* [Pet04a, Koh12]. In our experiments $\kappa_F R^*$ is approximately 0.9, corresponding to an intermediate regime where the interaction is near universal with substantial effective-range effects.

We probe the decoherence of the K atoms using a radio-frequency (rf) interferometric technique, as illustrated in Fig. 6.1. The K atoms are initially prepared in the second-lowest Zeeman sublevel K|2⟩ while the Li atoms remain in the Li|1⟩ state throughout the experiment. On the time scale of our measurements, the interactions between these atoms, characterized by the s-wave scattering length $a_{12}\approx a_{bg}$, can be neglected. We apply a $\pi/2$ rf pulse (typically 10 μs long) to prepare the K atoms in an equal superposition of the K|3⟩ and K|2⟩ states. After a variable interaction time τ, we apply a second $\pi/2$ rf pulse before determining the numbers N_2 and N_3 of atoms

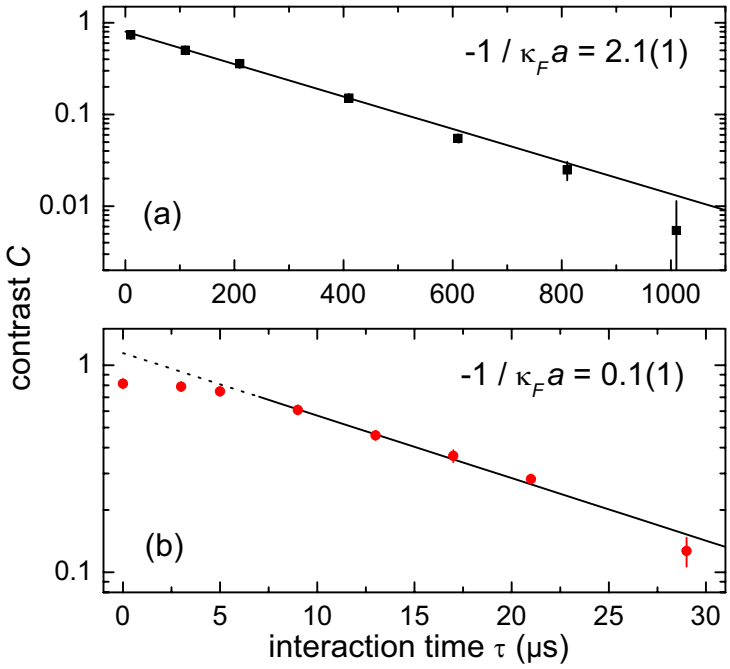

Figure 6.2: Contrast C as a function of interaction time τ. In (a), we show results for moderately attractive interspecies interactions ($-1/\kappa_F a$=2.1), corresponding to Fig. 6.1. In (b), we probe the system in the strongly interacting regime ($-1/\kappa_F a$=0.15) for T=0.20 ϵ_F/k_B by rapidly shifting the interaction parameter from 2.2 to 0.15 during the interaction time. The solid lines are exponential fits to the points with $\tau > 7\mu$s. The dotted line is an extrapolation to τ=0.

in the K$|2\rangle$ and K$|3\rangle$ states using absorption imaging (see Sec. 6.6.5). To decrease the sensitivity to the magnetic field noise and to the inhomogeneities in the atom densities, we perform a spin echo by splitting the interaction time into two equal halves separated by a π rf pulse.

Shifting the phase of the rf oscillator by ϕ between the π and the second $\pi/2$ pulses causes a sinusoidal variation in the fraction $f=N_3/(N_2+N_3)$ of the K atoms transferred to K$|3\rangle$, as shown in Fig. 6.1. We quantify the coherence of the state of the K atoms by the contrast $C=(f_{\max}-f_{\min})/(f_{\max}+f_{\min})$ of these oscillations. The interaction of the K atoms with the Li cloud causes an exponential decrease in the observed contrast with increasing interaction time τ, as shown in Fig. 6.2(a). The interaction also shifts

the rf transition frequency and decreases the rf coupling between the K$|2\rangle$ and K$|3\rangle$ states [Koh12], which we account for by adjusting the rf frequency and the duration of our rf pulses. In this way, we measure the decoherence of K atoms for $-1/\kappa_F a < -0.8$ and $-1/\kappa_F a > 1.4$. Near the center of the resonance, the fast loss of contrast during the rf pulses limits the applicability of this method.

To measure the decoherence of K in the strongly interacting regime, we use laser light to rapidly displace our magnetic FR [Bau09a, Bau09b, Cla15]. Optical control of our FR allows us to apply the rf pulses away from the FR and then rapidly bring the atoms into resonance for the duration of the interaction time τ[1]. This method circumvents the loss of contrast during the rf pulses and allows us to probe the K decoherence across the full range of interaction parameters. The displacement of our FR arises from the laser-induced differential ac Stark shift between the free-atom level and the molecular state involved in the FR. The ac Stark shift is induced by the 1064-nm trapping light, as we investigated in Ref. [Jag14]. Although the differential shift here amounts to only 10% of the total trapping potential, using a high-intensity beam with up to 65 kW/cm^2, we can displace B_0 by up to 40 mG in less than 200 ns – all while preserving the harmonic trapping potential (see Sec. 6.6.1). This displacement corresponds to a change in the interaction parameter of up to ± 2.1 on a time scale of $0.05\,\tau_F$, where $\tau_F = \hbar/\epsilon_F \approx 4.5\ \mu$s is the Fermi time.

In Fig. 6.2(b), we show the dependence of the contrast C on the interaction time τ near the center of our FR. The contrast starts to decay after an initial delay of approximately τ_F. This delay can be explained in terms of quantum evolution of the system with an interaction energy bounded from above by ϵ_F [Kna12]. For $\tau > 1.6 \times \tau_F \approx 7$ μs, the decrease in contrast is well described by an exponential decay. The fitted rate $\gamma_{coh} = 0.28(2)\,\tau_F^{-1}$ is comparable to the inverse Fermi time, indicating that our experiment cannot be fully described by the scattering of quasiparticles in the Fermi liquid picture, which assumes long-lived quasiparticles [Bay91].

In Fig. 6.3, we show the dependence of the fitted rate γ_{coh} on the interaction parameter. We present data with two decades of dynamic range and demonstrate a dramatic resonant enhancement of the decoherence rate, reaching values up to $0.4\,\tau_F^{-1}$. The data do not exhibit any clear dependence on $\bar{n}_K/\bar{n}_{Li}$ across the full range $0.17 \leq \bar{n}_K/\bar{n}_{Li} \leq 0.43$. In addition to the statistical errors indicated by the error bars, the data are subject to variations of $k_B T/\epsilon_F$, $\kappa_F R^*$, and $\bar{n}_K/\bar{n}_{Li}$ with standard deviations of 0.01, 0.02 and 0.07 about their mean values of 0.16, 0.93 and 0.27, respectively. The calibration of the Li atom number introduces a 6% systematic uncertainty in ϵ_F and τ_F, as well as a corresponding 3% uncertainty in κ_F. Further, our total error budget includes 3%

[1] For measurements on the attractive (repulsive) side of the FR, we shift B_0 upwards (downwards). For measurements near the resonance, we verify that the direction of the shift of B_0 does not affect the result.

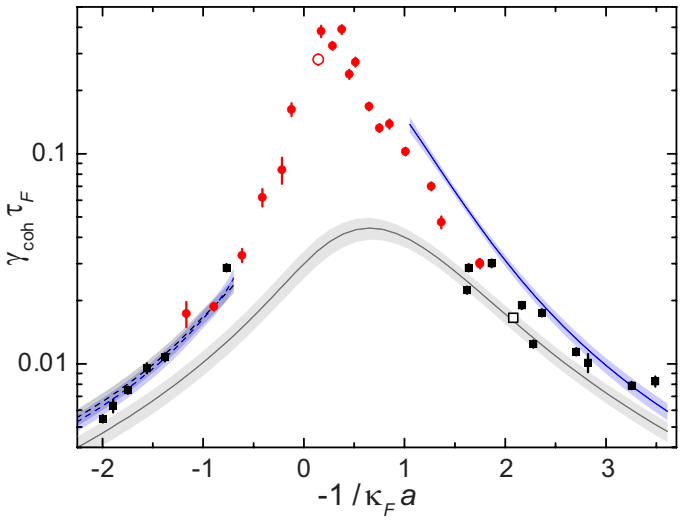

Figure 6.3: Decoherence rate of K in a Li Fermi sea as a function of the interaction parameter for an average temperature T=0.16 ϵ_F/k_B (see text). The measurements with (without) rapid shifting of the FR are shown as the red circles (black squares). The measurements from Fig. 6.2 are indicated by open symbols. The solid upper (blue) and lower (black) lines correspond to the prediction of the Fermi liquid theory with and without medium corrections, respectively. The dashed lines incorporate corrections due to decay to Feshbach molecules. The shaded areas show the 1σ effect of the experimental uncertainties on the theoretical predictions.

systematic errors in a and R^* arising from the uncertainty in ΔB, and a ± 0.05 error in $1/\kappa_F a$ resulting from an uncertainty in the determination of B_0 of ± 1 mG (see Sec. 6.6.3).

For weak to moderate interactions, there are well-defined K quasiparticles, and we now show that the evolution of the contrast C on time scales much longer than τ_F can be related to the mean quasiparticle scattering rate γ_s. Each scattering event provides which-way information that distinguishes between the two paths in the interferometer in Fig. 6.1 and, thus, erases the interference effect. At any given time, the interaction affects only one of the two paths, decreasing the probability for the system to stay in this path at the rate γ_s. Since our signal arises from the interference of the amplitudes in the two interferometer paths, we expect the interaction to lead to a decrease of the observed contrast at the rate $\gamma_s/2$.

6.3 Theory

From Fermi liquid theory, the scattering rate γ_{p_1} of a K quasiparticle with momentum $\mathbf{p}_1$ is given by [Bay91]

$$\gamma_{p_1} = \iint d\check{p}_2 d\Omega \frac{m_r p_r}{4\pi^2} |\mathcal{T}|^2 [f^{\mathrm{Li}}_{p_2}(1 - f^{\mathrm{K}}_{p_3} - f^{\mathrm{Li}}_{p_4}) + f^{\mathrm{K}}_{p_3} f^{\mathrm{Li}}_{p_4}]. \tag{6.1}$$

Here, $\mathcal{T}$ is the scattering matrix for the scattering of K atoms with Li atoms with momenta $\mathbf{p}_1$ and $\mathbf{p}_2$, respectively, to momenta $\mathbf{p}_3$ and $\mathbf{p}_4$. We have defined $d\check{p}_2 = d^3 p_2/(2\pi)^3$, and Ω is the solid angle for the direction of the outgoing relative momentum. The distribution functions are $f_p^{\mathrm{Li/K}} = [e^{\beta(E_p^{\mathrm{Li/K}} - \mu_{\mathrm{Li/K}})} + 1]^{-1}$ with the chemical potentials $\mu_{\mathrm{Li/K}}$ for the Li /K atoms respectively. The dominant medium effects can be shown to enter in the scattering matrix $\mathcal{T}$ via ladder diagrams, whereas the quasiparticles can be assumed to have the ideal gas energy dispersion $E_p^{\mathrm{K/Li}} = p^2/2m_{\mathrm{K/Li}}$ [Bru05, Ens12]. The details of the calculation of γ_{p_1} are described in [Chr15]. In addition, we account for the reduced quasiparticles residue Z by multiplying the collision rate by Z calculated from the ladder approximation [Mas14]. To obtain the mean scattering rate γ_s, we calculate the thermal average $\gamma_s = \int d\check{p} f_p^{\mathrm{K}} \gamma_p$. To include the effects of the trap, we use effective Fermi energies, which are obtained by averaging the local Fermi energy over the density of the K atoms in the trap. This approach is justified since the K atoms only probe a small region of the Li gas, and because the momentum distribution of the K atoms is nearly classical.

On the repulsive side of the FR, we need to consider additional effects arising from the decay of the atoms into the molecular state that underlies our FR. The rate Γ of this process was calculated and confirmed by measurements in Ref. [Koh12], reaching values as high as $0.02\ \tau_{\mathrm{F}}^{-1}$ close to resonance. Since the decay to molecules provides which-way information, it will contribute at least $\Gamma/2$ to the measured decoherence rate. The decay also releases energy and creates holes in the Li Fermi sea, increasing the value of $k_{\mathrm{B}}T/\epsilon_{\mathrm{F}}$ during our measurement to 0.20 (1) (see Sec. 6.6.6).

In Fig. 6.3, we plot the calculated decoherence rate $\gamma_s/2$ as a function of the interaction parameter. The lower solid line is obtained by using the vacuum scattering matrix $\mathcal{T}_{\mathrm{vac}}$ [Chr15] in Eq. (6.1), whereas the upper solid line is obtained by using a $\mathcal{T}$ matrix which includes medium effects using the ladder approximation. The dashed lines include the effects of decay into the molecular state. The calculated decoherence rate agrees with the experimental values very well for $-1/k_{\mathrm{F}}a \gtrsim 1.5$ and for $-1/k_{\mathrm{F}}a \lesssim -1$. This gives strong evidence that the observed decoherence is, indeed, due to quasiparticle collisions. The significant asymmetry of the decoherence rate around $1/k_{\mathrm{F}}a = 0$ arises from the narrow nature of the FR [Chr15]. The calculated decoherence rate

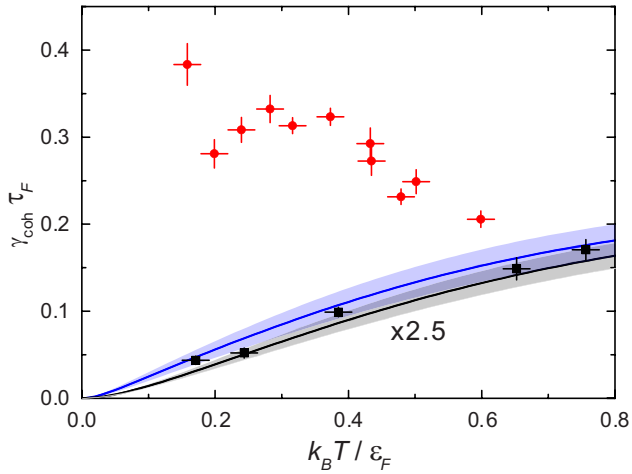

Figure 6.4: Decoherence rate of K in a fermionic Li cloud as a function of temperature. The data for $-1/\kappa_F a$=0.2, $\kappa_F R^*$=0.94, $\bar{n}_K/\bar{n}_{Li}$=0.2 ($-1/\kappa_F a$=2.4, $\kappa_F R^*$=0.89, $\bar{n}_K/\bar{n}_{Li}$=0.3) measured with (without) rapid shifting of the FR is shown as red circles (black squares). The solid blue and black lines correspond to the predictions of the Fermi liquid theory for $-1/\kappa_F a$=2.4 with and without medium corrections, respectively. The shaded areas show the 1σ effect of the experimental uncertainties on the theoretical predictions.

is larger when medium effects are included in the $\mathcal{T}$ matrix. This is due to pair correlations, which can increase the collisional cross section significantly [Chr15]. We see that the inclusion of these medium effects on the scattering matrix improves the agreement with the experimental data. For stronger interactions, the calculation does not fit the experiment, which is expected since there are no well-defined quasiparticles in the unitarity regime [Koh12]. Our model agrees with the observed absence of a dependence of γ_{coh} on $\bar{n}_K/\bar{n}_{Li}$ since the K cloud is close to the classical regime where $f^K_{p_3} \ll 1$ and the momentum distribution of the K atoms is solely determined by the temperature.

6.4 Temperature Dependence

Further insight into the nature of the observed decoherence can be gained by varying the temperature of our atom mixture, which we accomplish by changing the endpoint of our evaporative cooling. We show the dependence of the measured decoherence rate

on temperature in Fig. 6.4. In addition to the statistical errors shown by the error bars, the data are subject to small variations of $-1/\kappa_F a$, $\kappa_F R^*$, and $\bar{n}_K/\bar{n}_{Li}$ with standard deviations of 0.05, 0.03, and 0.1, respectively. Our total error budget also includes the above-mentioned systematic uncertainties in ϵ_F, κ_F, a, and R^*.

Away from the FR, the measured decoherence rates are in very good agreement with the predictions of the Fermi liquid theory. The linear dependence of γ_{coh} on temperature in this regime arises from the high relative mass of the K atoms, causing the Li-K scattering to resemble scattering by fixed impurities. This is similar to the situation in metals where the scattering of electrons by fixed nuclei gives rise to the well-known linear dependence of the nuclear decoherence rates on temperature [Kor50]. The red circles in Fig. 6.4 represent the measurements for resonant interactions. The rates obtained in this regime are more than an order of magnitude higher than the off-resonant rates and do not increase with temperature.

6.5 Conclusion

In conclusion, we established that, for weak to moderate interaction strengths, the decoherence of K in a Li Fermi sea is dominated by quasiparticle scattering. Our observations for strong interactions cannot be explained solely by quasiparticle scattering and indicate decoherence processes which persist at zero temperature. This offers an exciting opportunity to explore the many-body quantum dynamics of an impurity submerged in a Fermi sea.

Acknowledgements

We thank F. Schreck, C. Kohstall, I. Fritsche, P. Jeglič, Y. Ohashi, R. Schmidt, E. Demler, and, especially, M. Parish, J. Levinsen and M. Baranov for helpful discussions. We thank P. Massignan for sending us data for the quasiparticle residue and decay. We acknowledge funding by the Austrian Science Fund FWF within the SFB FoQuS (Project No. F40-P04) and support of the Villum Foundation via Grant No. VKR023163.

6.6 Supplemental Material

6.6.1 Optical Trap Setup

We perform our measurements in dipole traps formed by two single-frequency, 1064-nm laser beams produced by a solid-state laser system (Innolight Mephisto 42NE MOPA). The beams intersect at an angle of 16°. To avoid standing wave effects, the beams are offset in frequency by 5 to 10 MHz. To shift the Feshbach resonance (FR),

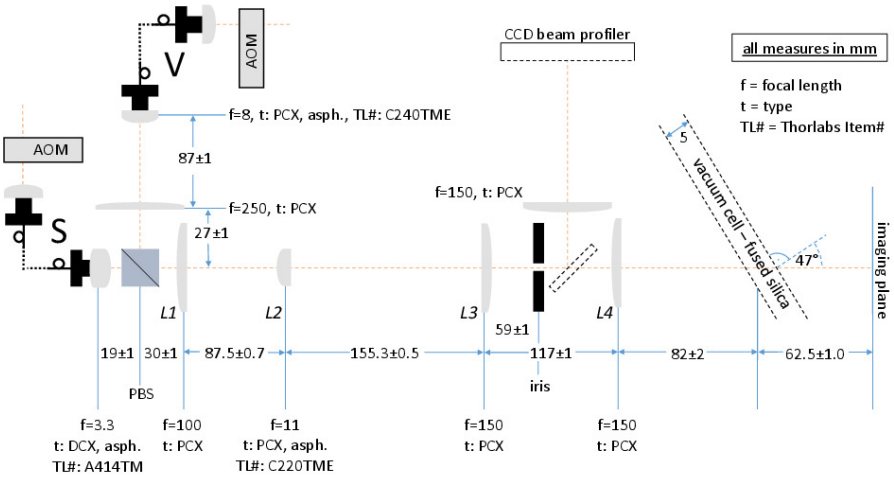

Figure 6.5: Illustration of the optical setup for producing and switching optical dipole traps of different sizes with highly stable relative position.

we keep one of the two beams ("*D*") static and use acousto-optic modulators (AOMs) to rapidly change the other beam. Changing only the intensity of this latter beam would excite strong oscillations of the atomic cloud. We counter this by switching from a beam with a low peak intensity and small size ("*S*") to a beam with a large intensity and large size ("*V*") propagating in the same direction. The waists, positions and intensities of the "*S*" and "*V*" beams are adjusted so as to match the centers and curvatures of the resulting optical potentials, preventing collective excitations of the atomic cloud.

This method for shifting the FR poses two technical challenges. First, the overlap between the optical axes of the "*S*" and "*V*" beams needs to be maintained with an accuracy that is much better than the smallest extent of the atomic clouds (about 5 μm). Second, to maximize the shift of the resonance, the curvature of the optical potential due to the larger beam needs to be minimized relative to its intensity. We address both of these challenges using the optical system shown in Fig. 6.5.

To ensure beam pointing stability, we couple the laser light into Panda polarization-maintaining fiber patchcords (Thorlabs P3-980PM-FC) with 6 μm core diameter. For the "*S*" and "*D*" beams, we use 5-m long fibers. When using a 5-m long fiber for the "*V*"-beam, we observed a saturation of the fiber output power at 1.1 W, together with

a sharp increase of the reflected power from the fiber. These effects were not observed with up to 10 W of output power from the fiber when a 2-m long fiber was used. We interpret these observations in terms of stimulated Brillouin scattering [Ruf04], whose threshold power is inversely proportional to the fiber length.

To prevent the degradation of the fiber ends, the "V" beam is operated with brief ($<$ 0.3 ms) and infrequent ($<$ 1/min) pulses. Although, in the P3-980PM-FC patchcords, the fiber is attached to the ferrule using an epoxy adhesive, we did not observe any degradation of the fiber transmission after one year of operation with peak powers up to 10 W.

To maintain relative pointing stability of the "S" and "V" beams, the outputs of the "S" and "V" fibers (e^{-2} divergence half-angle = 74(3) mrad) are combined on a polarizing beamsplitter. At this location, the "S" and "V" beams have waists of 0.31(1) mm and 0.75(1) mm, respectively. In the same plane, "S" and "V" beams are converging with radii of curvature of 370(20) mm and 390(20) mm, respectively. The output of the beamsplitter is projected with 7.6× demagnification onto the atoms using a telescope composed of the lenses labelled as L1, L2, L3 and L4 in Fig. 6.5. The distance between the lenses L2 and L3 is adjusted so as to obtain a nearly collimated "S" beam after the lens L3 with a 1.2(1)-mm waist.

Higher spatial frequency components in the beams (arising e.g. from stray reflections) increase the curvature of the optical potential relative to its depth. To mitigate this problem, we spatially filter the "S" and "V" beams by passing them through a 5.3-mm diameter graphite aperture in a plane that is Fourier-conjugate to the location of the atoms (Fig. 6.5).

We measured the sizes of the "S" and "V" beams at the location of the atoms by deflecting the beams using an auxiliary mirror and then focusing them onto a CCD beam profiler, as shown in Fig. 6.5. The $1/e^2$ radii of the "S" and "V" beams were determined to be 38(2) μm, and 91(3) μm, respectively. The size of the "D" beam at the location of the atoms was determined to be 48(2) μm.

6.6.2 Parameters of the 154.7 G Feshbach Resonance

The FR that we employ for tuning the interactions in our system occurs between ^{6}Li atoms in their lowest internal state, denoted Li$|1\rangle$ ($F = 1/2$, $m_F = +1/2$), and ^{40}K atoms in their third-to-lowest state K$|3\rangle$ ($F = 9/2, m_F = -5/2$). We parametrize the Li$|1\rangle$-K$|3\rangle$ scattering length near the 154.7 G FR by the usual expression [Chi10]

$$a(B) = a_{\mathrm{bg}}\left(1 - \frac{\Delta}{B - B_0}\right). \tag{6.2}$$

For the background scattering length a_{bg} and the resonance width Δ, we use the values $a_{\mathrm{bg}} = 63.0\, a_0$ and $\Delta = 0.880\,\mathrm{G}$ from the coupled-channel calculation in [Nai11].

The narrow nature of the Li$|1\rangle$-K$|3\rangle$ FR causes a significant variation of Li-K scattering across the range of the collision energies encountered in our experiment [Chi10]. We obtain quantitative information on this effect from measurements of the molecular binding energy. We measure the binding energy using two methods: radio-frequency (rf) association [Jag14] and magnetic field modulation spectroscopy [Lan09]. The combined results of these measurements are shown in Fig. 6.6.

In order to parametrize the dependence of the molecular binding energy E_{b} on the magnetic detuning $B - B_0$ near the dissociation threshold, we first introduce the wave number κ, in terms of which $E_{\mathrm{b}} = \hbar^2\kappa^2/2m_r$, where $m_r = m_{\mathrm{Li}} m_{\mathrm{K}} / \left(m_{\mathrm{Li}} + m_{\mathrm{K}}\right)$ is the reduced mass. We then express the magnetic detuning $B - B_0$ as a function of κ by a Taylor expansion up to second order of the form

$$B - B_0 \quad = \quad -a_{\mathrm{bg}}\,\Delta\,\kappa - \frac{\hbar^2\,\kappa^2}{2m_r\,\delta\mu}\ . \tag{6.3}$$

The coefficient $a_{\mathrm{bg}}\,\Delta$ in front of the linear term is determined by the well-known universal relation between κ and a near the resonance. We fit Eq. (6.3) to the data from Fig. 6.6 with $\delta\mu$ and B_0 as free parameters, while fixing a_{bg} and Δ to the values from Ref. [Nai11]. From this fit, we obtain $\delta\mu/h = 2.35\,(2)$ MHz/G. Our fitting model is equivalent to the prediction of the two-channel model from [Pet04a] with $R^* = \hbar^2/\left(2m_r\,a_{\mathrm{bg}}\,\delta\mu\,\Delta\right)$. We note that this model neglects the background scattering term in Eq. (6.2).

Our measurements of the binding energy allow us to determine the momentum dependence of Li-K collisions near the resonance. For small values of the collision momentum $\hbar k$, we can use the well-known effective range expansion to write the inverse scattering amplitude as

$$f\,(k)^{-1} = -\frac{1}{a} + \frac{1}{2}\,r_{\mathrm{eff}}\,k^2 - ik\ .$$

Since the existence of the bound state implies that the scattering amplitude has a pole at $k = i\kappa$, we obtain

$$0 = \frac{1}{a} - \frac{1}{2}\,r_{\mathrm{eff}}\,(i\kappa)^2 + i\,(i\kappa)\ .$$

Substituting the expression (6.2) for $a\,(B)$, we can then write

$$a_{\mathrm{bg}}^{-1}\left(1 - \frac{\Delta}{B - B_0}\right)^{-1} + \frac{1}{2}\,r_{\mathrm{eff}}\,\kappa - \kappa = 0\ .$$

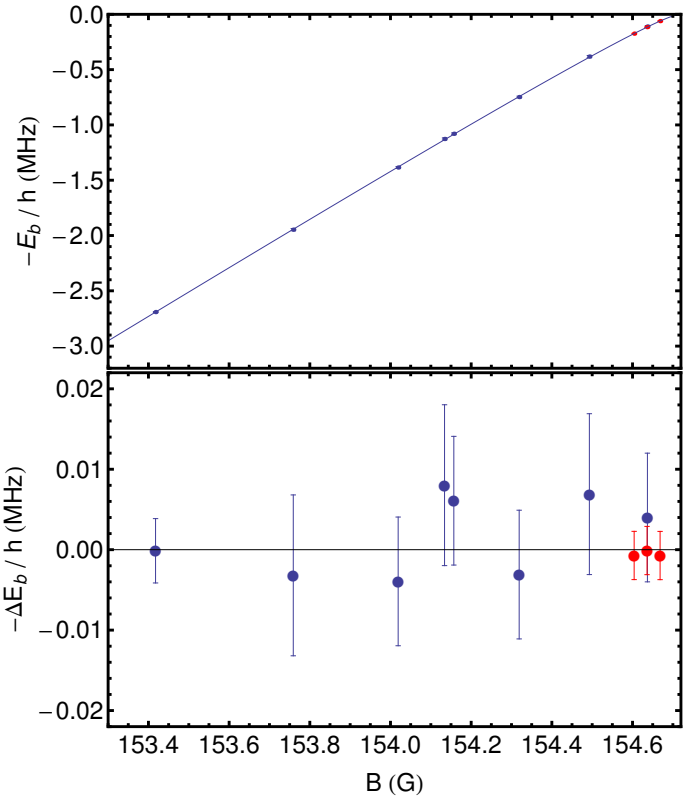

Figure 6.6: Molecular binding energy near the 154.7 G Li$|1\rangle$-K$|3\rangle$ Feshbach resonance measured using rf association (red points) and magnetic field modulation spectroscopy (blue points). The lower panel shows the residuals of a fit to the data with the model based on Eq. (6.3) with $\delta\mu$ and B_0 as free parameters.

Then, substituting the expression (6.3) for the detuning $B - B_0$, we obtain

$$a_{\mathrm{bg}}^{-1}\left(1 - \frac{\Delta}{-a_{\mathrm{bg}}\,\Delta\,\kappa - \frac{\hbar^2\,\kappa^2}{2m_r\,\delta\mu}}\right)^{-1} + \frac{1}{2}\,r_{\mathrm{eff}}\,\kappa - \kappa = 0\ .$$

Taylor-expanding this near $\kappa = 0$, we get

$$\left(-a_{\mathrm{bg}} + \frac{r_{\mathrm{eff}}}{2} + \frac{\hbar^2}{2a_{\mathrm{bg}}\,m_r\,\delta\mu\,\Delta}\right)\kappa^2 + O\left(\kappa^3\right) = 0\ ,$$

whence we obtain

$$r_{\mathrm{eff}} = 2\,a_{\mathrm{bg}} - \frac{\hbar^2}{a_{\mathrm{bg}}\,m_r\,\delta\mu\,\Delta}\ . \tag{6.4}$$

We can summarize the parameters of the Li$|1\rangle$-K$|3\rangle$ FR with three independent parameters:

$$\begin{aligned} a_{\mathrm{bg}} &= 63.0\,a_0\ , \\ \Delta &= 0.880\,\mathrm{G}\ , \\ \delta\mu/h &= 2.35\,(2)\ \mathrm{MHz/G}\ . \end{aligned}$$

From this, we can derive the values

$$\begin{aligned} R^* &= 2650\,(25)\ a_0\ , \\ r_{\mathrm{eff}} &= -5175\,(50)\ a_0\ . \end{aligned}$$

6.6.3 Light Shift of the Feshbach Resonance

As we pointed out in the main text, as well as in Refs. [Koh12, Jag14], the optical trap induces a differential light shift between the atom pair state and the molecular state giving rise to the FR near 154.7 G. This leads to a light-induced shift of the FR. To produce these shifts in the experiments presented in the main text, we use a near-infrared laser as discussed in Sec. 6.6.1 in four different trap settings (see Table 6.1).

To determine the resonance center B_0 for a given trap setting, we follow the experimental procedure outlined in the Supplemental Material of Ref. [Jag14]. For the data analysis, we use the updated binding energy model presented in the preceeding Section. For each trap setting, we perform rf association spectroscopy of the Feshbach molecules. We start by preparing a nonresonant mixture of Li atoms in the state Li$|1\rangle$ and K atoms in their second-to-lowest state K$|2\rangle$ several tens of mG below B_0. At this

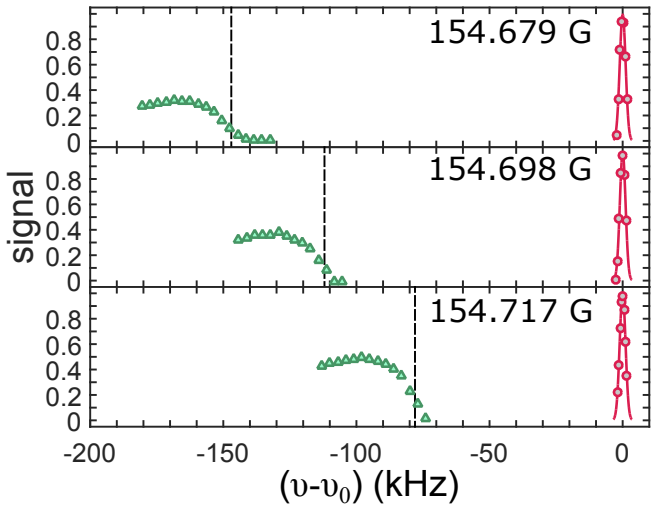

Figure 6.7: Data from the molecular rf-association spectroscopy for trap 3. The red points were taken with a 0.5-ms rf pulse with an intensity set to the value matching the π-pulse condition in the absence of interactions (no Li$|1\rangle$ present). The green points were recorded with more than 30× increased rf intensity. The dashed lines indicate the binding energy $E_b(B)$ as determined with the 20% criterion (see text).

field, we apply an rf pulse (duration of a few 100 μs) at a variable frequency ν, several kHz below the unperturbed K$|2\rangle \rightarrow$K$|3\rangle$ transition frequency ν_0. This pulse drives Li$|1\rangle$-K$|2\rangle$ atom pairs into the Li$|1\rangle$K$|3\rangle$ dimer state. To determine the number of dimers associated, we subsequently dissociate the dimers into pairs of Li$|1\rangle$ and K$|3\rangle$ atoms by a magnetic field ramp (duration of a few 100 μs) to a magnetic field above 154.8 G. By recording absorption images we then determine the populations N_2 and N_3 of the K spin states K$|2\rangle$ and K$|3\rangle$, respectively.

Plotting the signal, given by $N_3/(N_3 + N_2)$, against the rf detuning $\nu - \nu_0$, we resolve the molecule association spectrum. In Fig. 6.7 we show sample spectra recorded for one of the trap settings used in the experiments. We determine the energy of the molecules relative to the energy of noninteracting K$|3\rangle$ atoms from the onset frequency of the molecular association spectra. As the onset frequency, we use the upper rf frequency at which the fraction of atoms transferred is roughly 20% of its peak height. We have checked that, within the errors of our measurements, this criterion agrees with the result obtained by fitting the line-shape model of Ref. [Chi05] to the spectra,

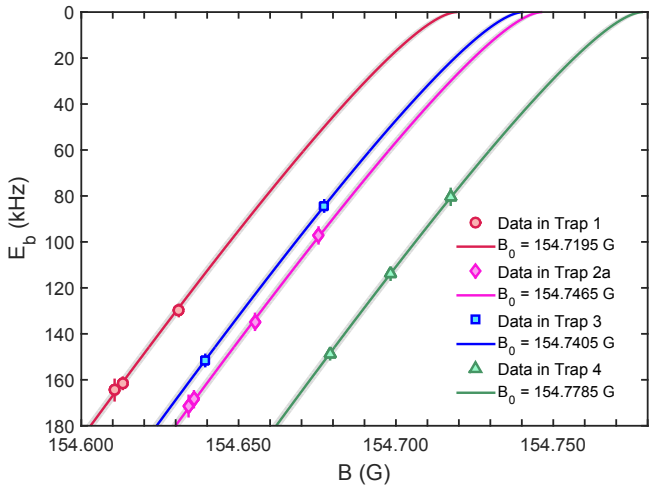

Figure 6.8: Determination of the FR center B_0 by rf association of dimers. The points show the experimentally determined molecular binding energies $E_b(B)$ for four trap settings. The solid curves are fits of the binding energy according to Eq. 6.3. The gray shaded areas indicate the typical error range of our fit analysis.

as was done in Ref. [Koh12]. This procedure is applied at various magnetic fields for each trap setting used in the experiments.

The interaction between the formed LiK molecules and the Li atoms leads to an energy shift of the molecular state. We use the mean-field model from [Jag14] to predict the corresponding shift in the onset frequency in the rf association measurements as +2.0(4) kHz. To determine the molecular binding energy in the absence of the Li cloud, we subtract this small offset from the onset frequencies determined above.

We fit the binding energy according to Eq. (6.3) to the data, with B_0 as the only free parameter (see Fig. 6.8). The other parameters are fixed to the values from Sec. 6.6.2. This procedure allows us to determine the resonance center in each trap setting with an uncertainty of ± 1.5 mG. The accuracy of our determination of the resonance position is limited by the uncertainty in the FR parameters in the model for the binding energy. The FR centers determined for our four trap settings of Fig. 6.8 are given in Table 6.1.

To record the data shown in Figs. 6.3 and 6.4 of the main text we switch between trap settings 1 and 2b as well as between settings 3 and 4 within less than 200 ns. In our experiments, switching between trap 1 and 2b (3 and 4) changes the interaction parameter $1/\kappa_F a$ by 1.2 (2.1), without changing the harmonic potential in which the

Trap	B_0 (G)	$\nu_{r,\mathrm{K}}$ (Hz)	$\nu_{a,\mathrm{K}}$ (Hz)	$\nu_{r,\mathrm{Li}}$ (Hz)	$\nu_{a,\mathrm{Li}}$ (Hz)	P_S (W)	P_D (W)	P_V (W)
1	154.7195	415	56	650	88	0.175	0.380	0
2b	154.7420					0	0.380	4.40
2a	154.7465	-	-	-	-	0	0.425	4.85
3	154.7405	580	80	945	130	0.380	0.815	0
4	154.7785					0	0.815	7.60

Table 6.1: Typical trap parameters for the various trap settings. In our experiments, we switch from trap 1 to 2b i.e. from trap 3 to 4 by switching the powers P_S and P_V of the S and V beams within less than 200 ns.

atoms are trapped. When we recorded the data for the FR center determination, the data in trap 2a of Fig. 6.8 was recorded with 11% higher trapping-light powers compared to trap 2b, in which measurements of the main text were taken. Therefore, the FR center $B_{0,2}$ is shifted 11% more relative to the center of the FR in the absence of the 1064-nm light. We determine the latter to be at 154.699(1) G by extrapolating the FR centers for various beam intensities to the zero trapping-light intensity. The correct value of the FR center of trap 2b, as used in the experiments of the main text, is therefore given by $154.699\,\mathrm{G} + (B_{0,2} - 154.699\,\mathrm{G})/1.11 = 154.7420(15)\,\mathrm{G}$.

The determination of the relative shifts of the FR centers of two trap settings can be done with an even higher accuracy. As an example: We record association spectra at a magnetic field B_3 (B_4) in trap 3 (4) with the FR center at $B_{0,3}$ ($B_{0,4}$). The magnetic fields are chosen such that the spectra are taken at roughly the same detuning $B_3 - B_{0,3} \approx B_4 - B_{0,4}$. We then compare these spectra from trap 3 and trap 4, and overlap their association onsets by shifting one of them, say the one in trap 4, with respect to the other, trap 3, along the frequency axis by $\delta\nu$. This frequency shift $\delta\nu$ can be translated into a magnetic detuning shift δB_0 by comparing it to the slope of the binding-energy at that detuning $\mathrm{d}E_\mathrm{b}/\mathrm{d}B$. Then δB_0 can be extracted from $\delta B_0 = h\delta\nu/[\mathrm{d}E_\mathrm{b}/\mathrm{d}B]$. Finally we can derive the relative shift of the FR centers in trap 3 and trap 4 to be $B_{0,4} - B_{0,3} = B_4 - B_3 - \delta B_0$. We estimate the accuracy of this relative FR center determination to be on the order of ± 0.5 mG.

Table 6.1 shows the typical resonance positions, trap frequencies and laser powers for the traps used in the measurements in the main text. The trap frequencies are determined by observing oscillations of the atomic clouds. We observe variations in

the FR centers of less than 1.5 mG and trap frequencies of less than 4% over weeks of measurement time, which we ascribe to variations of the 1064 nm trapping-laser power and drifts of the relative beam positions. We account for these variations in the data analysis.

6.6.4 Determination of the Li Atom Number

An accurate determination of the number N_{Li} of Li atoms in our experiment and the corresponding Fermi energy is an important, non-trivial task. Here we present four different methods to determine the number of Li atoms with an error of less than 10%.

6.6.4.1 Absorption Imaging on a Nearly Closed Transition

One method for determining the number of atoms is absorption imaging. In this method, the spatial dependence of the fraction A of the light absorbed by the atomic cloud is recorded using a camera and used to obtain a measure of the atom number

$$N_I = -\frac{2\pi}{3\lambda^2}\left(\frac{u}{M}\right)^2 \sum_{X,Y} \ln\left[1 - A\left(X,Y\right)\right] \ ,$$

where λ is the light wavelength, M is the magnification of the imaging system, u is the camera pixel size, and $A\left(X,Y\right)$ is the absorbed light fraction as measured by the camera with X and Y the camera pixel indices. If atoms at rest are imaged using a weak light pulse that resonantly excites a closed atomic transition, N_I will be equal to the true atom number. In this section, we will present reference experimental conditions that approximate this situation and use these conditions to obtain a measure $N_I^{\mathrm{high-B}}$ that is close to the Li atom number N_{Li}. We will then discuss the remaining systematic effects and thereby relate $N_I^{\mathrm{high-B}}$ to N_{Li}.

We approximate a closed transition by imaging Li atoms in the second-lowest Zeeman state ($\mathrm{Li}|2\rangle$, $m_J = -1/2$, $m_I = 0$) using σ^- light near $\lambda = 671$ nm that resonantly excites them to the second-lowest Zeeman state of the $^2\mathrm{P}_{3/2}$ manifold ($\mathrm{Li}\left|2'\right\rangle$, $m_J = -3/2$, $m_I = 0$) at the magnetic field of 1150 G. The dominant branching from this transition is due to the spontaneous decay of $\mathrm{Li}\left|2'\right\rangle$ to the $\mathrm{Li}|4\rangle$ ($m_J = 1/2$, $m_I = -1$) state. We calculate the corresponding branching ratio as 0.12% using the dipole selection rules and the expression of the relevant states in the $\left(m_J, m_I\right)$ basis. Under our imaging conditions, the other branching ratios are more than 100 times smaller.

We record the images of the atoms using a back-illuminated CCD camera (Andor DV-434) with a pixel size of $u = 11\ \mu$m. We determine the magnification $M = 2.93\,(5)$

of our imaging system by imaging the interference pattern formed by two 671-nm laser beams intersecting at an angle of 29.0 (4) mrad at the location of the atoms onto our camera.

We check the purity of the polarization of the imaging light by imaging an optically dense Li cloud. We obtain optical depths greater than 3, corresponding to a sum of the intensities of the unabsorbed σ^+ and π light components that is less than 5% of the intensity of the σ^- imaging light. We minimize the effect of the polarization errors by ensuring that the maximal optical depth of the imaged cloud is smaller than 0.4, implying a relative error in the determined atom number of less than 6%.

We minimize saturation effects by using a low light intensity $I \approx 0.05\, I_s$, where $I_s = 2.5$ mW/cm^2 is the saturation intensity of the Li D2 transition.

While mechanical effects exerted by light on atoms form the basis of laser cooling, the effect of these forces on absorption imaging of atoms is usually neglected. However, for light atoms, this effect can be significant. For Li, the scattering of a single photon of the 671-nm imaging light imparts a momentum $\hbar\, k_L = 2\pi\, \hbar/\lambda$ to the atom, leading to a Doppler shift of the imaging transition by $\delta_{\rm rec} = \hbar\, k_L^2/m_{\rm Li} = 0.025\, \Gamma_{\rm D2}$, where $\Gamma_{\rm D2} = 36.897\ \mu{\rm s}^{-1}$ is the spontaneous emission rate from the Li $^2P_{3/2}$ state [McA96]. For imaging Li atoms, we choose a reference set of conditions. The imaging pulse duration is set to 18 μs, the light intensity to $I \approx 0.05\, I_s$ and the detuning δ_0 is adjusted to obtain the maximal value of N_I. Under these conditions, we expect the radiation pressure to lead to a mean laser detuning during the imaging pulse that is smaller than $0.1\, \Gamma_{\rm D2}$, corresponding to a small effect on the measured atomic absorption.

We experimentally investigate the mechanical effects of the light on the atoms by varying the laser detuning δ and the duration of the imaging pulse. Fig. 6.9 shows the number N_I as a function of the duration t of the imaging pulse for different laser detunings. The red, orange, green and cyan points correspond to $\left(\delta_0 - \delta\right)/(2\pi) =$ 9 MHz, 7 MHz, 5 MHz and 3 MHz, respectively. The single blue point corresponds to the reference imaging conditions.

For pulse durations that are significantly longer than our reference pulse duration, we observe a large effect of the radiation pressure. We model this effect by the following set of differential equations:

$$\begin{aligned} \frac{dN_\gamma}{dt} &= \frac{\Gamma_{\rm D2}}{2}\frac{s}{1+s+\delta^2/(\Gamma/2)^2}\,\eta\ , \\ \frac{d\eta}{dt} &= -(1-r)\,\frac{dN_\gamma}{dt}\,\eta\ , \\ \frac{d\delta}{dt} &= \delta_{\rm rec}\,\frac{dN_\gamma}{dt}\ , \end{aligned} \tag{6.5}$$

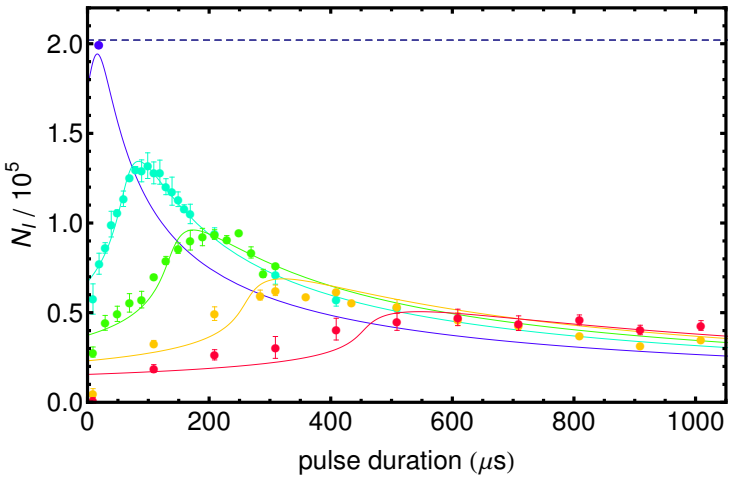

Figure 6.9: Li atom number determined by absorption imaging in the presence of a magnetic field of 1150 G as a function of the duration of the imaging light pulse. The lines show a multivariate fit to the model of Eq. (6.6). The dashed line indicates the Li atom number that would be obtained using a weak resonant light pulse.

where $s = I/I_s$, the parameter r is the branching ratio to the Li$|2\rangle$ state, and N_γ is the mean number of photons scattered per atom, and η is the fraction of atoms remaining in the nearly closed two-level system. The time $t = 0$ corresponds to the start of the imaging pulse, with $\eta(0) = 1$.

In the limit of $r = 1$ and small s, these equations can be solved by separation of variables to yield:

$$\begin{aligned} \delta(t) &= \frac{\Gamma_{D2}}{2} g\left(\delta_{\rm rec}\, s\, t\right) , \\ N_\gamma(t) &= \left[g\left(\delta_{\rm rec}\, s\, t\right) - g(0)\right] / \left(\frac{\delta_{\rm rec}}{\Gamma_{D2}/2}\right) , \end{aligned}$$

where $g(u)$ satisfies

$$\frac{g(u)^2 - g(0)^2}{2} + \frac{g(u)^4 - g(0)^4}{4} = u$$

with $g(0) = 2\delta(0)/\Gamma$. The number N_I is be proportional to the mean number of

photons scattered per unit time N_γ/t. Therefore, we write

$$N_I \quad = \quad N_I^0 \left[g\left(\delta_{\mathrm{rec}} st\right) - g\left(0\right) \right] / \left(\delta_{\mathrm{rec}} st\right) \ , \tag{6.6}$$

where N_I^0 is the value of N_I determined in the limit of a weak, resonant light pulse.

We fit the model of Eq. (6.6) to the data from Fig. 6.9 with δ_0, N_I^0 and s as free parameters and obtain $\delta_0 = -2\pi\times 1.2\,(1)\,\mathrm{MHz}$, $s = 0.043\,(2)$, and $N_I^0 = 2.02\,(4)\times 10^5$. The fitted value of N_I^0 is indicated by the dashed line in the Fig. 6.9.

The above model implies that, under the reference conditions, $\delta_0/2\pi = -1\,\mathrm{MHz}$ and $N_I^{\mathrm{high-B}}/N_I^0 = 0.96\,(1)$, with each atom scattering a mean number of 12 photons during the imaging pulse. Using Eq. (6.5) to include the effects of saturation and branching ratio, we obtain a relation between $N_I^{\mathrm{high-B}}$ and the true Li atom number N_{Li} as $N_I^{\mathrm{high-B}} = 0.91\,(2)\,N_{\mathrm{Li}}$. Including the effects of the imperfect light polarization and the uncertainty in the magnification, we obtain $N_I^{\mathrm{high-B}} = 0.89\,(5)\ N_{\mathrm{Li}}$.

6.6.4.2 Fitting of Li Fermi profiles

Another method to determine the Li atom number is to image a degenerate Li atom cloud after releasing the atoms from a trap. In the zero-temperature limit, the spatial extent of the imaged cloud is determined by the trap frequencies, the time elapsed after release from the trap and the atom number.

To account for the finite temperature of the Li atoms in our experiment, we use a non-degenerate sample of K atoms to measure the temperature of the Li atoms. We prepare a mixed sample of approximately 2.5×10^5 Li$|2\rangle$ atoms and 2×10^4 K$|1\rangle$ atoms at 1150 G in a deep crossed-dipole trap with frequencies $f_r^{\mathrm{K}} = 408\,(1)\,\mathrm{Hz}$, $f_r^{\mathrm{Li}} = 649\,(3)\,\mathrm{Hz}$, $f_z^{\mathrm{K}} = 56.1\,(4)\,\mathrm{Hz}$, $f_z^{\mathrm{Li}} = 89.1\,(2)\,\mathrm{Hz}$. After waiting 0.5 s for the Li and K to thermalize, we release the atoms from the trap. By imaging the non-degenerate K cloud after 5.5 ms time of flight, we determine the temperature of the atoms to be $T = 370\,(15)\,\mathrm{nK}$.

We image the Li atoms after t_{TOF}=2.5 ms time of flight using the reference imaging pulse described in Sec. 6.6.4.1. By averaging 45 absorption images, we obtain the image shown in Fig. 6.10. We fit the obtained absorption data to a function of the form $A + e^{-\sigma n_{2\mathrm{D}}}$, where

$$n_{2\mathrm{D}} = -\frac{k_{\mathrm{B}}^2\, m_{\mathrm{Li}}\, T^2}{4\pi^2\,\hbar^3\, f_r^{\mathrm{Li}}}\,\mathrm{Li}_2\left(-q\,\exp\left(-\frac{m_{\mathrm{Li}}\,u^2\,\left(X-X_0\right)^2}{2\,\chi_r\,M^2\,k_{\mathrm{B}}\,T} - \frac{m_{\mathrm{Li}}\,u^2\,\left(Z-Z_0\right)^2}{2\,\chi_z\,M^2\,k_{\mathrm{B}}\,T}\right)\right)$$

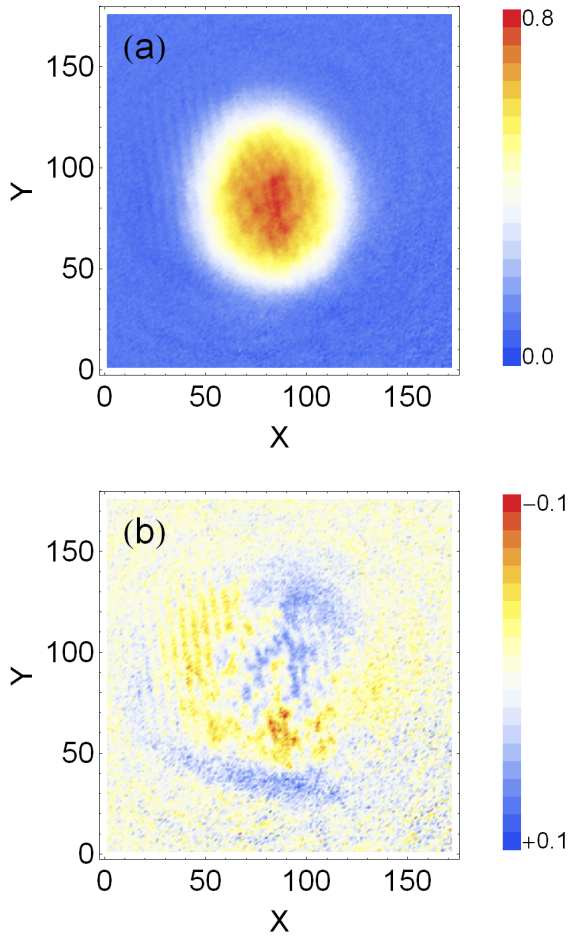

Figure 6.10: Fraction of the imaging light absorbed by a Li atomic cloud after release from an optical trap (a), together with residuals of a fit to the data (b).

is the 2D Fermi atom density profile with Li the polylogarithm function and $\chi_{r,z} = \sqrt{1 + \left(2\pi\, f_{r,z}^{\mathrm{Li}}\, t_{\mathrm{TOF}}\right)^2}$. The fit parameter A accounts for technical offsets in the absorption data while X_0 and Y_0 fit the location of the cloud center on the camera image. The fit parameters q and σ correspond to the atoms' fugacity and the light absorption cross-section. The fit residual is shown in Fig. 6.10(b). Taking into accounts the uncertainties in the magnification, the temperature and the trap frequencies, we obtain $\sigma = 0.82\,(9) \times 6\,\pi/k_L^2$, corresponding to $N_I^{\mathrm{high-B}} = 0.82\,(9)\ N_{\mathrm{Li}}$.

6.6.4.3 LiK Molecule Dissociation and K Number Determination

Another method to determine the Li atom number is to associate LiK Feshbach molecules and to compare the number of K and Li atoms after dissociating the molecules. The advantage of this method is that the K atoms can be imaged on a closed transition and that, being 6.6 times heavier than the Li atoms, the K atoms are much less affected by the radiation pressure of the imaging light.

We associate the Li$|1\rangle$K$|3\rangle$ molecules by a magnetic ramp across the FR and then thoroughly clean our trapped sample from any remaining free Li and K atoms by a combination of radio-frequency and laser light pulses; see [Jag14] for details. The obtained molecule samples are essentially pure, consisting of approximately 1.5×10^4 molecules and less than 300 remaining free Li and K atoms.

We subsequently dissociate the molecules by an inverse ramp across the FR and determine the number of free Li$|1\rangle$ and K$|3\rangle$ atoms via absorption imaging at a magnetic field near 154.7 G. For imaging the Li$|1\rangle$ atoms, we use the parameters from Sec. 6.6.5. We convert the atom number $N_I^{\mathrm{low-B}}$ determined using these parameters to the number $N_I^{\mathrm{high-B}}$ of Li atoms obtained by absorption imaging at 1150 G using the imaging ratios from Sec. 6.6.5.

We relate the number of atoms determined by absorption imaging of K$|3\rangle$ atoms near 154.7 G to the true K atom number in two steps. First, we transfer an independent sample of K atoms from the state K$|1\rangle$ to the state K$|3\rangle$ using two consecutive resonant rf pulses. Imaging these atoms before and after the transfer allows us to relate the number of K$|3\rangle$ atoms determined by absorption imaging after molecule dissociation to the number $N_{I,\mathrm{K}}^{\mathrm{low-B}}$ of K$|1\rangle$ atoms that would be measured by absorption imaging near 154.7 G. In the second step, using a similar procedure to the one described in Sec. 6.6.5, we compare $N_{I,\mathrm{K}}^{\mathrm{low-B}}$ to the number $N_{I,\mathrm{K}}^{\mathrm{high-B}}$ of K$|1\rangle$ atoms determined by absorption imaging at 1150 G using a weak laser-light pulse. We then find for the relative atom number of K and Li determined at 1150 G: $N_I^{\mathrm{high-B}} = 0.92(5)\, N_{I,\mathrm{K}}^{\mathrm{high-B}}$.

Accounting for the saturation of the K imaging light ($s \approx 0.05$) and the errors in the light polarization and the magnification of the K imaging system, we can relate $N_{I,\mathrm{K}}^{\mathrm{high-B}}$ to the true K atom number as $N_{I,\mathrm{K}}^{\mathrm{high-B}} = 0.92\,(5)\ N_{\mathrm{K}}$.

Finally, assuming the real numbers of K and Li atoms after dissociation to be equal, we obtain $N_I^{\mathrm{high-B}} = 0.85\,(7)\ N_{\mathrm{Li}}$.

6.6.4.4 Measurement of rf Shifts

A different method to determine the Li number is to use rf spectroscopy to measure the interaction energy of the K atoms with the Li cloud. By comparing the measured data to the predictions of a dressed quasiparticle model [Mas12] with accurately determined parameters of the FR, one can determine the mean Fermi energy of Li sampled by the K atoms. From the knowledge of the Li temperature and trap frequencies, one can then determine the Li atom number.

We prepare a sample of about $2.7{\times}10^5$ Li atoms and $2{\times}10^4$ K atoms at the temperature of $T = 290\,(15)$ nK in a crossed-beam optical dipole trap with trap frequencies $f_r^{\mathrm{K}} = 395\,(2)$ Hz, $f_r^{\mathrm{Li}} = 632\,(3)$ Hz, $f_z^{\mathrm{K}} = 50.0\,(5)$ Hz, $f_z^{\mathrm{Li}} = 80\,(1)$ Hz. We use a Blackman-shaped rf π-pulse to transfer the K atoms from the K$|2\rangle$ to the K$|3\rangle$ state at various magnetic fields B near the 154.7 G Li$|1\rangle$-K$|3\rangle$ Feshbach resonance. We compare the rf frequency at which we obtain maximal transfer of the K atoms when the Li atoms are in the Li$|1\rangle$ state (f) to the frequency for maximum transfer with the Li atoms in the Li$|2\rangle$ state (f_0).

Fig. 6.11 shows the frequency difference $f - f_0$ as a function of the magnetic field near 154.7 G. We verify that f_0 remains unchanged in the absence of the Li atoms. Therefore, $h\left(f - f_0\right)$ corresponds to the difference $E_3 - E_2$ of the mean interaction energies of the K atoms in the K$|3\rangle$ and K$|2\rangle$ states with Li atoms in the Li$|1\rangle$ state.

We assume a uniform distribution of the Li atoms across the K cloud and use the mean Li Fermi energy $\epsilon_{\mathrm{F}} = \hbar^2\,\kappa_{\mathrm{F}}^2/2\,m_{\mathrm{Li}}$ sampled by the K atoms as a free parameter. We calculate the interaction energy E_3 between the K$|3\rangle$ atoms and Li$|1\rangle$ atoms from a two-channel polaron model [Mas12] with the resonance parameters determined in Sec. 6.6.2: $a_{\mathrm{bg}} = 63.0\,a_0$, $r_{\mathrm{eff}} = -5175\,a_0$, $\Delta B = 0.880$ G . Since the interaction between the K$|2\rangle$ atoms and Li$|1\rangle$ atoms is weak, we may approximate E_2 by the mean-field expression $E_2 = 2\pi\,a_{\mathrm{bg}}\,\hbar^2\,\kappa_{\mathrm{F}}^3/\left(6\,\pi^2\right)$, where $a_{21} = 63\,a_0$ is the K$|2\rangle$-Li$|1\rangle$ scattering length [Nai11]. We use the position B_0 of the Feshbach resonance as the second free parameter. By fitting the above model to our data, we find $\epsilon_{\mathrm{F}} = h{\times}31.8\,(4)$, $B_0 = 154.715\,(1)$ G.

From the knowledge of the trap frequencies and the Li atom temperature, we can use ϵ_{F} to determine the Li atom number as $N_{\mathrm{Li}} = 275\,(15) \times 10^3$. Simultaneous with the above measurements, we record the number of Li atoms $N_I^{\mathrm{low-B}}$ determined using

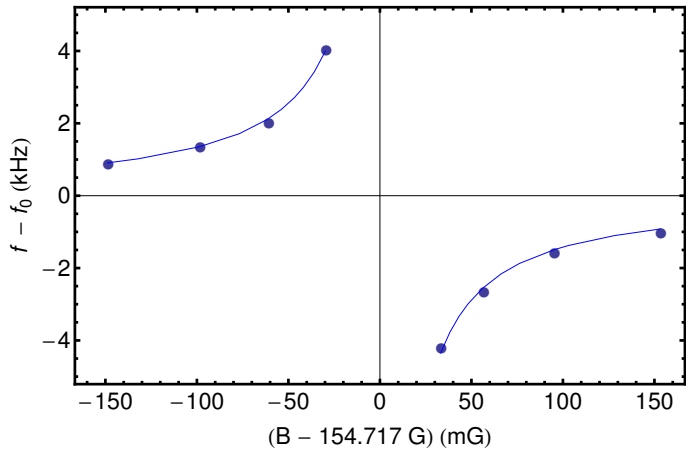

Figure 6.11: The measured shifts of the K$|2\rangle \rightarrow$K$|3\rangle$ rf transition frequency due to the presence of Li$|1\rangle$ atoms as a function of the magnetic field (dots) together with a fit using a quasiparticle model (see text).

absorption imaging near 154.7 G as described in the Sec. 6.6.5. We use the conversion between $N_I^{\text{low-B}}$ and $N_I^{\text{high-B}}$ described in the same section to find $N_I^{\text{high-B}} = 0.91\,(7)\ N_{\text{Li}}$.

6.6.4.5 Determination of Li Atom Number: Summary

We summarize the results of our measurements of the Li atom number by the obtained ratios $N_I^{\text{low-B}}/N_{\text{Li}}$. These ratios are subject to errors that are largely uncorrelated between the different methods, with the notable exception of the error in the determination of the magnification of the imaging system. To obtain the best estimate for the ratio $N_I^{\text{high-B}}/N_{\text{Li}}$, we fix the magnification to a certain value M_0 and calculate the mean $\mu\left(M_0\right)$ and variance $V\left(M_0\right)$ of the four results weighted by their inverse uncorrelated variances. We repeat the same procedure with M_0 sampled from a normal distribution whose mean and variance correspond to our experimental determination of M. We add the variance of μ due to the variation in M_0 to V to obtain:

$$N_I^{\text{low-B}}/N_{\text{Li}} = 0.86\,(5)\ .$$

In the main text, we use a more conservative error estimate of 16% for the relative uncertainty in the Li atom number determination. This corresponds to a relative

uncertainty in the Fermi energy of 6%.

6.6.5 Absorption Imaging Near 154.7 G

We commonly determine the Li atom number near the Li$|1\rangle$-K$|3\rangle$ FR at 154.7 G. We do this by absorption imaging of Li$|1\rangle$ atoms using σ^- light on the Li$|1\rangle$ ($m_I = 1$, $m_J = -1/2$)$\rightarrow$ Li$|3'\rangle$ ($m_I = 1$, $m_J = -3/2$) transition. The dominant loss channel for this imaging transition is the spontaneous decay from the Li$|3'\rangle$ state to the Li$|5\rangle$ ($m_I = 0$, $m_J = +1/2$) state. We calculate the corresponding branching ratio as 4% using the method from Sec. 6.6.4.1. The other loss processes are at least three orders of magnitude less probable. We use an 8-μs long imaging pulse whose intensity corresponds to $s = 0.26$ and whose frequency is adjusted to obtain the maximal value of N_I.

We calibrate this imaging method relative to the imaging of Li atoms in the $|2\rangle$ state at the magnetic field of 1150 G as follows. We first prepare a Li$|2\rangle$ sample at the field of 1150 G and image it as described above. Then, in a separate experiment, we ramp the magnetic field to 154.7 G, followed by a ramp back to 1150 G. We verify that these ramps lead to the loss of less than 5% of the atoms. In the third experiment, we execute only the first field ramp and then use rapid adiabatic passage to transfer the Li atoms into the Li$|1\rangle$ state with efficiency larger than 98%. We image these atoms as described above to obtain the atom number $N_I^{\mathrm{low-B}}$. We use the relationship between $N_I^{\mathrm{low-B}}$ and the average of the atom numbers recorded at the magnetic field of 1150 G with and without the double field ramp to determine $N_I^{\mathrm{high-B}} = 2.4\,(1)\ N_I^{\mathrm{low-B}}$.

6.6.6 Heating Due to Molecule Formation

As explained in the main text, on the repulsive side of the FR, the K atoms can pair with Li atoms to form molecules. By removing Li atoms from the Fermi sea and releasing energy, this pairing process leads to heating with a corresponding increase in $k_{\mathrm{B}}\,T/\epsilon_{\mathrm{F}}$.

To estimate the effects of this decay to molecules, we approximate our system by a uniform system with Li and K densities $\bar{n}_{\mathrm{Li}}$ and $\bar{n}_{\mathrm{K}}$, respectively. Before the impurity atoms are transferred into the interacting state, the system is in thermal equilibrium and we may write the number and energy densities of the Li atoms as

$$\bar{n}_{\mathrm{Li}} \;=\; -f_{3/2}\left(-q_0\right)/\lambda_{\mathrm{dB}}^3 \tag{6.7}$$

and

$$u_{\mathrm{Li}} \;=\; -f_{5/2}\left(-q_0\right)\times\frac{3}{2}\,\frac{k_{\mathrm{B}}\,T_0}{\lambda_{\mathrm{dB}}^3}\ , \tag{6.8}$$

where q_0 and T_0 are the fugacity and the temperature of the Li atoms before the start of the experiment, $\lambda_{\mathrm{dB}} = \left(2\,\pi\,\hbar^2/m\,k_{\mathrm{B}}\,T_0\right)^{1/2}$ is the thermal de Broglie wavelength of the Li atoms and $f_{3/2}$ i.e. $f_{5/2}$ are the polylogarithm functions [Hua87]. The Fermi energy ϵ_{F} of the Li atoms is related to $\bar{n}_{\mathrm{Li}}$ as

$$\epsilon_{\mathrm{F}} = \frac{\hbar^2}{2\,m_{\mathrm{Li}}}\left(6\,\pi^2\,\bar{n}_{\mathrm{Li}}\right)^{2/3} \tag{6.9}$$

and to the fugacity as

$$\frac{k_{\mathrm{B}}\,T}{\epsilon_{\mathrm{F}}} = \left[\frac{4}{3\,\sqrt{\pi}}\frac{-1}{f_{3/2}\left(-q_0\right)}\right]^{2/3} . \tag{6.10}$$

The heating due to molecule formation progresses during the interaction time. To estimate the effect of this heating on our measurements of the decoherence rate, we choose a typical interraction time $\tau_D = \gamma_{\mathrm{coh}}^{-1}$. We also assume that each decay event removes a single Li atom from the Fermi sea. We also assume that only 50% of the K atoms participate in the decay since the other 50% are in the non-interacting state during the echo sequence. This implies that the fraction $l = \Gamma\,\tau_D\,\bar{n}_{\mathrm{K}}/2\,\bar{n}_{\mathrm{Li}}$ of the Li atoms will be converted to molecules. As the decay rate Γ, we take the sum of the two-body and three-body decay rates from [Koh12].

We further assume that each decay to molecules releases energy $\alpha\,E_{\mathrm{F}}$ equal to the difference between the repulsive polaron energy and the middle of the molecule-hole continuum from [Koh12]. Since the Li is much lighter than LiK, we assume that the full energy released to the decay is delivered to the Li sea. Finally, we assume that remaining Li atoms thermalize with each other.

Under these conditions, we may express the number density $\bar{n}'_{\mathrm{Li}}$, the energy density u'_{Li} and the Fermi energy ϵ'_{F} of the Li atoms during the experiment as:

$$\begin{aligned}
\bar{n}'_{\mathrm{Li}} &= (1-l)\,\bar{n}_{\mathrm{Li}} , \\
u'_{\mathrm{Li}} &= (1-l)\,u_{\mathrm{Li}} + l\,\alpha\,n_{\mathrm{Li}}\,\epsilon_{F,0} , \\
\epsilon'_{\mathrm{F}} &= \epsilon_{\mathrm{F}}\,(1-l)^{2/3} .
\end{aligned}$$

Using Eqns. (6.7-6.10), we obtain

$$\begin{aligned}
-f_{3/2}\left(-q_1\right)\left(T_1/T_0\right)^{3/2} &= -(1-l)\,f_{3/2}\left(-q_0\right) , \\
-f_{5/2}\left(-q_1\right)\left(T_1/T_0\right)^{5/2} &= -(1-l)\,f_{5/2}\left(-q_0\right) + l\left[-f_{5/2}\left(-q_0\right)\right]^{5/3}(\pi/6)^{1/3}\,\alpha ,
\end{aligned}$$

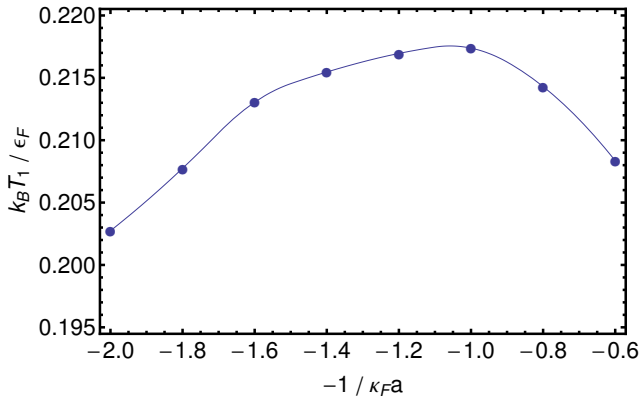

Figure 6.12: The predicted degeneracy parameter of the Li atoms during the echo sequence computed for $k_B T_0/\epsilon_F = 0.16$, $\bar{n}_K/\bar{n}_{Li} = 0.27$ and the typical interaction time τ_D, as a function of the interaction parameter. The line shows a second-order interpolation between the data points.

where q_1 and T_1 are the average fugacity and temperature of the Li atoms during the experiment. Using Eq. (6.9), we can then obtain the average degeneracy parameter $k_B T_1/\epsilon'_F$.

Fig. 6.12 shows the predicted typical degeneracy parameter $k_B T_1/\epsilon'_F$ of the Li atoms in the spin-echo measurements as a function of the interaction parameter, for the parameters from Fig. 6.3 of the main text.

6

CHAPTER 7

Ultrafast Many-body Interferometry of Impurities Coupled to a Fermi Sea

Published as:
M. Cetina, M. Jag, R. S. Lous, I. Fritsche, J. T.Walraven, R. Grimm,
J. Levinsen, M. Parish, R. Schmidt, M. Knap, E. Demler
Science **354**, 96 (2016)

Author contribution
The author contributed to the general lab work, the measurements of data, the development of the experimental method, the interpretation and analysis of the data, the discussion with our theory collaborators, and the writing of the manuscript.

Note
More details on the two theoretical models discussed in this Chapter can be found in Refs. [Par16, Liu18] (truncated basis method/variational approach) and [Sch18] (functional determinant approach). For briefness, this Chapter includes only the experimental data of the supplementary text. The supplementary text that focuses on the details of the theoretical modeling of the experimental observations, including an outlook on the orthogonality catastrophe, can be found on *Science* online.

CHAPTER 8

Observation of a Strong Atom-Dimer Attraction in a Mass-Imbalanced Fermi-Fermi Mixture

Published as:
M. Jag, M. Zaccanti, M. Cetina, R. S. Lous, F. Schreck, R. Grimm, D. S. Petrov, and J. Levinsen
Phys. Rev. Lett. **112**, 075302 (2014)

Author contribution
The author joined these experiments midway and participated in the last measurements as well as in the analysis and discussion of the data, and the writing of the manuscript.

We investigate a mixture of ultracold fermionic ^{40}K atoms and weakly bound ^{6}Li-^{40}K dimers on the repulsive side of a heteronuclear atomic Feshbach resonance. By radio-frequency spectroscopy we demonstrate that the normally repulsive atom-dimer interaction is turned into a strong attraction. The phenomenon can be understood as a three-body effect in which two heavy ^{40}K fermions exchange the light ^{6}Li atom, leading to attraction in odd partial-wave channels (mainly p wave). Our observations show that mass imbalance in a fermionic system can profoundly change the character of interactions as compared to the well-established mass-balanced case.

8.1 Introduction

Ultracold fermions with tunable interactions provide remarkable possibilities to model the many-body physics of strongly interacting states of quantum matter under well-controllable conditions [Gio08, Blo08]. Fermionic superfluids, realized by combining two different spin states of a fermionic atomic species and controlling their s-wave interaction through a Feshbach resonance [Chi10], have led to spectacular achievements. Beyond these experimentally well-established fermionic systems, mass imbalance offers an additional degree of freedom, with interesting prospects for new many-body phenomena having no counterpart in the mass-balanced case, such as novel quantum phases or superfluid states in various trapping environments [Isk06, Bau09c, Gez09, Key11, Sot12, Cui13, Gub09, Mat11, Qi12, Dai12, Pet07, Bar08, SC91, Ors10, Dal12, Nis08, Nis09b].

Striking effects of mass imbalance in fermionic systems already emerge at the few-body level. A resonantly interacting three-body system of one light (↓) and two heavy (↑) fermions is known to exhibit bound states depending on the mass ratio $m_\uparrow/m_\downarrow$. While Efimov trimer states require large mass ratios ($m_\uparrow/m_\downarrow > 13.6$), for repulsive interactions, non-Efimovian trimer states can exist in an intermediate regime ($13.6 > m_\uparrow/m_\downarrow > 8.17$) [Kar07]. Below the critical value of 8.17, the last state turns into an atom-dimer scattering resonance in the p-wave channel [Kar07].

The ^{40}K-^{6}Li mixture serves as the prime system for current experiments on tunable mass-imbalanced Fermi-Fermi mixtures [Wil08, Cos10, Tre11]. The corresponding mass ratio of $m_\uparrow/m_\downarrow \approx 6.64$ lies well in the regime of near-resonant atom-dimer interactions [Lev09, Lev11]: as the most prominent effect, theory predicts a substantial attraction resulting from higher partial waves (mainly p wave) in a regime where one would naively, based on s waves alone, expect a strong repulsion. This also makes the corresponding many-body problem in a ^{40}K-^{6}Li mixture significantly more com-

plicated and much richer than in the widely investigated mass-balanced case.

In this Letter, we investigate the interaction between ^{40}K atoms and weakly bound ^{6}Li-^{40}K dimers near an interspecies Feshbach resonance (FR). We employ radio-frequency (rf) spectroscopy by using two different internal states of ^{40}K, one strongly interacting with the dimers and the other one practically noninteracting [Koh12]. We observe line shifts and collisional broadening and interpret these in terms of the real and imaginary part of the forward-scattering amplitude $f(0)$ for atom-dimer collisions, calculated on the basis of the theoretical approach of Ref. [Lev11]. The comparison between theory and experiment shows excellent agreement and, in particular, demonstrates the predicted atom-dimer attraction on the repulsive side of the interspecies FR.

The interaction of a heavy atom with a heavy-light dimer can be understood in the Born-Oppenheimer approximation, where the atom-dimer potentials are taken to be the eigenenergies of the light atom for a given separation R between the heavy ones. As in the usual double-well problem with tunneling, the state localized near one heavy atom is mixed with the state localized near the other; the symmetric and antisymmetric superpositions lead to the attractive $U_+(R) < 0$ and repulsive $U_-(R) > 0$ potentials, respectively. Note the analogy to the well-known H_2^+ cation, where the exchange of the electron leads to a symmetric bound state and an antisymmetric unbound state [Pau28]. In our experiment, the heavy particles are identical fermions, making the atom-dimer interaction channel dependent. The symmetric (antisymmetric) state corresponds to odd (even) values of the total angular momentum l [Lev11]. In Fig. 8.1(a) we plot the total effective potentials $U_\pm + U_{\rm cb}$ (solid lines) and the bare centrifugal barriers $U_{\rm cb} = l(l+1)\hbar^2/m_\uparrow R^2$ (dashed lines) for $l = 0$, 1, and 2 (i.e., s-, p-, and d-wave channels) for typical experimental conditions. At distances on the order of typical de Broglie wavelength, $U_\pm$ can be comparable to $U_{\rm cb}$ and we expect significant interaction effects in nonzero partial waves.

8.2 Theory

The relevant quantity that characterizes the net effect of all partial waves is the atom-dimer forward scattering amplitude [Sob72, Bar58b, Bar58a],

$$f(0) = \sum_{l=0}^{\infty}(2l+1)\left[\frac{\sin 2\delta_l(k_{\rm coll})}{2k_{\rm coll}} + i\frac{\sin^2\delta_l(k_{\rm coll})}{k_{\rm coll}}\right], \tag{8.1}$$

where $k_{\rm coll} = \sqrt{2\mu_3 E_{\rm coll}}/\hbar$ is the wave number associated with the relative atom-dimer motion and μ_3 is the reduced atom-dimer mass. The phase shifts δ_l for the three

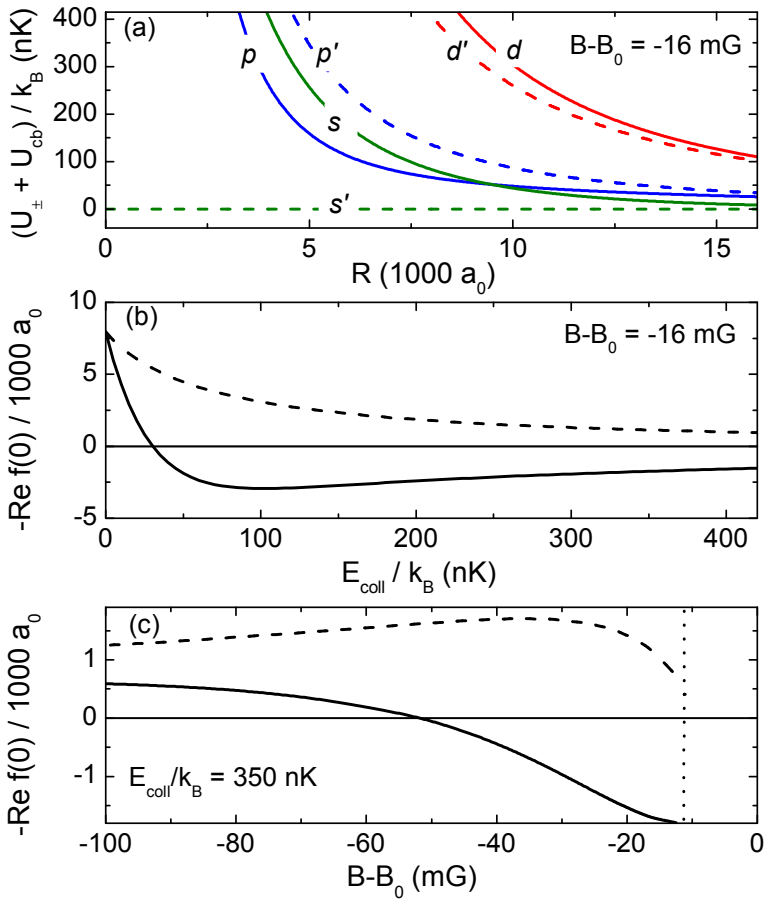

Figure 8.1: Interaction between ^{40}K atoms and ^{6}Li-^{40}K dimers near the 155 G interspecies FR. (a) Total interaction potentials as a function of the distance R between the two K atoms for the s, p, and d channels (dashed curves with labels s', p', d' refer to the unmodified centrifugal barriers). Here we have chosen a magnetic detuning of $B - B_0 = -16\,\mathrm{mG}$, corresponding to an s-wave scattering length of $a = 3528\,a_0$ and to a dimer binding energy of $E_\mathrm{b}/k_\mathrm{B} = 600\,\mathrm{nK}$. (b) Real part of the forward-scattering amplitude $f(0)$ as a function of the collision energy E_coll (solid line) in comparison with the s-wave contribution (dashed line). (c) Same as in (b), but as a function of the magnetic detuning $B - B_0$ for a fixed collision energy $E_\mathrm{coll}/k_\mathrm{B} = 350\,\mathrm{nK}$. The dotted line indicates the dimer breakup threshold, $E_\mathrm{coll} = E_\mathrm{b}$.

lowest partial waves have been computed in Ref. [Lev11], and here, we extend the result to higher ones since they give significant contributions (see Sec. 8.6). In Fig. 8.1(b) we show the resulting $-\mathrm{Re}\, f(0)$ as a function of the collision energy E_{coll} for the same conditions as in Fig. 8.1(a). In the limit of $E_{\mathrm{coll}} \to 0$, the quantity $-\mathrm{Re}\, f(0)$ corresponds to the atom-dimer s-wave scattering length. At $E_{\mathrm{coll}} \ll 0.1 E_{\mathrm{b}}$, with E_{b} being the dimer binding energy, s-wave scattering (dashed line) dominates and the net interaction is repulsive, $-\mathrm{Re}\, f(0) > 0$.

For $E_{\mathrm{coll}} \gtrsim 0.1 E_{\mathrm{b}}$, higher partial-wave contributions lead to a sign reversal of $\mathrm{Re}\, f(0)$, changing the character of the interaction from repulsive into attractive. This sign reversal also appears if, at a fixed collision energy, the magnetic detuning from the FR center is varied, see Fig. 8.1(c). In the realistic example of Fig. 8.1(c) the sign reversal takes place at a magnetic detuning of $B - B_0 = -53\,\mathrm{mG}$, where the binding energy is $E_{\mathrm{b}}/k_{\mathrm{B}} \approx 3.1\,\mu\mathrm{K}$, corresponding to roughly ten times the collision energy $E_{\mathrm{coll}}/k_{\mathrm{B}} = 350\,\mathrm{nK}$. The theory lines in Fig. 8.1(c) stop close to the FR center at the magnetic field detuning where $|E_{\mathrm{b}}| = E_{\mathrm{coll}}$ (dotted line), beyond which the inelastic channel of collisional dimer dissociation opens up.

8.3 Experimental Preparation and Method

The starting point of our experiments is an optically trapped, near-degenerate Fermi-Fermi mixture of typically 4×10^4 ^{40}K atoms and 1×10^5 ^{6}Li atoms. The preparation procedures are described in our previous work [Spi10, Tre11]. We choose a particular FR that occurs between Li atoms in the lowest Zeeman sublevel Li$|1\rangle$ ($f = 1/2, m_f = +1/2$) and K atoms in the third-to-lowest sublevel K$|3\rangle$ ($f = 9/2, m_f = -5/2$) [Nai11]. The s-wave interspecies scattering length a can be magnetically tuned as $a = a_{\mathrm{bg}}[1 - \Delta/(B - B_0)]$ with $a_{\mathrm{bg}} = 63.0\,a_0$ (a_0 is Bohr's radius) and $\Delta = 880\,\mathrm{mG}$ [Nai11]. The resonance is rather narrow, as characterized by the length parameter $R^* = 2700\,a_0$ [Pet04a]. The position of the FR center near $B \approx 154.7\,\mathrm{G}$ depends on the trap setting, as it includes small shifts induced by the trapping light. For each trap setting we have calibrated the FR center B_0 with $\leq 2\,\mathrm{mG}$ accuracy (see Sec. 8.6).

We create an atom-dimer mixture by a Feshbach ramp across the resonance and by subsequent purification and spin-manipulation techniques (see Sec. 8.6). While the dimers are formed in the Li$|1\rangle$-K$|3\rangle$ spin channel, we initially prepare the free atoms in the second-to-lowest spin state K$|2\rangle$ ($f = 9/2, m_f = -7/2$), for which the interaction with the dimers is negligible. The total number of dimers and atoms is $1.5{\times}10^4$ and $7{\times}10^3$, respectively. The interspecies attraction during the Feshbach ramp results in a collective oscillation of the dimer cloud, which we can take into account

by introducing an effective temperature T_{eff} (see Sec. 8.6). We use three different trap settings, for which $T_{\mathrm{eff}} = 165\,\mathrm{nK}$, 232 nK, and 370 nK. This corresponds to mean dimer densities as experienced by the atoms of $\bar{n}_{\mathrm{D}} = 5.2\times10^{11}\,\mathrm{cm}^{-3}$, $8.2\times10^{11}\,\mathrm{cm}^{-3}$, and $1.4\times10^{12}\,\mathrm{cm}^{-3}$, respectively.

To investigate the interaction between the K$|3\rangle$ atoms and the Li$|1\rangle$K$|3\rangle$ dimers, we carry out rf spectroscopy. This can be done in two different ways, either by driving the K atoms from the noninteracting state $|2\rangle$ into the interacting state $|3\rangle$ (method A) or vice versa (method B). With our K atoms initially prepared in the state $|2\rangle$, we carry out method A by applying a 1-ms rf pulse. For method B, we rapidly transfer the full K$|2\rangle$ population into K$|3\rangle$ using a short 90-μs preparation pulse without spectral resolution, and then drive the spectrally resolving transition with a 1-ms pulse. Our signal in both cases is the fraction of transferred atoms as a function of the rf detuning $\nu - \nu_0$ with respect to the unperturbed transition frequency ν_0, the latter being determined by the rf spectroscopy in the absence of dimers.

Sample spectra, at a magnetic detuning of $B - B_0 = -20\,\mathrm{mG}$, are shown in Fig. 8.2. The spectra recorded by methods A and B (circles and diamonds in Fig. 8.2) show both a broadening and a peak shift, as compared to the spectra recorded in the absence of dimers (triangles). Although the spectra very close to the FR center reveal asymmetries in their wings, which depend on the method applied, their peak shifts and broadenings are consistent for both methods. In the range of detunings $B - B_0$ studied in the present work the molecular dissociation signal is always well separated from the atomic line (inset of Fig. 8.2), and thus does not affect the line shape of the atomic signal.

8.4 Results and Discussion

Figure 8.3 shows the widths and peak shifts[1] of the rf spectroscopic signal, recorded by method A, as a function of $B - B_0$ for our three values of T_{eff}. When the FR center is approached, the spectrum broadens and its peak shifts from a positive to a negative rf detuning. With increasing temperature, the corresponding zero crossing shows a trend to move towards larger detunings.

We interpret the obtained results in the framework of the impact theory of pressure-induced effects on spectral lines, which assumes the collisions to be effectively instantaneous. This theory predicts Lorentzian profiles centered near the unperturbed frequency ν_0 whose line shifts and broadenings are proportional to the real and imaginary parts of the thermally averaged atom-dimer forward scattering amplitude $f(0)$ [Sob72, Bar58b, Bar58a], respectively. The real part of $f(0)$ shifts the energy of the K atoms,

[1] To determine the peak shift and the width, we apply a double-Gaussian fit to the spectra. From the fit, we identify the rf detuning of maximum signal and the width.

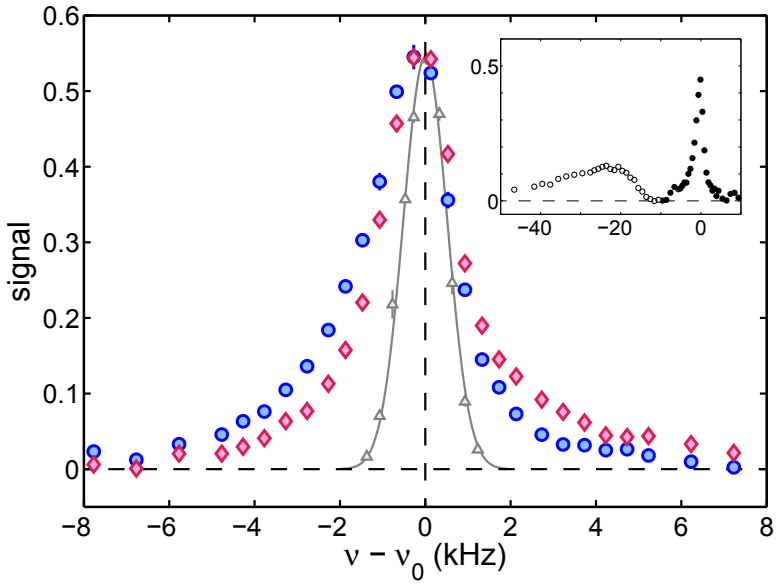

Figure 8.2: Sample rf spectra taken at $B - B_0 = -20\,\mathrm{mG}$ at $T_{\mathrm{eff}} = 232\,\mathrm{nK}$. The red diamonds (blue circles) show data recorded using method A (B). For reference, the gray triangles show data recorded in the absence of dimers together with a Gaussian fit (gray line). Inset: Spectrum at $-17\,\mathrm{mG}$ over an extended frequency range. The molecular dissociation signal (open symbols), recorded with 30× increased rf power, is clearly separated from the atomic peak (filled symbols).

causing an average shift in the frequency of their peak rf response of $\delta\nu = -\hbar\bar{n}_{\mathrm{D}}\mathrm{Re}\langle f(0)\rangle/\mu_3$, where $\langle f(0)\rangle$ denotes the thermal average of $f(0)$ over all atom-dimer collision energies E_{coll}. The red solid lines in Fig. 8.3 show the theoretical results for $\delta\nu$ for the respective molecule densities and collision energies. The optical theorem relates the imaginary part of $f(0)$ to the average elastic scattering rate τ^{-1} as $\tau^{-1} = 4\pi\,\hbar\,\bar{n}_{\mathrm{D}}\,\mathrm{Im}\langle f(0)\rangle/\mu_3$. The resulting finite lifetime τ of the atoms' wave packets causes Lorentzian broadening with a full width at half maximum (FWHM) $1/(2\pi\,\tau)$. The blue solid lines in Fig. 8.3 show the predicted FWHM, including additional broadening due to the finite duration of our rf pulse[2].

The collisional broadening yields information on the elastic scattering rate. At typical detunings of $B - B_0 \approx -20\,\mathrm{mG}$, our data show an elastic atom-dimer scattering

[2]The finite duration of our rf pulse causes an additional Gaussian broadening of typically 1.2 kHz (FWHM).

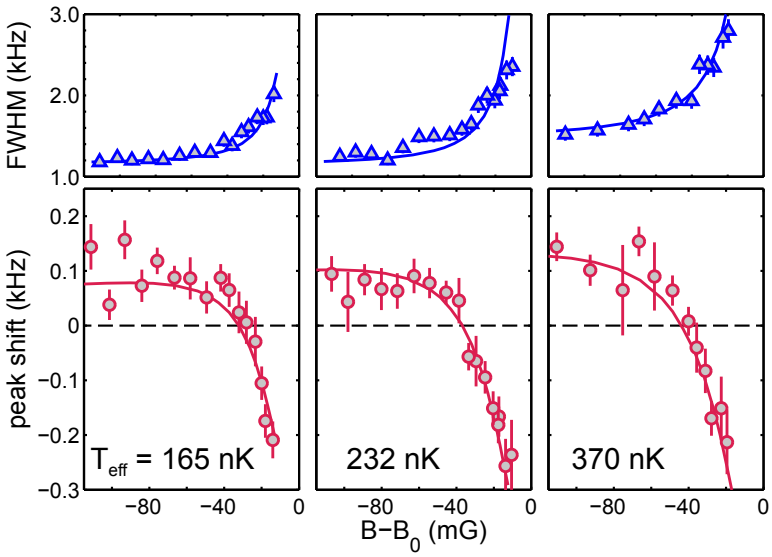

Figure 8.3: Widths (blue triangles) and peak shifts (red circles) extracted from the rf spectra as a function of the magnetic field detuning $B - B_0$ for the three different values of T_{eff}. The lines are the corresponding theoretical predictions. To account for fluctuations in the dimer number of different spectra, the widths and peak shifts are scaled to a dimer number of 15 000, which is typical for all spectra.

rate on the order of $1/(100\,\mu\mathrm{s})$. A comparison with the observed dimer decay rate of about $1/(5\,\mathrm{ms})$ gives a lower limit for the ratio of elastic to inelastic atom-dimer collisions of 50. We note that in our system the dimers spontaneously dissociate on a time scale of about 10 ms [Nai11].

The comparison between the experimentally observed and the theoretically calculated line shifts and broadenings shows remarkable agreement over the whole parameter range investigated. The somewhat asymmetric spectral wings are beyond the impact theory [Szu96] and, thus, cannot be reproduced. Indeed, a substantial contribution to the wings comes from the photon emission or absorption events for which K atoms find themselves inside the atom-dimer interaction range, i.e., during atom-dimer collisions, which are assumed instantaneous in the impact theory. It is, then, understood that, for example, the left "attractive" wing of the B spectrum is larger than that of the A spectrum. Since, in the former case potassium atoms are initially attracted by dimers, the probability to find them near dimers is enhanced. Effects that are beyond

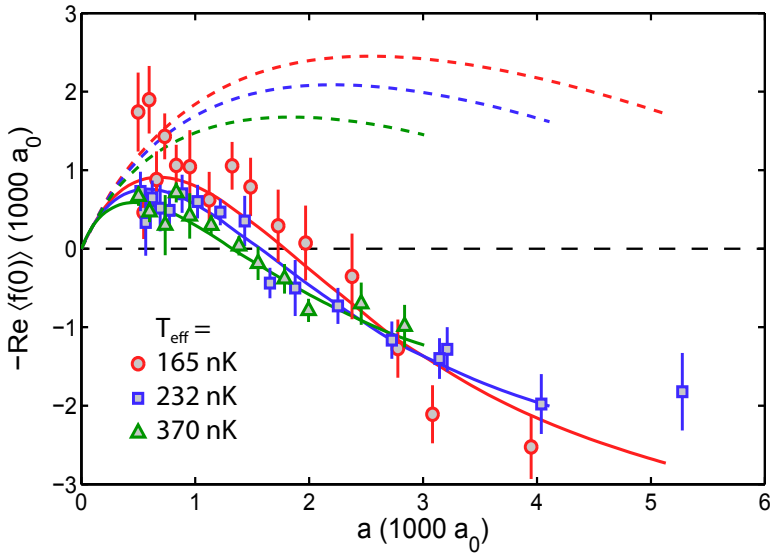

Figure 8.4: Real part of the atom-dimer forward-scattering amplitude as a function of the atom-atom scattering length a for the three different values of T_{eff}. The symbols and the lines show the data and the theoretical predictions from Fig. 8.3. For comparison, the dashed lines indicate the respective s-wave contributions. The theoretical lines stop at $k_{\mathrm{B}}T_{\mathrm{eff}} = E_{\mathrm{b}}/2$.

the impact theory become more pronounced as we approach the FR because of the increased atom-dimer collision time.

Finally, we discuss the interaction strength in our mixture in terms of $-\mathrm{Re}\langle f(0)\rangle$, which characterizes the interactions in a way that is analogous to a in the s-wave mean-field picture. We use the experimental peak-shift data from Fig. 8.3 to extract $-\mathrm{Re}\langle f(0)\rangle$ and plot it together with the corresponding theoretical results in Fig. 8.4. The sign reversal shows up for values of a being somewhat below $2000\,a_0$, with the expected temperature dependence of the zero crossing. For $a \approx 4000\,a_0$, the attractive interaction already corresponds to about $-2000\,a_0$. For even larger values of a, we would enter the more complicated regime of collisional dimer dissociation, which is beyond the scope of the present investigations. We note, however, that rf spectra acquired more deeply in the strongly interacting regime show strongly asymmetric line shapes and have peaks shifted to even larger negative detunings.

8.5 Conclusion and Outlook

In conclusion, we have demonstrated a three-body phenomenon in a mixture of heavy and light fermions, which leads to a sign reversal of the atom-dimer interaction near a FR, turning repulsion into a strong attraction. The effect is due to higher partial-wave (mainly p wave) contributions, which are present even at very low collision energies in the nanokelvin regime. Remarkably, this few-body effect changes the character of the interaction without introducing detrimental losses. In contrast to few-body phenomena of the Efimov type [Fer11], the centrifugal barrier still protects the atoms from approaching each other too closely. The resulting collisional stability is a promising feature for many-body physics in Fermi-Fermi mixtures.

Our work lays the ground for a wealth of future studies on mass-imbalanced fermionic mixtures in the strongly interacting regime. Asymmetric phases with coexisting dimers and heavy atoms are energetically favored in a way not present in mass-balanced systems [Qi12]. Related mechanisms in quantum-degenerate situations may lead to exotic new many-body effects, including the emergence of imbalanced superfluids [Qi12], the condensation into nonzero momentum states [Mat11], and the appearance of p-wave superfluidity of heavy atoms mediated by light atoms [Nis09a]. On the few-body side, a direct prospect for our K-Li system is to confine the K atoms in an optical lattice, which is predicted to lead to the formation of stable trimer states [Pet07, Nis09b, Lev09].

Acknowledgements

We acknowledge funding by the Austrian Science Fund FWF with Grant No. SFB FoQuS (F40-P04). M. Z. was supported by the FWF within the Lise Meitner Program (No. M1318), D. S. P. by the Institut Francilien de Recherche sur les Atomes Froids (IFRAF), and J. L. acknowledges support from the Carlsberg Foundation.

8

8.6 Supplemental Material

8.6.1 Light Shift of the Feshbach Resonance

The Feshbach resonance (FR) that we employ for tuning the interactions in our system occurs between ^{6}Li atoms in their lowest internal state, denoted Li$|1\rangle$ ($f = 1/2, m_f = +1/2$), and ^{40}K atoms in their third-to-lowest state K$|3\rangle$ ($f = 9/2, m_f = -5/2$). This resonance has been investigated in detail in Ref. [Nai11]. The magnetic field dependent

Li-K s-wave scattering length is given by

$$a(B) = a_{\mathrm{bg}} \left(1 - \frac{\Delta}{B - B_0} \right) \tag{8.2}$$

where $a_{\mathrm{bg}} = 63.0\, a_0$ is the background scattering length, $\Delta = 0.88\,\mathrm{G}$ is the width, and B_0 is the center of the resonance near 154.7 G.

As we already pointed out in Ref. [Koh12], the optical trap induces a differential light shift between the atom pair state and the molecular state. This leads to a light-induced shift of the FR center. For the experiments presented in the main text, we use a near-infrared laser with a wavelength of 1064 nm (single-mode operation) in three different trap settings. Therefore, the center of the FR needs to be determined for each trap setting.

To determine B_0 we perform radio-frequency (rf) spectroscopy of the Feshbach molecules. For each trap setting, this is done in the following way: We prepare a nonresonant mixture of Li atoms in state Li$|1\rangle$ and K atoms in their second-to-lowest state K$|2\rangle$ several tens of mG below the approximate position of the resonance center. Here, we apply a strong 500-μs rf pulse at a variable frequency ν, several kHz below the unperturbed K$|2\rangle\rightarrow$K$|3\rangle$ transition frequency ν_0. This pulse drives Li$|1\rangle$-K$|2\rangle$ atom pairs into the Li$|1\rangle$K$|3\rangle$ dimer state. To determine the number of dimers associated, we subsequently dissociate the dimers into a Li$|1\rangle$ and a K$|3\rangle$ atom by a 300-μs magnetic field ramp to 154.8 G. By recording absorption images we then determine the populations N_2 and N_3 of the K spin states K$|2\rangle$ and K$|3\rangle$, respectively.

By plotting the signal, given by $N_3/(N_3 + N_2)$, against the rf detuning $\nu - \nu_0$, we resolve the molecule association spectrum; see Fig. 8.5. The unperturbed transition frequency ν_0, corresponding to the Zeeman splitting of the two states, is determined by rf spectroscopy in the absence of Li$|1\rangle$ (red points). We determine the binding energy of the molecules from the onset frequency of the molecular association spectra. As the onset frequency, we use the upper rf frequency at which the fraction of atoms transferred is roughly 10% of its peak height. We have checked that, within the errors of our measurements, this criterion agrees with the result obtained by fitting the line-shape model [Chi05] to the spectra, as was done in Ref. [Koh12]. This procedure is repeated for each trap power at various magnetic fields.

We then fit a model [Koh12] for the molecular binding energy near our FR to the data with B_0 as the only free parameter; see Fig. 8.6. This procedure allows us to determine the resonance center in each trap setting with an uncertainty of ± 2 mG. The accuracy of our determination of the resonance position is limited by the uncertainty in the FR parameters [Nai11] used in the model for the binding energy. We determine the center of the FR of trap 1, 2, and 3 to be at the magnetic field of 154.704 G, 154.708 G, and 154.719 G, respectively.

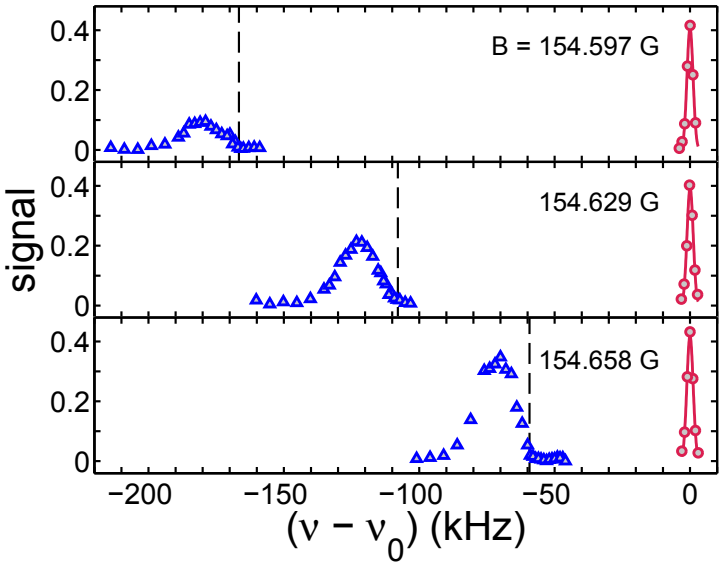

Figure 8.5: Data from the molecular rf association spectroscopy in trap 2. Red circles were taken with a rf power set to the value to match the π-pulse condition in the absence of interactions (no Li$|1\rangle$ present) and is scaled by 0.5. Blue points were taken with a 30× larger rf power. The dashed lines indicate the binding energy $E_b(B)$.

8.6.2 Preparation of the Atom-Dimer Mixture

To cool our atomic sample, we evaporate a Li$|1\rangle$-Li$|2\rangle$ spin mixture at a magnetic field near 1150 G on the attractive side of the 834-G Li$|1\rangle$-Li$|2\rangle$ Feshbach resonance in a single-beam optical dipole trap [Spi10]. During evaporation, a few 10^4 K atoms are sympathetically cooled by the Li environment. The endpoint of evaporation is always set to the same final value. After evaporation, we follow the scheme described in Ref. [Spi10] to transfer the atoms into a crossed-beam optical dipole trap and reach a magnetic field of 154.8 G with typically 10^6 Li atoms in state Li$|1\rangle$ and 4×10^4 K atoms in state K$|1\rangle$. We finally vary the temperature of our sample by increasing the power of our crossed beams to adiabatically recompress the trapped sample. This scheme allows us to maintain a similar population imbalance and degeneracy for the three trap settings used.

To prepare for dimer association, we first create a weakly interacting Li$|1\rangle$-K$|3\rangle$ mixture at B_0+180 mG. A first rf pulse transfers ∼80% of the K$|1\rangle$ population into state

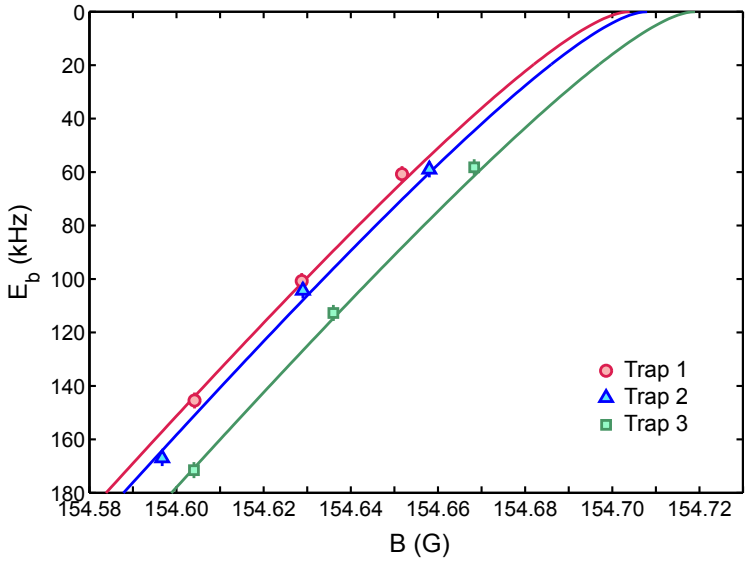

Figure 8.6: Determination of the FR center B_0 by rf association of dimers. The points show the experimentally determined molecular binding energies $E_b(B)$ for the three trap settings. The solid curves are fits of a theoretical model (see text) to the experimental data.

K$|2\rangle$ and a second rf pulse then transfers the total K$|2\rangle$ population into the interacting state K$|3\rangle$. The ∼7 000 K atoms, which remain in the K$|1\rangle$ state, later serve for the spectroscopy.

We associate dimers using a two-step magnetic field ramp. In a first 20-ms step we ramp the magnetic field from $B_0 + 180$ mG to $B_0 + 5$ mG. This ramp is sufficiently slow for the Li atoms to be attracted into the regions of high K density, increasing the density overlap between the two clouds. We then associate the Li$|1\rangle$K$|3\rangle$ dimers via a 0.5-ms Feshbach ramp to $B_0 - 17$ mG. We note that, during these magnetic field ramps, two-body inelastic losses [Nai11] are negligible.

To obtain a pure sample of about 15 000 Li$|1\rangle$K$|3\rangle$ dimers, we remove all unbound atoms from the states Li$|1\rangle$ and K$|3\rangle$. The Li$|1\rangle$ atoms are removed by a sequence of rf and laser pulses. This procedure consists of a first 250-μs rf pulse resonant with the free Li$|1\rangle\rightarrow$Li$|2\rangle$ transition, followed by a 10-μs resonant light pulse, which selectively removes the Li$|2\rangle$ atoms from the trap. This scheme removes about 95% of the excess Li atoms without causing any observable loss of K-Li dimers. A second 250-μs rf pulse

Trap	T_{eff} (nK)	T_{K} (nK)	$\bar{T}_{\mathrm{D}}$ (nK)	$\nu_{r,\mathrm{K}}$ (Hz)	$\nu_{a,\mathrm{K}}$ (Hz)	$\nu_{r,\mathrm{Li}}$ (Hz)	$\nu_{a,\mathrm{Li}}$ (Hz)	$\nu_{r,\mathrm{D}}$ (Hz)	$\nu_{a,\mathrm{D}}$ (Hz)	$\sigma_{r,\mathrm{K}}$ (μm)	$\sigma_{a,\mathrm{K}}$ (μm)	$\bar{\sigma}_{r,\mathrm{D}}$ (μm)	$\sigma_{a,\mathrm{D}}$ (μm)
1	165(15)	138(5)	195(15)	197(5)	25.5(10)	314(5)	34.0(10)	216(5)	27.0(10)	4.3(1)	33(2)	4.4(1)	36(2)
2	232(15)	225(5)	240(15)	284(5)	36.4(10)	446(5)	54.6(10)	310(5)	39.3(10)	3.8(1)	30(2)	3.4(1)	33(2)
3	370(15)	345(5)	398(15)	415(5)	54.0(10)	671(5)	85.0(10)	457(5)	59.0(10)	3.2(1)	25(2)	2.9(1)	26(2)

Table 8.1: Parameters characterizing the three exploited trap settings. The table shows the effectice atom-dimer temperature T_{eff}, the temperature of the K atoms, T_{K}, and the average dimer temperature, $\bar{T}_{\mathrm{D}}$. From the radial (axial) trap frequencies of K and Li, $\nu_{r(a),\mathrm{K}}$ and $\nu_{r(a),\mathrm{Li}}$, we determine the trap frequencies $\nu_{r(a),\mathrm{D}}$ of the dimers. We also show the axial and radial in-situ Gaussian widths of dimers (K atoms), $\sigma_{a,\mathrm{D}(K)}$ and $\sigma_{r,\mathrm{D}(K)}$, respectively.

transfers the leftover 5% of Li$|1\rangle$ atoms into the noninteracting Li$|2\rangle$ state, where they remain without further affecting the experiment.

Simultaneously with this “double-cleaning" of the unbound Li atoms, we remove the unbound K$|3\rangle$ atoms in a similar way. Using a 90-μs rf pulse resonant with the K$|3\rangle\rightarrow$K$|2\rangle$ transition, followed by a second 145-μs rf pulse resonant with the K$|3\rangle\rightarrow$ K$|4\rangle$ transition, we empty the K$|3\rangle$ state with >99 % efficiency. The pulse lengths are chosen such that they are short, i.e. spectroscopically wide, compared to the frequency shifts due to atom-dimer and atom-atom interactions but long, i.e spectroscopically narrow, compared to the binding energy $E_{\mathrm{b}} = h \times 17\,\mathrm{kHz}$ (h is Planck's constant) of the dimers, avoiding the dissociation of dimers.

In a final step, the ∼7 000 K atoms which resided in state K$|1\rangle$ during the entire dimer association process, are transferred in the K$|2\rangle$ state and thus prepared for the rf spectroscopy. This is accomplished by a rf pulse which flips the K$|1\rangle$ and K$|2\rangle$ populations. We note that these K atoms remain unaffected by the dimer association since their interactions with the other components are negligible over the timescales of the experiment.

From here, we reach the specific magnetic field detunings $B - B_0$, at which the spectroscopy is performed, by a 200-μs magnetic field ramp.

8

8.6.3 Determination of the Temperatures and the Densities

Here, we describe how we determine the temperatures and the densities of the atom cloud and the dimer cloud. The resulting experimental parameters are summarized in Table 8.1.

Atom and dimer temperatures – The temperatures of our atom and dimer clouds are obtained by Gaussian fits to absorption images of the clouds after a long time-of-flight of $t_{\mathrm{tof}} = 6\,\mathrm{m}s$. With the measured radial Gaussian width $\sigma_{\mathrm{tof},K(D)}$ the atom (dimer)

temperature $T_{\mathrm{K}(D)}$ is given by

$$k_{\mathrm{B}} T_{\mathrm{K}(D)} = m_{\mathrm{K}(D)} \left(\sigma_{\mathrm{tof},K(D)}/t_{\mathrm{tof}}\right)^2, \tag{8.3}$$

where $m_{\mathrm{K}(D)}$ is the mass of the atom (dimer).

The magnetic field ramps and the removal of the surrounding Li shell, described in the previous section, excite collective oscillations of the dimer cloud. We trace these oscillations in momentum space as a function of a wait time t_{wait} after the cleaning procedure to release from the trap. An example of such an oscillation is shown in Fig. 8.7. In order to characterize the temperature at the time of the experiment, i.e. during the application of the 1-ms rf pulse (shaded area), we introduce the average temperature

$$\bar{T}_{\mathrm{D}} = \frac{1}{\tau_{\mathrm{rf}}} \int_{\mathrm{rf}} T_{\mathrm{D}} \, \mathrm{d}t. \tag{8.4}$$

Axial and radial sizes – To determine the densities of the atom (K) cloud and the dimer (D) cloud, we measure their Gaussian radial (r) and axial (a) widths $\sigma_{r,\mathrm{K}(D)}$ and $\sigma_{a,\mathrm{K}(D)}$, respectively. The axial widths are measured from a Gaussian fit to the axial profiles of in-situ absorption images. Since the radial widths are on the order of our imaging resolution, they can not be determined from in-situ images. We instead determine the radial widths of the K atom cloud as

$$\sigma_{r,\mathrm{K}} = \sqrt{\frac{k_{\mathrm{B}} T_{\mathrm{K}}}{m_{\mathrm{K}} (2\pi \nu_{r,\mathrm{K}})^2}}, \tag{8.5}$$

where T_{K} and $\nu_{r,\mathrm{K}}$ denote the temperature and the radial trap frequency of the K atoms, respectively. Accordingly we determine the average radial in-situ width of the dimers,

$$\bar{\sigma}_{r,\mathrm{D}} = \sqrt{\frac{k_{\mathrm{B}} \bar{T}_{\mathrm{D}}}{m_{\mathrm{D}} (2\pi \nu_{r,\mathrm{D}})^2}}, \tag{8.6}$$

using the averaged dimer temperature $\bar{T}_{\mathrm{D}}$, and the radial dimer trap frequency $\nu_{r,\mathrm{D}}$.

Trap frequencies of the dimers – We use the measured trap frequencies of the K and Li atoms to determine the trap frequencies $\nu_{r(a),\mathrm{D}}$ of the Li-K dimers. Since the dimers are weakly bound over the magnetic field range investigated, their polarizabilities are approximately given by the sum of the polarizabilities of the Li and the K atoms. We want to point out that the differential light shift, shifting the FR center (see Sec. 8.6.1), gives only a $< 10\%$ correction to the trap potential and is neglected. Therefore, to a good aproximation, the dimer trap frequencies are given by

$$\nu_{a(r),\mathrm{D}} = \sqrt{(m_{\mathrm{K}} \nu_{a(r),\mathrm{K}}^2 + m_{\mathrm{Li}} \nu_{a(r),\mathrm{Li}}^2)/m_{\mathrm{D}}}, \tag{8.7}$$

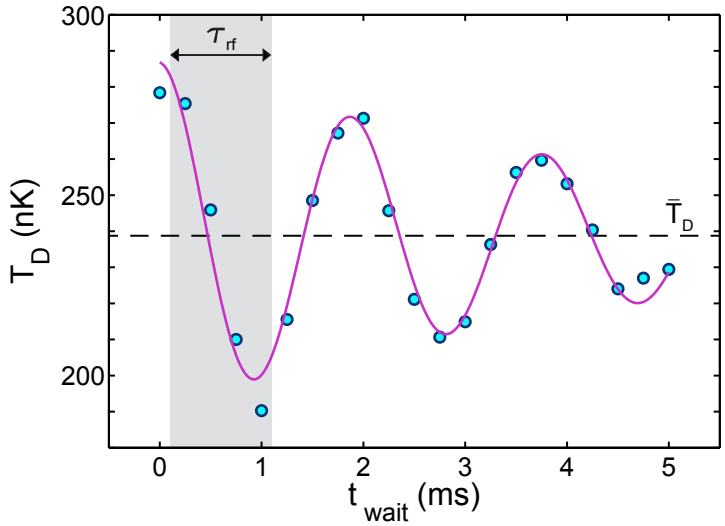

Figure 8.7: Radial oscillation of the dimer cloud after the magnetic field ramp and the removal of the Li atoms. We plot the dimer temperature T_D versus the wait time t_{wait} after the first rf cleaning pulse to release from the trap. The filled circles are the experimental data, the solid line is a fit of a damped harmonic oscillation to the data. The shaded area indicates the time at which the spectroscopy rf pulses are applied and the dashed line marks the experimentally relevant averaged dimer temperature $\bar{T}_D$.

with m_{Li} being the mass of a Li atom.

Mean dimer density – For a given dimer number, N_D, the mean dimer density experienced by the K atoms $\bar{n}_D$ is given by

$$\bar{n}_D = \frac{N_D}{(2\pi)^{3/2}(\sigma_{r,K}^2 + \bar{\sigma}_{r,D}^2)\sqrt{\sigma_{a,K}^2 + \sigma_{a,D}^2}}, \tag{8.8}$$

where we have assumed Gaussian-shaped atom and dimer clouds.

Effective temperature – Due to heating and oscillations caused by our preparation procedure, the dimer temperature T_D in our system is different from the temperature of the non-interacting K$|2\rangle$ atoms that we use for rf spectroscopy. However, since our dimer and atom clouds are both non-degenerate, the energies of the atom-dimer collisions still assume a Boltzmann distribution. Averaging this distribution over the

oscillations of the dimer cloud results in an effective atom-dimer collision temperature

$$T_{\text{eff}} = \mu_3(T_{\text{K}}/m_{\text{K}} + \bar{T}_{\text{D}}/m_{\text{D}}), \tag{8.9}$$

where $\mu_3 = m_{\text{K}}m_{\text{D}}/(m_{\text{K}} + m_{\text{D}})$ is the atom-dimer reduced mass.

8.6.4 Importance of Higher Partial Wave Scattering and Comparison to the Equal-Mass Case

In this section, we justify several important statements made in the main text. First, we have argued that the range of the atom-dimer interaction is comparable with the typical de Broglie wavelength and, therefore, quite a few partial waves are necessary to quantitatively characterize the line shift. In Fig. 8.8, we display $-\text{Re}\, f(0)$, the quantity which is thermally averaged in the main text to obtain the line shifts. The method of calculating the scattering amplitude is described in Ref. [Lev09]. Remarkably, the real part of the forward-scattering amplitude is seen to change sign at a collision energy much smaller than the binding energy, even for a relatively large detuning of 21 mG. The second change of sign of $-\text{Re}\, f(0)$ seen in Fig. 8.8(a) is attributed to the fact that δ_p exceeds $\pi/2$ above $E_{\text{coll}} \approx 0.1E_{\text{b}}$, the point of the p-wave resonance. The p-wave contribution at larger collision energies then becomes positive (repulsive) (see Eq. 8.1). However, this peculiar phenomenon takes place only in a very close vicinity of the wide resonance limit as the p-wave phase shift drops rather abruptly with R^*/a [Lev09]. We also note how, as the collision energy is increased, more and more partial wave channels are needed to accurately describe the forward-scattering amplitude. The calculation presented here includes the first 16 partial waves, which is sufficient to obtain an essentially converged scattering amplitude at the dimer breakup threshold.

As far as the equal mass case is concerned, the competition between the attraction in odd partial waves and repulsion in even partial waves is also quite significant, yet much less pronounced compared to the K-Li case. In Fig. 8.9 we display $-\text{Re}\, f(0)$ as a function of E_{coll} for equal masses. Here the broad resonance case in Fig. 8.9(a) is relevant since it is readily available in current experiments and since there the effect of higher partial waves is most noticeable. We see that the forward-scattering amplitude does change sign in this case. However, in contrast to the K-Li case, this happens at a high collision energy close to the dimer breakup threshold and, in fact, already for $R^*/a \gtrsim 0.03$ the crossing is no longer on the scale. Thus, in the narrow resonance case illustrated in Fig. 8.9(b) and (c) the interaction is found to be repulsive below the dimer breakup threshold. In all cases the thermally averaged quantity $-\text{Re}\,\langle f(0)\rangle$ is positive.

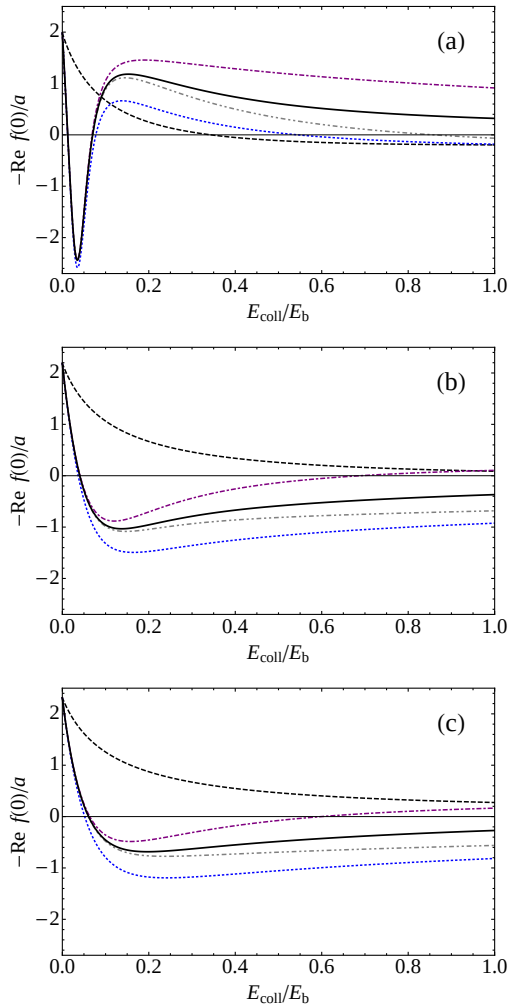

Figure 8.8: Scattering of a ^{40}K atom with a ^{6}Li^{40}K dimer. The quantitiy $-\mathrm{Re}\, f(0)$ is plotted as a function of atom-dimer collision energy for (a) $R^*/a = 0$ [$B - B_0 = 0$], (b) $R^*/a = 1/2$ [$B - B_0 = -10\,\mathrm{mG}$], and (c) $R^*/a = 1$ [$B - B_0 = -21\,\mathrm{mG}$]. The lines are including s-wave scattering only (black, dashed), including up to p-wave (blue, dotted), up to d-wave (purple, dot-dashed), and up to f-wave (gray, double dot-dashed). The solid black line is $-\mathrm{Re}\, f(0)$ including the first 16 partial waves.

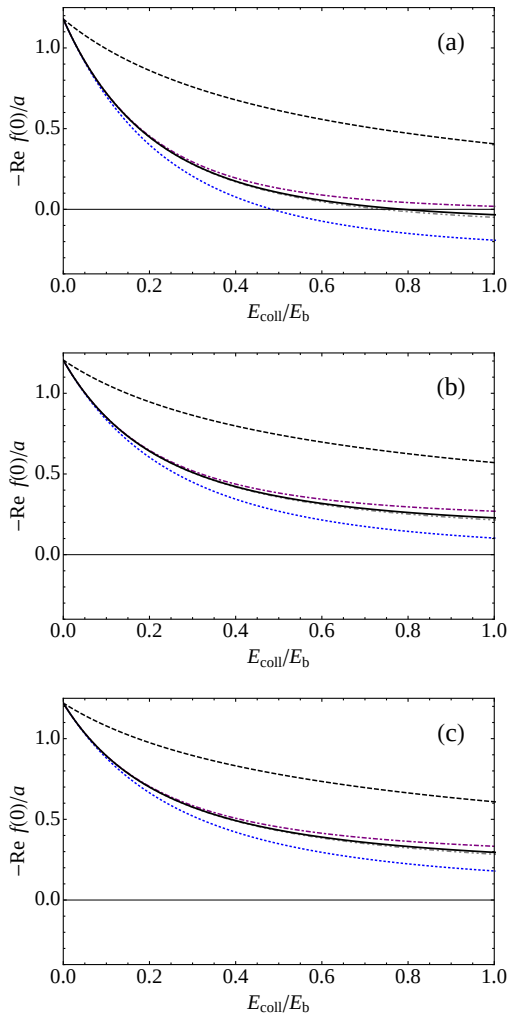

Figure 8.9: Equal-mass case of atom-dimer scattering. We plot $-\mathrm{Re}\, f(0)$ as a function of collision energy for the homonuclear case, $m_\uparrow = m_\downarrow$. The conventions used for the lines as well as the detunings in (a) to (c) are the same as in Fig. 8.8. The solid black line includes the first 9 partial waves.

Finally, let us also make a remark concerning the thermal averaging of the scattering amplitude which we use in the main text. In principle, the averaging procedure requires the knowledge of the phase shifts above the atom-dimer breakup threshold. However, we always restrict ourselves to temperatures $k_{\mathrm{B}}T \lesssim E_{\mathrm{b}}/2$ and we check that in this case the integration result is insensitive to the exact extrapolation scheme. In practice we extrapolate the phase shift $\delta_l(k)$ using the log function, which works very well when we calculate the phase shifts above the breakup threshold in the Born-Oppenheimer approximation [Lev11].

CHAPTER 9

Lifetime of Feshbach dimers in a Fermi-Fermi mixture of ^{6}Li and ^{40}K

Published as:
M. Jag, M. Cetina, R. S. Lous, R. Grimm,
J. Levinsen, D. S. Petrov
Phys. Rev. A **94**, 062706 (2016)

Author contribution
The author contributed to the development of the experimental method, the calibration of the FRs, and the data acquisition as well as the discussion of both the data and the manuscript.

We present a joint experimental and theoretical investigation of the lifetime of weakly bound dimers formed near narrow interspecies Feshbach resonances in mass-imbalanced Fermi-Fermi systems, considering the specific example of a mixture of ^{6}Li and ^{40}K atoms. Our work addresses the central question of the increase in the stability of the dimers resulting from Pauli suppression of collisional losses, which is a well-known effect in mass-balanced fermionic systems near broad resonances. We present measurements of the spontaneous dissociation of dimers in dilute samples, and of the collisional losses in dense samples arising from both dimer-dimer processes and from atom-dimer processes. We find that all loss processes are suppressed close to the Feshbach resonance. Our general theoretical approach for fermionic mixtures near narrow Feshbach resonances provides predictions for the suppression of collisional decay as a function of the detuning from resonance, and we find excellent agreement with the experimental benchmarks provided by our ^{6}Li-^{40}K system. We finally present model calculations for other Feshbach-resonant Fermi-Fermi systems, which are of interest for experiments in the near future.

9.1 Introduction

The creation of weakly bound dimers near Feshbach resonances has led to major advances in the field of ultracold quantum gases [Köh06, Fer09, Chi10]. Such Feshbach dimers have been the key to molecular Bose-Einstein condensation [Joc03a, Gre03, Zwi03] and to other applications, including the detection of atom pairs in strongly interacting fermionic superfluids [Reg04b, Zwi04] and in optical lattices [Tha06, Win06, Mei13]. The weakly bound dimers can also serve as an excellent starting point for accessing the complex level structure of more deeply bound states [Lan08a] and, in particular, for creating ground-state molecules [Lan08b, Ni08, Dan10, Tak14, Mol14, Par15a, Guo16].

For many applications, the stability of the dimers is of crucial importance. In particular, collisional quenching to lower vibrational states can release an amount of energy that greatly exceeds the depth of the trapping potential, and thus results in immediate losses from the stored sample. A special situation can arise for bosonic dimers formed in a two-component sample of fermionic atoms close to a Feshbach resonance. Here, a Pauli suppression effect [Pet04b, Pet05b, Pet05a] can dramatically reduce collisional losses to lower vibrational states, rendering such dimers exceptionally stable and facilitating their highly efficient evaporative cooling. This Pauli suppression effect has been observed and studied in strongly interacting spin mixtures of

^{6}Li [Cub03, Joc03b] and ^{40}K [Reg04a], which both exhibit broad resonances. This has paved the way to spectacular achievements, such as molecular Bose-Einstein condensation [Joc03a, Gre03, Zwi03], the experimental realization of the crossover to a Bardeen-Cooper-Schrieffer-type superfluid [Gio08], and the exploration of the universal properties of resonantly interacting Fermi gases [Zwe12].

A central question for experiments exploring the many-body physics of fermionic mixtures is how far this suppression extends to mixtures of different species, featuring mass imbalance and narrow resonances. Theoretical investigations have considered the important roles of the mass ratio [Pet05a, Mar08a] and of the resonance width [Lev11]. The combination of ^{6}Li and ^{40}K atoms [Tag08, Wil08, Tie10, Nai11, Tre11] is the only Fermi-Fermi mixture with tunable interactions that has been experimentally realized so far and thus is the only available heteronuclear system that can provide experimental benchmarks. Dimers composed of ^{6}Li and ^{40}K atoms have been observed at LMU Munich in Ref. [Voi09], including preliminary lifetime studies, as well as in various recent experiments in our group [Koh12, Jag14].

In this article, we present a joint experimental and theoretical investigation of the lifetime and decay properties of Feshbach dimers formed in a mixture of ^{6}Li and ^{40}K atoms. In Sec. 9.2, we describe the basic procedures for creating and investigating pure samples of Feshbach dimers and atom-dimer mixtures near a Feshbach resonance. In Sec. 9.3, we report on the measurements of spontaneous dissociation and of inelastic collisions in optically trapped dimer samples and in atom-dimer mixtures. Our results demonstrate the suppression of losses near the Feshbach resonance, but much weaker than that reported in Ref. [Voi09]. In Sec. 9.4, we present theoretical calculations based on the approach of Ref. [Lev11] and find very good agreement with our observations. Finally, anticipating the creation of new mixtures, we present predictions for other Fermi-Fermi combinations with different mass ratios.

9.2 Experimental Procedures

9.2.1 Feshbach resonances

We employ two different Li-K interspecies Feshbach resonances (FRs). The first resonance has been widely used in our previous work on Fermi-Fermi mixtures, including the observation of the hydrodynamic expansion of a strongly interacting mixture [Tre11], the investigation of polarons [Koh12, Cet15, Cet16], and the study of K-LiK atom-dimer interactions [Jag14]. This resonance occurs near 155 G (width 0.88 G) with lithium in its lowest Zeeman sub-level Li$|1\rangle$ ($f = 1/2$, $m_f = +1/2$) and potassium in its third-lowest sub-level K$|3\rangle$ ($f = 9/2$, $m_f = -5/2$). The other resonance occurs near 158 G (width 0.14 G) with Li and K in their lowest-energy spin

Table 9.1: Parameters characterizing the two Feshbach resonances. We summarize the values from Refs. [Cet15, Nai11] for the position B_0[1], background scattering length a_{bg}, and width Δ, as well as for the differential magnetic moment $\delta\mu$. The values given for B_0 include a small shift (9 mG) induced by the trapping-laser light [Cet15].

Channel	B_0 (G)	a_{bg} (a_0)	Δ (G)	$\delta\mu/h$ (MHz/G)	R^* (a_0)
Li|1⟩K|3⟩	154.708(2)	63.0	0.88	2.35	2 650
Li|1⟩K|1⟩	157.530(3)	65.0	0.14	2.3	16 500

states Li$|1\rangle$ and K$|1\rangle$ ($f = 9/2, m_f = -9/2$), respectively. We use the latter, narrower resonance for comparison as it has the advantage of an absence of any Li-K two-body losses.

The dependence of the Li-K s-wave scattering length a on the magnetic field B near a FR can be described by the standard expression $a(B) = a_{bg}\left[1 - \Delta/(B - B_0)\right]$ [Chi10] with the relevant background scattering length a_{bg}, the width Δ, and the resonance center B_0. In Table 9.1 we summarize the values of these parameters for both resonances. To fully characterize the FRs, we also present the differential magnetic moments $\delta\mu$ between the relevant open and closed channels. From these parameters, we derive the length parameter $R^* = \hbar^2/(2m_r\Delta a_{bg}\delta\mu)$ [Pet04a], characterizing the coupling strength between the open and the closed channel. Here m_r represents the Li-K reduced mass. The values for a_{bg} and Δ have been obtained from a coupled-channels calculation [Nai11]. The values for $\delta\mu$ as well as B_0 for the Li$|1\rangle$-K$|3\rangle$ FR, were experimentally determined, with very high accuracy, as described in Ref. [Cet15]. For $\delta\mu$ near the Li$|1\rangle$-K$|1\rangle$ FR we use the data obtained from a coupled-channels calculation [Nai11], and for B_0, we use the value of an independent experimental determination[1].

9.2.2 Sample preparation

Our procedure to prepare Li$|1\rangle$K$|3\rangle$ dimer samples is essentially the same as the one described in Ref. [Jag14]. To produce Li$|1\rangle$K$|1\rangle$ dimer samples, we slightly adapt this procedure to account for the narrower character of the FR. In both cases, the starting point for our experiments is an optically trapped and thermally equilibrated mixture of typically 10^5 Li atoms and approximately 3×10^4 K atoms at a temperature of $\sim$

[1] M. Jag, M. Cetina, R. S. Lous, and R. Grimm (unpublished). We determined B_0 by measuring the energy shift of K atoms in a Li cloud and comparing it to the predictions of a dressed quasiparticle model [Mas12].

370 nK and at a magnetic field of 156.4 G. We reach these conditions by a preparation procedure described in detail in Ref. [Spi10]. The cigar-shaped optical confinement of the atom mixture, realized by two 1064 nm laser-light beams intersecting at an angle of about 16°, is characterized by the radial and axial trap frequencies $\nu_{\mathrm{r,K}} = 420(10)$ Hz and $\nu_{\mathrm{a,K}} = 55(2)$ Hz for the K atoms and $\nu_{\mathrm{r,Li}} = 600(10)$ Hz and $\nu_{\mathrm{a,Li}} = 90(3)$ Hz for the Li atoms. At this stage, all Li atoms are in their lowest Zeeman sub-level Li$|1\rangle$ and all K atoms are in their second-lowest sub-level K$|2\rangle$ ($f = 9/2$, $m_f = -7/2$).

The subsequent preparation steps differ depending on the Li-K spin-state combination from which the dimers are created. To prepare for the creation of Li$|1\rangle$K$|3\rangle$ (Li$|1\rangle$K$|1\rangle$) dimers from these mixtures, we slowly ramp the magnetic field over 2 s to a value of 154.89 G (157.565 G), approximately 180 mG (35 mG) above the center of the FR. Here, we transfer all K atoms into the K$|3\rangle$ (K$|1\rangle$) state by a radio-frequency rapid adiabatic passage.

We then associate approximately 10^4 LiK dimers by a Feshbach ramp [Köh06, Chi10]. To associate dimers from the Li$|1\rangle$-K$|3\rangle$ mixture, we do this in two steps, as illustrated in Fig. 9.1(a). In a first step, we ramp the magnetic field to $B_0 + 5$ mG in 20 ms, which is sufficiently slow for the Li atoms to be attracted into the regions of high K density, increasing the density overlap between the two clouds. This is followed by the second step, in which we quickly ramp the magnetic field to $B_0 - 20$ mG in 0.5 ms. For the Li$|1\rangle$-K$|1\rangle$ mixture, we associate the dimers by a single 2 ms Feshbach ramp to a magnetic field $B = B_0 - 16$ mG, since here, at the much narrower FR, it is very hard to optimize a two-step ramping procedure. Typical dimer numbers of Li$|1\rangle$K$|3\rangle$ samples are roughly 20% larger than the typical numbers of Li$|1\rangle$K$|1\rangle$ samples.

To obtain pure dimer samples, we apply cleaning sequences to remove unbound atoms. For the Li$|1\rangle$K$|3\rangle$ samples, this sequence consists of a combination of radio-frequency (rf) and laser-light pulses; see Fig. 9.1(b). A 100 μs rf π-pulse selectively transfers the free Li atoms from the Li$|1\rangle$ state into the Li$|2\rangle$ state. A subsequent 10-μs laser pulse selectively removes the Li$|2\rangle$ atoms from the trap. Simultaneous with this Li-cleaning procedure, we remove the unbound K atoms in a similar way. Applying two rf π-pulses with durations of 80 μs and 40 μs, we transfer the free K$|3\rangle$ atoms into the K$|1\rangle$ state, and successively remove them from the trap by applying a laser-light pulse resonant to the K$|1\rangle$ atoms. As these cleaning procedures remove about 95% of the free Li and K atoms, they are repeated one more time to clean the respective states more thoroughly. For the Li$|1\rangle$K$|1\rangle$ samples, the Li cleaning is identical to the one explained above and the K cleaning is only slightly adapted. We revert the order of the 80 μs and 40 μs rf π-pulses to transfer the free K$|1\rangle$ atoms into the K$|3\rangle$ state and we then apply a laser pulse resonant to the K$|3\rangle$ atoms to remove them from the trap. After the cleaning procedure, we quickly, within 200 μs, ramp the magnetic field to its variable final value, at which we then perform the measurements.

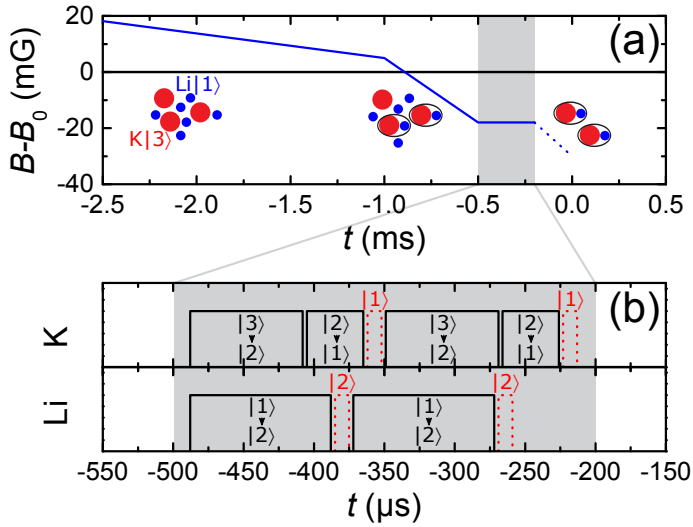

Figure 9.1: Schematic of the preparation of a pure Li$|1\rangle$K$|3\rangle$ dimer sample. (a) Starting from the magnetic field $B = B_0 + 180\,\text{mG}$, we approach the resonance by a first 20-ms ramp to $B_0 + 5\,\text{mG}$ (last 1.5 ms shown). Then, we associate dimers by a quick (0.5 ms) ramp across the FR to a magnetic field $B_0 - 20\,\text{mG}$. Here, within 0.3 ms (gray shaded), we remove unbound K and Li atoms from the sample. After this cleaning procedure we reach the final magnetic field B, at which we perform the lifetime measurement, by a 200 -μs ramp (dotted line). (b) The cleaning procedure for both Li and K consists of radio-frequency pulses (solid black), selectively transferring unbound atoms into another spin state, and successive removal of these atoms from the trap by a resonant laser-light pulse (dotted red). This cleaning procedure is repeated one more time to increase the purity of the dimer sample.

9.2.3 Dimer detection and dimer-temperature determination

We determine the LiK-dimer numbers from absorption images of Li and K atoms after dissociation of the dimers into Li-K pairs by a reverse Feshbach ramp [Köh06, Chi10]. For both resonances, we ramp the magnetic field B up to a value $\geq B_0 + 50\,\text{mG}$ within 10 μs. After an additional wait time of a few 10 μs, we simultaneously take absorption images of the Li and the K cloud, from which we determine the numbers of Li and K atoms. In some measurements, we detected only the number of Li atoms remaining after the reverse Feshbach ramp.

The temperature of the dimers is determined from Gaussian fits to absorption images of the clouds after a time-of-flight expansion duration of $t_{\text{TOF}} = 4\,\text{ms}$. The pro-

cedure is discussed in detail in Ref. [Jag14]. From the measured radial width σ_r, we obtain the dimer temperature T_D from $k_B T_D = m_D(\sigma_r/t_{TOF})^2$, where $m_D = m_{Li} + m_K$ is the mass of a Li-K dimer. Typically, the temperatures of our dimer samples are about $T_D = 550\,\mathrm{nK}$. This corresponds to peak phase-space densities of about 0.1 for typical dimer number densities in our samples. We explain the increased temperature of our dimer cloud compared to the temperature prior to the dimer association (370 nK) by heating and collective excitations caused by our preparation procedure [Jag14].

9.3 Measurements of Dimer Decay

In this section, we present measurements characterizing various processes that lead to losses of LiK dimers. In Sec. 9.3.1, we first discuss spontaneous dissociation, which, being a one-body process, can also occur in very dilute samples. In Secs. 9.3.2 and 9.3.3, we then present our experimental results on dimer-dimer collisions and atom-dimer collisions, which, as two-body processes, limit the lifetime of dense samples.

9.3.1 Spontaneous dissociation

A dimer created from an atom pair with at least one atom in an excited Zeeman state can spontaneously decay via processes mediated by the coupling between the two spins [Chi10]. Such decay has previously been studied theoretically and experimentally for the case of $^{85}Rb_2$ molecules [Köh05, Tho05]. Our Li$|1\rangle$K$|3\rangle$ dimers are also subject to this decay process, in contrast to the Li$|1\rangle$K$|1\rangle$ combination. The spontaneous decay of Li$|1\rangle$K$|3\rangle$ dimers has been theoretically investigated in detail in Ref. [Nai11], where predictions for the lifetimes of the dimers were obtained from coupled-channels calculations.

We experimentally investigate the lifetime of Li$|1\rangle$K$|3\rangle$ with respect to spontaneous decay using dimer samples with a very low number density, so that density-dependent collisional losses do not play a significant role. We realize such dilute dimer samples by allowing the optically trapped dimer cloud to expand after switching off the trap. After a variable expansion time t, we determine the molecule number in the sample. Note that the 1064-nm light induces a shift of the FR center B_0, as described in Ref. [Cet15]. When the optical trap is off, the FR center B_0 of the Li$|1\rangle$-K$|3\rangle$ resonance is found at 154.699 G, i.e., 9 mG lower than in the trap (Table 9.1). For the Li$|1\rangle$-K$|1\rangle$ channel we assume the same small shift.

In Fig. 9.2, we show a typical decay curve of a Li$|1\rangle$K$|3\rangle$ dimer sample, recorded at a magnetic detuning $B - B_0 = -296\,\mathrm{mG}$ (blue squares). For our analysis, we only consider data obtained for $t \geq 1.5\,\mathrm{ms}$, where the mean dimer number density in the

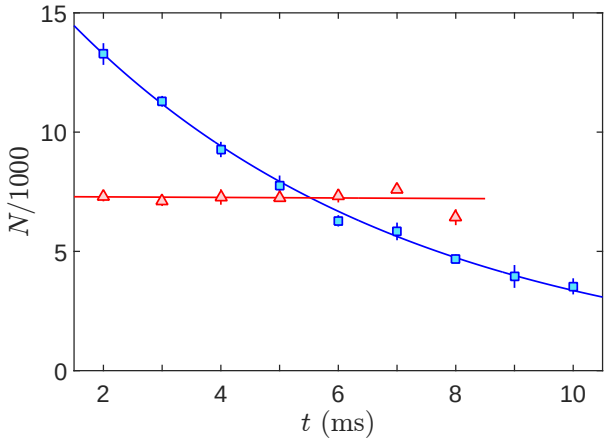

Figure 9.2: Comparison of the dimer number evolution near the Li|1⟩-K|3⟩ and the Li|1⟩-K|1⟩ FR. The blue squares show a typical decay curve of a Li|1⟩K|3⟩ dimer sample at $B = B_0 - 296\,\mathrm{mG}$. Fitting an exponential decay to the data yields the 1/e lifetime $\tau = 5.8(4)\,\mathrm{ms}$. The fit is represented by the blue solid line. The results from similar measurements with a Li|1⟩K|1⟩ dimer sample at a magnetic detuning of $-75\,\mathrm{mG}$ from the respective resonance center, are shown as the red triangles. Here, we observe the dimer number to remain essentially constant. A fit of an exponential decay to the data (red solid line) is consistent with infinite lifetime. The error bars represent 1σ uncertainties; in some cases, they are smaller than the symbol size.

sample is below $5 \times 10^{10}/\mathrm{cm}^3$, low enough for collisional losses to play a negligible role. To these data we fit a simple exponential decay, $N_0 \exp(-t/\tau)$, with the initial dimer number N_0 and the lifetime τ as free parameters. For the specific example of Fig. 9.2, this procedure yields $\tau = 5.8(4)\,\mathrm{ms}$ and the fit result is shown as the blue solid line.

For comparison, we also show the evolution of the number of Li|1⟩K|1⟩ dimers recorded 75 mG below the center of the Li|1⟩-K|1⟩ resonance (red triangles). Here, the spontaneous decay mechanism is absent. Indeed, we observe an essentially constant number of Li|1⟩K|1⟩ dimers, with the fit yielding the decay rate $1/\tau = 0.008(7)\,\mathrm{s}^{-1}$. This result is essentially consistent with an infinite lifetime and, at a 95% confidence level, provides a lower bound of 50 ms.

In Fig. 9.3, the blue circles show the measured lifetimes of the dimers with respect to spontaneous decay over a wide range of magnetic detunings, $B - B_0$. Comparing our experimental results to the predictions from Ref. [Nai11] (black solid line), we

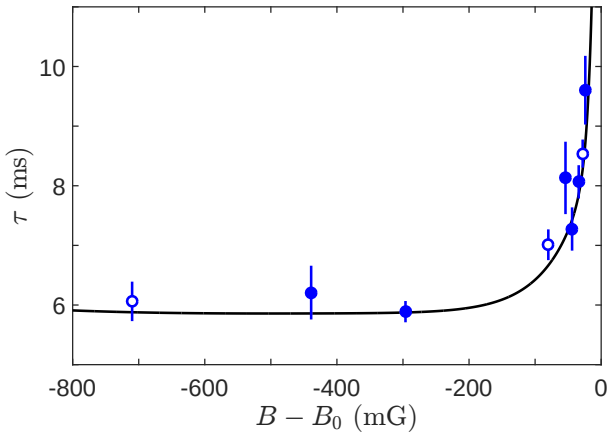

Figure 9.3: Lifetime of dimers against spontaneous decay near the Li|1⟩-K|3⟩ FR. The data points show the experimental results and the black solid line represents the theoretical prediction from Ref. [Nai11]. While the filled symbols are obtained from decay curves, where both the Li and the K component have been imaged after dissociation, the open symbols are based on detecting K alone. The error bars represent the 1σ fit uncertainties.

find an excellent agreement over the whole magnetic-field range investigated. While for magnetic detunings of around a few hundred mG the lifetime is about 6 ms, we in particular confirm the predicted substantial increase near the FR, where we determine lifetimes approaching 10 ms. This increase can be attributed to the increasing halo character of the dimer wave function as the FR is approached. This leads to a decreased probability to find a pair of Li and K atoms within the short range where the spin coupling occurs [Nai11]. Our measurements of the lifetime of the Li|1⟩K|3⟩ dimers in *dilute* samples can be fully understood in terms of spontaneous dissociation.

9.3.2 Dimer-dimer collisions

In a second series of experiments, we investigate the collisional decay of a trapped dimer cloud. In collisions with other dimers, our shallowly bound dimers can relax into more deeply bound states. The binding energy that is released in this process is much larger than the depth of the trapping potential, and thus the relaxation products are always lost from the trap. This two-body decay occurs at a rate $\beta_D n$, which is equal to

the product of the dimer-dimer two-body loss-rate coefficient β_D and the dimer number density n.

To experimentally determine the rate coefficient β_D for these collisional decay processes, we investigate the decay of a trapped sample of dimers. The initial number of typically $N_0 = 1.3 \times 10^4$ dimers corresponds to an initial number density N_0/V_{eff} of about $1 \times 10^{12}/\mathrm{cm}^3$, where $V_{\mathrm{eff}} = [(4\pi k_B T_D)/(m_D \bar{\omega}_D^2)]^{3/2}$ is the effective volume of a thermalized sample, and $\bar{\omega}_D = 2\pi(\nu_{r,D}^2 \nu_{a,D})^{1/3} \approx 2\pi \times 230\,\mathrm{Hz}$ is the mean dimer trapping frequency[2]. After a hold time t at a magnetic field B we measure the number of dimers, $N(t)$, remaining in the sample. In Fig. 9.4, we show an example for a decay curve obtained at a magnetic detuning of $-710\,\mathrm{mG}$ from the Li$|1\rangle$-K$|3\rangle$ FR (blue squares).

We model the decay with the common loss-rate equation

$$\dot{N}/N = -1/\tau - (\beta_D/V_{\mathrm{eff}})N. \tag{9.1}$$

Under the assumption that the sample remains in thermal equilibrium at the initial temperature T_D, this differential equation has the solution

$$N(t) = \frac{N_0 \exp(-t/\tau)}{1 + \frac{\beta_D}{V_{\mathrm{eff}}} N_0 \tau \left[1 - \exp(-t/\tau)\right]}. \tag{9.2}$$

We fit Eq. (9.2) to the experimental data to extract the loss-rate coefficient β_D. While β_D and N_0 are free parameters, we fix τ to the corresponding theoretical value, which was verified in the independent measurements presented before. For the data of Fig. 9.4, the fit result is shown as the blue solid line. For comparison, we also show the decay curve of a dilute dimer sample, where collisional loss is absent (red triangles), together with the result of a fit of a simple exponential decay to this data (red line). Our measurements show that, under typical experimental conditions, the collisional relaxation and the spontaneous dissociation give similar contributions to the total decay of the trapped dimer sample.

The given values for the loss coefficients β_D are subject to a systematic error arising from an uncertainty in the dimer number density. We estimate a combined systematic error of about 40%, arising from largely uncorrelated uncertainties of 25%, 7%, and 20% in the dimer number, the dimer trapping frequencies, and the dimer temperature, respectively. Furthermore, by assuming a constant temperature T_D of the decaying

[2] There is a differential light shift between the closed-channel molecule and a Li-K pair state induced by the 1064-nm trapping light [Jag14, Cet15, Cet16]. For our experimental conditions, this gives rise to an upward correction of the stated dimer trapping frequency by $< 5\%$, dependent on the magnetic detuning from the FR. In our analysis, this small correction is taken into account.

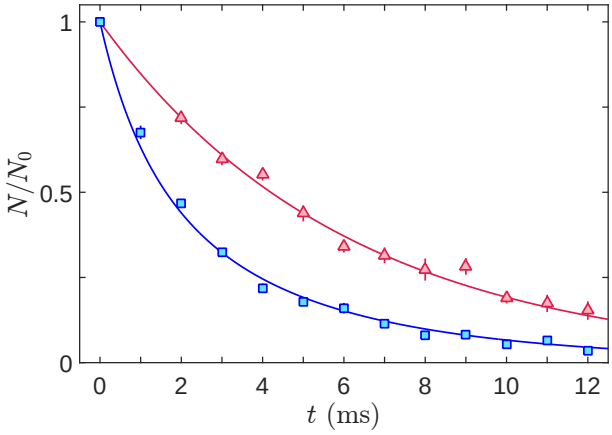

Figure 9.4: Comparison of the decay of a trapped and an expanding Li$|1\rangle$K$|3\rangle$ dimer sample. The blue squares show the measured dimer number in a trapped sample vs hold time t in the trap. The red triangles show the dimer number determined in a dilute, expanding sample, 1.5 ms after release from the trap. The blue and red lines correspond to the fit of our model to the data without and with two-body decay (see text). To enable a direct comparison, the experimental data are normalized to the initial dimer number $N_0 = 13000\,(15300)$ obtained from the fit to the data acquired from the trapped (expanding) sample. The error bars represent 1σ uncertainties; in some cases they are smaller than the symbol size.

dimer sample, and thus a constant $V_{\rm eff}$ in Eq. (9.1), we neglect a small effect of anti-evaporation heating [Web03b]. We have checked that including the latter into our analysis would lead to slightly larger values for $\beta_{\rm D}$. We found this correction to stay well below 15%.

We determine the values for the loss coefficient $\beta_{\rm D}$ at various magnetic detunings. Our experimental results, obtained with Li$|1\rangle$K$|3\rangle$ (Li$|1\rangle$K$|1\rangle$) dimer samples, are shown in Fig. 9.5 as the blue circles (red squares). For the Li$|1\rangle$K$|1\rangle$ dimer samples we obtain values for the loss-rate coefficient $\beta_{\rm D}$ of roughly 3×10^{-10}cm^3/s without significant dependence on the magnetic detuning. Also, for the Li$|1\rangle$K$|3\rangle$ dimer samples we obtain roughly the same value for detunings, $B - B_0 \lesssim -400$ mG. At these large magnetic detunings, the Feshbach molecules have a very small admixture of the entrance channel and are thus strongly closed-channel dominated. As we discuss in more detail in Sec. 9.4, the decay of such molecules is largely independent of the exact state they are in [Sta06, Zah06, Gao10, Jul11, Qué11], which explains why the

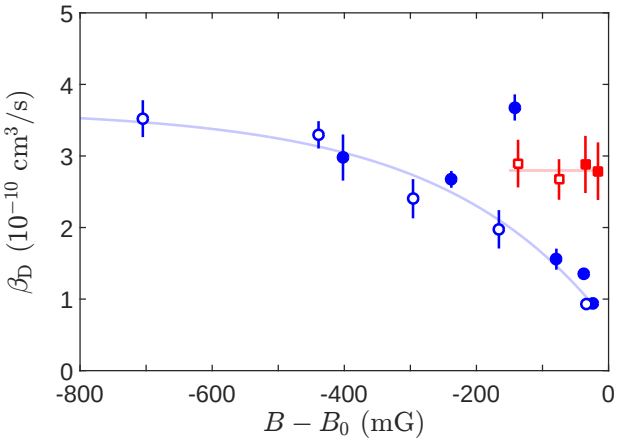

Figure 9.5: Measured loss-rate coefficient for inelastic dimer-dimer collisions as a function of magnetic detuning. The blue circles (red squares) correspond to the experimental results obtained with samples of Li|1⟩K|3⟩ (Li|1⟩K|1⟩) dimers. The filled symbols correspond to results we obtained when determining the molecule number from both Li and K absorption images. Open circles (squares) represent fit results based on analyzing Li (K) images alone. The error bars represent the 1σ fit uncertainties; in some cases, they are smaller than the symbol size. We show the light blue and a light red line as guides to the eye.

measurements for both FRs at large detunings result in nearly the same values.

As the Li|1⟩-K|3⟩ resonance is approached, our experimental results (with the exception of one clear outlier[3]) show a reduction of collisional losses, which we interpret in terms of the Pauli suppression effect. For our data points closest to resonance (about -30 mG detuning), this suppression effect amounts to more than a factor of three. Note that measurements closer to resonance are prevented by the onset of collisional dissociation [Joc03b].

9.3.3 Atom-dimer collisions

In another set of experiments, we study the decay of dimers arising from their collisions with Li atoms in a mixture of LiK dimers and Li atoms. Such decay occurs at a rate

[3]The data point at -142 mG clearly lies beyond the trend of the other data. Thoroughly re-checking the settings of our experimental setup for this measurement yielded no hint for what could have caused the discrepancy.

$\beta_{\mathrm{LiD}} n_{\mathrm{Li}}$, equal to the product of the Li atom-dimer loss coefficient β_{LiD} and the Li density n_{Li}. The measurement of atom-dimer collisions is challenging because the corresponding decay has to be distinguished from both the spontaneous decay and the dimer-dimer collisional decay.

We realize mixtures of Li atoms and LiK dimers by adapting the preparation procedure presented in Sec. 9.2.2. Here we start with the lithium component in a nearly balanced spin mixture of Li$|1\rangle$ and Li$|2\rangle$. The Feshbach ramp then produces a mixture of Li-K dimers, some remaining Li$|1\rangle$ atoms, and the unaffected Li$|2\rangle$ atoms. Then, at $B = B_0 - 20\,\mathrm{mG}$, we apply only one radio-frequency π pulse, which exchanges the populations of the Li$|1\rangle$ and Li$|2\rangle$ states. We subsequently remove the Li$|2\rangle$ atoms from the trap using a laser-light pulse. All other preparation steps, in particular the K spin-state cleaning, remain as described in Sec. 9.2.2. After this procedure, the number density distribution of the Li atoms in the trap, n_{Li}, can be well approximated by the density of a noninteracting Fermi gas at a temperature equal to the initial Li temperature. Typically, we obtain samples of $\sim 9\times10^3$ dimers and a mildly degenerate Fermi sea of $\sim 6\times10^4$ Li atoms at a temperature that is about 55% of the Fermi temperature. This corresponds to a mean dimer density of $6\times10^{11}/\mathrm{cm}^3$ and a Li density averaged over the dimer distribution [Cet16], $\langle n_{\mathrm{Li}}\rangle$, of about $1.5\times10^{12}/\mathrm{cm}^3$.

To experimentally determine the rate coefficient β_{LiD}, we again investigate the decay of dimers from our sample. We ramp the magnetic field to a desired value B and, after a variable hold time t, we measure the number of dimers, N, remaining in the sample. For each decay curve in the atom-dimer mixture, we record a corresponding reference curve in a pure dimer sample. These reference measurements, which independently provide the dimer-dimer loss coefficient β_{D}, are the ones that we have presented in the preceding Section. To minimize systematic errors resulting from long-term drifts of the experiment, the measurements in the atom-dimer mixtures and the pure dimer samples are carried out in alternating order.

We model the decay of dimers with a simple extension of the decay model from the previous Section. Our Li sample is much larger than the dimer sample, such that losses from the Li sample can be neglected. In this case, the Li sample represents a constant-density bath and the loss of dimers arising from Li atom-dimer collisions appears as a one-body loss, which we include into our model by adding $-\beta_{\mathrm{LiD}}\langle n_{\mathrm{Li}}\rangle$ to the right-hand side of Eq. (9.1). Under these assumptions, the solution of our model is given by substituting τ^{-1} with $\beta_{\mathrm{LiD}}\langle n_{\mathrm{Li}}\rangle + \tau^{-1}$ in Eq.(9.2). We fit this solution to our experimental data to determine the Li atom-dimer loss coefficient β_{LiD}. For the fit, we fix τ to the corresponding theoretical value and the decay coefficient β_{D} to the value we determined in the corresponding reference measurement on a pure dimer sample.

In Fig. 9.6, we show our results for the Li atom-dimer loss coefficient β_{LiD} at various magnetic detunings. The blue circles (red squares) correspond to data acquired

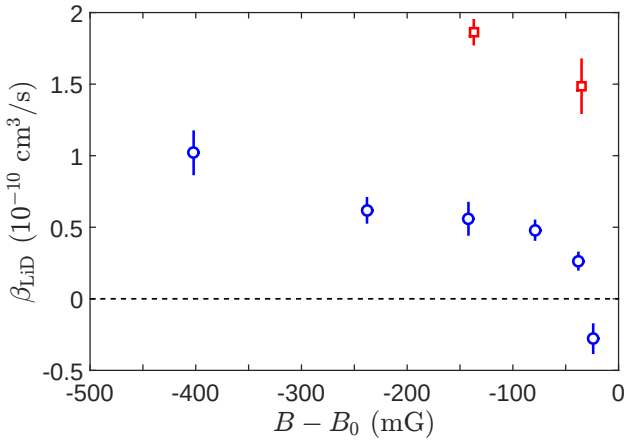

Figure 9.6: Measured loss-rate coefficient for inelastic Li atom-dimer collisions as a function of the magnetic detuning. The blue circles (red squares) correspond to the experimental results obtained with samples of Li|1⟩K|3⟩ (Li|1⟩K|1⟩) dimers co-trapped with Li|1⟩ atoms. In these experiments, the dimer number was determined from the K absorption images only. The error bars include the combined fit uncertainties (see text).

with a Li|1⟩K|3⟩ (Li|1⟩K|1⟩) dimer sample. The error bars reflect the 1σ fit uncertainty of β_{LiD} as well as the contribution arising from the uncertainty in our determination of β_{D}. We obtain atom-dimer loss-rate coefficients of roughly $1.5\times10^{-10}\mathrm{cm}^3/\mathrm{s}$ near the Li|1⟩K|1⟩ FR, where the molecules have closed-channel character. The data obtained with Li|1⟩K|3⟩ dimers show a suppression of atom-dimer collisional losses, which becomes stronger as we approach the FR and the open-channel fraction of the dimers increases. The data point at a magnetic detuning of about -40 mG already shows a suppression by a factor of roughly five. From the data point at -24 mG, we determine a negative loss coefficient. We speculate that this unphysical result is due to the repulsive mean-field interaction between the dimers and the Li atoms, effectively increasing the cloud sizes and therefore decreasing the mean densities of the dimers and the Li atoms. Such an effect is beyond the assumptions of the model underlying our data analysis and can therefore produce unphysical results. We estimate that all other values, taken at larger detunings, do not suffer from such interaction effects. The observed suppression of atom-dimer collisional losses appears very similar to the effect observed in dimer-dimer decay, and can also be attributed to the Pauli suppression effect.

9.3.4 Summary of experimental results and comparison with previous work

Our experimental results characterize three different loss processes of ^{6}Li-^{40}K dimers close to a Feshbach resonance. Spontaneous dissociation was identified as a density-independent one-body loss mechanism. This process is possible for Feshbach molecules composed of atoms that are not in the energetically lowest combination of spin states. For the case of the 155 G resonance in the Li$|1\rangle$-K$|3\rangle$ mixture, this limits lifetimes to values below 10 ms for typical experimental conditions. We have also investigated losses due to inelastic collisions in pure dimer samples, and obtained loss-rate coefficients of typically 3×10^{-10} cm^3/s. At the typical densities of near-degenerate molecular samples, the corresponding loss rate is similar to the effect of spontaneous dissociation. Additional losses occur in atom-dimer mixtures, as we have shown for the example of free excess Li atoms.

Very close to the resonance center, in a roughly 100-mG wide range, we observe a suppression of loss in both spontaneous and collisional decays. In the former case, the suppression is a direct consequence of the halo character of the molecular wavefunction [Köh05, Tho05, Nai11]. In the latter case, the suppression effect can be attributed to Pauli blocking [Pet04b, Pet05a], as we will discuss in more detail in Sec. 9.4. For the specific FR employed in the Li-K mixture, the suppression of loss only leads to an increase of dimer lifetimes by up to a factor of three.

Weakly bound ^{6}Li^{40}K dimers have been created in previous work by the Munich-Singapore group [Voi09, Cos10], who investigated lifetime properties without distinguishing between different processes. Below the FR center, their observations are consistent with our results and can be understood as a combination of spontaneous and collisional losses. Above the FR center, in a 100 mG wide range, their work reports on molecules with lifetimes of more than 100 ms [Voi09]. These long lifetimes were later interpreted in terms of a many-body effect [Cos10]. In our present work, using the same FR, we do not observe any molecules above resonance. In our previous work [Koh12], with K impurities in a degenerate Li Fermi sea, we indeed observed indications of many-body pairs above resonance, though restricted to a narrow, less than 20 mG-wide magnetic-field range. For the 155 G FR in the Li-K mixture, we cannot confirm the existence of long-lived ($\approx$ 100 ms) molecules.

9.4 Theoretical Analysis of Relaxation Rates

In this Section, we present a theoretical description of atom-dimer and dimer-dimer relaxation processes near a narrow resonance. The model has been introduced in Ref. [Lev11] for characterizing atom-dimer and a subset of the dimer-dimer inelastic

channels. In Sec. 9.4.1, we extend the discussion to all relevant dimer-dimer relaxation processes. In Sec. 9.4.2, we then compare the theory with our experimental results and find a very good agreement.

9.4.1 Theoretical model

The collisional decay requires at least three atoms to approach each other to within distances comparable to the van der Waals range R_e of the interatomic interactions (we call this the "recombination region"). For the Li-K interaction, the van der Waals range takes the value $R_e = 40.8a_0$ [Nai11]. In relaxation channels involving three atoms, two atoms form a deeply bound state and the large binding energy is released as kinetic energy. As the central point of our model, the probability of such a relaxation event may be calculated within a theory that only describes the few-body kinematics at length scales greatly exceeding R_e, the short-range relaxation physics being characterized by the loss-rate constant for collisions of atoms with closed-channel (cc) molecules. One can show [Lev11] that in the narrow-resonance limit, $R_e \ll R^*, a$, three atoms enter the recombination region predominantly as a free atom and a cc molecule rather than three free (open-channel) atoms. Thus, the recombination process is microscopically the relaxation in collisions of cc molecules with atoms. We assume that the corresponding interaction is not resonant and is characterized by a coupling constant $-i\Delta_{\mathrm{AD}} \sim -i\hbar^2 R_e/m_{\mathrm{AD}}$, where m_{AD} is the atom-molecule reduced mass. The atom-cc molecule relaxation rate constant equals $\beta_{\mathrm{AD}}^{(0)} = 2\Delta_{\mathrm{AD}}/\hbar$. This relation can be derived by relating the lifetime of the atom and cc molecule to the imaginary part of their mean-field interaction energy shift in unit volume. The "bare" relaxation-rate constant $\beta_{\mathrm{AD}}^{(0)}$ is an external parameter of our theory.

In our approach, the atom-dimer relaxation-rate constant β_{AD} factorizes into the product

$$\beta_{\mathrm{AD}} = \beta_{\mathrm{AD}}^{(0)} \eta_{\mathrm{AD}}(R^*/a), \tag{9.3}$$

where the dependence on the short-range physics is fully absorbed into $\beta_{\mathrm{AD}}^{(0)}$ and the long-range kinematics enters as the probability of finding an atom and cc molecule in the recombination region. This probability can be interpreted as the reduction of atom-dimer relaxation at finite R^*/a and we refer to it as the "suppression function," $\eta_{\mathrm{AD}}(R^*/a)$. It depends only on R^*/a and is proportional to the squared modulus of the atom-dimer wave function calculated under the assumption $\Delta_{\mathrm{AD}} = 0$. The task of computing the normalization integral for this wave function, which is quite complex (particularly, in the four-body case discussed below) and contains closed- and open-channel components, can be avoided by using an equivalent diagrammatic formulation of the problem; see Ref. [Lev11] where this approach was used for K-(K-Li) collisions.

Namely, we calculate the atom-dimer scattering length $a_{\rm AD}$ perturbatively to first order in $\Delta_{\rm AD}$ and deduce the atom-dimer relaxation rate constant from $\mathrm{Im}(a_{\rm AD})$. The suppression function $\eta_{\rm AD}(R^*/a)$ is shown in Fig. 9.7(a) for the case of a light atom (A = Li) and for a heavy atom (A = K). It is seen how the relaxation can be substantially reduced for $R^*/a \lesssim 1$, and that the suppression is stronger in the collision of the heavy K atom with the dimer.

In molecule-molecule collisions, there are three possible relaxation channels: the Li-cc molecule, K-cc molecule, and cc molecule-cc molecule relaxation (we call it four-atom mechanism). The latter originates from inelastic collisions of cc molecules with each other involving no free atoms. This configuration dominates the four-body wave function when all four atoms are at distances smaller than R^*. We assume that three coupling constants $\Delta_{\rm LiD}$, $\Delta_{\rm KD}$, and $\Delta_{\rm DD}$ are proportional to the corresponding van der Waals ranges, which are small compared to R^* and a. This allows us to treat these interactions independently as first-order perturbations on top of the zero-order solution –the properly normalized four-body wave function calculated for $\Delta_{\rm LiD} = \Delta_{\rm KD} = \Delta_{\rm DD} = 0$. The contribution of a relaxation channel, say Li-cc molecule channel, to the total dimer-dimer relaxation-rate constant $\beta_{\rm D}$ is the product of $\beta^{(0)}_{\rm LiD} = 2\Delta_{\rm LiD}/\hbar$ and the probability $\tilde{\eta}_{\rm LiD}(R^*/a)$ to find a Li atom close to a cc molecule in dimer-dimer collisions. The quantity $\tilde{\eta}_{\rm LiD}(R^*/a)$, which is not to be confused with $\eta_{\rm LiD}$ defined for atom-dimer collisions, can in principle be calculated from the squared modulus of the zero-order four-body wave function by integrating it over the coordinates of one K atom (for the Li-cc molecule loss channel) and taking into account combinatorial factors (choice between two Li atoms). However, as in the atom-dimer case, we calculate the dimer-dimer scattering length $a_{\rm DD}$ to first order in $\Delta_{\rm LiD}$, $\Delta_{\rm KD}$, and $\Delta_{\rm DD}$ and deduce the dimer-dimer relaxation-rate constant from $\mathrm{Im}(a_{\rm DD})$. The total relaxation-rate constant in dimer-dimer collisions is written in the form

$$\beta_{\rm D} = \beta^{(0)}_{\rm LiD}\tilde{\eta}_{\rm LiD}(R^*/a) + \beta^{(0)}_{\rm KD}\tilde{\eta}_{\rm KD}(R^*/a) + \beta^{(0)}_{\rm D}\eta_{\rm DD}(R^*/a). \tag{9.4}$$

The function $\eta_{\rm DD}(R^*/a)$ has been computed in Ref. [Lev11]. Here we calculate $\tilde{\eta}_{\rm LiD}(R^*/a)$ and $\tilde{\eta}_{\rm KD}(R^*/a)$, as described in the Appendix. We show these functions together in Fig. 9.7(b); again we see how collisional losses can be strongly suppressed for $R^*/a \lesssim 1$, and that relaxation losses originating from light atoms and cc molecules are more important than those from heavy atoms and cc molecules.

Let us now discuss the limiting case of large detuning, $R^* \gg a$. Neglecting the open-channel population, we obtain $\eta_{\rm DD}(R^*/a \to \infty) = 1$ and $\tilde{\eta}_{\rm AD}(R^*/a \to \infty) = 0$, where A=Li, K. Note that $\tilde{\eta}_{\rm AD}$ is not equal to $\eta_{\rm AD}$, which is defined for atom-molecule collisions and tends to 1 in the large R^*/a limit. As expected, these results mean that $\beta_{\rm D}(R^*/a \to \infty) = \beta^{(0)}_{\rm D}$ and $\beta_{\rm AD}(R^*/a \to \infty) = \beta^{(0)}_{\rm AD}$. For large but finite R^*/a, we

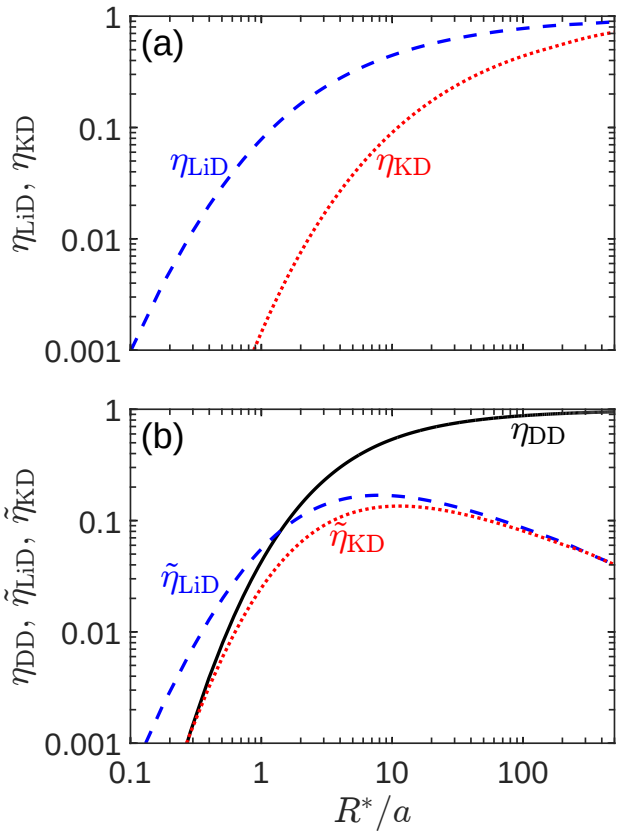

Figure 9.7: Suppression functions for relaxation in (a) atom-dimer and (b) dimer-dimer collisions.

can perturbatively take into account the probability to be in the open channel $P_{\text{open}} \approx \sqrt{a/4R^*} \ll 1$, arriving at $\tilde{\eta}_{\text{AD}} \approx 2P_{\text{open}} \approx \sqrt{a/R^*}$ and $\eta_{\text{DD}} \approx P^2_{\text{closed}} \approx 1 - \sqrt{a/R^*}$.

In the opposite limit of small detuning, $R^*/a \ll 1$, the feature of particular interest is the suppression of collisional relaxation which arises from the large open-channel probability combined with Pauli suppression: The inelastic process requires at least three atoms – of which two are identical fermions – to approach each other. More precisely, the Pauli suppression mechanism is efficient at distances (hyper-radii) $R^* \ll r \ll a$, which is called the universal region, where the atoms behave as free (open-channel) atoms. At shorter distances, the three-atom configuration changes to the atom plus cc molecule one, which is insensitive to the statistical suppression. This argument applies to the atom-cc molecule relaxation mechanism in both atom-dimer and dimer-dimer collisions, thus suppressed by the factor

$$\eta_{\text{AD}} \propto \tilde{\eta}_{\text{AD}} \propto (R^*/a)^{2\nu_s+1}. \tag{9.5}$$

The exponent ν_s characterizes the three-body wave function in the universal region and depends on the masses, quantum statistics of atoms, and the total angular momentum (the subscript s means $l = 0$)[4]. For the relevant cases of Li (K) atoms scattering on LiK dimers, we have $\nu_s \approx 1.01$ ($\nu_s \approx 2.02$), respectively [Lev11]. The onset of the power-law suppression can be seen in Fig. 9.7.

For $R^*/a \ll 1$, the four-atom loss mechanism is also suppressed. This suppression has the same origin (Pauli principle) as in the three-atom case: Four atoms consisting of two pairs of identical fermions have to approach each other to the recombination region. In this case, we have $\eta_{\text{DD}} \propto (R^*/a)^{2\nu_{\text{4-body}}+4}$. Here the power $\nu_{\text{4-body}}$ characterizes the scaling of the four-atom wave function in the universal region and can be inferred from the energy of four trapped fermions at unitarity: Ref. [Ste08a] gives $\nu_{\text{4-body}} \approx 0.0$, 0.3, and 0.5 for mass ratios of 1, 4, and 8, respectively. Our calculation for the LiK mass ratio is consistent with this sequence.

9.4.2 Comparison with experimental data

Here we compare our theoretical predictions for the collisional loss-rate coefficients to our measured values, which we already presented in Figs. 9.5 and 9.6. In our theoretical model, the three bare rate constants $\beta^{(0)}_{\text{D}}$, $\beta^{(0)}_{\text{LiD}}$, and $\beta^{(0)}_{\text{KD}}$ are free parameters,

[4] In dimer-dimer collisions, three atoms can approach each other in different angular momentum channels. In the narrow resonance case, the p-wave contribution to β_{D} for small R^*/a scales as $(R_e/R^*)^2(R^*/a)^{2\nu_p+1}$ and should be multiplied by a quantity of order $\hbar R_e/\mu$. The factor $(R_e/R^*)^2$ comes from the centrifugal barrier which the cc molecule and atom experience at distances $\lesssim R^*$. In our case this factor gives a four order of magnitude suppression and we neglect this relaxation channel. However, in the wide-resonant case this channel is dominant since $\nu_p < \nu_s$ [Pet04b, Pet05b, Pet05a].

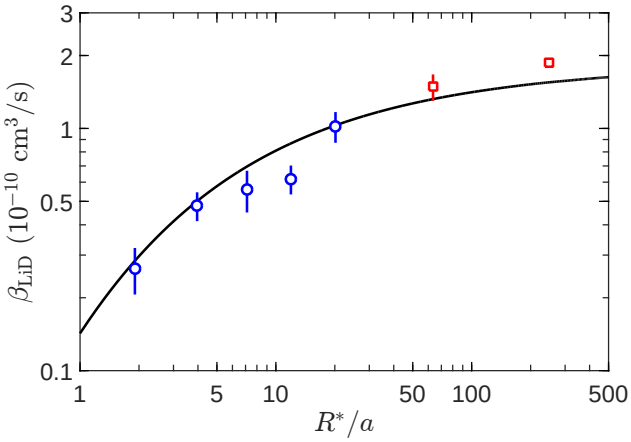

Figure 9.8: Atom-dimer loss-rate coefficient β_{LiD} as a function of R^*/a. The experimental data (blue circles and red squares obtained with Li|1⟩K|3⟩ and Li|1⟩K|1⟩ dimers, respectively) are identical to the ones displayed in Fig. 9.6, with the unphysical negative value excluded. The black solid line corresponds to a fit of our theoretical model to the data, yielding $\beta^{(0)}_{\mathrm{LiD}} = 1.8(2)\times 10^{-10}\mathrm{cm}^3/\mathrm{s}$.

and they can in principle be determined by fitting to the experimental data. Alternatively, estimates can be obtained from a simple quantum Langevin model [Gao10, Jul11, Qué11]. This model uses only the van der Waals range of the corresponding atom-dimer or dimer-dimer interaction potential and assumes total absorption (loss) at shorter distances.

For collisions of Li atoms with LiK dimers, the comparison is straightforward, since $\beta^{(0)}_{\mathrm{LiD}}$ is the only free parameter, which enters as a prefactor according to Eq. (9.3). Accordingly, we fit $\beta_{\mathrm{LiD}}(R^*/a) = \beta^{(0)}_{\mathrm{LiD}}\eta_{\mathrm{LiD}}(R^*/a)$ to the experimental data and extract the value $\beta^{(0)}_{\mathrm{LiD}} = 1.8(2)\times 10^{-10}\mathrm{cm}^3/\mathrm{s}$. The fit curve is shown as the black solid line in Fig. 9.8 and shows that the theory matches the experimentally observed behavior very well. In particular, we can clearly confirm that the observed reduction of losses can be attributed to the Pauli suppression effect.

The value for $\beta^{(0)}_{\mathrm{LiD}}$ obtained from our fit analysis corresponds to about half of the value suggested by the quantum Langevin model amounting to $3.5\times 10^{-10}\mathrm{cm}^3/\mathrm{s}$. Similar deviations have previously been observed in other experiments, in particular

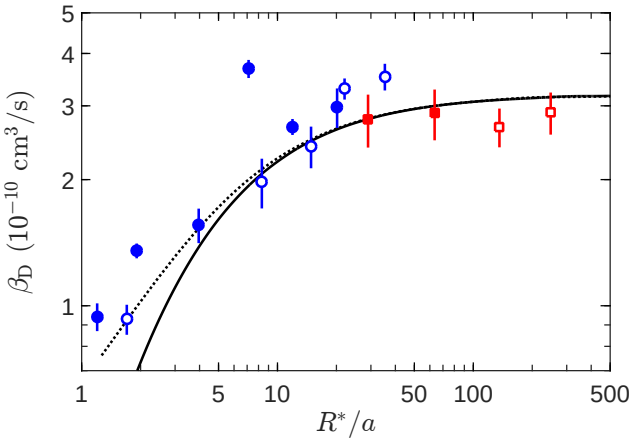

Figure 9.9: Total dimer-dimer loss-rate coefficient β_D as a function of R^*/a. The experimental data (blue circles and red squares obtained with Li|1⟩K|3⟩ and Li|1⟩K|1⟩ dimers, respectively) are the same as those displayed in Fig. 9.5. The solid line corresponds to a fit of our theoretical prediction for $\beta_D = \beta_D^{(0)}\eta_{DD} + \beta_{LiD}^{(0)}\tilde{\eta}_{LiD} + \beta_{KD}^{(0)}\tilde{\eta}_{KD}$ to the data, with $\beta_D^{(0)}$ being the only free parameter (see text). The dotted line corresponds to our prediction from an extended, finite-temperature theory[6].

those involving light atoms [Wan13].

For collisions between dimers, the situation is more involved because of the three different channels—Li-cc molecule, K-cc molecule, and cc molecule-cc molecule—with the corresponding three free parameters $\beta_{LiD}^{(0)}$, $\beta_{KD}^{(0)}$, and $\beta_D^{(0)}$; see Eq. (9.4). According to our model, the dominant loss contribution is expected from the four-body channel. In order to extract the corresponding bare rate coefficient $\beta_D^{(0)}$, we perform a one-parameter fit after fixing $\beta_{LiD}^{(0)}$ to the measured value discussed before and fixing $\beta_{KD}^{(0)}$ to the value 1.4×10^{-10}cm^3/s calculated within the quantum Langevin model[5]. We finally obtain $\beta_D^{(0)} = 3.2(6) \times 10^{-10}$cm^3/s, which we find to be very close the quan-

[5]Treating $\beta_{KD}^{(0)}$ also as a free parameter leads to an unphysically large value for $\beta_{KD}^{(0)}$. We attribute this to strong correlations between the fit parameters and residual finite-temperature effects. For the fit we discard the three data points below $R^*/a < 2$ to make it less sensitive to the finite-temperature effects. We also discard the outlier point at $R^*/a = 7.1$. By trying out different fit strategies we find that the final value obtained for $\beta_D^{(0)}$ is robust, with variations staying well below 20%.

tum Langevin value, $\beta_D^{(0)} = 3.0\times10^{-10}\mathrm{cm}^3/\mathrm{s}$. The resulting total decay rate $\beta_D(R^*/a)$ is shown as the black solid line in Fig. 9.9. Our theoretical approach reproduces the observed suppression of collisional relaxation as we approach the Feshbach resonance for $R^*/a \gtrsim 3$.

Closer to the Feshbach resonance ($R^*/a < 3$), we see clear deviations. We ascribe this discrepancy to temperature effects, which become more prominent when $k_B T$ is comparable to or larger than the dimer binding energy [Lev11]. In this case, the identical fermions may more easily approach each other, thereby reducing the Pauli suppression factor. A theoretical prediction obtained from a finite-temperature calculation for $T = 550\,\mathrm{nK}$[6] is shown as the black dotted line. Including finite temperature into our theoretical approach improves the match of theory and experiment near the resonance. From our finite-temperature calculations, we also find that corresponding effects on the collisions of Li atoms with LiK dimers, as discussed before, remain much smaller[6].

The good agreement between our theoretical approach and our experimentally obtained values for the loss coefficients validates the assumptions of our theoretical approach to collisional losses developed in Ref. [Lev11]. Furthermore, our results demonstrate that the bare rate coefficients can be well estimated by the value obtained from the quantum Langevin model. The agreement with our measurements therefore suggests a predictive power of our theory applied to other Fermi-Fermi systems.

9.5 Other potential Fermi-Fermi systems

Fermi-Fermi systems that feature mass imbalance, collisional stability and tunable interactions may be created with mixtures other than ^{6}Li-^{40}K. To date, Fermi degeneracy has been demonstrated for isotopes of eight chemical elements, i.e., He [McN06], Li [Tru01, Sch01a], K [DeM99], Cr [Nay15], Sr [DeS10, Tey10], Dy [Lu12], Er [Aik14], and Yb [Fuk07b], providing a wealth of possible combinations. We focus our attention on mixtures of ^{161}Dy and ^{40}K (mass ratio 4.0) and ^{53}Cr and ^{6}Li (8.8), and we discuss the corresponding suppression functions for collisional losses. Larger mass ratios (comparable or larger than 13.6) require an analysis beyond the scope of our present work. In this case, the Efimov [Efi73] and other few-body effects [Kar07, Cas10, Blu12] can lead to the appearance of new loss-rate features [Mar08a].

The suppression functions for losses in atom-dimer collisions are shown in the upper panels of Fig. 9.10 for (a) the mass-balanced system, (b) the ^{161}Dy-^{40}K mixture, and (c) the ^{53}Cr-^{6}Li mixture. We observe that mixtures of heavy-species atoms and

[6] D.S. Petrov and J. Levinsen, *unpublished*

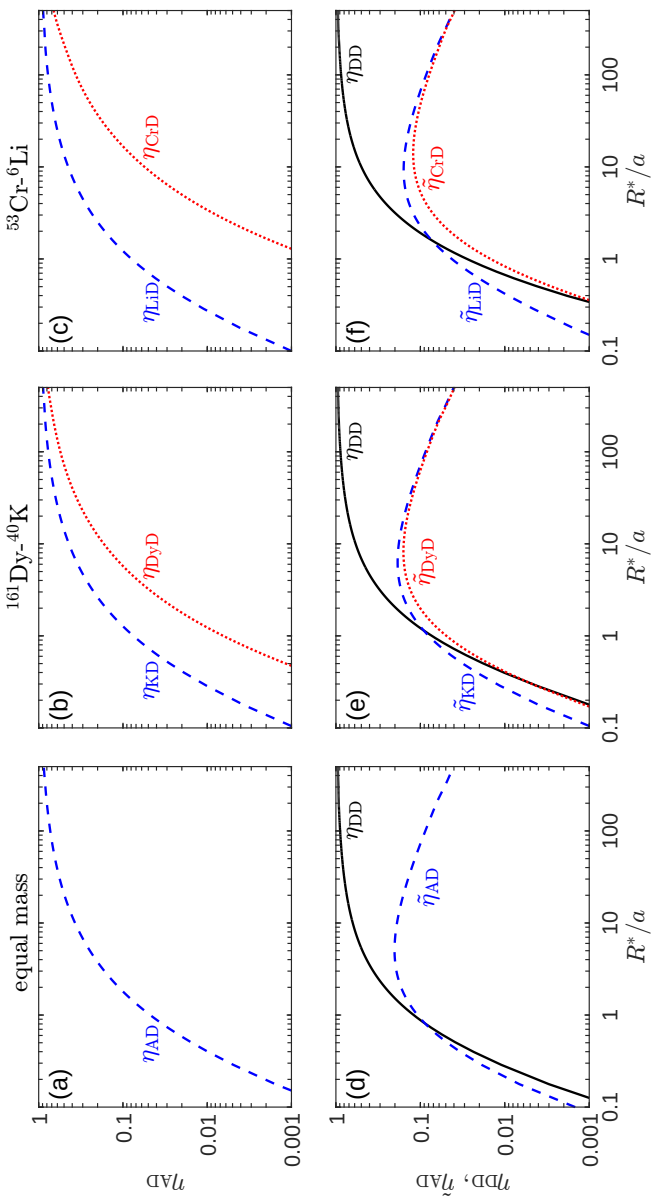

Figure 9.10: (a) Suppression functions for losses in (a)-(c) atom-dimer and (d)-(f) dimer-dimer collisions. We consider these for equal masses, Dy-K mixtures with a mass ratio of 4.0, and mixtures of Cr and Li where the mass ratio is 8.8.

dimers (red dotted lines) show a much stronger suppression compared to the mass-balanced case (blue dashed line in Fig. 9.10(a)), which strengthens with increasing mass imbalance. For the case of the Dy-K (Cr-Li) mixture, this increase amounts to almost one (two) orders of magnitude at R^*/a corresponding to about 1. On the contrary, the mixtures composed of light-species atoms and dimers [blue dashed lines in Fig. 9.10(b) and (c)] show only a weak enhancement of losses as compared to the mass-balanced case, amounting to a factor of about 1.5 for both the Dy-K and the Cr-Li mixture at $R^*/a = 1$.

The suppression functions for losses in collisions between dimers are shown in Figs. 9.10(d)- 9.10(f) for the equal-mass system, and the systems with a mass imbalance of 4 and 8.8, respectively. All three contributions, i.e., from the light atom-dimer, heavy atom-dimer, and dimer-dimer part, shown in Figs. 9.10(e) and 9.10(f) as the blue dashed, red dotted, and black solid lines, respectively, are significantly smaller than their equal-mass counterparts [blue dashed and black solid lines in Fig. 9.10(d)].

In view of future experiments on strongly interacting Fermi-Fermi systems, we can now provide estimates for the minimum strength of a suitable Feshbach resonance. The conditions of the successful experiments with spin mixtures of ^{40}K or ^{6}Li suggest a minimum required suppression of losses by two orders of magnitudes for all possible channels. According to our theoretical results (Figs. 9.7 and 9.10), this would correspond to a condition of $R^*/a \lesssim 0.3$ for all mass-imbalanced mixtures considered. For the relevant scattering length, we may take $a \approx 3000\, a_0$ as a typical value for dimers entering the strongly interacting Fermi gas regime. We thus obtain the approximate condition $R^* \lesssim 1000\, a_0$ for a Feshbach resonance to provide sufficient collisional stability.

9.6 Summary and Conclusion

In a joint experimental and theoretical effort, we have investigated the stability of weakly bound dimers formed near narrow interspecies Feshbach resonances in Fermi-Fermi mixtures. In our laboratory system —the mixture of ^{6}Li and ^{40}K atoms— we have characterized the dependence of three different decay processes on the magnetic detuning from the Feshbach-resonance center. In dilute samples, spontaneous dissociation (one-body process) is observed for dimers composed of atoms that are not in the lowest spin channel, and the measured lifetimes are found to be in a full agreement with a previous theoretical prediction. In dense samples, we have measured the rate coefficients for inelastic dimer-dimer collisions as well as collisions of the lighter atomic species with the dimers. For all decay processes, we find a significant suppression when the resonance center is approached.

Our theoretical framework for the description of collisional losses near narrow Feshbach resonances is based on a model that has been developed in Ref. [Lev11]. The basic idea is a separation of the problem into a long-range description of the three- and four-body kinematics and a simple relaxation model at short range. The reduction of collisional decay near the resonance center is described by corresponding suppression functions. In extension of the previous work [Lev11], we have calculated the suppression functions for all relevant loss channels in atom-dimer and dimer-dimer collisions. The comparison of theoretical and experimental results for the mixture of ^{6}Li and ^{40}K shows excellent agreement, thus validating the assumptions of our theoretical model.

The observed collisional suppression does not exceed a factor of about five, and thus stays far below what has been observed in homonuclear systems near broad resonances. Nevertheless, our present work shows that the ^{6}Li-^{40}K system, in spite of the narrow nature of interspecies resonances [Wil08, Nai11, Tie10], can potentially exhibit a strong Pauli suppression of collisional losses, provided the density and resonance detunings can be substantially reduced. Under such conditions, spontaneous dissociation can be expected to become the dominant loss mechanism, with a strong effect on the system. This loss process could be avoided by choosing resonances in the lowest spin channel, which are all very narrow. The level of control required to manipulate the Li-K mixture at very low densities near the narrow resonances is very challenging, going far beyond typical conditions of the present Fermi gas experiments.

Other Fermi-Fermi mixtures are very promising for new experiments in the near future, and we have discussed the ^{161}Dy-^{40}K case (mass ratio 4.0) and the ^{53}Cr-^{6}Li case (8.8) as two illustrative examples. Efforts to realize these systems are under way in different laboratories, and their yet unknown interaction properties need to be explored. The suppression functions that we have calculated for the corresponding mass ratios provide a guide for identifying suitable Feshbach resonances in future experimental

work. In general, our results suggest that broad Feshbach resonances are not necessarily required to obtain sufficient collisional stability. Instead, moderately narrow resonances are also promising for realizing new experimental model systems and for exploring the multifaceted many-body physics of fermionic mixtures [Liu03, Cal05, Isk06, Lin06, Par07, Isk08, Bar08, Bau09c, Gez09, Baa10, Bra14, Bra15].

Acknowledgments

We thank J. Walraven and M. Zaccanti for stimulating discussions. M. J., M. C., R. S. L., and R. G. acknowledge support by the Austrian Science Fund FWF within the Spezialforschungsbereich (SFB) FoQuS, project part P04 (Grant No. F4004-N23). The research leading to the theoretical results received funding from the European Research Council (FR7/2007-2013 Grant Agreement No. 341197). D. S. P. thanks IFRAF for support.

9.7 Appendix: Theoretical approach to collisional decay

Here, we present our calculation of the probability to find an atom close to a closed-channel molecule in dimer-dimer collisions. As discussed in the main text, this probability allows us to extract the contribution from the corresponding relaxation channel to the dimer-dimer relaxation rate constant β_{D}. This extends our previous calculation of the cc molecule–cc molecule relaxation channel, as presented in Ref. [Lev11]. Throughout this appendix, we set $\hbar = 1$ and work in a unit volume.

We now briefly recapitulate the theoretical description of our system. We consider two species of fermions labeled by $\sigma = \uparrow, \downarrow$ and employ the two-channel Hamiltonian [Tim99],

$$\begin{aligned}\hat{H} = &\sum_{\mathbf{k},\sigma=\uparrow,\downarrow} \epsilon_{\mathbf{k},\sigma} \hat{a}^\dagger_{\mathbf{k},\sigma} \hat{a}_{\mathbf{k},\sigma} + \sum_{\mathbf{p}} \left(\omega_0 + \epsilon_{\mathbf{p},\mathrm{M}}\right) \hat{b}^\dagger_{\mathbf{p}} \hat{b}_{\mathbf{p}} \\ &+ g \sum_{\mathbf{k},\mathbf{p}} \left(\hat{b}^\dagger_{\mathbf{p}} \hat{a}_{\frac{\mathbf{p}}{2}+\mathbf{k},\uparrow} \hat{a}_{\frac{\mathbf{p}}{2}-\mathbf{k},\downarrow} + \hat{b}_{\mathbf{p}} \hat{a}^\dagger_{\frac{\mathbf{p}}{2}-\mathbf{k},\downarrow} \hat{a}^\dagger_{\frac{\mathbf{p}}{2}+\mathbf{k},\uparrow} \right). \end{aligned} \tag{9.6}$$

Here, $\hat{a}^\dagger_{\mathbf{k},\sigma}$ ($\hat{a}_{\mathbf{k},\sigma}$) creates (annihilates) a spin σ atom of mass m_σ with momentum $\mathbf{k}$ and single-particle energy $\epsilon_{\mathbf{k},\sigma} = \frac{k^2}{2m_\sigma}$. Likewise, $\hat{b}^\dagger_{\mathbf{k}}$ and $\hat{b}_{\mathbf{k}}$ are the creation and annihilation operators of the cc molecule with mass $M = m_\uparrow + m_\downarrow$, kinetic energy $\epsilon_{\mathbf{k},\mathrm{M}} = \frac{k^2}{2M}$, and detuning ω_0 from the $\uparrow\downarrow$ scattering threshold. The interaction between the atoms is mediated by the cc molecule as described by the last term of the Hamiltonian, where

the strength g of the interconversion term is taken to be constant up to a momentum cutoff Λ. The bare parameters of the model are related to the physical scales, the scattering length and length parameter R^*, through (see, e.g., [Gur07])

$$a = \frac{m_r g^2}{2\pi} \frac{1}{\frac{g^2 m_r \Lambda}{\pi^2} - \omega_0}, \qquad R^* = \frac{\pi}{m_r^2 g^2}, \tag{9.7}$$

with $m_r = m_\uparrow m_\downarrow / M$ the reduced mass. The propagator of the atoms takes the form

$$G_\sigma(\mathbf{p}, p_0) = \frac{1}{p_0 - \epsilon_{\mathbf{p},\sigma} + i0}, \tag{9.8}$$

where the notation $+i0$ specifies that the pole of p_0 is shifted slightly into the lower half of the complex plane. The propagator of dimers is obtained by dressing the cc molecule propagator by pairs of free $\uparrow\downarrow$ atoms, resulting in

$$D(\mathbf{p}, p_0) = \frac{2\pi/m_r}{2m_r R^* \left(p_0 - \frac{p^2}{2M} + i0\right) + \frac{1}{a} - \sqrt{2m_r}\sqrt{-p_0 + \frac{p^2}{2M} - i0}}. \tag{9.9}$$

At zero momentum, this has a pole at the dimer binding energy $\epsilon_0 = -(\sqrt{1 + 4R^*/a} - 1)^2/(8m_r R^{*2})$.

To extract the relaxation rate for the three-atom process in a dimer-dimer collision, we introduce a weak short-range interaction potential between the $\uparrow$ atom and the bare molecule in the Hamiltonian (see Ref. [Lev11]):

$$\delta \hat{H}_{\uparrow \mathrm{D}} = -i\Delta_{\uparrow \mathrm{D}} \sum_{\mathbf{Q},\mathbf{k},\mathbf{p}} \hat{b}^\dagger_{\mathbf{p}} \hat{a}^\dagger_{\uparrow,\mathbf{Q}-\mathbf{p}} \hat{b}_{\mathbf{k}} \hat{a}_{\uparrow,\mathbf{Q}-\mathbf{k}}. \tag{9.10}$$

The coefficient $\Delta_{\uparrow \mathrm{D}}$ is related to the relaxation coupling constant through $g_{\uparrow \mathrm{D}} = -i\Delta_{\uparrow \mathrm{D}}$. The probability to find the $\uparrow$ atom close to the cc molecule in dimer-dimer scattering at zero collisional energy is then

$$\tilde{\eta}_{\uparrow \mathrm{D}}(R^*/a) = -\mathrm{Im}[\delta T(0)]/(2\Delta_{\uparrow \mathrm{D}}), \tag{9.11}$$

where $\delta T(0)$ is the change in the s-wave dimer-dimer scattering T matrix to linear order in $\Delta_{\uparrow \mathrm{D}}$. The change in the dimer-dimer scattering length to the same order is in turn $\delta a_{\mathrm{DD}} = \delta T(0) M/(4\pi)$. We calculate this change diagrammatically as illustrated in Fig. 9.11: First, we consider all diagrams contributing to δT which are two-dimer irreducible (i.e. do not have two dimers propagating simultaneously). We then include

all two-dimer reducible processes by replacing the incoming and/or outgoing dimers by the full dimer-dimer T matrix.

Consider first the sum of diagrams in Fig. 9.11(a) constituting all two-dimer irreducible contributions to $\delta T(0)$. Taking the incoming [outgoing] dimers to have four momenta $(\pm\mathbf{p}, p_0 + \epsilon_0)$ $[(\pm\mathbf{q}, q_0 + \epsilon_0)]$, we denote this sum by $\delta\tilde{T}(p, p_0; q, q_0)$. This does not depend on the angle between $\mathbf{p}$ and $\mathbf{q}$ as we take the s-wave projection. Integrating over frequencies in the closed loops of the diagrams in Fig. 9.11(a) yields, for the two-dimer irreducible contribution to $\delta T(0)$,

$$\begin{aligned}
\delta\tilde{T}(p, p_0; q, q_0) = -2i\Delta_{\uparrow\mathrm{D}} g^2 Z^2 \int \frac{d\Omega_{\mathbf{p}}}{4\pi} \int \frac{d\Omega_{\mathbf{q}}}{4\pi} \\
\times \Bigg[2 \sum_{\mathbf{Q}} G_\uparrow(\mathbf{p}-\mathbf{Q}, \epsilon_0 + p_0 - \epsilon_{\mathbf{Q},\downarrow}) G_\uparrow(\mathbf{q}-\mathbf{Q}, \epsilon_0 + q_0 - \epsilon_{\mathbf{Q},\downarrow}) \\
+ \sum_{\mathbf{p}_1,\mathbf{p}_2} \chi(p, p_0; \mathbf{p}_1, \mathbf{p}_2) D(\mathbf{p}_1 + \mathbf{p}_2, 2\epsilon_0 - \epsilon_{\mathbf{p}_1,\uparrow} - \epsilon_{\mathbf{p}_2,\downarrow}) G_\uparrow(\mathbf{q}-\mathbf{p}_1, \epsilon_0 + q_0 - \epsilon_{\mathbf{p}_1,\uparrow}) \\
+ \sum_{\mathbf{p}_1,\mathbf{p}_2} \chi(q, q_0; \mathbf{p}_1, \mathbf{p}_2) D(\mathbf{p}_1 + \mathbf{p}_2, 2\epsilon_0 - \epsilon_{\mathbf{p}_1,\uparrow} - \epsilon_{\mathbf{p}_2,\downarrow}) G_\uparrow(\mathbf{p}-\mathbf{p}_1, \epsilon_0 + p_0 - \epsilon_{\mathbf{p}_1,\uparrow}) \\
+ \sum_{\mathbf{p}_1,\mathbf{p}_2,\mathbf{p}_2'} \chi(p, p_0; \mathbf{p}_1, \mathbf{p}_2) \chi(q, q_0; \mathbf{q}_1, \mathbf{q}_2) D(\mathbf{p}_1 + \mathbf{p}_2, 2\epsilon_0 - \epsilon_{\mathbf{p}_1,\uparrow} - \epsilon_{\mathbf{p}_2,\downarrow}) \times \\
D(\mathbf{p}_1 + \mathbf{p}_2', 2\epsilon_0 - \epsilon_{\mathbf{p}_1,\uparrow} - \epsilon_{\mathbf{p}_2',\downarrow}) \Bigg],
\end{aligned} \tag{9.12}$$

where we integrate over the angles of $\mathbf{p}$ and $\mathbf{q}$. $Z = 1 - 1/\sqrt{1 + 4R^*/a}$ is the dimer residue at the energy pole. The function $\chi(p, p_0; \mathbf{p}_1, \mathbf{p}_2)$ is the sum of all diagrams with two incoming dimers at four momenta $(\pm\mathbf{p}, p_0 + \epsilon_0)$, an outgoing $\uparrow$ [$\downarrow$] atom with $(\mathbf{p}_1, \epsilon_{\mathbf{p}_1,\uparrow})$ $[(\mathbf{p}_2, \epsilon_{\mathbf{p}_2,\downarrow})]$, and an outgoing dimer with $(-\mathbf{p}_1 - \mathbf{p}_2, 2\epsilon_0 - \epsilon_{\mathbf{p}_1,\uparrow} - \epsilon_{\mathbf{p}_2,\downarrow})$. The sum is averaged over the angle of $\mathbf{p}$. χ satisfies an integral equation derived in Ref. [Lev11]; for the expression, we refer the reader to Eq. (29) of that paper.

Finally, we relate δT to the two-dimer irreducible diagrams by allowing for any number of dimer-dimer scattering events on the left and/or right side of $\delta\tilde{T}$; see Fig. 9.11(b). The relation is

$$\begin{aligned}
\delta T(0) =& \delta\tilde{T}(0, 0; 0, 0) + 2 \int \frac{i\, dp_0}{2\pi} \sum_{\mathbf{p}} F(p, p_0) \delta\tilde{T}(p, p_0; 0, 0) \\
&+ \int \frac{i\, dp_0}{2\pi} \frac{i\, dq_0}{2\pi} \sum_{\mathbf{p},\mathbf{q}} F(p, p_0) \delta\tilde{T}(p, p_0; q, q_0) F(q, q_0),
\end{aligned} \tag{9.13}$$

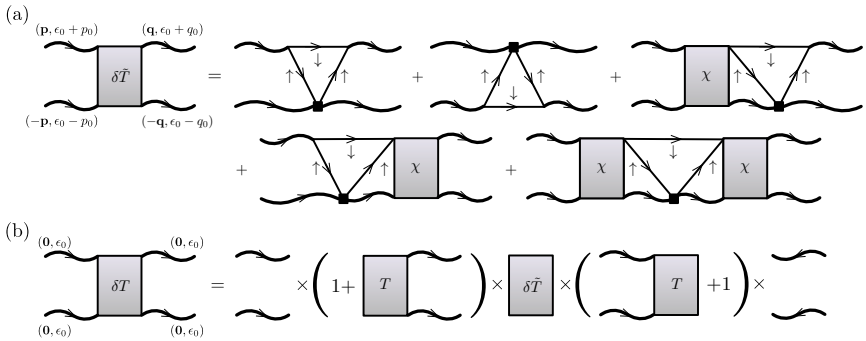

Figure 9.11: Diagrams contributing to the ↑ atom-cc molecule loss process in dimer-dimer collisions. The loss vertex (9.10) is depicted as a black square. Straight lines are atom propagators, while the dimer propagators are illustrated with wavy lines. All filled boxes represent sums of diagrams. (a) The two-dimer irreducible diagrams denoted $\delta\tilde{T}$ contributing to δT can be obtained from the vertex χ (see text). (b) All diagrams in δT can be obtained from the two-dimer irreducible diagrams by the use of the full dimer-dimer T matrix (see text). In both subfigures, the external dimer lines are for illustration only.

where $F(p, p_0) \equiv \frac{1}{g^2 Z} T(p, p_0) D(\mathbf{p}, p_0 + \epsilon_0) D(-\mathbf{p}, -p_0 + \epsilon_0)$, with $T(p, p_0)$ the dimer-dimer T matrix in the absence of the perturbation (9.10). To avoid poles and branch cuts, the p_0 and q_0 integration contours are rotated to the imaginary axis. The dimer-dimer T matrix satisfies an integral equation derived in Ref. [Lev11]; see Eq. (28) of that paper.

APPENDIX A

Cooling and Trapping of ^{41}K

Bosonic ^{41}K is one of the three naturally occurring isotopes of potassium. Potassium is an alkali-metal with an atomic number $Z = 19$ and an electron configuration of $1s^2 2s^1 2p^6 3s^2 3p^6 4s^1$. Besides ^{41}K, with an natural abundance of 6.73%, there is bosonic ^{39}K (93.26%) and fermionic ^{40}K (0.01%) [Ros98]. The latter is a long-lived radioisotope with a half-life of 1.277×10^9 years. For a thorough review of the properties of all three potassium isotopes see Ref. [Tie09a]. All three species have been trapped and cooled to degeneracy [Mod01, Roa07, DeM99] and ^{40}K was the first degenerate Fermi gas created.

In this Appendix, I will describe the adjustments I made to the FeLi(Bo)Kx experiment for trapping and cooling a pure spin state of ^{41}K instead of the earlier implemented ^{40}K isotope [Wil09]. This includes the changes to the existing laser setup and to the experimental sequence, where potassium is sympathetically cooled by a lithium spin mixture [Spi10]. Switching between the two isotopes only involves rotating two waveplates on the laser table and selecting the different isotope in the control software, which automatically changes the loading sequence. Thus, the experiment can now make ultracold mixtures of ^{6}Li and either ^{40}K or ^{41}K. With some slight changes the more abundant bosonic isotope of ^{39}K can also be cooled and trapped. However, the predicted Feshbach resonances between ^{39}K and ^{6}Li are relatively narrow, with a width below 50 mG [Han17], and this makes it experimentally challenging to access the strongly interacting regime, without being limited by the FR associated losses. For ^{41}K a fairly broad heteronuclear Feshbach resonance exists, as explored in Chap. 5 and
.

A.1 Optical Transitions and Spin States

The energy diagrams of the D-line doublet and the optical transitions used for cooling and trapping of all three potassium isotopes are shown in figure A.1. For ^{41}K, the nuclear angular momentum I is $3/2$. The electronic ground state is a $4\,^2S_{1/2}$ state and the zero field splitting between the $F = 2$ and $F = 1$ state is 254 MHz [Tie09a].

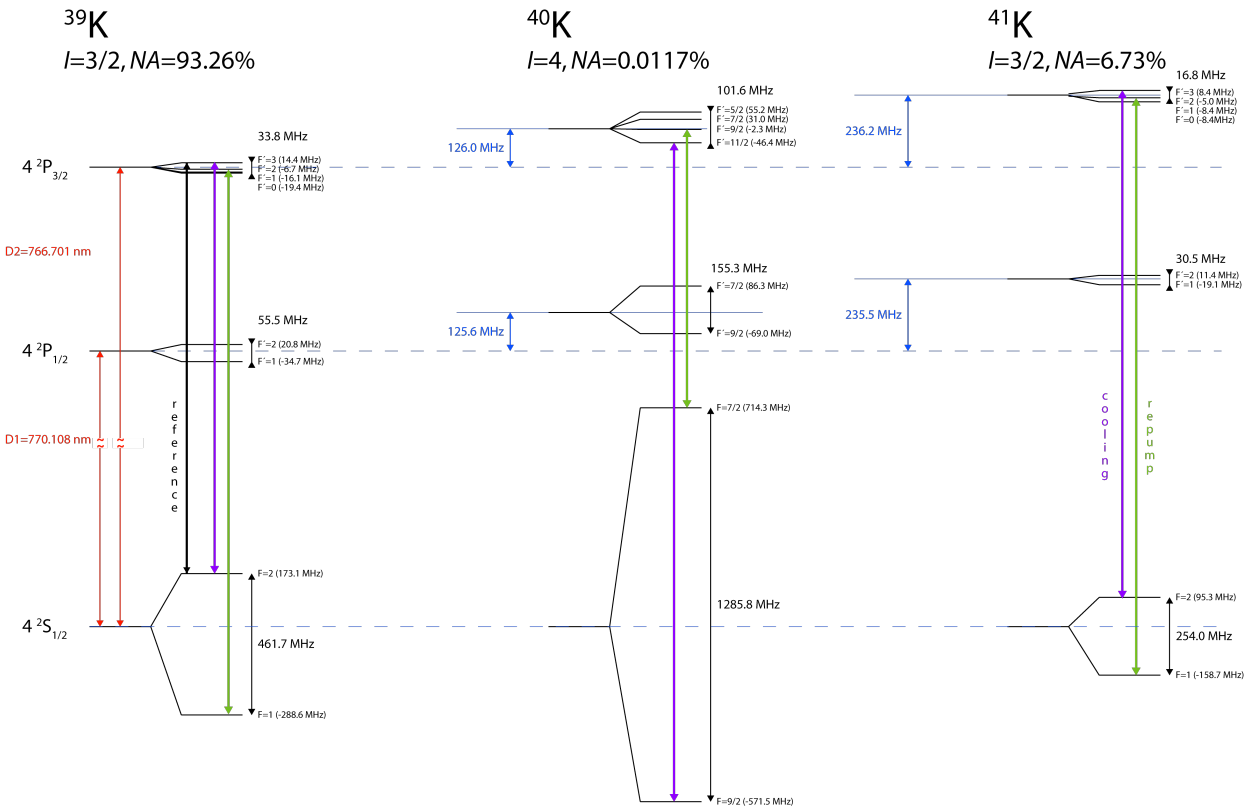

Figure A.1: Energy level diagrams of the three potassium isotopes. The purple arrows show the cooling transitions and the green arrows the repump transitions. The transition to which the main laser is locked is shown as the black arrow. The nuclear angular momentum quantum number I and the natural abundance NA of the isotopes are also indicated. Figure adjusted from [Wil09] and based on data from [Tie09a].

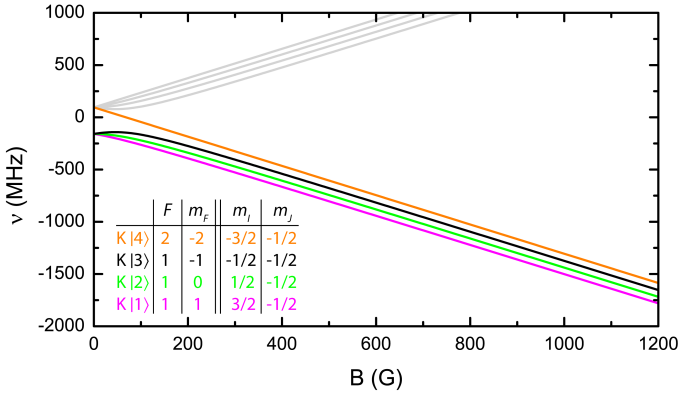

Figure A.2: Magnetic field dependence of the hyperfine structure of the $4\,^2S_{1/2}$ state of ^{41}K. Both the low-field quantum numbers F and m_F as well as the high-field quantum numbers m_I and m_J are indicated for the four spin states accessible in the experiment.

The D2 line between the ground state and the $4\,^2P_{3/2}$ excited state, is used for the ^{41}K magneto-optical trap (MOT) and Zeeman slower light. The cooling light is red detuned from the $F = 2 \rightarrow F' = 3$ transition and the repump light is red detuned from the $F = 1 \rightarrow F' = 2$ transition. The excited states $F' = 3$ and $F' = 2$ of the $4\,^2P_{3/2}$ level are only 13.4 MHz apart and atoms can therefore be pumped into the $F = 1$ state. To bring the atoms back into the cycling cooling transition, repump light is needed. The line widths of the transitions are about 6 MHz and the saturation intensity is $I_s = 1.75\,\mathrm{mW/cm^2}$ [Tie09a]. The reference frequency to which we directly lock the master laser is the $F = 2 \rightarrow F' = 3$ atomic transition of ^{39}K.

The magnetic field dependence of the hyperfine structure of the $4^2S_{1/2}$ state of ^{41}K can be calculated with the Breit-Rabi formula [Tie09a]. For the magnetic fields addressed in the experiment, four low-field seeking hyperfine states of ^{41}K are of interest as is shown in Fig. A.2. These are labeled from lowest-to-highest energy as $\mathrm{K}|1,2,3,4\rangle$. The splitting between these hyperfine states is typically 50-80 MHz and allows for the manipulation of the spin state of the atoms with radio-frequency pulses.

A.2 MOT and CMOT Properties

In our oven, we have solid K metal, which acts as the source for ^{41}K. It is enriched to have 6% of ^{40}K and contains about 7% of ^{41}K. The K reservoir containing the metal is

Table A.1: Experimentally optimized parameters for the ^{41}K MOT and CMOT stages. δ_{cool} is the detuning from the cooling ($F = 2 \rightarrow F' = 3$) transition and δ_{repump} is the detuning from the repump ($F = 1 \rightarrow F' = 2$) transition.

	δ_{cool} (MHz)	δ_{repump} (MHz)	I_{cool}/I_{repump}	$\partial B/\partial z$ (G/cm)	$\partial B/\partial x$ (G/cm)
MOT	-22	-25	3	22	12
CMOT	-21	-9	9	83	46

heated up to about 200 °C and the atomic beam coming out of this oven chamber passes through two differential pumping sections before entering the Zeeman slower [Wil09]. For the Zeeman slower, the cooling light has a power of about 70 mW and a detuning of about -165 MHz from the $F = 2 \rightarrow F' = 3$ transition. The repump light in the Zeeman slower is equally detuned and is a factor of 2 lower in power.

Next, the atoms are captured in the glass cell by a MOT composed of 6 beams with a diameter of about 21 mm and a power per beam of typically 10 mW. This gives a peak intensity of 6 mW/cm^2, which is about six times the saturation intensity. For 10 s of initial MOT loading, we have about 10^5 K atoms. Subsequentially the K MOT is compressed by increasing the magnetic gradient and decreasing the repump light intensity by a factor of three. In this compressed MOT (CMOT), typically a temperature of 250 μK is reached which is above the Doppler temperature of 145 μK. The temperature could be further reduced by implementing sub-Doppler cooling techniques [Lan11] or a blue MOT [McK11]; however in our current scheme we do not rely on this. During the CMOT stage about 10% of the atoms are loaded into an optical dipole trap (ODT) with a wavelength of 1064 nm, a power of 150 W and waist of about 38 μm. The typical trap depth for K at loading is about 6.5 mK. The characteristic experimental parameters for the ^{41}K MOT and CMOT stages are listed in table A.1 and were optimized for loading the highest atom number into the single beam ODT trap in the presence of the Li MOT.

After the atoms are loaded into the ODT, we rely on sympathetic cooling of K while evaporating a Li spin mixture (see Chap. 4). The details of the procedure in combination with lithium are similar to the cooling and loading sequence of ^{40}K [Spi10]. The trap depth for potassium is roughly twice the trap depth for lithium, ensuring that potassium remains trapped during the evaporation. The *s*-wave background interaction between the ^{41}K atoms is about 60 a_0, which is similar to the background scattering length between K and Li, which is also about 60 a_0 [Tie17, D'E07, Pat14] (see Sec. 5.6.2). Therefore, away from inter- and intra-species Feshbach resonances,

the interactions between Li and K and among K atoms are relatively weak. Both the evaporation scheme at 1180 G with a Li$|1\rangle$-Li$|2\rangle$ spin mixture (see Chap. 4) and at 483 G with a Li$|1\rangle$-Li$|3\rangle$ spin mixture (see Sec. 5.6.1) work and create a BEC of ^{41}K. Here, Li$|1, 2, 3\rangle$ indicates the first, second and third lowest Zeeman spin states. In the final stage of the evaporation sequence, we reach a temperature of about 100 nK and typical atom numbers of 3×10^4 K atoms and 10^5 Li atoms in a crossed ODT.

A.3 Spin Relaxation

After loading into the ODT, we have a mixture of Li$|1\rangle, |2\rangle$ and K$|1\rangle, |2\rangle, |3\rangle$. The ratio between the different K states is about 1:1:2, where most atoms are in the K$|3\rangle$ state. Cooling down this sample with multiple K spin states can lead to atom losses or a spinor condensate [SK13] with miscible/immiscibile features [Liu16]. Therefore it is important to create a polarized sample of K, and we exploit a spin relaxation stage at the beginning of the evaporation sequence to do this. Already for ^{40}K we showed that spin exchange collisions can be used to populate a single spin state [Spi10]. The inverted hyperfine structure of ^{40}K favors spin relaxation into the lowest Zeeman spin state and by holding the Li-^{40}K sample at 40 G or at 207 G a spin pure ^{40}K sample could be obtained. For ^{41}K, we found a similar feature at about 200 G.

When a Li$|2\rangle$ atom collides with a ^{41}K$|1, 2, 3\rangle$ atom it can change its spin state to Li$|1\rangle$. Due to preservation of total m_F the K atom will end up in the $|2, 3, 4\rangle$ state, respectively. This inelastic collision is accompanied by a release of energy when the energy difference between the Li$|2\rangle$ and Li$|1\rangle$ states is higher than the energy difference between the initial and final K spin state. Vice versa a K atom in the $|2, 3, 4\rangle$ can collide with a Li$|1\rangle$ atom and change its spin state to K$|1, 2, 3\rangle$, whereby the Li atom will end up in Li$|2\rangle$. Also here depending on the energy difference between the spin states energy is released. Figure A.3 shows the difference between the subsequent spin states of potassium and the two lowest spin states of lithium for varying magnetic fields. This figure shows that in our mixture energy is released when spin exchange collisions between Li$|2\rangle$ and K$|1, 2\rangle$ happen and this will be on the order of a few tens of MHz. Furthermore above 400 G K$|3\rangle$ can spin flip into the K$|4\rangle$ state and at 400 G the energy difference between the K$|3\rangle$ and K$|4\rangle$ states matches that of the lithium spin states. The energy released E_r is distributed among the two colliding atoms, where most of the energy is carried away by lithium. Assuming the initial kinetic energy to be zero and fulfilling energy and momentum conservation, the kinetic energies of the

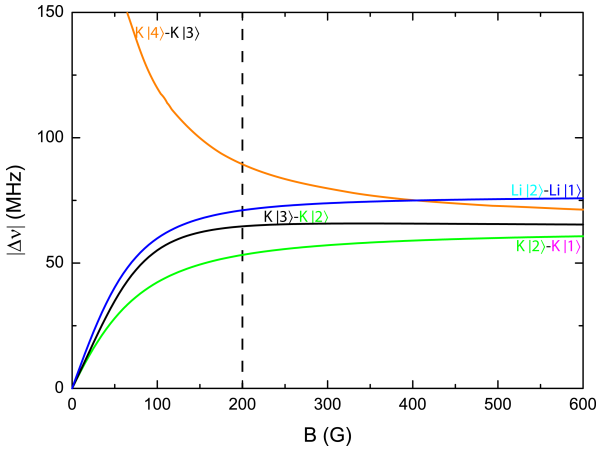

Figure A.3: Energy difference between hyperfine states for potassium and lithium as a function of magnetic field. The dashed line shows the magnetic field at which the spin relaxation stage takes place.

atoms after a Li-K spin exchange collision are

$$E_{kin,Li} = \frac{m_{\mathrm{K}}}{m_{\mathrm{K}} + m_{\mathrm{Li}}} E_{\mathrm{r}} \approx 0.87\, E_{\mathrm{r}}, \tag{A.1}$$

$$E_{kin,K} = \frac{m_{\mathrm{Li}}}{m_{\mathrm{K}} + m_{\mathrm{Li}}} E_{\mathrm{r}} \approx 0.13\, E_{\mathrm{r}}, \tag{A.2}$$

where $m_{\mathrm{K}}(m_{\mathrm{Li}})$ is the mass of potassium (lithium). As can be seen from Fig. A.3, the kinetic energy $E_{kin,K}$ a K atom can acquire due to spin exchange collisions is only a few MHz for magnetic fields up to 600 G. The initial trap depth of the ODT for potassium, after loading the atoms from the CMOT, is about 12 mK (240 MHz) and is subsequently decreased to about 1 mK (18 MHz) during the first evaporation stage. Comparing this trap depth to $E_{kin,K}$ shows that potassium will remain in the trap, even if spin exchange collisions are enhanced in the magnetic field range of 0-600 G.

We measure the effect of spin exchange collisions in a mixture of Li$|1,2\rangle$ and K$|1,2,3\rangle$ by looking at changes in the atom number for various magnetic fields. Right after loading into the ODT, we wait with the mixture for 500 ms at a given magnetic field. Then, we ramp the magnetic field to 1180 G and sympathetically cool the K atoms with the Li spin mixture before we take absorption images of the atoms after time-of-flight. At these high magnetic fields the different spin states of K and Li can

be imaged independently by using different imaging frequencies and the imaging transitions are almost closed. The measurements are shown in Fig. A.4 and we observe a lot of loss features in the K states. The loss features are temperature broadened, since the atoms have a temperature of a couple of microkelvin during the hold time. As will be discussed in Appendix B, the loss features can be associated with Feshbach resonances [Chi10] and we additionally perform Feshbach spectroscopy with much colder samples of Li and K to observe the inter- and intraspecies FRs. The enhancement and loss in the lithium atom number can be associated with the *p*-wave resonances that occur around 160 G for Li$|1\rangle$-Li$|1\rangle$, 185 G for Li$|1\rangle$-Li$|2\rangle$, and 215 G for Li$|2\rangle$-Li$|2\rangle$ [Zha04, Sch05].

In the case of spin relaxation, we are particularly interested in the magnetic fields where the atom number in a single spin state is enhanced. In Fig. A.4 a clear enhancement of the atom number in K$|4\rangle$ at 400 G can be seen. This coincides with the point in Fig A.3 where the energy difference between the K$|3\rangle$ and K$|4\rangle$ states is equal to that of lithium. However, we also see a strong decrease of the total K atom number at this magnetic field. The enhancement of the K$|3\rangle$ atom number near 200 G shows no loss of K atoms and this is the field we exploit for spin relaxation. Waiting at this magnetic field leads to a complete removal of the atoms in the K$|1\rangle$ state and we end up with a final mixture of typically 85% K$|3\rangle$ and 15% K$|2\rangle$. The latter population can be removed either by a resonant laser pulse or during the subsequent magnetic field ramps, as discussed in Sec. 5.6.1.

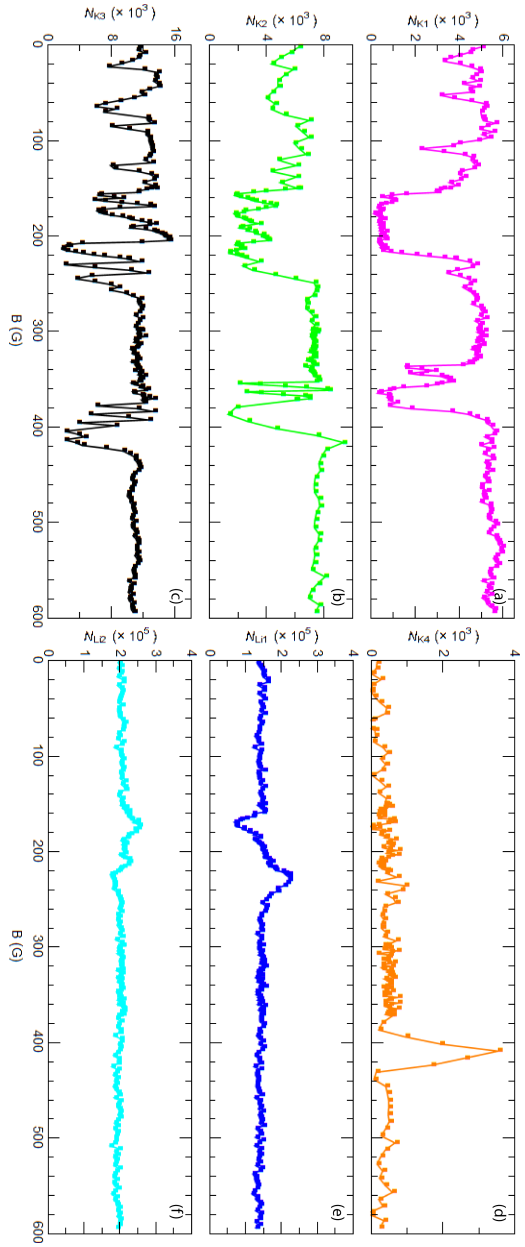

Figure A.4: Loss spectroscopy of potassium and lithium atoms for various magnetic fields. A spin mixture of (a) K|1⟩, (b) K|2⟩, (c) K|3⟩, (e) Li|1⟩, and (f) Li|2⟩ is held for 500 ms at the given magnetic field. Around 400 G, spin exchange collisions lead to the population of (d) K|4⟩ and around 200 G the atom number in the K|3⟩ state is enhanced. This feature is exploited when creating a polarized sample of K. Each data point represents the average of two measurements and the data points are connected as a guide to the eye.

A.4 Laser Setup and Frequencies

The laser setup to cool and trap K and the changes made to implement ^{41}K are shown in Fig. A.5. Using modulation transfer spectroscopy and a spectroscopy cell filled with K vapor, the master laser is locked to the $F = 2 \rightarrow F' = 3$ transition of ^{39}K. The output of the master laser is split up into four pathways. Two pathways create the cooling and repump frequencies for ^{40}K and the other two those for ^{41}K . Depending on the shutter and waveplate settings either the pathway for ^{40}K or ^{41}K is seeding the two tapered amplifiers which provide enough power for the cooling and repump light for the Zeemanslower and the MOT as well as the imaging light. For ^{41}K, the typical settings of the acoustic optical modulators (AOMs) used for cooling, trapping and imaging the lowest four spin states are depicted in Fig. A.6.

To cool and trap ^{39}K two acoustic optical modulators (AOMs) in the laser setup should be realigned. Using the laser setup for ^{40}K, the order of the D204 AOM should be changed from -1 to +1 as well as the order of the C203 AOM, such that it compensates for the B202 AOM. Typical cooling and trapping frequencies can be found in the saved parameter files of the control software.

Figure A.5: Schematic of the K laser setup. The additional components added to obtain the frequencies to cool, trap and image ^{41}K are shown. These components involve AOMs (purple), switchable waveplates (green) and shutters (orange). Image adjusted from internal repository.

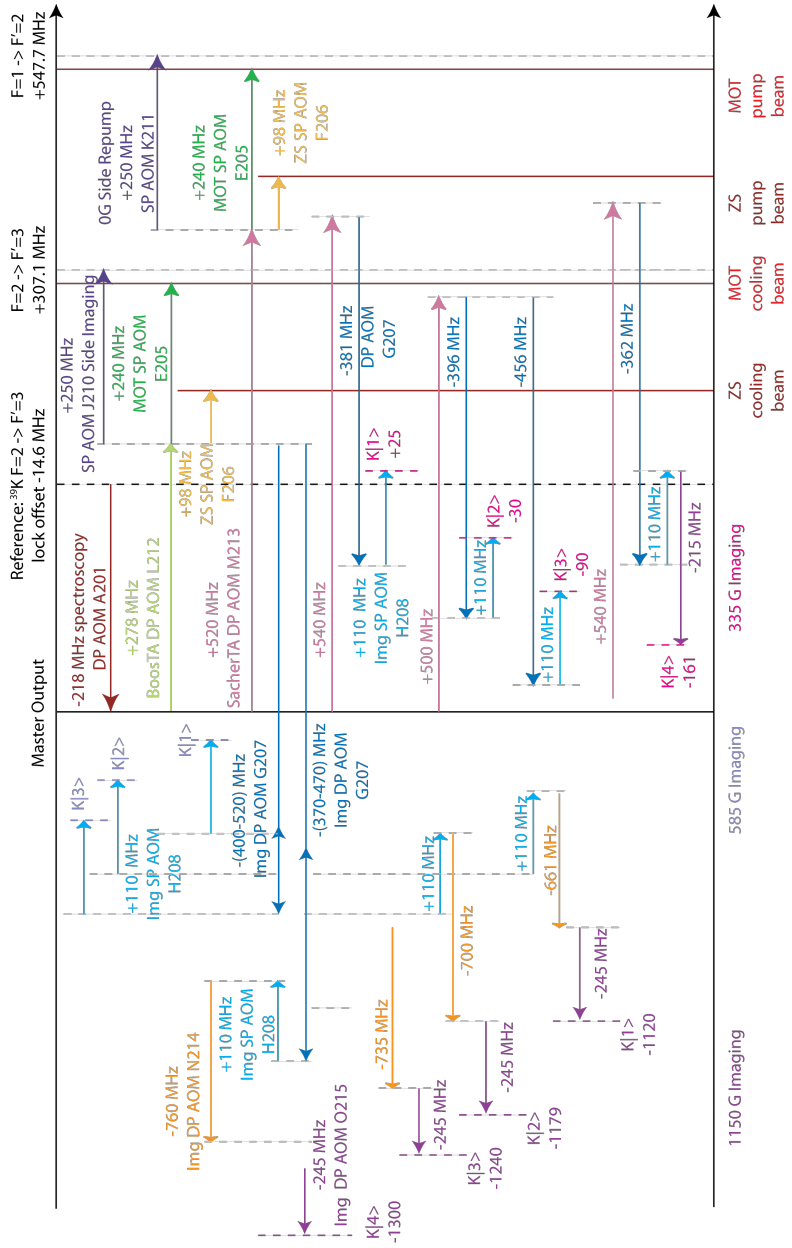

Figure A.6: Characteristic settings of the AOM frequencies for cooling, trapping and imaging ^{41}K.

A

Feshbach Resonances in Ultracold Mixtures of ^{41}K and ^{6}Li

The typical evaporation scheme for cooling the ^{41}K and ^{6}Li mixture takes place at about 1180 G, while the predicted Feshbach resonance (FR) of interest is at 335 G (see Chap. 5). When ramping down to this final field, several intra- and interspecies FRs have to be crossed and it is important to avoid them, since the occurrence of a FR is associated with atom loss. This loss of atoms can actually be exploited when trying to measure FRs and with the new ^{41}K-^{6}Li Bose-Fermi mixture an extensive set of loss measurements was taken for magnetic fields varying between 0 and 1200 G. This appendix provides a summary of the results.

A magnetic Feshbach resonance [Chi10] arises when a pair of ultracold atoms couples to a near-threshold molecular state that is tuned to be close in energy by an applied magnetic field. The enhanced interaction properties near the Feshbach resonances are often accompanied by increased three-body recombination and inelastic collisions. Colliding atoms can release internal energy when changing to a lower internal state or forming a molecule. This energy release gives a gain in kinetic energy which is usually large enough for all atoms involved in the collision to leave the trap. These losses provide an easy tool for the identification of resonances, but can at the same time affect the timescales for experiments in the vicinity of the resonances, as Chap 9 showed. The width and depth of the loss features associated with the FR, depends on the measurement conditions. The temperature of the mixture can broaden the width of the loss feature, while the density of the atoms and the hold time at a given magnetic field determine the amount of atom loss. Furthermore, the trap should be shallow enough that the atoms, with their increase in kinetic energy, can leave the trap and losses can be observed.

For the Feshbach spectroscopy measurements, various spin mixtures are created with K in the lowest $|1\rangle$, second-to-lowest $|2\rangle$, and third-to-lowest $|3\rangle$ Zeeman spin state and Li in either of its two lowest spin states, i.e. Li$|1\rangle$ or Li$|2\rangle$. The preparation

procedure was similar to the one described in Chap. 4. The spin relaxation stage is omitted to ensure that all three spin states of K are present. After evaporative cooling, one of the Li spin states is removed by a resonant laser pulse. Subsequently we ramp down in 100 ms to a given magnetic field and wait there for 500 ms before ramping back to 1180 G where we take absorption images after time of flight. By removing both Li spin states with resonant laser pulses, a K pure spin mixture can be studied and, by applying the spin relaxation stage and/or laser pulses resonant to the K spin states, several combinations of K$|1\rangle$, $|2\rangle$, and $|3\rangle$ can be probed. By varying the components in the mixture, we can verify whether the observed loss features are inter- or intraspecies FRs and between which spin states they occur.

For both species, the trap frequencies of the final crossed optical dipole trap are measured by exciting either the radial breathing mode or the axial mode [Gri08] of the Li and K cloud and observing the size of the Li or K cloud for various wait times in the trap. Fitting these oscillations with a damped sine function leads to the trap frequency. Typical values for lithium are $\omega_{\mathrm{r,Li}} = 2\pi \times 533(4)$ Hz and $\omega_{\mathrm{a,Li}} = 2\pi \times 78.6(5)$ Hz for the radial and axial direction, respectively. For potassium the measured trap frequencies are $\omega_{\mathrm{r,K}} = 2\pi \times 333(5)$ Hz and $\omega_{\mathrm{a,K}} = 2\pi \times 46.4(8)$ Hz.

The typical temperature of the mixture is about 270 nK and is extracted by measuring the size of the thermal K cloud for various expansion times after its release from the trap. Assuming that the K cloud expands ballistically, i.e. all interactions are switched off, the temperature T can be calculated from the increase in width of the cloud σ as a function of time t, according to [Ket99]

$$\sigma(t) = \sqrt{\sigma_0^2 + \frac{k_{\mathrm{B}} T}{m_{\mathrm{K}}} t^2}. \tag{B.1}$$

Here, σ_0 is the initial width of the cloud, k_{B} the Boltzmann constant and m_{K} the mass of potassium.

A single pair of coils is used to vary the magnetic fields between 0-600 G. For higher magnetic fields, 600-1200 G, an additional offset was created by a second pair of coils at a fixed current. At these high magnetic fields, rf spectroscopy between K$|3\rangle$ and $|4\rangle$ is used to determine the relation between the current I and the magnetic field $B_{\mathrm{high-field}}$ as

$$B_{\mathrm{high-field}}/\mathrm{G} = 1.47931(5)\, I/\mathrm{A} + 595.219(9). \tag{B.2}$$

For lower magnetic fields, the offset changes as the second pair of coils is not used and the magnetic field $B_{\mathrm{low-field}}$ follows

$$B_{\mathrm{low-field}}/\mathrm{G} = 1.47931(5)\, I/\mathrm{A} + 2.00(3). \tag{B.3}$$

Table B.1: Lithium p-wave Feshbach resonances. Experimental uncertainties reflect the fit error of a Gaussian fit to the loss feature.

Li-state	Li-state	B_0^{exp} (G)	ΔB_{exp} (G)	B_0^{Theory} (G)
1	1	159.14(2)	0.22(1)	159.15(4) [Sch05], 159 [Zha04]
2	2	214.91(2)	0.15(2)	214.90(4) [Sch05], 215 [Zha04]

Here, the offset was deduced from comparing the loss associated with the Li p-wave FRs to their well-known positions [Sch05, Zha04].

The atom loss measurements up to 450 G are shown in Fig. B.1 and B.2 for a mixture with either Li$|1\rangle$ or Li$|2\rangle$ and K$|1\rangle$, $|2\rangle$, and $|3\rangle$. Each data point represents the average of two measurements and the error reflects the standard deviation. The resolution of the magnetic field is typically 1.5 G, which limits the observation of FRs with a narrower loss feature. The atom number of lithium is an order of magnitude higher and is not significantly affected by the interspecies inelastic processes. However, the p-wave FRs in Li are clearly visible. In another data set, with a smaller magnetic field resolution, we determine the position of these two features with a Gaussian fit and extract the magnetic field offset of 2.00(3) G for low magnetic fields. Table B.1 shows the results of the Gaussian fit as compared to the theoretical values when using Eq. B.3 for magnetic field calibration. The lithium atom loss near their p-wave FR, also affects the K atom number and in all spin states a clear loss feature is present at the p-wave FR position.

A summary of the found interspecies resonances between K and Li$|1\rangle$ and between K and Li$|2\rangle$ is shown in Table B.2 and B.3). Several additional scans, either with a better resolution or a combination of different spin states, are taken to characterize the loss spectra. The measured loss features are fitted with a simple Gaussian curve, which determines the position of the loss mimima B_0^{exp} and their Gaussian width ΔB_{exp}. Note that ΔB_{exp} is not related to the width Δ of a FR, which characterizes the difference in magnetic field between the resonance pole and the zero-crossing. The width of the loss feature, ΔB_{exp}, merely reflects the range of magnetic fields where inelastic losses are enhanced due to enhanced interactions. The errors in Table B.2 and B.3 represent fit errors. For some features, only one data point characterizes the atom loss as the resolution of the magnetic field is too coarse. In those cases only the position of the feature is given and the error represents our detection limit. Table B.2 and B.3 as well as Fig. B.1 and Fig. B.2 also show the theoretically predicted FR positions from the coupled-channels calculations of T. Hanna and E. Tiesinga [Han10] based on the potentials from [Tie09b]. There is a remarkable agreement between the predicted FRs

and those observed, although also unpredicted FRs can be seen.

In Chap. 5, the FR at 334 G is further explored and the resonance center was determined more accurately by measuring the binding energy of the feshbach molecules using rf spectroscopy (see Sec. 5.6.2). The Feshbach resonance center was found to be B_0=335.057(1) G, which is 1 G above the position found by the loss spectroscopy measurements. This indicates that we have a systematic deviation of the measured loss features of about 1 G.

For magnetic fields larger than 450 G, we find almost no Li-K FRs, however we do see K intraspecies FRs, especially in the region of 650 to 770 G as is shown in Fig. B.3. These measurements were taken in the presence of Li$|2\rangle$, however the observed loss features remain when the measurements were repeated in a mixture with Li$|1\rangle$. Additional scans with only K also confirm that these losses occur independent of Li. The found K intraspecies FRs between identical or different spin states are summarized in Table B.4 and B.5, respectively, as well as the theory predictions [Lys10, D'E07]. No atom losses in any of the mixture constituents are observed in the region from 950 G to 1200 G.

There are several routes that can be used to avoid the found FRs when transferring the K and Li mixture after evaporation at 1180 G to 335 G, where the the FR between Li$|1\rangle$ and K$|1\rangle$ is. After the evaporation at 1180 G, the remaining Li$|2\rangle$ and K$|2\rangle$ are removed with a resonant laser pulse. Down to 770 G the pure spin mixture of K$|3\rangle$ and Li$|1\rangle$ can be easily ramped without collisional loss. Most of the intraspecies K FRs between 770 and 650 G can be avoided by ramping down to about 440 G in a few tenths of milliseconds. Moreover, the K$|3\rangle$-K$|3\rangle$ FR at 753 G could also be circumvented by transferring the K atoms to K$|1\rangle$ using a π rf-pulse, followed by another transfer back to the K$|3\rangle$ around 730 G and a quick ramp to 440 G. The region between 400 and 365 G can be dodged by transferring the atoms to K$|1\rangle$. At about 345 G the atoms should be transferred to K$|2\rangle$, before ramping to a field below 335 G. The exact magnetic field where this transfer takes place needs to be carefully calibrated since there is both a Li$|1\rangle$-K$|2\rangle$ and a Li$|1\rangle$-K$|1\rangle$ FR nearby.

For our latest measurements, a different evaporation scheme has been used as described in Sec. 5.6.1. We evaporate at 483 G with a Li$|1\rangle$-Li$|3\rangle$ spin mixture and then ramp to 565 G to remove the Li$|3\rangle$ component by a resonant light pulse. Here we also transfer K$|3\rangle$ to K$|2\rangle$ and then to K$|2\rangle$ to K$|1\rangle$, before ramping down to about 345 G. Then, the atoms are transferred to K$|2\rangle$ and we ramp to a field below 335 G.

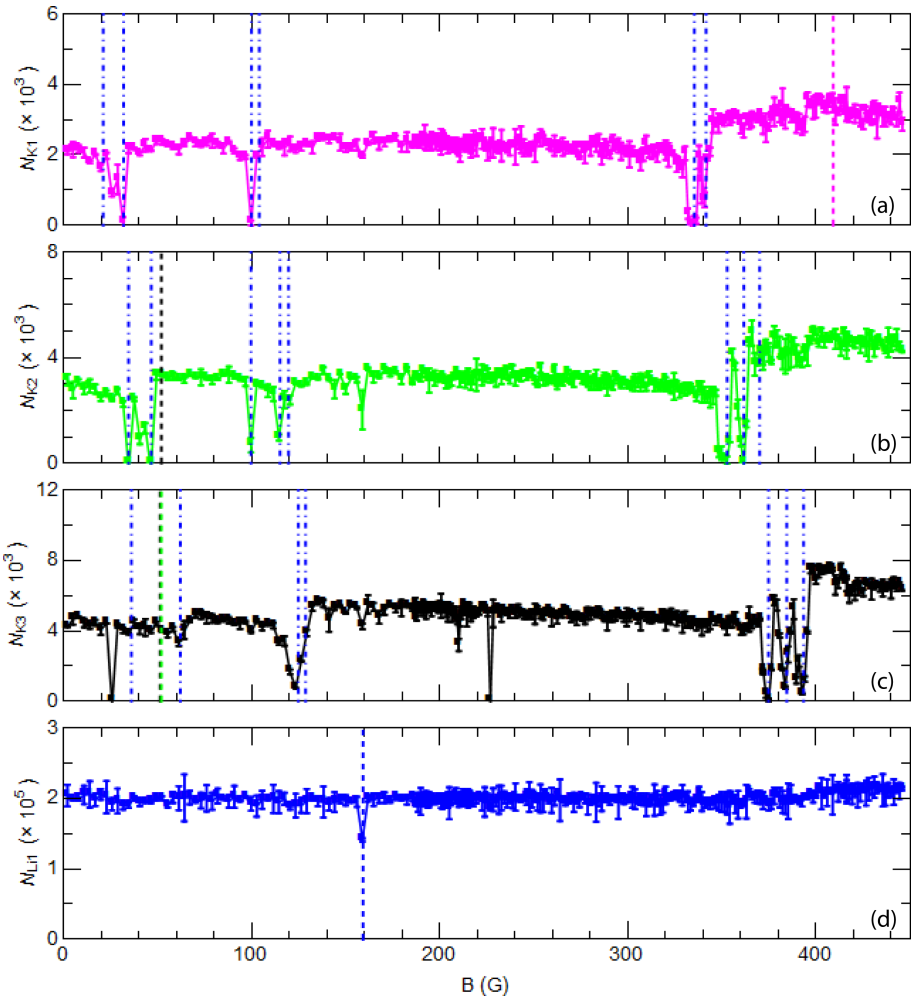

Figure B.1: Loss spectrum of a mixture of (a) K|1⟩, (b) K|2⟩, and (c) K|3⟩ in the presence of (d) Li|1⟩. The data points are connected as guide to the eye. The dot-dashed horizontal lines show the theoretically predicted interspecies FRs from [Han10] and the dashed lines indicate the theoretical potassium intraspecies FRs from [Lys10, D'E07]. The color code of the lines represents the other spin state involved in the FR.

B

Table B.2: Interspecies Feshbach resonances between Li$|1\rangle$ and K$|1\rangle$, $|2\rangle$, and $|3\rangle$. The position B_0^{exp} and Gaussian width ΔB_{exp} are determine from a Gaussian fit to the observed loss features. The uncertainties reflect the fit error. The position of the FRs B_0^{Theory} as predicted by coupled-channels calculations [Han10] are also given. The FR indicated by * is explored in more detail in Chap 5 and B_0 is measured to be 335.057(1) G.

Li-state	K-state	B_0^{exp} (G)	ΔB_{exp} (G)	B_0^{Theory} (G) [Han10]
1	1	21.2(2)	0.17(9)	21
1	1	26.8(4)	2.3(5)	-
1	1	31.2(1)	0.7(1)	31.8
1	1	99.6(4)	1.5(2)	99.85
1	1	154.34(4)	0.19(2)	-
1	1	334.0(1)*	3.2(2)	335.3
1	1	341.25(7)	0.7(1)	341.5
1	1	771(1)	-	-
1	2	34.4(3)	1.5(2)	34.5
1	2	43(1)	4(1)	46.5
1	2	100(1)	1.1(6)	99.5
1	2	114.7(5)	1.7(4)	115
1	2	350.8(6)	2.6(6)	352.7
1	2	361.2(4)	1.4(3)	361.6
1	3	25.69(2)	0.19(1)	-
1	3	60(1)	4(1)	62
1	3	122.1(9)	4.3(9)	124.7
1	3	210.03(8)	0.46(5)	-
1	3	226.9(4)	0.5(1)	-
1	3	374.2(2)	1.5(2)	374.7
1	3	383.4(2)	1.5(2)	384.4
1	3	392.0(3)	2.6(3)	393.4
1	3	771.4(5)	0.7(3)	-

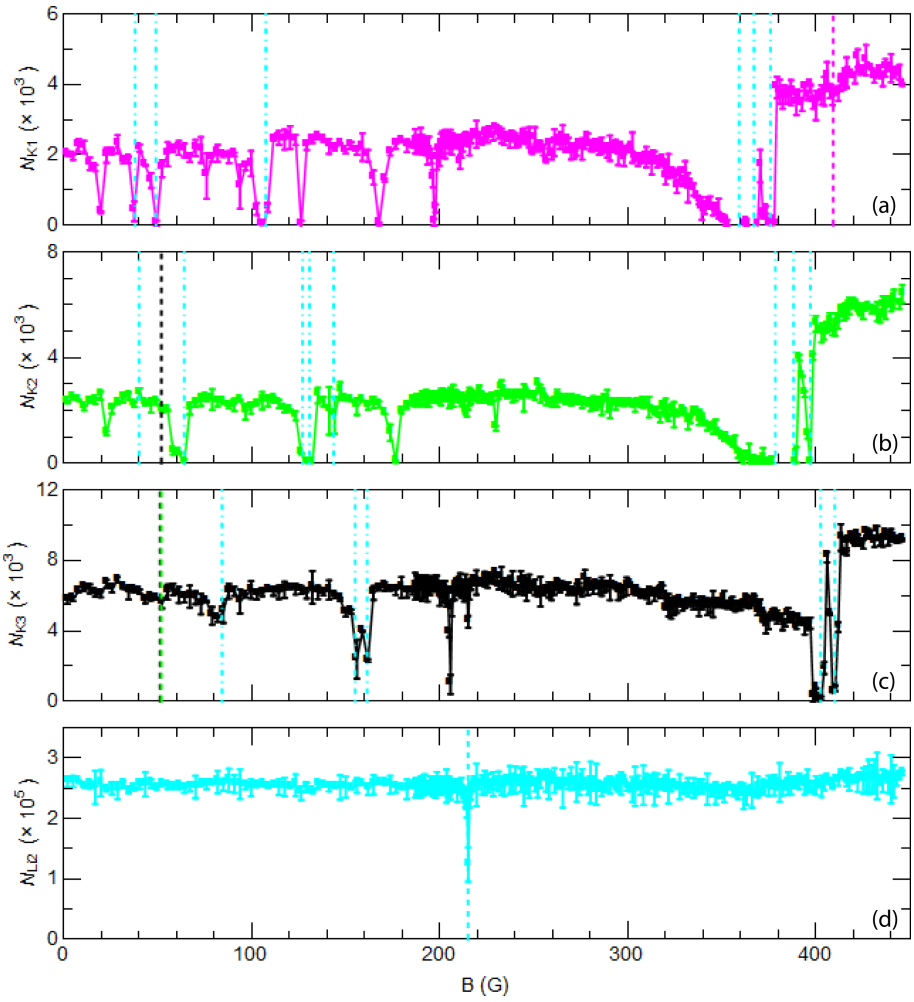

Figure B.2: Loss spectrum of a mixture of (a) K|1⟩, (b) K|2⟩, and (c) K|3⟩ in the presence of (d) Li|2⟩. The data points are connected as guide to the eye. The dot-dashed horizontal lines show the theoretically predicted interspecies FRs from [Han10] and the dashed lines indicate the theoretical potassium intraspecies FRs from [Lys10, D'E07]. The color code of the lines represents the other spin state involved in the FR.

B

Table B.3: Interspecies Feshbach resonances between Li$|2\rangle$ and K$|1\rangle$, $|2\rangle$, and $|3\rangle$. The position B_0^{exp} and Gaussian width ΔB_{exp} are determine from a Gaussian fit to the observed loss features. The uncertainties reflect the fit error. The position of the FRs B_0^{Theory} as predicted by coupled-channels calculations [Han10] are also given.

Li-state	K-state	B_0^{exp} (G)	ΔB_{exp} (G)	B_0^{Theory} (G) [Han10]
2	1	19.3(6)	1.6(4)	-
2	1	37.5(1)	0.5(1)	38
2	1	49.1(1)	1.8(1)	49
2	1	106(1)	3(1)	107.5
2	1	126.6(2)	1.2(1)	-
2	1	167.8(2)	2.4(2)	-
2	1	197.20(5)	0.70(5)	-
2	1	211(1)	-	-
2	1	354(1)	14(3)	359
2	1	375.2(4)	1.7(5)	375.7
2	2	23(3)	-	-
2	2	61.2(3)	3.2(5)	64.1
2	2	128.9(4)	2.5(4)	130.7
2	2	175.8(1)	1.8(2)	-
2	2	213.97(3)	0.45(3)	-
2	2	229.7(6)	0.6(3)	-
2	2	370(2)	15(2)	378.4
2	2	395.3(3)	2.0(3)	397
2	3	80.0(9)	4(1)	84.2
2	3	155.4(6)	3.7(5)	155
2	3	163(2)	-	-
2	3	205.55(4)	0.48(3)	-
2	3	400.7(2)	2.7(2)	402.4
2	3	409.5(1)	2.1(1)	410
2	3	455.1(3)	0.4(2)	-

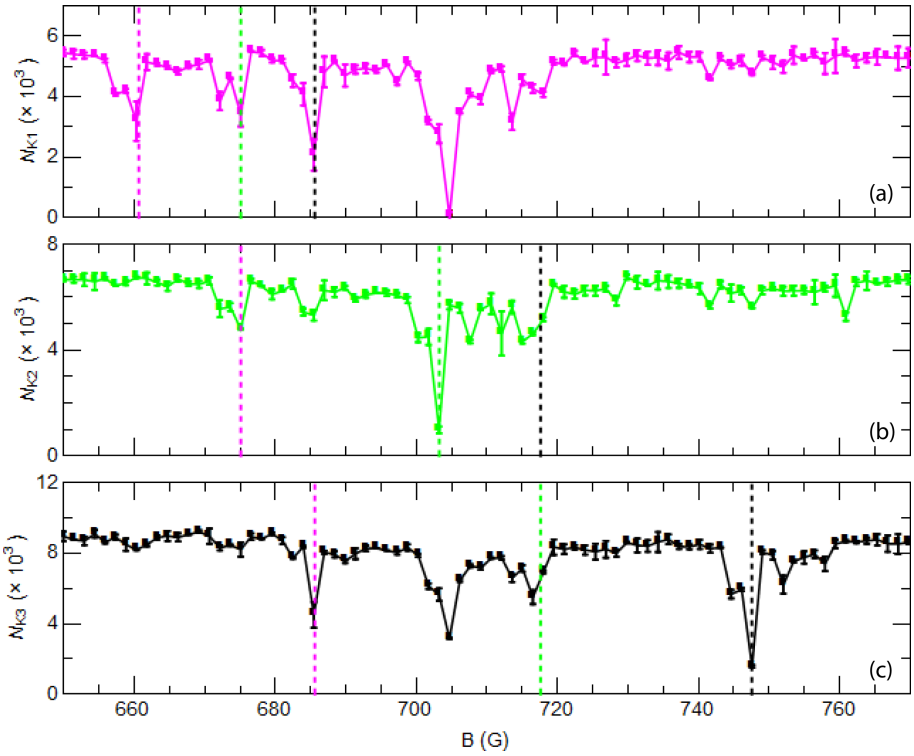

Figure B.3: Loss spectrum of a mixture of (a) K$|1\rangle$, (b) K$|2\rangle$, and (c) K$|3\rangle$ in the presence of Li$|2\rangle$. The observed loss features remain when the measurements were repeated in the presence of Li$|1\rangle$. The data points are connected as guide to the eye. The dashed horizontal lines indicated the predicted theoretical FRs from [Lys10, D'E07]. The color code of the lines represents the other spin state involved in the FR.

B

Table B.4: Potassium intraspecies Feshbach resonances between identical spin states. Experimental uncertainties reflect the fit error of a Gaussian fit to the loss feature. The waittime is 500 ms, however the two features marked with * were observed for $t = 1$ s.

K-state	K-state	B^{exp} (G)	ΔB_{exp} (G)	B_0^{Theory1} (G) [D'E07]	B_0^{Theory2} (G) [Lys10]
1	1	658.0(7)	-	-	-
1	1	660.5(7)	-	660.1	661.2
1	1	713.6(1)	0.2(1)	-	-
1	1	717.4(2)	1.0(3)	-	-
2	2	360(1)	-	-	-
2	2	451.46(9)	1.06(9)	451.5	452.4
2	2	700.8(1)	0.5(1)	-	-
2	2	703.0(1)	0.9(2)	702.7	703.8
2	2	707.7(7)	-	-	-
2	2	712.1(7)	-	-	-
2	2	748.8(2)	1.2(1)	-	-
2	2	760.9(7)	-	-	-
2	2	786.1(4)	0.5(2)	-	-
3	3	46.7(6)*	2.2(7)	-	-
3	3	51.3(2)*	1.1(2)	51.4	51.17
3	3	453.10(8)	0.37(5)	-	-
3	3	455.3(7)	-	-	-
3	3	745.4(7)	0.68(7)		
3	3	747.5(1)	0.6(1)	747	748.1
3	3	752.8(3)	1.4(3)	-	-
3	3	757.6(5)	0.9(6)	-	-
4	4	748.9(2)	2.2(3)		

Table B.5: Potassium intraspecies Feshbach resonances between different spin states. Experimental uncertainties reflect the fit error of a Gaussian fit to the loss feature.

K-state	K-state	B^{exp} (G)	ΔB_{exp} (G)	B_0^{Theory1} (G) [D'E07]	B_0^{Theory2} (G) [Lys10]
1	2	672(1)	-	-	-
1	2	674.5(2)	0.4(2)	-	675.1
1	2	742(1)	-	-	-
1	2	748(1)	-	-	-
1	3	685.01(3)	0.22(2)	-	-
1	3	685.79(3)	0.30(1)	-	685.6
1	3	689.66(6)	0.2(1)	-	-
1	3	702.2(2)	0.8(1)	-	-
1	3	704.72(9)	0.93(9)	-	-
2	3	714.4(3)	0.8(3)	-	-
2	3	716.92(7)	0.58(5)	-	717.6
2	3	786.1(1)	0.40(8)	-	-
2	3	931.05(8)	0.24(5)	-	-
4	4	748.9(2)	2.2(3)		

Bibliography

[AS01] J. R. Abo-Shaeer, C. Raman, J. M. Vogels, and W. Ketterle. "Observation of Vortex Lattices in Bose-Einstein Condensates", *Science* **292**, 476 (2001).

[Ada12] A. Adams, L. D. Carr, T. Schäfer, P. Steinberg, and J. E. Thomas. "Strongly correlated quantum fluids: ultracold quantum gases, quantum chromodynamic plasmas and holographic duality", *New J. Phys.* **14**, 115009 (2012).

[Aik12] K. Aikawa, A. Frisch, M. Mark, S. Baier, A. Rietzler, R. Grimm, and F. Ferlaino. "Bose-Einstein Condensation of Erbium", *Phys. Rev. Lett.* **108**, 210401 (2012).

[Aik14] K. Aikawa, A. Frisch, M. Mark, S. Baier, R. Grimm, and F. Ferlaino. "Reaching Fermi Degeneracy via Universal Dipolar Scattering", *Phys. Rev. Lett.* **112**, 010404 (2014).

[Alt07] A. Altmeyer, S. Riedl, C. Kohstall, M. J. Wright, R. Geursen, M. Bartenstein, C. Chin, J. Hecker Denschlag, and R. Grimm. "Precision Measurements of Collective Oscillations in the BEC-BCS Crossover", *Phys. Rev. Lett.* **98**, 040401 (2007).

[And95] M. H. Anderson, J. R. Ensher, M. R. Matthews, C. E. Wieman, and E. A. Cornell. "Observation of Bose-Einstein Condensation in a Dilute Atomic Vapor", *Science* **269**, 198 (1995).

[And67] P. W. Anderson. "Infrared catastrophe in Fermi gases with local scattering potentials", *Phys. Rev. Lett.* **18**, 1049 (1967).

[And97] M. R. Andrews, C. G. Townsend, H.-J. Miesner, D. S. Durfee, D. M. Kurn, and W. Ketterle. "Observation of Interference Between Two Bose Condensates", *Science* **275**, 637 (1997).

[Baa10] J. E. Baarsma, K. B. Gubbels, and H. T. C. Stoof. "Population and mass imbalance in atomic Fermi gases", *Phys. Rev. A* **82**, 013624 (2010).

[Bak09] W. S. Bakr, J. I. Gillen, A. Peng, S. Fölling, and M. Greiner. "A quantum gas microscope for detecting single atoms in a Hubbard-regime optical lattice", *Nature (London)* **462**, 74 (2009).

[Bar58a] M. Baranger. "General impact theory of pressure broadening", *Phys. Rev.* **112**, 855 (1958).

[Bar58b] M. Baranger. "Simplified quantum-mechanical theory of pressure broadening", *Phys. Rev.* **111**, 481 (1958).

[Bar08] M. A. Baranov, C. Lobo, and G. V. Shlyapnikov. "Superfluid pairing between fermions with unequal masses", *Phys. Rev. A* **78**, 033620 (2008).

[Bar12] M. A. Baranov, M. Dalmonte, G. Pupillo, and P. Zoller. "Condensed Matter Theory of Dipolar Quantum Gases", *Chem. Rev.* **112**, 5012 (2012).

[Bar18] V. Barbé, A. Ciamei, B. Pasquiou, L. Reichsöllner, F. Schreck, P. S. Żuchowski, and J. M. Hutson. "Observation of Feshbach resonances between alkali and closed-shell atoms", *Nat. Phys.* (2018).

[Bar14] A. B. Bardon, S. Beattie, C. Luciuk, W. Cairncross, D. Fine, N. S. Cheng, G. J. A. Edge, E. Taylor, S. Zhang, S. Trotzky, and J. H. Thywissen. "Transverse Demagnetization Dynamics of a Unitary Fermi Gas", *Science* **344**, 722 (2014).

[Bar04] M. Bartenstein, A. Altmeyer, S. Riedl, S. Jochim, C. Chin, J. Hecker Denschlag, and R. Grimm. "Collective Excitations of a Degenerate Gas at the BEC-BCS Crossover", *Phys. Rev. Lett.* **92**, 203201 (2004).

[Bau09a] D. M. Bauer, M. Lettner, C. Vo, G. Rempe, and S. Dürr. "Combination of a magnetic Feshbach resonance and an optical bound-to-bound transition", *Phys. Rev. A* **79**, 062713 (2009).

[Bau09b] D. M. Bauer, M. Lettner, C. Vo, G. Rempe, and S. Dürr. "Control of a magnetic Feshbach resonance with laser light", *Nat. Phys.* **5**, 339 (2009).

[Bau11] F. Baumer, F. Münchow, A. Görlitz, S. E. Maxwell, P. S. Julienne, and E. Tiesinga. "Spatial separation in a thermal mixture of ultracold ^{174}Yb and ^{87}Rb atoms", *Phys. Rev. A* **83**, 040702 (2011).

[Bau09c] I. Bausmerth, A. Recati, and S. Stringari. "Chandrasekhar-Clogston limit and phase separation in Fermi mixtures at unitarity", *Phys. Rev. A* **79**, 043622 (2009).

[Bay91] G. Baym and C. Pethick. *Landau Fermi Liquid Theory*. Wiley-VCH, Weinheim (1991).

[Ber98] K. Bergmann, H. Theuer, and B. W. Shore. "Coherent population transfer among quantum states of atoms and molecules", *Rev. Mod. Phys.* **70**, 1003 (1998).

[Ber95] Y. Berk, A. Kamanev, A. Palevski, L. N. Pfeiffer, and K. W. West. "Resonance magnetoresistance of coupled quantum wells", *Phys. Rev. B* **51**, 2604 (1995).

[Ber13] G. Bertaina, E. Fratini, S. Giorgini, and P. Pieri. "Quantum Monte Carlo Study of a Resonant Bose-Fermi Mixture", *Phys. Rev. Lett.* **110**, 115303 (2013).

[Bij00] M. J. Bijlsma, B. A. Heringa, and H. T. C. Stoof. "Phonon exchange in dilute Fermi-Bose mixtures: Tailoring the Fermi-Fermi interaction", *Phys. Rev. A* **61**, 053601 (2000).

[Bin84] K. Binder and D. P. Landau. "Finite-size scaling at first-order phase transitions", *Phys. Rev. B* **30**, 1477 (1984).

[Blo08] I. Bloch, J. Dalibard, and W. Zwerger. "Many-body physics with ultracold gases", *Rev. Mod. Phys.* **80**, 885 (2008).

[Blo99] I. Bloch, T. W. Hänsch, and T. Esslinger. "Atom Laser with a cw Output Coupler", *Phys. Rev. Lett.* **82**, 3008 (1999).

[Blo12] I. Bloch, J. Dalibard, and S. Nascimbène. "Quantum simulations with ultracold quantum gases", *Nat. Phys.* **8**, 267 (2012).

[Blu12] D. Blume. "Universal Four-Body States in Heavy-Light Mixtures with a Positive Scattering Length", *Phys. Rev. Lett.* **109**, 230404 (2012).

[Boh17] J. L. Bohn, A. M. Rey, and J. Ye. "Cold molecules: Progress in quantum engineering of chemistry and quantum matter", *Science* **357**, 1002 (2017).

[Bos24] S. N. Bose. "Planckschen Gesetz und Lichtquantenhypothese", *Z. Phys.* **26**, 178 (1924).

[Bou03] T. Bourdel, J. Cubizolles, L. Khaykovich, K. M. F. Magalhães, S. J.J.M. F. Kokkelmans, G. V. Shlyapnikov, and C. Salomon. "Measurement of the Interaction Energy near a Feshbach Resonance in a ^{6}Li Fermi Gas", *Phys. Rev. Lett.* **91**, 020402 (2003).

[Bou04] T. Bourdel, L. Khaykovich, J. Cubizolles, J. Zhang, F. Chevy, M. Teichmann, L. Tarruell, S. J.J.M. F. Kokkelmans, and C. Salomon. "Experimental Study of the BEC-BCS Crossover Region in Lithium 6", *Phys. Rev. Lett.* **93**, 050401 (2004).

[Bra95] C. C. Bradley, C. A. Sackett, J. J. Tollett, and R. G. Hulet. "Evidence of Bose-Einstein condensation in an atomic gas with attractive interactions", *Phys. Rev. Lett.* **75**, 1687 (1995). Erratum: *Phys. Rev. Lett.* **79** (1997).

[Bra97] C. C. Bradley, C. A. Sackett, and R. G. Hulet. "Bose-Einstein condensation of lithium: Observation of limited condensate number", *Phys. Rev. Lett.* **78**, 985 (1997).

[Bra14] J. Braun, J. E. Drut, T. Jahn, M. Pospiech, and D. Roscher. "Phases of spin- and mass-imbalanced ultracold Fermi gases in harmonic traps", *Phys. Rev. A* **89**, 053613 (2014).

[Bra15] J. Braun, J. E. Drut, and D. Roscher. "Zero-Temperature Equation of State of Mass-Imbalanced Resonant Fermi Gases", *Phys. Rev. Lett.* **114**, 050404 (2015).

[Bré85] E. Brézin and J. Zinn-Justin. "Finite size effects in phase transitions", *Nucl. Phys. B* **257**, 867 (1985).

[Bru05] G. M. Bruun and H. Smith. "Viscosity and thermal relaxation for a resonantly interacting Fermi gas", *Phys. Rev. A* **72**, 043605 (2005).

[Bur14a] A. Burchianti, G. Valtolina, J. A. Seman, E. Pace, M. De Pas, M. Inguscio, M. Zaccanti, and G. Roati. "Efficient all-optical production of large ^6Li quantum gases using D_1 gray-molasses cooling", *Phys. Rev. A* **90**, 043408 (2014).

[Bur14b] A. Burchianti, G. Valtolina, J. A. Seman, E. Pace, M. De Pas, M. Inguscio, M. Zaccanti, and G. Roati. "Efficient all-optical production of large ^{6}Li quantum gases using D_1 gray-molasses cooling", *Phys. Rev. A* **90**, 043408 (2014).

[Bur97] E. A. Burt, R. W. Ghrist, C. J. Myatt, M. J. Holland, E. A. Cornell, and C. E. Wieman. "Coherence, Correlations, and Collisions: What One Learns about Bose-Einstein Condensates from Their Decay", *Phys. Rev. Lett.* **79**, 337 (1997).

[Cab18] C. R. Cabrera, L. Tanzi, J. Sanz, B. Naylor, P. Thomas, P. Cheiney, and L. Tarruell. "Quantum liquid droplets in a mixture of Bose-Einstein condensates", *Science* **359**, 301 (2018).

[Cal05] H. Caldas, C. W. Morais, and A. L. Mota. "Phase transition in asymmetrical superfluids: Equal Fermi surfaces", *Phys. Rev. D* **72**, 045008 (2005).

[Cal18] G. Calvanese Strinati, P. Pieri, G. Roepke, P. Schuck, and M. Urban. "The BCS-BEC crossover: From ultra-cold Fermi gases to nuclear systems", *Phys. Rep.* **738**, 1 (2018).

[Car09] L. D. Carr, D. DeMille, R. V. Krems, and J. Ye. "Cold and ultracold molecules: Science, technology and applications", *New J. Phys.* **11**, 055049 (2009).

[Cas10] Y. Castin, C. Mora, and L. Pricoupenko. "Four-Body Efimov Effect for Three Fermions and a Lighter Particle", *Phys. Rev. Lett.* **105**, 223201 (2010).

[Cat12] J. Catani, G. Lamporesi, D. Naik, M. Gring, M. Inguscio, F. Minardi, A. Kantian, and T. Giamarchi. "Quantum dynamics of impurities in a one-dimensional Bose gas", *Phys. Rev. A* **85**, 023623 (2012).

[Cet15] M. Cetina, M. Jag, R. S. Lous, J. T. M. Walraven, R. Grimm, R. S. Christensen, and G. M. Bruun. "Decoherence of Impurities in a Fermi Sea of Ultracold Atoms", *Phys. Rev. Lett.* **115**, 135302 (2015).

[Cet16] M. Cetina, M. Jag, R. S. Lous, I. Fritsche, J. T. M. Walraven, R. Grimm, J. Levinsen, M. M. Parish, R. Schmidt, M. Knap, and E. Demler. "Ultrafast many-body interferometry of impurities coupled to a Fermi sea", *Science* **354**, 96 (2016).

[Cha62] B. S. Chandrasekhar. "A note on the maximum critical field of high-field superconductors", *Applied Physics Letters* **1**, 7 (1962).

[Che15] L. W. Cheuk, M. A. Nichols, M. Okan, T. Gersdorf, V. V. Ramasesh, W. S. Bakr, T. Lompe, and M. W. Zwierlein. "Quantum-Gas Microscope for Fermionic Atoms", *Phys. Rev. Lett.* **114**, 193001 (2015).

[Che16] F. Chevy and C. Salomon. “Strongly correlated Bose gases”, *J. Phys. B* **49**, 192001 (2016).

[Chi15] C.-C. Chien, S. Peotta, and M. Di Ventra. “Quantum transport in ultracold atoms”, *Nat. Phys.* **11** (2015).

[Chi04] C. Chin, M. Bartenstein, A. Altmeyer, S. Riedl, S. Jochim, J. Hecker Denschlag, and R. Grimm. “Observation of the Pairing Gap in a Strongly Interacting Fermi Gas”, *Science* **305**, 1128 (2004).

[Chi05] C. Chin and P. S. Julienne. “Radio-frequency transitions on weakly bound ultracold molecules”, *Phys. Rev. A* **71**, 012713 (2005).

[Chi10] C. Chin, R. Grimm, P. S. Julienne, and E. Tiesinga. “Feshbach resonances in ultracold gases”, *Rev. Mod. Phys.* **82**, 1225 (2010).

[Cho16] L. Chomaz, S. Baier, D. Petter, M. J. Mark, F. Wächtler, L. Santos, and F. Ferlaino. “Quantum-Fluctuation-Driven Crossover from a Dilute Bose-Einstein Condensate to a Macrodroplet in a Dipolar Quantum Fluid”, *Phys. Rev. X* **6**, 041039 (2016).

[Cho15] L. Chomaz, L. Corman, T. Bienaimé, R. Desbuquois, C. Weitenberg, S. Nascimbéne, J. Beugnon, and J. Dalibard. “Emergence of coherence via transverse condensation in a uniform quasi-two-dimensional Bose gas”, *Nat. Commun.* **6**, 6162 (2015).

[Chr15] R. S. Christensen and G. M. Bruun. “Quasiparticle scattering rate in a strongly polarized Fermi mixture”, *Phys. Rev. A* **91**, 042702 (2015).

[Chu98] S. Chu. “Nobel Lecture: The manipulation of neutral particles”, *Rev. Mod. Phys.* **70**, 685 (1998).

[Cla15] L. W. Clark, L.-C. Ha, C.-Y. Xu, and C. Chin. “Quantum Dynamics with Spatiotemporal Control of Interactions in a Stable Bose-Einstein Condensate”, *Phys. Rev. Lett.* **115**, 155301 (2015).

[Clo62] A. M. Clogston. “Upper Limit for the Critical Field in Hard Superconductors”, *Phys. Rev. Lett.* **9**, 266 (1962).

[CT98] C. N. Cohen-Tannoudji. “Nobel Lecture: Manipulating atoms with photons”, *Rev. Mod. Phys.* **70**, 707 (1998).

[Cor02] E. A. Cornell and C. E. Wieman. “Nobel Lecture: Bose-Einstein condensation in a dilute gas, the first 70 years and some recent experiments”, *Rev. Mod. Phys.* **74**, 875 (2002).

[Cor00] S. L. Cornish, N. R. Claussen, J. L. Roberts, E. A. Cornell, and C. E. Wieman. “Stable ^{85}Rb Bose-Einstein condensates with widely tunable interactions”, *Phys. Rev. Lett.* **85**, 1795 (2000).

[Cos10] L. Costa, J. Brachmann, A.-C. Voigt, C. Hahn, M. Taglieber, T. W. Hänsch, and K. Dieckmann. “s-wave interaction in a two-species Fermi-Fermi mixture at a narrow Feshbach resonance”, *Phys. Rev. Lett.* **105**, 123201 (2010). Erratum: *Phys. Rev. Lett.* **105** (2010).

[Cou98] P. Courteille, R. S. Freeland, D. J. Heinzen, F. A. van Abeelen, and B. J. Verhaar. “Observation of a Feshbach Resonance in Cold Atom Scattering”, *Phys. Rev. Lett.* **81**, 69 (1998).

[Cro09] A. D. Cronin, J. Schmiedmayer, and D. E. Pritchard. “Optics and interferometry with atoms and molecules”, *Rev. Mod. Phys.* **81**, 1051 (2009).

[Cub03] J. Cubizolles, T. Bourdel, S. J.J.M. F. Kokkelmans, G. V. Shlyapnikov, and C. Salomon. “Production of Long-Lived Ultracold Li_2 Molecules from a Fermi Gas”, *Phys. Rev. Lett.* **91**, 240401 (2003).

[Cui13] X. Cui and T.-L. Ho. “Phase Separation in Mixtures of Repulsive Fermi Gases Driven by Mass Difference”, *Phys. Rev. Lett.* **110**, 165302 (2013).

[Dai12] K. M. Daily and D. Blume. “Thermodynamics of the two-component Fermi gas with unequal masses at unitarity”, *Phys. Rev. A* **85**, 013609 (2012).

[Dal99] F. Dalfovo, S. Giorgini, L. P. Pitaevskii, and S. Stringari. “Theory of Bose-Einstein condensation in trapped gases”, *Rev. Mod. Phys.* **71**, 463 (1999).

[Dal12] M. Dalmonte, K. Dieckmann, T. Roscilde, C. Hartl, A. E. Feiguin, U. Schollwöck, and F. Heidrich-Meisner. “Dimer, trimer, and Fulde-Ferrell-Larkin-Ovchinnikov liquids in mass- and spin-imbalanced trapped binary mixtures in one dimension”, *Phys. Rev. A* **85**, 063608 (2012).

[Dan10] J. G. Danzl, M. J. Mark, E. Haller, M. Gustavsson, R. Hart, J. Aldegunde, J. M. Hutson, and H.-C. Nägerl. “An ultracold high-density sample of rovibronic ground-state molecules in an optical lattice”, *Nat. Phys.* **6**, 265 (2010).

[Das65] P. Das, R. B. de Ouboter, and K. W. Taconis. “A Realization of a London-Clarke-Mendoza Type Refrigerator”. In: *Low Temperature Physics LT9: Proceedings of the IXth International Conference on Low Temperature Physics Columbus, Ohio, 1964*. Ed. by J. G. Daunt, D. O. Edwards, F. J. Milford, and M. Yaqub. Boston, MA: Springer (1965), 1253.

[Dav96] H. Davis. *Statistical Mechanics of Phases, Interfaces and Thin Films*. Advances in Interfacial Engineering Series. New York: Wiley (1996).

[Dav95] K. B. Davis, M. O. Mewes, M. R. Andrews, N. J. van Druten, D. S. Durfee, D. M. Kurn, and W. Ketterle. “Bose-Einstein condensation in a gas of sodium atoms”, *Phys. Rev. Lett.* **75**, 3969 (1995).

[Deh10] B. Deh, W. Gunton, B. G. Klappauf, Z. Li, M. Semczuk, J. Van Dongen, and K. W. Madison. “Giant Feshbach resonances in ^{6}Li-^{85}Rb mixtures”, *Phys. Rev. A* **82**, 020701 (2010).

[Del15] M. Delehaye, S. Laurent, I. Ferrier-Barbut, S. Jin, F. Chevy, and C. Salomon. “Critical Velocity and Dissipation of an Ultracold Bose-Fermi Counterflow”, *Phys. Rev. Lett.* **115**, 265303 (2015).

[DeM99] B. DeMarco and D. S. Jin. “Onset of Fermi Degeneracy in a Trapped Atomic Gas”, *Science* **285**, 1703 (1999).

[D’E07] C. D’Errico, M. Zaccanti, M. Fattori, G. Roati, M. Inguscio, G. Modugno, and A. Simoni. “Feshbach resonances in ultracold ^{39}K”, *New J. Phys.* **9**, 223 (2007).

[DeS10] B. J. DeSalvo, M. Yan, P. G. Mickelson, Y. N. Martinez de Escobar, and T. C. Killian. “Degenerate Fermi Gas of ^{87}Sr”, *Phys. Rev. Lett.* **105**, 030402 (2010).

[DeS17] B. J. DeSalvo, K. Patel, J. Johansen, and C. Chin. “Observation of a Degenerate Fermi Gas Trapped by a Bose-Einstein Condensate”, *Phys. Rev. Lett.* **119**, 233401 (2017).

[Dir26] P. A. M. Dirac. “On the theory of quantum mechanics”, *Proc. Royal Soc. A* **112**, 661 (1926).

[Don01] E. A. Donley, N. R. Clausen, S. L. Cornish, J. L. Roberts, E. A. Cornell, and C. E. Wieman. “Dynamics of Collapsing and Exploding Bose-Einstein Condensates”, *Nature (London)* **412**, 295 (2001).

[Ebn71] C. Ebner and D. Edwards. “The low temperature thermodynamic properties of superfluid solutions of 3He in 4He”, *Phys. Rep.* **2**, 77 (1971).

[Edg15] G. J. A. Edge, R. Anderson, D. Jervis, D. C. McKay, R. Day, S. Trotzky, and J. H. Thywissen. “Imaging and addressing of individual fermionic atoms in an optical lattice”, *Phys. Rev. A* **92**, 063406 (2015).

[Efi73] V. Efimov. “Energy levels of three resonantly interacting particles”, *Nucl. Phys. A* **210**, 157 (1973).

[Efr02] D. V. Efremov and L. Viverit. "p-wave Cooper pairing of fermions in mixtures of dilute Fermi and Bose gases", *Phys. Rev. B* **65**, 134519 (2002).

[Ein24] A. Einstein. "Quantentheorie des einatomigen idealen Gases I", *Sitzungsber. Kgl. Preuss. Akad. Wiss.* **261** (1924).

[Ein25] A. Einstein. "Quantentheorie des einatomigen idealen Gases II", *Sitzungsber. Kgl. Preuss. Akad. Wiss.* **3** (1925).

[Ens12] T. Enss. "Quantum critical transport in the unitary Fermi gas", *Phys. Rev. A* **86**, 013616 (2012).

[Esr01] B. D. Esry, C. H. Greene, and H. Suno. "Threshold laws for three-body recombination", *Phys. Rev. A* **65**, 010705 (2001).

[Ess10] T. Esslinger. "Fermi-Hubbard Physics with Atoms in an Optical Lattice", *Annu. Rev. Condens. Matter Phys.* **1**, 129 (2010).

[Fer09] F. Ferlaino, S. Knoop, and R. Grimm. "Ultracold Feshbach molecules". In: *Cold Molecules: Theory, Experiment, Applications*. Ed. by R. V. Krems, B. Friedrich, and W. C. Stwalley. CRC Press (2009).

[Fer11] F. Ferlaino, A. Zenesini, M. Berninger, B. Huang, H.-C. Nägerl, and R. Grimm. "Efimov Resonances in Ultracold Quantum Gases", *Few-Body Syst.* **51**, 113 (2011).

[Fer26] E. Fermi. "Sulla quantizzazione del gas perfetto monoatomico", *Rend. Lincei* **3**, 145 (1926). For an english translation by A. Zannoni see arXiv:cond-mat/9912229v1.

[Fer12] D. R. Fernandes, F. Sievers, N. Kretzschmar, S. Wu, C. Salomon, and F. Chevy. "Sub-Doppler laser cooling of fermionic 40 K atoms in three-dimensional gray optical molasses", *EPL* **100**, 63001 (2012).

[FB14] I. Ferrier-Barbut, M. Delehaye, S. Laurent, A. T. Grier, M. Pierce, B. S. Rem, F. Chevy, and C. Salomon. "A mixture of Bose and Fermi Superfluids", *Science* **345**, 1035 (2014).

[FB16a] I. Ferrier-Barbut, M. Schmitt, M. Wenzel, H. Kadau, and T. Pfau. "Liquid quantum droplets of ultracold magnetic atoms", *J. Phys. B* **49**, 214004 (2016).

[FB16b] I. Ferrier-Barbut, H. Kadau, M. Schmitt, M. Wenzel, and T. Pfau. "Observation of Quantum Droplets in a Strongly Dipolar Bose Gas", *Phys. Rev. Lett.* **116**, 215301 (2016).

[Fey82] R. Feynman. "Simulating Physics with Computers", *Int. J. Theor. Phys.* **21**, 467 (1982).

[Fri98] D. G. Fried, T. C. Killian, L. Willmann, D. Landhuis, S. C. Moss, D. Kleppner, and T. J. Greytak. "Bose-Einstein Condensation of Atomic Hydrogen", *Phys. Rev. Lett.* **81**, 3811 (1998).

[Fri15] I. Fritsche. Master Thesis, University of Innsbruck (2015).

[Frö50] H. Fröhlich, H. Pelzer, and S. Zienau. "Properties of slow electrons in polar materials", *Philos. Mag.* **41**, 221 (1950).

[Fuk07a] T. Fukuhara, S. Sugawa, and Y. Takahashi. "Bose-Einstein condensation of an ytterbium isotope", *Phys. Rev. A* **76**, 051604(R) (2007).

[Fuk07b] T. Fukuhara, Y. Takasu, M. Kumakura, and Y. Takahashi. "Degenerate Fermi gases of ytterbium", *Phys. Rev. Lett.* **98**, 030401 (2007).

[Fuk09] T. Fukuhara, S. Sugawa, Y. Takasu, and Y. Takahashi. "All-optical formation of quantum degenerate mixtures", *Phys. Rev. A* **79**, 021601(R) (2009).

[Gao10] B. Gao. "Universal Model for Exoergic Bimolecular Reactions and Inelastic Processes", *Phys. Rev. Lett.* **105**, 263203 (2010).

[Gau13] A. L. Gaunt, T. F. Schmidutz, I. Gotlibovych, R. P. Smith, and Z. Hadzibabic. "Bose-Einstein Condensation of Atoms in a Uniform Potential", *Phys. Rev. Lett.* **110**, 200406 (2013).

[Gez08] A. Gezerlis and J. Carlson. "Strongly paired fermions: Cold atoms and neutron matter", *Phys. Rev. C* **77**, 032801 (2008).

[Gez09] A. Gezerlis, S. Gandolfi, K. E. Schmidt, and J. Carlson. "Heavy-light fermion mixtures at unitarity", *Phys. Rev. Lett.* **103**, 060403 (2009).

[Gio96] S. Giorgini, L. P. Pitaevskii, and S. Stringari. "Condensate fraction and critical temperature of a trapped interacting Bose gas", *Phys. Rev. A* **54**, R4633 (1996).

[Gio08] S. Giorgini, L. P. Pitaevskii, and S. Stringari. "Theory of ultracold atomic Fermi gases", *Rev. Mod. Phys.* **80**, 1215 (2008).

[Gol04] J. Goldwin, S. Inouye, M. L. Olsen, B. Newman, B. D. DePaola, and D. S. Jin. "Measurement of the interaction strength in a Bose-Fermi mixture with ^{87}Rb and ^{40}K", *Phys. Rev. A* **70**, 021601 (2004).

[Goo11] J. Goold, T. Fogarty, N. Lo Gullo, M. Paternostro, and T. Busch. "Orthogonality catastrophe as a consequence of qubit embedding in an ultracold Fermi gas", *Phys. Rev. A* **84**, 063632 (2011).

[Gre10] C. H. Greene. "Universal insights from few-body land", *Phys. Today* **63(3)**, 40 (2010).

[Gre02] M. Greiner, O. Mandel, T. Esslinger, T. W. Hänsch, and I. Bloch. "Quantum phase transition from a superfluid to a Mott insulator in a gas of ultracold atoms", *Nature (London)* **415**, 39 (2002).

[Gre03] M. Greiner, C. A. Regal, and D. S. Jin. "Emergence of a Molecular Bose-Einstein Condensate from a Fermi Gas", *Nature (London)* **426**, 537 (2003).

[Gri13] A. T. Grier, I. Ferrier-Barbut, B. S. Rem, M. Delehaye, L. Khaykovich, F. Chevy, and C. Salomon. "Λ enhanced sub-Doppler cooling of lithium atoms in D1 gray molasses", *Phys. Rev. A* **87**, 063411 (2013).

[Gri05] A Griesmaier, J Werner, S Hensler, J Stuhler, and T Pfau. "Bose-Einstein condensation of chromium", *Phys. Rev. Lett.* **94**, 160401 (2005).

[Gri08] R. Grimm. "Ultracold Fermi gases in the BEC-BCS crossover: a review from the Innsbruck perspective". In: *Ultra-cold Fermi Gases*. Ed. by M. Inguscio, W. Ketterle, and C. Salomon. Proceedings of the International School of Physics "Enrico Fermi", Course CLXIV, Varenna, 20-30 June 2006 (2008).

[Gri00] R. Grimm, M. Weidemüller, and Y. B. Ovchinnikov. "Optical dipole traps for neutral atoms", *Adv. At. Mol. Opt. Phys.* **42**, 95 (2000).

[Grö16] M. Gröbner, P. Weinmann, F. Meinert, K. Lauber, E. Kirilov, and H.-C. Nägerl. "A new quantum gas apparatus for ultracold mixtures of K and Cs and KCs ground-state molecules", *J. Mod. Opt.* **63**, 1829 (2016).

[Gro17] C. Gross and I. Bloch. "Quantum simulations with ultracold atoms in optical lattices", *Science* **357**, 995 (2017).

[Gub09] K. B. Gubbels, J. E. Baarsma, and H. T. C. Stoof. "Lifshitz Point in the Phase Diagram of Resonantly Interacting ^{6}Li-^{40}K Mixtures", *Phys. Rev. Lett.* **103**, 195301 (2009).

[Guo16] M. Guo, B. Zhu, B. Lu, X. Ye, F. Wang, R. Vexiau, N. Bouloufa-Maafa, G. Quéméner, O. Dulieu, and D. Wang. "Creation of an Ultracold Gas of Ground-State Dipolar ^{23}Na^{87}Rb Molecules", *Phys. Rev. Lett.* **116**, 205303 (2016).

[Gur07] V. Gurarie and L. Radzihovsky. “Resonantly paired fermionic superfluids”, *Ann. Phys. (NY)* **322**, 2 (2007).

[Had02] Z. Hadzibabic, C. A. Stan, K. Dieckmann, S. Gupta, M. W. Zwierlein, A. Görlitz, and W. Ketterle. “Two-Species Mixture of Quantum Degenerate Bose and Fermi Gases”, *Phys. Rev. Lett.* **88**, 160401 (2002).

[Had06] Z. Hadzibabic, P. Krüger, M. Cheneau, B. Battelier, and J. Dalibard. “Berezinskii-Kosterlitz-Thouless crossover in a trapped atomic gas”, *Nature (London)* **441**, 1118 (2006).

[Hal11] E. Haller, M. Rabie, M. J. Mark, J. G. Danzl, R. Hart, K. Lauber, G. Pupillo, and H.-C. Nägerl. “Three-Body Correlation Functions and Recombination Rates for Bosons in Three Dimensions and One Dimension”, *Phys. Rev. Lett.* **107**, 230404 (2011).

[Hal15] E. Haller, J. Hudson, A. Kelly, D. A. Cotta, B. Peaudecerf, G. D. Bruce, and S. Kuhr. “Single-atom imaging of fermions in a quantum-gas microscope”, *Nat. Phys.* **11**, 738 (2015).

[Han01] D. J. Han, M. T. DePue, and D. S. Weiss. “Loading and compressing Cs atoms in a very far-off-resonant light trap”, *Phys. Rev. A* **63**, 023405 (2001).

[Han17] T. M. Hanna, E. Tiesinga, and P. S. Julienne, *private communication* (2017).

[Han10] T. Hanna and E. Tiesinga, *private communication* (2010).

[Han13] J.-P. Hansen and I. R. McDonald. *Theory of Simple Liquids*. 4th Edition. New York: Academic (2013).

[Har15] R. A. Hart, P. M. Duarte, T.-L. Yang, X. Liu, T. Paiva, E. Khatami, R. T. Scalettar, N. Trivedi, D. A. Huse, and R. G. Hulet. “Observation of antiferromagnetic correlations in the Hubbard model with ultracold atoms”, *Nature (London)* **519**, 211 (2015).

[Hau07] R. Haussmann, W. Rantner, S. Cerrito, and W. Zwerger. “Thermodynamics of the BCS-BEC crossover”, *Phys. Rev. A* **75**, 023610 (2007).

[Ho04] T.-L. Ho. “Universal Thermodynamics of Degenerate Quantum Gases in the Unitarity Limit”, *Phys. Rev. Lett.* **92**, 090402 (2004).

[Hu16] M.-G. Hu, M. J. Van de Graaff, D. Kedar, J. P. Corson, E. A. Cornell, and D. S. Jin. “Bose Polarons in the Strongly Interacting Regime”, *Phys. Rev. Lett.* **117**, 055301 (2016).

[Hua87] K. Huang. *Statistical Mechanics*. Wiley (1987).

[Hun08] C.-L. Hung, X. Zhang, N. Gemelke, and C. Chin. “Accelerating evaporative cooling of atoms into Bose-Einstein condensation in optical traps”, *Phys. Rev. A* **78**, 011604(R) (2008).

[Hun13] C.-L. Hung, V. Gurarie, and C. Chin. “From Cosmology to Cold Atoms: Observation of Sakharov Oscillations in a Quenched Atomic Superfluid”, *Science* **341**, 1213 (2013).

[Ilz18] P. Ilzhöfer, G. Durastante, A. Patscheider, A. Trautmann, M. J. Mark, and F. Ferlaino. “Two-species five-beam magneto-optical trap for erbium and dysprosium”, *Phys. Rev. A* **97**, 023633 (2018).

[Ima06] A. Imambekov, C. J. Bolech, M. Lukin, and E. Demler. “Breakdown of the local density approximation in interacting systems of cold fermions in strongly anisotropic traps”, *Phys. Rev. A* **74**, 053626 (2006).

[Ing99] M. Inguscio, S. Stringari, and C. Wieman, eds. *Bose-Einstein condensation in atomic gases*. Proceedings of the International School of Physics “Enrico Fermi”, Course CXL, Varenna, 7-17 July 1998. North Holland, Amsterdam (1999).

[Ing08] M. Inguscio, W. Ketterle, and C. Salomon, eds. *Ultra-cold Fermi Gases*. Proceedings of the International School of Physics "Enrico Fermi", Course CLXIV, Varenna, 20-30 June 2006. IOS Press, Amsterdam (2008).

[Ino98] S. Inouye, M. R. Andrews, J. Stenger, H.-J. Miesner, D. M. Stamper-Kurn, and W. Ketterle. "Observation of Feshbach resonances in a Bose-Einstein condensate", *Nature (London)* **392**, 151 (1998).

[Ino04] S. Inouye, J. Goldwin, M. L. Olsen, C. Ticknor, J. L. Bohn, and D. S. Jin. "Observation of Heteronuclear Feshbach Resonances in a Mixture of Bosons and Fermions", *Phys. Rev. Lett.* **93**, 183201 (2004).

[Isk06] M. Iskin and C. A. R. Sá de Melo. "Two-Species Fermion Mixtures with Population Imbalance", *Phys. Rev. Lett.* **97**, 100404 (2006).

[Isk08] M. Iskin and C. J. Williams. "Trap-imbalanced fermion mixtures", *Phys. Rev. A* **77**, 013605 (2008).

[Jag14] M. Jag, M. Zaccanti, M. Cetina, R. S. Lous, F. Schreck, R. Grimm, D. S. Petrov, and J. Levinsen. "Observation of a Strong Atom-Dimer Attraction in a Mass-Imbalanced Fermi-Fermi Mixture", *Phys. Rev. Lett.* **112**, 075302 (2014).

[Jag16] M. Jag, M. Cetina, R. S. Lous, R. Grimm, J. Levinsen, and D. S. Petrov. "Lifetime of Feshbach dimers in a Fermi-Fermi mixture of ^{6}Li and ^{40}K", *Phys. Rev. A* **94**, 062706 (2016).

[Jak98] D. Jaksch, C. Bruder, J. I. Cirac, C. W. Gardiner, and P. Zoller. "Cold bosonic atoms in optical lattices", *Phys. Rev. Lett.* **81**, 3108 (1998).

[Jer14] D. Jervis and J. H. Thywissen. "Making an Ultracold Gas". In: *Quantum Gas Experiments: Exploring Many-Body States*. Ed. by P. Törmä and K. Sengstock. Imperial College Press (2014). Chap. 2.

[Jin96] D. S. Jin, J. R. Ensher, M. R. Matthews, C. E. Wieman, and E. A. Cornell. "Collective Excitations of a Bose-Einstein Condensate in a Dilute Gas", *Phys. Rev. Lett.* **77**, 420 (1996).

[Joc03a] S. Jochim, M. Bartenstein, A. Altmeyer, G. Hendl, S. Riedl, C. Chin, J. Hecker Denschlag, and R. Grimm. "Bose-Einstein Condensation of Molecules", *Science* **302**, 2101 (2003).

[Joc03b] S. Jochim, M. Bartenstein, A. Altmeyer, G. Hendl, C. Chin, J. Hecker Denschlag, and R. Grimm. "Pure Gas of Optically Trapped Molecules Created from Fermionic Atoms", *Phys. Rev. Lett* **91**, 240402 (2003).

[Joh17] J. Johansen, B. J. DeSalvo, K. Patel, and C. Chin. "Testing universality of Efimov physics across broad and narrow Feshbach resonances", *Nat. Phys.* **13**, 731 (2017).

[Jør16] N. B. Jørgensen, L. Wacker, K. T. Skalmstang, M. M. Parish, J. Levinsen, R. S. Christensen, G. M. Bruun, and J. J. Arlt. "Observation of Attractive and Repulsive Polarons in a Bose-Einstein Condensate", *Phys. Rev. Lett.* **117**, 055302 (2016).

[Jul11] P. S. Julienne, T. M. Hanna, and Z. Idziaszek. "Universal ultracold collision rates for polar molecules of two alkali-metal atoms", *Phys. Chem. Chem. Phys.* **13**, 19114 (2011).

[Kad16] H. Kadau, M. Schmitt, M. Wenzel, C. Wink, T. Maier, I. Ferrier-Barbut, and T. Pfau. "Observing the Rosensweig instability of a quantum ferrofluid", *Nature (London)* **530**, 194 (2016).

[Kag85] Y. Kagan, B. V. Svistunov, and G. V. Shlyapnikov. "Effect of Bose condensation on inelastic processes in gases", *JETP Lett.* **42**, 209 (1985).

[Kar07] O. I. Kartavtsev and A. V. Malykh. "Low-energy three-body dynamics in binary quantum gases", *J. Phys. B* **40**, 1429 (2007).

[Kem16] S. L. Kemp, K. L. Butler, R. Freytag, S. A. Hopkins, E. A. Hinds, M. R. Tarbutt, and S. L. Cornish. "Production and characterization of a dual species magneto-optical trap of cesium and ytterbium", *Rev. Sci. Instrum.* **87**, 023105 (2016).

[Ket96] W. Ketterle and N. J. van Druten. "Evaporative Cooling of Trapped Atoms", *Adv. At. Mol. Opt. Phys.* Advances In Atomic, Molecular, and Optical Physic **37**, 181 (1996).

[Ket99] W. Ketterle, D. S. Durfee, and D. M. Stamper-Kurn. "Making, probing and understanding Bose-Einstein condensates". In: *Bose-Einstein Condensation in Atomic Gases*. Ed. by M. Inguscio, S. Stringari, and C. E. Wieman. Vol. 140. Proceedings of the International School of Physics "Enrico Fermi", Course CXL, Varenna, 7-17 July 1998. IOS Press (1999).

[Ket07] W. Ketterle and M. Zwierlein. "Making, probing and understanding Fermi gases". In: *Ultracold Fermi Gases*. Ed. by M. Inguscio, W. Ketterle, and C. Salomon. Proceedings of the International School of Physics "Enrico Fermi", Course CLXIV (20 - 30 June 2006). IOS Press (2007), 95.

[Ket02] W. Ketterle. "Nobel lecture: When atoms behave as waves: Bose-Einstein condensation and the atom laser", *Rev. Mod. Phys.* **74**, 1131 (2002).

[Key11] C. W. von Keyserlingk and G. J. Conduit. "Itinerant ferromagnetism in an interacting Fermi gas with mass imbalance", *Phys. Rev. A* **83**, 053625 (2011).

[Kin04a] J. Kinast, S. L. Hemmer, M. E. Gehm, A. Turlapov, and J. E. Thomas. "Evidence for Superfluidity in a Resonantly Interacting Fermi Gas", *Phys. Rev. Lett.* **92**, 150402 (2004).

[Kin15] J. J. Kinnunen and G. M. Bruun. "Induced interactions in a superfluid Bose-Fermi mixture", *Phys. Rev. A* **91**, 041605 (2015).

[Kin04b] T. Kinoshita, T. Wenger, and D. S. Weiss. "Observation of a One-Dimensional Tonks-Girardeau Gas", *Science* **305**, 1125 (2004).

[Kir57] D. Kirzhnits. "Quantum Corrections to the Thomas-Fermi Equation", *JETP* **5**, 64 (1957).

[Kna12] M. Knap, A. Shashi, Y. Nishida, A. Imambekov, D. A. Abanin, and E. Demler. "Time-Dependent Impurity in Ultracold Fermions: Orthogonality Catastrophe and Beyond", *Phys. Rev. X* **2**, 041020 (2012).

[Köh06] T. Köhler, K. Goral, and P. S. Julienne. "Production of cold molecules via magnetically tunable Feshbach resonances", *Rev. Mod. Phys.* **78**, 1311 (2006).

[Köh05] T. Köhler, E. Tiesinga, and P. S. Julienne. "Spontaneous Dissociation of Long-Range Feshbach Molecules", *Phys. Rev. Lett.* **94**, 020402 (2005).

[Koh12] C. Kohstall, M. Zaccanti, M. Jag, A. Trenkwalder, P. Massignan, G. M. Bruun, F. Schreck, and R. Grimm. "Metastability and coherence of repulsive polarons in a strongly interacting Fermi mixture", *Nature (London)* **485**, 615 (2012).

[Kon64] J. Kondo. "Resistance Minimum in Dilute Magnetic Alloys", *Prog. Theor. Phys.* **32**, 37–49 (1964).

[Kon16] H. Konishi, F. Schäfer, S. Ueda, and Y. Takahashi. "Collisional stability of localized Yb($^3P_2$) atoms immersed in a Fermi sea of Li", *New J. Phys.* **18**, 103009 (2016).

[Kor50] J. Korringa. "Nuclear magnetic relaxation and resonnance line shift in metals", *Physica* **16**, 601 (1950).

[Kos12] M. Koschorreck, D. Pertot, E. Vogt, B. Frölich, M. Feld, and M. Köhl. "Attractive and repulsive Fermi polarons in two dimensions", *Nature (London)* **485**, 619 (2012).

[Kra06] T. Kraemer, M. Mark, P. Waldburger, J. G. Danzl, C. Chin, B. Engeser, A. D. Lange, K. Pilch, A. Jaakkola, H.-C. Nägerl, and R. Grimm. "Evidence for Efimov quantum states in an ultracold gas of caesium atoms", *Nature (London)* **440**, 315 (2006).

[Kra09] S. Kraft, F. Vogt, O. Appel, F. Riehle, and U. Sterr. "Bose-Einstein condensation of alkaline earth atoms: ^{40}Ca", *Phys. Rev. Lett.* **103**, 130401 (2009).

[Ku12] M. J. H. Ku, A. T. Sommer, L. W. Cheuk, and M. W. Zwierlein. "Revealing the Superfluid Lambda Transition in the Universal Thermodynamics of a Unitary Fermi Gas", *Science* **335**, 563 (2012).

[Lan56] L. Landau. "Theory of Fermi-liquids", *Sov. Phys. JETP* **3**, 920 (1956).

[Lan57] L. Landau. "Oscillations in a Fermi-liquid", *Sov. Phys. JETP* **5**, 101 (1957).

[Lan11] M. Landini, S. Roy, L. Carcagní, D. Trypogeorgos, M. Fattori, M. Inguscio, and G. Modugno. "Sub-Doppler laser cooling of potassium atoms", *Phys. Rev. A* **84**, 043432 (2011).

[Lan08a] F. Lang, P. van der Straten, B. Brandstätter, G. Thalhammer, K. Winkler, P. S. Julienne, R. Grimm, and J. Hecker Denschlag. "Cruising through molecular bound-state manifolds with radiofrequency", *Nat. Phys.* **4**, 223 (2008).

[Lan08b] F. Lang, K. Winkler, C. Strauss, R. Grimm, and J. Hecker Denschlag. "Ultracold Triplet Molecules in the Rovibrational Ground State", *Phys. Rev. Lett.* **101**, 133005 (2008).

[Lan09] A. D. Lange, K. Pilch, A. Prantner, F. Ferlaino, B. Engeser, H.-C. Nägerl, R. Grimm, and C. Chin. "Determination of atomic scattering lengths from measurements of molecular binding energies near Feshbach resonances", *Phys. Rev. A* **79**, 013622 (2009).

[Lau17] S. Laurent, M. Pierce, M. Delehaye, T. Yefsah, F. Chevy, and C. Salomon. "Connecting Few-Body Inelastic Decay to Quantum Correlations in a Many-Body System: A Weakly Coupled Impurity in a Resonant Fermi Gas", *Phys. Rev. Lett.* **118**, 103403 (2017).

[LeB07] L. J. LeBlanc and J. H. Thywissen. "Species-specific optical lattices", *Phys. Rev. A* **75**, 053612 (2007).

[Lee16] K. L. Lee, N. B. Jørgensen, I.-K. Liu, L. Wacker, J. J. Arlt, and N. P. Proukakis. "Phase separation and dynamics of two-component Bose-Einstein condensates", *Phys. Rev. A* **94**, 013602 (2016).

[Lev09] J. Levinsen, T. G. Tiecke, J. T. M. Walraven, and D. S. Petrov. "Atom-dimer scattering and long-lived trimers in fermionic mixtures", *Phys. Rev. Lett.* **103**, 153202 (2009).

[Lev11] J. Levinsen and D. Petrov. "Atom-dimer and dimer-dimer scattering in fermionic mixtures near a narrow Feshbach resonance", *Eur. Phys. J. D* **65**, 67 (2011).

[Lew04] M. Lewenstein, L. Santos, M. A. Baranov, and H. Fehrmann. "Atomic Bose-Fermi Mixtures in an Optical Lattice", *Phys. Rev. Lett.* **92**, 050401 (2004).

[Lew12] M. Lewenstein, A. Anna Sanpera, and V. Ahufinger. *Ultracold Atoms in Optical Lattices: Simulating quantum many-body systems*. Oxford University Press, Oxford (2012).

[Lin06] G.-D. Lin, W. Yi, and L.-M. Duan. "Superfluid shells for trapped fermions with mass and population imbalance", *Phys. Rev. A* **74**, 031604 (2006).

[Lin14] M. G. Lingham, K. Fenech, S. Hoinka, and C. J. Vale. "Local Observation of Pair Condensation in a Fermi Gas at Unitarity", *Phys. Rev. Lett.* **112**, 100404 (2014).

[Liu16] I.-K. Liu, R. W. Pattinson, T. P. Billam, S. A. Gardiner, S. L. Cornish, T.-M. Huang, W.-W. Lin, S.-C. Gou, N. G. Parker, and N. P. Proukakis. "Stochastic growth dynamics and composite defects in quenched immiscible binary condensates", *Phys. Rev. A* **93**, 023628 (2016).

[Liu18] W. E. Liu, J. Levinsen, and M. M. Parish. "Variational approach for impurity dynamics at finite temperature", *ArXiv e-prints*, 1805.10013 (2018).

[Liu03] W. V. Liu and F. Wilczek. "Interior Gap Superfluidity", *Phys. Rev. Lett.* **90**, 047002 (2003).

[Lob06] C. Lobo, A. Recati, S. Giorgini, and S. Stringari. "Normal State of a Polarized Fermi Gas at Unitarity", *Phys. Rev. Lett.* **97**, 200403 (2006).

[Lof02] T. Loftus, C. A. Regal, C. Ticknor, J. L. Bohn, and D. S. Jin. "Resonant Control of Elastic Collisions in an Optically Trapped Fermi Gas of Atoms", *Phys. Rev. Lett.* **88**, 173201 (2002).

[Löf01] T Löfwander, V. S. Shumeiko, and G Wendin. "Andreev bound states in high- T c superconducting junctions", *Supercond. Sci. Technol.* **14**, R53 (2001).

[Lon38] F. London. "The λ-Phenomenon of Liquid Helium and the Bose-Einstein Degeneracy", *Nature (London)* **141**, 643 (1938).

[Lou17a] R. S. Lous, B. Huang, I. Fritsche, F. Lehmann, M. Jag, E. Kirilov, and R. Grimm, *DPG spring meeting* (2017).

[Lou17b] R. S. Lous, I. Fritsche, M. Jag, B. Huang, and R. Grimm. "Thermometry of a deeply degenerate Fermi gas with a Bose-Einstein condensate", *Phys. Rev. A* **95**, 053627 (2017).

[Lou18] R. S. Lous, I. Fritsche, M. Jag, F. Lehmann, E. Kirilov, B. Huang, and R. Grimm. "Probing the Interface of a Phase-Separated State in a Repulsive Bose-Fermi Mixture", *Phys. Rev. Lett.* **120**, 243403 (2018).

[Lu12] M. Lu, N. Q. Burdick, and B. L. Lev. "Quantum Degenerate Dipolar Fermi Gas", *Phys. Rev. Lett.* **108**, 215301 (2012).

[Lu11] M. Lu, N. Q. Burdick, S. H. Youn, and B. L. Lev. "Strongly Dipolar Bose-Einstein Condensate of Dysprosium", *Phys. Rev. Lett.* **107**, 190401 (2011).

[Lud11] D. Ludwig, S. Floerchinger, S. Moroz, and C. Wetterich. "Quantum phase transition in Bose-Fermi mixtures", *Phys. Rev. A* **84**, 033629 (2011).

[Luo07] L. Luo, B. Clancy, J. Joseph, J. Kinast, and J. E. Thomas. "Measurement of the Entropy and Critical Temperature of a Strongly Interacting Fermi Gas", *Phys. Rev. Lett.* **98**, 080402 (2007).

[Lys10] M. Lysebo and L. Veseth. "Feshbach resonances and transition rates for cold homonuclear collisions between ^{39}K and ^{41}K atoms", *Phys. Rev. A* **81**, 032702 (2010).

[Mad00] K. W. Madison, F. Chevy, W. Wohlleben, and J. Dalibard. "Vortex Formation in a Stirred Bose-Einstein Condensate", *Phys. Rev. Lett.* **84**, 806 (2000).

[Mar08a] B. Marcelis, S. J.J.M. F. Kokkelmans, G. V. Shlyapnikov, and D. S. Petrov. "Collisional properties of weakly bound heteronuclear dimers", *Phys. Rev. A* **77**, 032707 (2008).

[Mar08b] F. M. Marchetti, C. J. M. Mathy, D. A. Huse, and M. M. Parish. "Phase separation and collapse in Bose-Fermi mixtures with a Feshbach resonance", *Phys. Rev. B* **78**, 134517 (2008).

[Mar09] Y. N. Martinez de Escobar, P. G. Mickelson, M. Yan, B. J. DeSalvo, S. B. Nagel, and T. C. Killian. "Bose-Einstein Condensation of ^{84}Sr", *Phys. Rev. Lett.* **103**, 200402 (2009).

[Mar13] T. Maruyama and H. Yabu. "Longitudinal and transverse breathing oscillations in Bose-Fermi mixtures of Yb atoms at zero temperature in the largely prolate deformed traps", *J. Phys. B* **46**, 055201 (2013).

[Mar09] C. Marzok, B. Deh, C. Zimmermann, P. W. Courteille, E. Tiemann, Y. V. Vanne, and A. Saenz. "Feshbach resonances in an ultracold ^{7}Li and ^{87}Rb mixture", *Phys. Rev. A* **79**, 012717 (2009).

[Mas12] P. Massignan. "Polarons and dressed molecules near narrow Feshbach resonances", *Europhys. Lett.* **98**, 10012 (2012).

[Mas11] P. Massignan and G. M. Bruun. "Repulsive polarons and itinerant ferromagnetism in strongly polarized Fermi gases", *Eur. Phys. J. D* **65**, 83 (2011).

[Mas14] P. Massignan, M. Zaccanti, and G. M. Bruun. "Polarons, dressed molecules and itinerant ferromagnetism in ultracold Fermi gases", *Rep. Prog. Phys.* **77**, 034401 (2014).

[Mat11] C. J. M. Mathy, M. M. Parish, and D. A. Huse. "Trimers, Molecules, and Polarons in Mass-Imbalanced Atomic Fermi Gases", *Phys. Rev. Lett.* **106**, 166404 (2011).

[Mat99] M. R. Matthews, B. P. Anderson, P. C. Haljan, D. S. Hall, C. E. Wieman, and E. A. Cornell. "Vortices in a Bose-Einstein Condensate", *Phys. Rev. Lett.* **83**, 2498 (1999).

[McA96] W. I. McAlexander, E. R. I. Abraham, and R. G. Hulet. "Radiative lifetime of the $2P$ state of lithium", *Phys. Rev. A* **54**, R5 (1996).

[McC11] D. J. McCarron, H. W. Cho, D. L. Jenkin, M. P. Koeppinger, and S. L. Cornish. "Dual-species Bose-Einstein condensate of 87Rb and 133Cs", *Phys. Rev. A* **84**, 011603 (2011).

[McK11] D. C. McKay, D. Jervis, D. J. Fine, J. W. Simpson-Porco, G. J. A. Edge, and J. H. Thywissen. "Low-temperature high-density magneto-optical trapping of potassium using the open $4S \rightarrow 5P$ transition at 405 nm", *Phys. Rev. A* **84**, 063420 (2011).

[McN06] J. M. McNamara, T. Jeltes, A. S. Tychkov, W. Hogervorst, and W. Vassen. "Degenerate Bose-Fermi Mixture of Metastable Atoms", *Phys. Rev. Lett.* **97**, 080404 (2006).

[Mei13] F. Meinert, M. J. Mark, E. Kirilov, K. Lauber, P. Weinmann, A. J. Daley, and H.-C. Nägerl. "Quantum Quench in an Atomic One-Dimensional Ising Chain", *Phys. Rev. Lett.* **111**, 053003 (2013).

[Met99] H. J. Metcalf and P. van der Straten. *Laser Cooling and Trapping*. Springer, New York (1999).

[Mew96] M.-O. Mewes, M. R. Andrews, N. J. van Druten, D. M. Kurn, D. S. Durfee, C. G. Townsend, and W. Ketterle. "Collective Excitations of a Bose-Einstein Condensate in a Magnetic Trap", *Phys. Rev. Lett.* **77**, 988 (1996).

[Mod01] G. Modugno, G. Ferrari, G. Roati, R. J. Brecha, A. Simoni, and M. Inguscio. "Bose-Einstein Condensation of Potassium Atoms by Sympathetic Cooling", *Science* **294**, 1320 (2001).

[Mod02] G. Modugno, G. Roati, F. Riboli, F. Ferlaino, R. Brecha, and M. Inguscio. "Collapse of a degenerate Fermi gas", *Science* **297**, 2240 (2002).

[Mø98] K. Mølmer. "Bose Condensates and Fermi Gases at Zero Temperature", *Phys. Rev. Lett.* **80**, 1804 (1998).

[Mol14] P. K. Molony, P. D. Gregory, Z. Ji, B. Lu, M. P. Köppinger, C. R. Le Sueur, C. L. Blackley, J. M. Hutson, and S. L. Cornish. "Creation of Ultracold ^{87}Rb^{133}Cs Molecules in the Rovibrational Ground State", *Phys. Rev. Lett.* **113**, 255301 (2014).

[Mos17] S. A. Moses, J. P. Covey, M. T. Miecnikowski, D. S. Jin, and J. Ye. "New frontiers for quantum gases of polar molecules", *Nat. Phys.* **13**, 13 (2017).

[Mos15] S. A. Moses, J. P. Covey, M. T. Miecnikowski, B. Yan, B. Gadway, J. Ye, and D. S. Jin. "Creation of a low-entropy quantum gas of polar molecules in an optical lattice", *Science* **350**, 659 (2015).

[Mos01] A. Mosk, S. Kraft, M. Mudrich, K. Singer, W. Wohlleben, R. Grimm, and M. Weidemüller. "Mixture of ultracold lithium and cesium atoms in an optical dipole trap", *Appl. Phys. B* **73**, 791 (2001).

[Mud02] M. Mudrich, S. Kraft, K. Singer, R. Grimm, A. Mosk, and M. Weidemüller. "Sympathetic Cooling with Two Atomic Species in an Optical Trap", *Phys. Rev. Lett.* **88**, 253001 (2002).

[Muk17] B. Mukherjee, Z. Yan, P. B. Patel, Z. Hadzibabic, T. Yefsah, J. Struck, and M. W. Zwierlein. "Homogeneous Atomic Fermi Gases", *Phys. Rev. Lett.* **118**, 123401 (2017).

[Mur95] S. Q. Murphy, J. P. Eisenstein, L. N. Pfeiffer, and K. W. West. "Lifetime of two-dimensional electrons measured by tunneling spectroscopy", *Phys. Rev. B* **52**, 14825 (1995).

[Mya97] C. J. Myatt, E. A. Burt, R. W. Ghrist, E. A. Cornell, and C. E. Wieman. "Production of Two Overlapping Bose-Einstein Condensates by Sympathetic Cooling", *Phys. Rev. Lett.* **78**, 586 (1997).

[Nai11] D. Naik, A. Trenkwalder, C. Kohstall, F. M. Spiegelhalder, M. Zaccanti, G. Hendl, F. Schreck, R. Grimm, T. Hanna, and P. Julienne. "Feshbach resonances in the ^{6}Li-^{40}K Fermi-Fermi mixture: Elastic versus inelastic interactions", *Eur. Phys. J. D* **65**, 55 (2011).

[Nas09] S. Nascimbène, N. Navon, K. J. Jiang, L. Tarruell, M. Teichmann, J. McKeever, F. Chevy, and C. Salomon. "Collective Oscillations of an Imbalanced Fermi Gas: Axial Compression Modes and Polaron Effective Mass", *Phys. Rev. Lett.* **103**, 170402 (2009).

[Nas10] S. Nascimbène, N. Navon, K. J. Jiang, F. Chevy, and C. Salomon. "Exploring the thermodynamics of a universal Fermi gas", *Nature (London)* **463**, 1057 (2010).

[Nas11] S. Nascimbène, N. Navon, S. Pilati, F. Chevy, S. Giorgini, A. Georges, and C. Salomon. "Fermi-Liquid Behavior of the Normal Phase of a Strongly Interacting Gas of Cold Atoms", *Phys. Rev. Lett.* **106**, 215303 (2011).

[Nav10] N. Navon, S. Nascimbène, F. Chevy, and C. Salomon. "The Equation of State of a Low-Temperature Fermi Gas with Tunable Interactions", *Science* **328**, 729 (2010).

[Nav15] N. Navon, A. L. Gaunt, R. P. Smith, and Z. Hadzibabic. "Critical dynamics of spontaneous symmetry breaking in a homogeneous Bose gas", *Science* **347**, 167 (2015).

[Nay15] B. Naylor, A. Reigue, E. Maréchal, O. Gorceix, B. Laburthe-Tolra, and L. Vernac. "Chromium dipolar Fermi sea", *Phys. Rev. A* **91**, 011603 (2015).

[Ni08] K.-K. Ni, S. Ospelkaus, M. H. G. de Miranda, A. Pe'er, B. Neyenhuis, J. J. Zirbel, S. Kotochigova, P. S. Julienne, D. S. Jin, and J. Ye. "A High Phase-Space-Density Gas of Polar Molecules", *Science* **322**, 231 (2008).

[Nis09a] Y. Nishida. "Casimir interaction among heavy fermions in the BCS-BEC crossover", *Phys. Rev. A* **79**, 013629 (2009).

[Nis13] Y. Nishida. "SU(3) Orbital Kondo Effect with Ultracold Atoms", *Phys. Rev. Lett.* **111**, 135301 (2013).

[Nis08] Y. Nishida and S. Tan. "Universal Fermi gases in mixed dimensions", *Phys. Rev. Lett.* **101**, 170401 (2008).

[Nis09b] Y. Nishida and S. Tan. "Confinement-induced Efimov resonances in Fermi-Fermi mixtures", *Phys. Rev. A* **79**, 060701(R) (2009).

[NIS12] NIST/SEMATECH. *e-Handbook of Statistical Methods*. `http://www.itl.nist.gov/div898/handbook/`. Accessed online: 2017-10-05 (2012).

[O'H02] K. M. O'Hara, S. L. Hemmer, M. E. Gehm, S. R. Granade, and J. E. Thomas. "Observation of a Strongly Interacting Degenerate Fermi Gas", *Science* **298**, 2179 (2002).

[Omr15] A. Omran, M. Boll, T. A. Hilker, K. Kleinlein, G. Salomon, I. Bloch, and C. Gross. "Microscopic Observation of Pauli Blocking in Degenerate Fermionic Lattice Gases", *Phys. Rev. Lett.* **115**, 263001 (2015).

[Ono16] R Onofrio. "Cooling and thermometry of atomic Fermi gases", *Phys. Usp.* **59**, 1129 (2016).

[Ors10] G. Orso, E. Burovski, and T. Jolicoeur. "Luttinger Liquid of Trimers in Fermi Gases with Unequal Masses", *Phys. Rev. Lett.* **104**, 065301 (2010).

[Osp06a] C. Ospelkaus, S. Ospelkaus, K. Sengstock, and K. Bongs. "Interaction-Driven Dynamics of ^{40}K-^{87}Rb Fermion-Boson Gas Mixtures in the Large-Particle-Number Limit", *Phys. Rev. Lett.* **96**, 020401 (2006).

[Osp06b] S. Ospelkaus, C. Ospelkaus, O. Wille, M. Succo, P. Ernst, K. Sengstock, and K. Bongs. "Localization of Bosonic Atoms by Fermionic Impurities in a Three-Dimensional Optical Lattice", *Phys. Rev. Lett.* **96**, 180403 (2006).

[Osp06c] S. Ospelkaus, C. Ospelkaus, L. Humbert, K. Sengstock, and K. Bongs. "Tuning of Heteronuclear Interactions in a Degenerate Fermi-Bose Mixture", *Phys. Rev. Lett.* **97**, 120403 (2006).

[Oza14] T. Ozawa, A. Recati, M. Delehaye, F. Chevy, and S. Stringari. "Chandrasekhar-Clogston limit and critical polarization in a Fermi-Bose superfluid mixture", *Phys. Rev. A* **90**, 043608 (2014).

[Pap08a] S. B. Papp, J. M. Pino, R. J. Wild, S. Ronen, C. E. Wieman, D. S. Jin, and E. A. Cornell. "Bragg Spectroscopy of a Strongly Interacting ^{85}Rb Bose-Einstein Condensate", *Phys. Rev. Lett.* **101**, 135301 (2008).

[Pap08b] S. B. Papp, J. M. Pino, and C. E. Wieman. "Tunable Miscibility in a Dual-Species Bose-Einstein Condensate", *Phys. Rev. Lett.* **101**, 040402 (2008).

[Par04] B. Paredes, A. Widera, V. Murg, O. Mandel, S. Fölling, I. Cirac, G. V. Shlyapnikov, T. Hänsch, and I. Bloch. "Tonks-Girardeau gas of ultracold atoms in an optical lattice", *Nature (London)* **729**, 277 (2004).

[Par07] M. M. Parish, F. M. Marchetti, A. Lamacraft, and B. D. Simons. "Polarized Fermi Condensates with Unequal Masses: Tuning the Tricritical Point", *Phys. Rev. Lett.* **98**, 160402 (2007).

[Par16] M. M. Parish and J. Levinsen. "Quantum dynamics of impurities coupled to a Fermi sea", *Phys. Rev. B* **94**, 184303 (2016).

[Par15a] J. W. Park, S. A. Will, and M. W. Zwierlein. "Ultracold Dipolar Gas of Fermionic ^{23}Na^{40}K Molecules in Their Absolute Ground State", *Phys. Rev. Lett.* **114**, 205302 (2015).

[Par15b] M. F. Parsons, F. Huber, A. Mazurenko, C. S. Chiu, W. Setiawan, K. Wooley-Brown, S. Blatt, and M. Greiner. "Site-Resolved Imaging of Fermionic ^{6}Li in an Optical Lattice", *Phys. Rev. Lett.* **114**, 213002 (2015).

[Par05] G. B. Partridge, K. E. Strecker, R. I. Kamar, M. W. Jack, and R. G. Hulet. "Molecular Probe of Pairing in the BEC-BCS Crossover", *Phys. Rev. Lett.* **95**, 020404 (2005).

[Par06] G. B. Partridge, W. Li, R. I. Kamar, Y. Liao, and R. G. Hulet. "Pairing and Phase Separation in a Polarized Fermi Gas", *Science* **311**, 503 (2006).

[Pat14] H. J. Patel, C. L. Blackley, S. L. Cornish, and J. M. Hutson. "Feshbach resonances, molecular bound states, and prospects of ultracold-molecule formation in mixtures of ultracold K and Cs", *Phys. Rev. A* **90**, 032716 (2014).

[Pau46] W. Pauli. “Nobel Lecture: Exclusion Principle and Quantum Mechanics”, *Nobelprize.org* (1946).

[Pau28] L. Pauling. “The Application of the Quantum Mechanics to the Structure of the Hydrogen Molecule and Hydrogen Molecule-Ion and to Related Problems.”, *Chem. Rev.* **5**, 173 (1928).

[PDS01] F. Pereira Dos Santos, J. Léonard, J. Wang, C. J. Barrelet, F. Perales, E. Rasel, C. S. Unnikrishnan, M. Leduc, and C. Cohen-Tannoudji. “Bose-Einstein Condensation of Metastable Helium”, *Phys. Rev. Lett.* **86**, 3459 (2001).

[Pet04a] D. S. Petrov. “Three-boson problem near a narrow Feshbach resonance”, *Phys. Rev. Lett.* **93**, 143201 (2004).

[Pet00] D. S. Petrov, G. V. Shlyapnikov, and J. T. M. Walraven. “Regimes of Quantum Degeneracy in Trapped 1D Gases”, *Phys. Rev. Lett.* **85**, 3745 (2000).

[Pet04b] D. S. Petrov, C. Salomon, and G. V. Shlyapnikov. “Weakly bound molecules of fermionic atoms”, *Phys. Rev. Lett.* **93**, 090404 (2004).

[Pet05a] D. S. Petrov, C Salomon, and G. V. Shlyapnikov. “Diatomic molecules in ultracold Fermi gases - novel composite bosons”, *J. Phys. B* **38**, S645 (2005).

[Pet05b] D. S. Petrov, C. Salomon, and G. V. Shlyapnikov. “Scattering properties of weakly bound dimers of fermionic atoms”, *Phys. Rev. A* **71**, 012708 (2005).

[Pet07] D. S. Petrov, G. E. Astrakharchik, D. J. Papoular, C. Salomon, and G. V. Shlyapnikov. “Crystalline Phase of Strongly Interacting Fermi Mixtures”, *Phys. Rev. Lett.* **99**, 130407 (2007).

[Phi98] W. D. Phillips. “Nobel Lecture: Laser cooling and trapping of neutral atoms”, *Rev. Mod. Phys.* **70**, 721 (1998).

[Pir14] R. Pires, J. Ulmanis, S. Häfner, M. Repp, A. Arias, E. D. Kuhnle, and M. Weidemüller. “Observation of Efimov Resonances in a Mixture with Extreme Mass Imbalance”, *Phys. Rev. Lett.* **112**, 250404 (2014).

[Pit16] L. Pitaevskii and S. Stringari. *Bose-Einstein Condensation and Superfluidity*. Oxford University Press (2016).

[Pob07] F. Pobell. “The 3He-4He Dilution Refrigerator”. In: *Matter and Methods at Low Temperatures*. Springer-Verlag, Berlin (2007), 149.

[Pow05] S. Powell, S. Sachdev, and H. P. Büchler. “Depletion of the Bose-Einstein condensate in Bose-Fermi mixtures”, *Phys. Rev. B* **72**, 024534 (2005).

[Qi12] R. Qi and H. Zhai. “Highly polarized Fermi gases across a narrow Feshbach resonance”, *Phys. Rev. A* **85**, 041603(R) (2012).

[Qué11] G. Quéméner, J. Bohn, A. Petrov, and S. Kotochigova. “Universalities in ultracold reactions of alkali-metal polar molecules”, *Phys. Rev. A* **84**, 062703 (2011).

[Ram11] B. Ramachandhran, S. G. Bhongale, and H. Pu. “Finite-temperature study of Bose-Fermi superfluid mixtures”, *Phys. Rev. A* **83**, 033607 (2011).

[Rav18] C. Ravensbergen, V. Corre, E. Soave, M. Kreyer, S. Tzanova, E. Kirilov, and R. Grimm. “Accurate Determination of the Dynamical Polarizability of Dysprosium”, *Phys. Rev. Lett.* **120**, 223001 (2018).

[Reg03] C. A. Regal, C. Ticknor, J. L. Bohn, and D. S. Jin. “Tuning *p*-wave Interactions in an Ultracold Fermi Gas of Atoms”, *Phys. Rev. Lett.* **90**, 053201 (2003).

[Reg04a] C. A. Regal, M. Greiner, and D. S. Jin. "Lifetime of Molecule-Atom Mixtures near a Feshbach Resonance in K", *Phys. Rev. Lett.* **92**, 083201 (2004).

[Reg04b] C. A. Regal, M. Greiner, and D. S. Jin. "Observation of Resonance Condensation of Fermionic Atom Pairs", *Phys. Rev. Lett.* **92**, 040403 (2004).

[Rei17] L. Reichsöllner, A. Schindewolf, T. Takekoshi, R. Grimm, and H.-C. Nägerl. "Quantum Engineering of a Low-Entropy Gas of Heteronuclear Bosonic Molecules in an Optical Lattice", *Phys. Rev. Lett.* **118**, 073201 (2017).

[Rev16] M. C. Revelle, J. A. Fry, B. A. Olsen, and R. G. Hulet. "1D to 3D Crossover of a Spin-Imbalanced Fermi Gas", *Phys. Rev. Lett.* **117**, 235301 (2016).

[Rid11] A. Ridinger, S. Chaudhuri, T. Salez, U. Eismann, D. R. Fernandes, K. Magalhães, D. Wilkowski, C. Salomon, and F. Chevy. "Large atom number dual-species magneto-optical trap for fermionic 6Li and 40K atoms", *Eur. Phys. J. D* **65**, 223 (2011).

[Roa02] G. Roati, F. Riboli, G. Modugno, and M. Inguscio. "Fermi-Bose Quantum Degenerate K-Rb Mixture with Attractive Interaction", *Phys. Rev. Lett.* **89**, 150403 (2002).

[Roa07] G. Roati, M. Zaccanti, C. D'Errico, J. Catani, M. Modugno, A. Simoni, M. Inguscio, and G. Modugno. "^{39}K Bose-Einstein Condensate with Tunable Interactions", *Phys. Rev. Lett.* **99**, 010403 (2007).

[Rob01] A. Robert, O. Sirjean, A. Browaeys, J. Poupard, S. Nowak, D. Boiron, C. I. Westbrook, and A. Aspect. "A Bose-Einstein Condensate of Metastable Atoms", *Science* **292**, 461 (2001).

[Ros98] K. Rosman and P. Taylor. "Isotopic compositions of the elements 1997 (Technical Report)", *Pure Appl. Chem.* **70**, 217 (1998).

[Rot02] R. Roth. "Structure and stability of trapped atomic boson-fermion mixtures", *Phys. Rev. A* **66**, 013614 (2002).

[Roy17] R. Roy, A. Green, R. Bowler, and S. Gupta. "Two-Element Mixture of Bose and Fermi Superfluids", *Phys. Rev. Lett.* **118**, 055301 (2017).

[Ruf04] A. B. Ruffin. "Stimulated brillouin scattering: an overview of measurements, system impairments, and applications". In: *NIST Symposium on Optical Fiber Measurements*. National Institute of Standards and Technology, Boulder, Colorado (2004).

[Rva17] T. M. Rvachov, H. Son, A. T. Sommer, S. Ebadi, J. J. Park, M. W. Zwierlein, W. Ketterle, and A. O. Jamison. "Long-Lived Ultracold Molecules with Electric and Magnetic Dipole Moments", *Phys. Rev. Lett.* **119**, 143001 (2017).

[Sac99] C. A. Sackett, J. M. Gerton, M. Welling, and R. G. Hulet. "Measurements of Collective Collapse in a Bose-Einstein Condensate with Attractive Interactions", *Phys. Rev. Lett.* **82**, 876 (1999).

[Saf10] M. Saffman, T. G. Walker, and K. Mølmer. "Quantum information with Rydberg atoms", *Rev. Mod. Phys.* **82**, 2313 (2010).

[Saf13] M. S. Safronova, U. I. Safronova, and C. W. Clark. "Magic wavelengths for optical cooling and trapping of potassium", *Phys. Rev. A* **87**, 052504 (2013).

[Sag15] Y. Sagi, T. E. Drake, R. Paudel, R. Chapurin, and D. S. Jin. "Breakdown of the Fermi Liquid Description for Strongly Interacting Fermions", *Phys. Rev. Lett.* **114**, 075301 (2015).

[SC91] C. Sanchez-Castro and K. S. Bedell. "Two-component Fermi liquids and the induced-interaction model", *Phys. Rev. B* **43**, 12874 (1991).

[Sat17] M. Sato and Y. Ando. "Topological superconductors: a review", *Rep. Prog. Phys.* **80**, 076501 (2017).

[Sav97] T. A. Savard, K. M. O'Hara, and J. E. Thomas. "Laser-noise-induced heating in far-off resonance optical traps", *Phys. Rev. A* **56**, R1095 (1997).

[Sca17] F. Scazza, G. Valtolina, P. Massignan, A. Recati, A. Amico, A. Burchianti, C. Fort, M. Inguscio, M. Zaccanti, and G. Roati. "Repulsive Fermi Polarons in a Resonant Mixture of Ultracold ^{6}Li Atoms", *Phys. Rev. Lett.* **118**, 083602 (2017).

[Sce13] R. Scelle, T. Rentrop, A. Trautmann, T. Schuster, and M. K. Oberthaler. "Motional Coherence of Fermions Immersed in a Bose Gas", *Phys. Rev. Lett.* **111**, 070401 (2013).

[Sch08] A. Schirotzek, Y.-i. Shin, C. H. Schunck, and W. Ketterle. "Determination of the Superfluid Gap in Atomic Fermi Gases by Quasiparticle Spectroscopy", *Phys. Rev. Lett.* **101**, 140403 (2008).

[Sch09] A. Schirotzek, C.-H. Wu, A. Sommer, and M. W. Zwierlein. "Observation of Fermi polarons in a tunable Fermi liquid of ultracold atoms", *Phys. Rev. Lett.* **102**, 230402 (2009).

[Sch18] R. Schmidt, M. Knap, D. A. Ivanov, J.-S. You, M. Cetina, and E. Demler. "Universal many-body response of heavy impurities coupled to a Fermi sea: a review of recent progress", *Rep. Prog. Phys.* **81**, 024401 (2018).

[Sch14] T. F. Schmidutz, I. Gotlibovych, A. L. Gaunt, R. P. Smith, N. Navon, and Z. Hadzibabic. "Quantum Joule-Thomson Effect in a Saturated Homogeneous Bose Gas", *Phys. Rev. Lett.* **112**, 040403 (2014).

[Sch16] M. Schmitt, M. Wenzel, F. Böttcher, I. Ferrier-Barbut, and T. Pfau. "Self-bound droplets of a dilute magnetic quantum liquid", *Nature (London)* **539**, 259 (2016).

[Sch01a] F. Schreck, L. Khaykovich, K. L. Corwin, G. Ferrari, T. Bourdel, J. Cubizolles, and C. Salomon. "Quasipure Bose-Einstein Condensate Immersed in a Fermi Sea", *Phys. Rev. Lett.* **87**, 080403 (2001).

[Sch05] C. H. Schunck, M. W. Zwierlein, C. A. Stan, S. M. F. Raupach, W. Ketterle, A. Simoni, E. Tiesinga, C. J. Williams, and P. S. Julienne. "Feshbach resonances in fermionic ^{6}Li", *Phys. Rev. A* **71**, 045601 (2005).

[Sch01b] J. Schuster, A. Marte, S. Amtage, B. Sang, G. Rempe, and H. C. W. Beijerinck. "Avalanches in a Bose-Einstein Condensate", *Phys. Rev. Lett.* **87**, 170404 (2001).

[Sed18] A. Sedrakian and J. W. Clark. "Superfluidity in nuclear systems and neutron stars", *ArXiv e-prints*, 1802.00017 (2018).

[She10] J. F. Sherson, C. Weitenberg, M. Endres, M. Cheneau, I. Bloch, and S. Kuhr. "Single-atom-resolved fluorescence imaging of an atomic Mott insulator", *Nature (London)* **467**, 68 (2010).

[Shi08] Y. Shin, C. H. Schunck, A. Schirotzek, and W. Ketterle. "Phase diagram of a two-component Fermi gas with resonant interactions", *Nature (London)* **451**, 689 (2008).

[Sid13] L. A. Sidorenkov, M. K. Tey, R. Grimm, Y.-H. Hou, L. Pitaevskii, and S. Stringari. "Second sound and the superfluid fraction in a Fermi gas with resonant interactions", *Nature (London)* **498**, 78 (2013).

[Sie15] F. Sievers, N. Kretzschmar, D. R. Fernandes, D. Suchet, M. Rabinovic, S. Wu, C. V. Parker, L. Khaykovich, C. Salomon, and F. Chevy. "Simultaneous sub-Doppler laser cooling of fermionic ^{6}Li and ^{40}K on the D_1 line: Theory and experiment", *Phys. Rev. A* **91**, 023426 (2015).

[Slu96] M. Slutzky, O. Entin-Wohlman, Y. Berk, A. Palevski, and H. Shtrikman. “Electron-electron scattering in coupled quantum wells”, *Phys. Rev. B* **53**, 4065 (1996).

[Sob72] I. I. Sobelman. *An introduction to the theory of atomic spectra*. Pergamon Press, Oxford (1972).

[Söd99] J. Söding, D. Guéry-Odelin, P. Desbiolles, F. Chevy, H. Inamori, and J. Dalibard. “Three-body decay of a rubidium Bose–Einstein condensate”, *Appl. Phys. B* **69**, 257 (1999).

[Som11] A. Sommer, M. Ku, G. Roati, and M. W. Zwierlein. “Universal spin transport in a strongly interacting Fermi gas”, *Nature (London)* **472**, 201 (2011).

[Sot12] A. Sotnikov, D. Cocks, and W. Hofstetter. “Advantages of Mass-Imbalanced Ultracold Fermionic Mixtures for Approaching Quantum Magnetism in Optical Lattices”, *Phys. Rev. Lett.* **109**, 065301 (2012).

[Spi09] F. M. Spiegelhalder, A. Trenkwalder, D. Naik, G. Hendl, F. Schreck, and R. Grimm. “Collisional stability of ^{40}K immersed in a strongly interacting Fermi Gas of ^{6}Li”, *Phys. Rev. Lett.* **103**, 223203 (2009).

[Spi10] F. M. Spiegelhalder, A. Trenkwalder, D. Naik, G. Kerner, E. Wille, G. Hendl, F. Schreck, and R. Grimm. “All-optical production of a degenerate mixture of ^{6}Li and ^{40}K and creation of heteronuclear molecules”, *Phys. Rev. A* **81**, 043637 (2010).

[Sta06] P. Staanum, S. D. Kraft, J. Lange, R. Wester, and M. Weidemüller. “Experimental Investigation of Ultracold Atom-Molecule Collisions”, *Phys. Rev. Lett.* **96**, 023201 (2006).

[SK12] D. M. Stamper-Kurn and J. Thywissen. “Chapter 1 - Experimental Methods of Ultracold Atomic Physics”. In: *Ultracold Bosonic and Fermionic Gases*. Ed. by A. L. F. Kathryn Levin and D. M. Stamper-Kurn. Vol. 5. Contemporary Concepts of Condensed Matter Science. Elsevier (2012), 1.

[SK13] D. M. Stamper-Kurn and M. Ueda. “Spinor Bose gases: Symmetries, magnetism, and quantum dynamics”, *Rev. Mod. Phys.* **85**, 1191 (2013).

[Sta04] C. A. Stan, M. W. Zwierlein, C. H. Schunck, S. M. F. Raupach, and W. Ketterle. “Observation of Feshbach Resonances between Two Different Atomic Species”, *Phys. Rev. Lett.* **93**, 143001 (2004).

[Ste08a] J. von Stecher, C. H. Greene, and D. Blume. “Energetics and structural properties of trapped two-component Fermi gases”, *Phys. Rev. A* **77**, 043619 (2008).

[Ste09] S. Stellmer, M. K. Tey, B. Huang, R. Grimm, and F. Schreck. “Bose-Einstein condensation of strontium”, *Phys. Rev. Lett.* **103**, 200401 (2009).

[Ste10] S. Stellmer, M. K. Tey, R. Grimm, and F. Schreck. “Bose-Einstein condensation of ^{86}Sr”, *Phys. Rev. A* **82**, 041602 (2010).

[Ste98] J. Stenger, S. Inouye, D. M. Stamper-Kurn, H.-J. Miesner, A. P. Chikkatur, and W. Ketterle. “Spin domains in ground-state Bose-Einstein condensates”, *Nature (London)* **396**, 345 (1998).

[Ste08b] J. T. Stewart, J. P. Gaebler, and D. S. Jin. “Using photoemission spectroscopy to probe a strongly interacting Fermi gas”, *Nature (London)* **454**, 744 (2008).

[Stw76] W. C. Stwalley and L. H. Nosanow. “Possible "New" Quantum Systems”, *Phys. Rev. Lett.* **36**, 910 (1976).

[Suz08] K. Suzuki, T. Miyakawa, and T. Suzuki. “p-wave superfluid and phase separation in atomic Bose-Fermi mixtures”, *Phys. Rev. A* **77**, 043629 (2008).

[Szu96] J. Szudy and W. E. Baylis. “Profiles of line wings and rainbow satellites associated with optical and radiative collisions”, *Phys. Rep.* **266**, 127 (1996).

[Tag08] M. Taglieber, A.-C. Voigt, T. Aoki, T. W. Hänsch, and K. Dieckmann. “Quantum Degenerate Two-Species Fermi-Fermi Mixture Coexisting with a Bose-Einstein Condensate”, *Phys. Rev. Lett.* **100**, 010401 (2008).

[Tak03] Y. Takasu, K. Maki, K. Komori, T. Takano, K. Honda, M. Kumakura, T. Yabuzaki, and Y. Takahashi. “Spin-singlet Bose-Einstein condensation of two-electron atoms”, *Phys. Rev. Lett.* **91**, 040404 (2003).

[Tak14] T. Takekoshi, L. Reichsöllner, A. Schindewolf, J. M. Hutson, C. R. Le Sueur, O. Dulieu, F. Ferlaino, R. Grimm, and H.-C. Nägerl. “Ultracold Dense Samples of Dipolar RbCs Molecules in the Rovibrational and Hyperfine Ground State”, *Phys. Rev. Lett.* **113**, 205301 (2014).

[Tan10] L.-Y. Tang, Z.-C. Yan, T.-Y. Shi, and J. Mitroy. “Dynamic dipole polarizabilities of the Li atom and the Be^+ ion”, *Phys. Rev. A* **81**, 042521 (2010).

[Tey10] M. K. Tey, S. Stellmer, R. Grimm, and F. Schreck. “Double-degenerate Bose-Fermi mixture of strontium”, *Phys. Rev. A* **82**, 011608 (2010).

[Tha06] G. Thalhammer, K. Winkler, F. Lang, S. Schmid, R. Grimm, and J. Hecker Denschlag. “Long-lived Feshbach molecules in a three-dimensional optical lattice”, *Phys. Rev. Lett.* **96**, 050402 (2006).

[Tho05] S. T. Thompson, E. Hodby, and C. E. Wieman. “Spontaneous dissociation of ^{85}Rb Feshbach molecules”, *Phys. Rev. Lett.* **94**, 020401 (2005).

[Tie10] T. G. Tiecke, M. R. Goosen, A. Ludewig, S. D. Gensemer, S. Kraft, S. J.J.M. F. Kokkelmans, and J. T. M. Walraven. “Broad Feshbach resonance in the ^{6}Li-^{40}K mixture”, *Phys. Rev. Lett.* **104**, 053202 (2010).

[Tie09a] T. G. Tiecke. “Feshbach resonances in ultracold mixtures of the fermionic quantum gases ^{6}Li and ^{40}K”. PhD thesis. University of Amsterdam (2009).

[Tie17] E. Tiemann, *private communication* (2017).

[Tie09b] E. Tiemann, H. Knöckel, P. Kowalczyk, W. Jastrzebski, A. Pashov, H. Salami, and A. J. Ross. “Coupled system $a\,^3\Sigma^+$ and $X\,^1\Sigma^+$ of KLi: Feshbach resonances and corrections to the Born-Oppenheimer approximation”, *Phys. Rev. A* **79**, 042716 (2009).

[Tim01] E. Timmermans. “Degenerate Fermion Gas Heating by Hole Creation”, *Phys. Rev. Lett.* **87**, 240403 (2001).

[Tim99] E. Timmermans, P. Tommasini, M. Hussein, and A. Kerman. “Feshbach resonances in atomic Bose-Einstein condensates”, *Phys. Rep.* **315**, 199 (1999).

[Tis38] L. Tisza. “Transport Phenomena in Helium II”, *Nature (London)* **141**, 913 (1938).

[Toj10] S. Tojo, Y. Taguchi, Y. Masuyama, T. Hayashi, H. Saito, and T. Hirano. “Controlling phase separation of binary Bose-Einstein condensates via mixed-spin-channel Feshbach resonance”, *Phys. Rev. A* **82**, 033609 (2010).

[Tör14] P. Törmä and K. Sengstock. *Quantum Gas Experiments: Exploring Many-Body States*. Imperial College Press (2014).

[Tör16] P. Törmä. “Physics of ultracold Fermi gases revealed by spectroscopies”, *Phys. Scr.* **91**, 043006 (2016).

[Tra16] M.-I. Trappe, P. Grochowski, M. Brewczyk, and K. Rz**k**ażewski. "Ground-state densities of repulsive two-component Fermi gases", *Phys. Rev. A* **93**, 023612 (2016).

[Tre11] A. Trenkwalder, C. Kohstall, M. Zaccanti, D. Naik, A. I. Sidorov, F. Schreck, and R. Grimm. "Hydrodynamic Expansion of a Strongly Interacting Fermi-Fermi Mixture", *Phys. Rev. Lett.* **106**, 115304 (2011).

[Tru01] A. G. Truscott, K. E. Strecker, W. I. McAlexander, G. B. Partridge, and R. G. Hulet. "Observation of Fermi Pressure in a Gas of Trapped Atoms", *Science* **291**, 2570 (2001).

[Tun14] S.-K. Tung, K. Jiménez-García, J. Johansen, C. V. Parker, and C. Chin. "Geometric Scaling of Efimov States in a ^{6}Li–^{133}Cs Mixture", *Phys. Rev. Lett.* **113**, 240402 (2014).

[Tur12] A. V. Turlapov. "Fermi gas of atoms", *JETP Lett.* **95**, 96 (2012).

[Tyl16] M. Tylutki, A. Recati, F. Dalfovo, and S. Stringari. "Dark-bright solitons in a superfluid Bose-Fermi mixture", *New J. Phys.* **18**, 053014 (2016).

[Ulm16] J. Ulmanis, S. Häfner, R. Pires, F. Werner, D. S. Petrov, E. D. Kuhnle, and M. Weidemüller. "Universal three-body recombination and Efimov resonances in an ultracold Li-Cs mixture", *Phys. Rev. A* **93**, 022707 (2016).

[Vai15] V. D. Vaidya, J. Tiamsuphat, S. L. Rolston, and J. V. Porto. "Degenerate Bose-Fermi mixtures of rubidium and ytterbium", *Phys. Rev. A* **92**, 043604 (2015).

[Val17] G. Valtolina, F. Scazza, A. Amico, A. Burchianti, A. Recati, T. Enss, M. Inguscio, M. Zaccanti, and G. Roati. "Exploring the ferromagnetic behaviour of a repulsive Fermi gas through spin dynamics", *Nat. Phys.* **13**, 704 (2017).

[VS09] B. Van Schaeybroeck and A. Lazarides. "Trapped phase-segregated Bose-Fermi mixtures and their collective excitations", *Phys. Rev. A* **79**, 033618 (2009).

[Vas12] W. Vassen, C. Cohen-Tannoudji, M. Leduc, D. Boiron, C. I. Westbrook, A. Truscott, K. Baldwin, G. Birkl, P. Cancio, and M. Trippenbach. "Cold and trapped metastable noble gases", *Rev. Mod. Phys.* **84**, 175 (2012).

[Ven17] W. N. Venables, D. M. Smith, and the R Core Team. *An introduction to R*. `https://cran.r-project.org/doc/manuals/r-release/R-intro.pdf`. Accessed online: 2017-11-25 (2017).

[Viv00] L. Viverit, C. J. Pethick, and H. Smith. "Zero-temperature phase diagram of binary boson-fermion mixtures", *Phys. Rev. A* **61**, 053605 (2000).

[Voi09] A.-C. Voigt, M. Taglieber, L. Costa, T. Aoki, W. Wieser, T. W. Hänsch, and K. Dieckmann. "Ultracold heteronuclear Fermi-Fermi molecules", *Phys. Rev. Lett.* **102**, 020405 (2009). *Erratum: Phys. Rev. Lett.* **105**, 269904(E) (2010).

[Vol75] G. E. Volovik, V. P. Mineev, and I. M. Khalatnikov. "Theory of solutions of a superfluid Fermi liquid in a superfluid Bose liquid", *JETP* **42**, 342 (1975).

[Wac15] L. Wacker, N. B. Jørgensen, D. Birkmose, R. Horchani, W. Ertmer, C. Klempt, N. Winter, J. Sherson, and J. J. Arlt. "Tunable dual-species Bose-Einstein condensates of ^{39}K and ^{87}Rb", *Phys. Rev. A* **92**, 053602 (2015).

[Wan16] F. Wang, X. Li, D. Xiong, and D. Wang. "A double species 23 Na and 87 Rb Bose-Einstein condensate with tunable miscibility via an interspecies Feshbach resonance", *J. Phys. B* **49**, 015302 (2016).

[Wan17] J. Wang, Y. Che, L. Zhang, and Q. Chen. "Enhancement effect of mass imbalance on Fulde-Ferrell-Larkin-Ovchinnikov type of pairing in Fermi-Fermi mixtures of ultracold quantum gases", *Sci. Rep.* **7**, 39783 (2017).

[Wan13] T. T. Wang, M.-S. Heo, T. M. Rvachov, D. A. Cotta, and W. Ketterle. "Deviation from Universality in Collisions of Ultracold $^6Li_2$ Molecules", *Phys. Rev. Lett.* **110**, 173203 (2013).

[Web03a] T. Weber, J. Herbig, M. Mark, H.-C. Nägerl, and R. Grimm. "Bose-Einstein condensation of cesium", *Science* **299**, 232 (2003).

[Web03b] T. Weber, J. Herbig, M. Mark, H.-C. Nägerl, and R. Grimm. "Three-body recombination at large scattering lengths in an ultracold atomic gas", *Phys. Rev. Lett.* **91**, 123201 (2003).

[Wen17] M. Wenzel, F. Böttcher, T. Langen, I. Ferrier-Barbut, and T. Pfau. "Striped states in a many-body system of tilted dipoles", *Phys. Rev. A* **96**, 053630 (2017).

[Wil15] S. Will, D. Iyer, and M. Rigol. "Observation of coherent quench dynamics in a metallic many-body state of fermionic atoms", *Nat. Commun.* **6**, 6009 (2015).

[Wil08] E. Wille, F. M. Spiegelhalder, G. Kerner, D. Naik, A. Trenkwalder, G. Hendl, F. Schreck, R. Grimm, T. G. Tiecke, J. T. M. Walraven, S. J.J.M. F. Kokkelmans, E. Tiesinga, and P. S. Julienne. "Exploring an ultracold Fermi-Fermi mixture: Interspecies Feshbach resonances and scattering properties of ^{6}Li and ^{40}K", *Phys. Rev. Lett.* **100**, 053201 (2008).

[Wil09] E. Wille. "Preparation of an Optically Trapped Fermi-Fermi Mixture of ^{6}Li and ^{40}K Atoms and Characterization of the Interspecies Interactions by Feshbach Spectroscopy". PhD thesis. Innsbruck University (2009).

[Win06] K. Winkler, G. Thalhammer, F. Lang, R. Grimm, J. Hecker Denschlag, A. J. Daley, A. Kantian, H. P. Büchler, and P. Zoller. "Repulsively bound atom pairs in an optical lattice", *Nature (London)* **441**, 853 (2006).

[Wu11] C.-H. Wu, I. Santiago, J. W. Park, P. Ahmadi, and M. W. Zwierlein. "Strongly interacting isotopic Bose-Fermi mixture immersed in a Fermi sea", *Phys. Rev. A* **84**, 011601 (2011).

[Yao16] X.-C. Yao, H.-Z. Chen, Y.-P. Wu, X.-P. Liu, X.-Q. Wang, X. Jiang, Y. Deng, Y.-A. Chen, and J.-W. Pan. "Observation of Coupled Vortex Lattices in a Mass-Imbalance Bose and Fermi Superfluid Mixture", *Phys. Rev. Lett.* **117**, 145301 (2016).

[Yef13] T. Yefsah, A. T. Sommer, M. J. H. Ku, L. W. Cheuk, W. Ji, W. S. Bakr, and M. W. Zwierlein. "Heavy solitons in a fermionic superfluid", *Nature (London)* **499**, 426 (2013).

[Zac06] M. Zaccanti, C. D'Errico, F. Ferlaino, G. Roati, M. Inguscio, and G. Modugno. "Control of the interaction in a Fermi-Bose mixture", *Phys. Rev. A* **74**, 041605 (2006).

[Zac09] M. Zaccanti, B. Deissler, C. D'Errico, M. Fattori, M. Jona-Lasinio, S. Müller, G. Roati, M. Inguscio, and G. Modugno. "Observation of an Efimov spectrum in an atomic system", *Nat. Phys.* **5**, 586 (2009).

[Zah06] N. Zahzam, T. Vogt, M. Mudrich, D. Comparat, and P. Pillet. "Atom-Molecule Collisions in an Optically Trapped Gas", *Phys. Rev. Lett.* **96**, 023202 (2006).

[Zha04] J. Zhang, E. G. M. van Kempen, T. Bourdel, L. Khaykovich, J. Cubizolles, F. Chevy, M. Teichmann, L. Tarruell, S. J.J.M. F. Kokkelmans, and C. Salomon. "P-wave Feshbach Resonances of ultracold ^{6}Li", *Phys. Rev. A* **70**, 030702(R) (2004).

[Zir08] J. J. Zirbel, K.-K. Ni, S. Ospelkaus, J. P. D'Incao, C. E. Wieman, J. Ye, and D. S. Jin. "Collisional Stability of Fermionic Feshbach Molecules", *Phys. Rev. Lett.* **100**, 143201 (2008).

[Zür13] G. Zürn, T. Lompe, A. N. Wenz, S. Jochim, P. S. Julienne, and J. M. Hutson. "Precise Characterization of ^{6}Li Feshbach Resonances Using Trap-Sideband-Resolved RF Spectroscopy of Weakly Bound Molecules", *Phys. Rev. Lett.* **110**, 135301 (2013).

[Zwe12] W. Zwerger, ed. *The BCS-BEC Crossover and the Unitary Fermi Gas*. Vol. 836. Lecture Notes in Physics. Springer, Berlin Heidelberg (2012).

[Zwi03] M. W. Zwierlein, C. A. Stan, C. H. Schunck, S. M. F. Raupach, S. Gupta, Z. Hadzibabic, and W. Ketterle. "Observation of Bose-Einstein Condensation of Molecules", *Phys. Rev. Lett.* **91**, 250401 (2003).

[Zwi04] M. W. Zwierlein, C. A. Stan, C. H. Schunck, S. M. F. Raupach, A. J. Kerman, and W. Ketterle. "Condensation of Pairs of Fermionic Atoms near a Feshbach Resonance", *Phys. Rev. Lett.* **92**, 120403 (2004).

[Zwi05] M. W. Zwierlein, J. R. Abo-Shaeer, A. Schirotzek, C. H. Schunck, and W. Ketterle. "Vortices and Superfluidity in a Strongly Interacting Fermi Gas", *Nature (London)* **435**, 1047 (2005).

[Zwi06a] M. W. Zwierlein, A. Schirotzek, C. H. Schunck, and W. Ketterle. "Direct observation of the superfluid phase transition in ultracold Fermi gases", *Nature (London)* **442**, 54 (2006).

[Zwi06b] M. W. Zwierlein, A. Schirotzek, C. H. Schunck, and W. Ketterle. "Fermionic Superfluidity with Imbalanced Spin Populations", *Science* **311**, 492 (2006).

[Zwi15] M. W. Zwierlein. "Superfluidity in Ultracold Fermi Gases". In: *Novel Superfluids*. Ed. by K.-H. Bennemann and K. J. B. Vol. 2. Oxford University Press, Oxford (2015).

Acknowledgements

Tell me and I will forget
Show me and I may remember
Involve me and I will understand.

Attributed to Confucius, ∼450 BC

This is it; the work of several years accumulated in one booklet. Let me use the last page to express my sincere gratitude and appreciation to all of those who supported, involved, and believed in me throughout my PhD. Thank you so much!

In particular, I would like to thank Prof. Rudi Grimm for giving me the opportunity to do research in his group. I have learned a lot from his expertise and I am grateful for all the feedback, the meetings in Maria Waldrast, and the conferences I could attend. I am indebted to Prof. Florian Schreck for sharing his knowledge of the experimental apparatus and for being my second supervisor as well as for the times I could visit his lab in Amsterdam. It was always a pleasure when Prof. Jook Walraven came to visit us and I would like to thank him for the valuable and constructive discussions.

Doing research is all about sharing knowledge, and I am grateful to the many people I have encountered and those who shaped my knowledge throughout the year. I would like to acknowledge all our theory collaborators and the members of the IQOQI and the ultracold atoms groups in Innsbruck. A special thank you to Bo and Isabella for the good time in the lab and to Andrea and Cosetta for spell-checking my thesis. Thank you Emil, Michael, and all the former/current colleagues from the Dy-K and FeLi(Bo)Kx teams. I'm grateful to Albert, Andi, Cornee, Deborah, Philipp, Lukas, Slava, and Tadas for making my time in and outside of university enjoyable and for exploring both mountains and physics together.

A big thank you to the IQOQI workshops, IT department, and administrative staff for providing us with the framework in which we can do research. I greatly value their work and professionalism and am thankful for the Pilates class which was organized. I would also like to thank Christine and the administrative staff at the university for everything they took care of.

Thank you Aisha, Berit, Johanneke, Lianne, Pauldy, and Steffi for your friendship. A 'heel erg bedankt' to my parents, my brother, and my family for all the support and visits, and a 'Donkschion' to Felix for everything and more.

Rianne
Innsbruck, July 2018